Modelleren van convectief warmtetransport in kantoren met nachtkoeling

Convective Heat Transfer Modelling in Offices with Night Cooling

Kim Goethals

Promotor: prof. dr. ir. -architect A. Janssens
Proefschrift ingediend tot het behalen van de graad van
Doctor in de Ingenieurswetenschappen: Architectuur

Vakgroep Architectuur en Stedenbouw
Voorzitter: prof. dr. ir. -architect P. Uyttenhove
Faculteit Ingenieurswetenschappen en Architectuur
Academiejaar 2011 - 2012

UNIVERSITEIT
GENT

ISBN 978-90-8578-515-6
NUR 950
Wettelijk depot: D/2012/10.500/41

Universiteit Gent
Faculteit Ingenieurswetenschappen en Architectuur
Vakgroep Architectuur en Stedenbouw

Promotor: prof. dr. ir. arch. Arnold Janssens

Universiteit Gent
Faculteit Ingenieurswetenschappen en Architectuur
Vakgroep Architectuur en Stedenbouw
Jozef Plateaustraat 22, B-9000 Gent, België
Tel.: +32(0)9 264 37 42
Fax.: +32(0)9 264 41 85

Dit werk kwam tot stand in het kader van het SBO-IWT project 050154
(agentschap voor Innovatie door Wetenschap en Technologie).

Examencommissie:
prof. dr. ir. Rik Van de Walle (Universiteit Gent, voorzitter)
prof. dr. ir. arch. Arnold Janssens (Universiteit Gent, promotor)
prof. ir. Wim Boydens (Universiteit Gent, secretaris)
prof. dr. ir. Ian Beausoleil-Morrison (Carleton University)
prof. dr. ir. Hilde Breesch (Katholieke Hogeschool Sint-Lieven)
prof. dr. ir. Michel De Paepe (Universiteit Gent)
prof. dr. ir. Erik Dick (Universiteit Gent)
prof. dr. ir. arch. Dirk Saelens (Katholieke Universiteit Leuven)

Proefschrift ingediend tot het behalen van de graad van
Doctor in de Ingenieurswetenschappen: Architectuur
Academiejaar 2011-2012

Impactfactor (dankwoord)

Ongebruikelijke titel voor een dankwoord, maar niet mis te verstaan. Technisch gesproken staat de term impactfactor voor: ‘maat om het relatieve belang van een wetenschappelijk tijdschrift aan te geven.’ Publicaties uit bijvoorbeeld Nature – impactfactor van rond de 30 – halen geregeld de kranten. Toch blijft het doorgaans een kleine stap voor het ‘wereldje’. Voor de onderzoeker in kwestie daarentegen betekent het een grote stap; zo ook mijn traject van de afgelopen jaren. De afgestudeerde anno 2007 is niet meer; voor een groot stuk dankzij een rist ‘indruk-wekkende’ mensen, op én naast de werkvloer. Elk van hen verdient dan ook een plaats in dit dankwoord.

In eerste instantie wil ik mijn promotor, prof. Arnold Janssens, bedanken. Niet alleen vertrouwde hij mij dit onderzoek toe, hij stond ook paraat wanneer nodig. Met zijn veelomvattend of net bijzonder inzicht hielp hij mij telkens opnieuw vooruit. Ook is hij gelukkig erin geslaagd een dynamische onderzoeksgroep uit de grond te stampen. Collega’s bieden tenslotte een broodnodig klankbord. Vreemd genoeg vond ik het ook nog eens leuk tussen die snuiters (plus Anne-Françoise Morel). Zeker het freewheelen blijft mij bij: bovenal interessant/niet oninteressant – al naargelang Jelle (Laverge) of Marc (Delghust) erbij was. Daarnaast kon ik rekenen op een resem experts buiten mijn onderzoeksgroep. Per slot, onderzoek wordt meer en meer multidisciplinair. Zo kon ik voor vragen omtrent experimentele methodes en (numerieke) stromingsmechanica steeds terecht bij prof. Michel De Paepe en zijn medewerkers, in het bijzonder Peter De Jaeger, Henk Huisseune en Marnix Van Belleghem. Ook prof. Bert Blocken, prof. Erik Dick en prof. Marcel Loomans hebben mijn simulatieaanpak destijds onder de loep genomen, waarvoor dank. Verder schat ik de inspanningen van Gilles Flamant, Didier L’Heureux en Philippe Voordecker naar waarde. Samen hebben wij de experimenten in de PASLINK-cel tot een goed einde gebracht. Ook wil ik prof. Tom Dhaene en Ivo Couckuyt vermelden. Beiden hebben mij wegwijs gemaakt in de Matlab SUMO toolbox en met verve de optimalisatie-oefening gevolgd. Prof. Hilde Breesch ben ik eveneens schatplichtig: haar werk was steeds een referentie.

Uiteraard hebben ook familie en vrienden hun stempel gedrukt; zeker mijn ouders en hun partners. Ma, pa, jullie steun en vertrouwen hebben mij geholpen steeds opnieuw grenzen te verleggen. Ook mijn lieve Delphine krijgt een bijzondere plaats. Zonder jouw zorg en steun had ik nooit de tijd en rust gevonden om dit onderzoek af te ronden. Frederik, ook een beetje mijn ‘best man’, verdient daarentegen een ‘Oorkonde van de Vriendschap’. Bedankt om mij af en toe van mijn eiland te halen. Tot slot denk ik aan mijn grootouders. Hoewel zij slechts weinig of niet mij hebben kunnen volgen, toch hebben zij mijn traject sterk bepaald. Iedereen bedankt!

Table of contents

Nomenclature

1	n-dimensional vector with ones	
a	Thermal diffusivity	$m^2.s^{-1}$
A	Surface	m^2
b	Contact coefficient	$J.m^{-2}.s^{-0.5}.K^{-1}$
C	Correlation constant or correction factor	(-) or (-)
c	Heat capacity	$J.kg^{-1}.K^{-1}$
D_h	Hydraulic diameter ($4 \cdot A \cdot P^1$)	m
d	Distance or thickness	m
E	Energy	J
E[I(x)]	Expected improvement	(-)
f	Function value	(-)
F	Momentum force	N
F_s	Safety factor	(-)
g	Gravitational acceleration ($9.81 m.s^{-2}$)	$m.s^{-2}$
g_p	Coefficient of the p^{th} order error term in a Taylor series	(-)
H	Height or distance to the zero point	m or m
h	Heat transfer coefficient or measure of grid spacing/time step or height	$W.m^{-2}.K^{-1}$ or m or s or m
I	Turbulence intensity ($u_{inst} \cdot u_{avg}^{-1} \cdot 100$)	%
J	Jet momentum number ($n \cdot u_{sup} \cdot g^{-1} \cdot 3600$)	(-)
k	Turbulent kinetic energy	m^2s^{-2}
L	Length	m
ℓ	Turbulence length scale	m
M	Molecular weight	$kg.kg^{-1}.mol^{-1}$
$\dot{m}$	Mass flow rate	$kg.s^{-1}$
n	Air change rate	h^{-1}
Nu	Nusselt number. Dimensionless heat transfer coefficient	(-)
P	Power or perimeter	W or m
p	Pressure	Pa
Pr	Prandtl number. Ratio of kinematic viscosity and thermal diffusivity	(-)
Q	Heat flow	W
q	Heat flux	$W.m^{-2}$
R	Thermal resistance or universal gas constant ($8.31 J.mol^{-1}.K^{-1}$) or ratio of solution changes	$m^2.K.W^{-1}$ or $J.mol^{-1}.K^{-1}$ or (-)
r	Refinement ratio	(-)

r	Vector of correlations between **x*** and n sample points	
R	n x n correlation matrix	
Re	Reynolds number. Ratio of inertia and viscous forces	(-)
Ri	Richardson number. Ratio of buoyancy and inertia forces	(-)
$\hat{s}^2$	Variance	(-)
T	Temperature	°C
t	Time	s
u	Velocity	$m.s^{-1}$
V	Volume	m^3
w	Nozzle width	m
W	Width	m
x*	New vector	
$\mathbf{x_i}$	d-dimensional vector	
$\hat{y}$	Mean function value	
$Y(\mathbf{x_i})$	Normally distributed variable	(-)
θ_ℓ, p_ℓ	Parameters part of the kriging correlation function	(-)

Greek symbols

α	Absorptance or inclination angle	(-) or °
β	Volumetric thermal expansion coefficient	K^{-1}
Γ	Diffusivity	$m^{-2}.s$
δ	Penetration depth or uncertainty	m or (-)
Δ	Difference	(-)
ε	Emissivity or error or turbulent dissipation rate	(-) or $m^2.s^{-3}$
ϑ	Turbulence velocity scale	$m.s^{-1}$
λ	Thermal conductivity	$W.m^{-1}.K^{-1}$
μ	Dynamic viscosity or process mean	Pa.s or (-)
ν	Kinematic viscosity	$m^2.s^{-1}$
ρ	Density	$kg.m^{-3}$
σ^2	Process variance	(-)
ω	Specific turbulent dissipation rate	s^{-1}

Subscripts and superscripts

∞	Free stream
a	Air
alu	Aluminium
avg	Average
C,ls	Losses (cooling)
C,nd	Cooling need
cond	Conductive
conv	Convective
cool	Cooling
e	Exterior
eff	Effective
exact	Exact
exh	Exhaust
for	Forced
h	Hydraulic
i	Indoor
inner	Interior side
inst	Instantaneous
int	Internal
l	Local
M	Momentum
meas	Measured
min	Minimum
nat	Natural
op	Operative or operating
ori	Original
outer	Exterior side
p	Order
r	Room
rad	Radiative
regr	Regressed
rep	Representative
set	Set point
sol	Solar
source	Heat source
sup	Air supply
t	Turbulent
tot	Total
tr	Transmission
ve	Ventilation
w	Wall surface

Acronyms

AHU	Air handling unit
alu	Aluminium
BES	Building energy simulation. Numerical modelling of energy related processes in buildings
BL	Boundary layer
BLUP	Best linear unbiased predictor
BM	Box model
CFD	Computational fluid dynamics. Numerical modelling of fluid mechanics
DIRECT	Dividing rectangles
DOE	Design of experiments
EPS	Expanded polystyrene
GCI	Grid convergence index
GLS	Generalized least squares
HDD/CDD (H)	Heating/Cooling degree days (hours)
HRN	High-Reynolds number
LRN	Low-Reynolds number
MC	Mechanical cooling, by chiller(s)
MM	Momentum model
NC	Night cooling
ORMT	Outdoor running mean temperature
PAS	Pseudo-adiabatic shell
PDF	Probability density function
PISO	Pressure-implicit with splitting operators
ply	Plywood
PRESTO!	Pressure staggering option
PVM	Prescribed velocity model
RANS	Reynolds-averaged Navier-Stokes
RE	Richardson extrapolation
regr	Regressed
RNG	Renormalization group
RSM	Reynolds stress model
SBO	Surrogate-based optimization
SGM	Simplified geometrical model
SQP	Sequential quadratic programming
SST	Shear stress transport
SUMO	Surrogate modelling
TC	Thermocouple
TE	Temperature excess hours

Samenvatting

Nachtkoeling, zeker in kantoren, wekt interesse, want het kan het zomercomfort verbeteren en kan de koelbehoefte verminderen. Echter, de mate waarin gebouwontwerpers erin slagen een optimaal ontwerp te maken hangt sterk af van de gebruikte simulatietool. Vandaag de dag zijn standalone energiesimulatieprogramma's (BES) best populair, maar de manier waarop zij de convectieve warmteoverdracht modelleren roept vragen op. Zij modelleren de complexe warmteoverdracht in de grenslaag en het omliggende gebied met behulp van een convectieve warmteoverdrachtscoëfficiënt die doorgaans gebaseerd is op gevalspecifieke experimentele data. Daarom gaat deze thesis na of deze modelleringsmethode volstaat om nauwkeurig de prestatie van nachtkoeling te voorspellen en onderzoekt het verder de invloed van het kamer-/systeemontwerp op de convectieve warmteoverdracht tijdens nachtkoeling.

Eerst illustreert dit werk de bovengenoemde onvolkomenheid van BES. Het begint met een bespreking van de bestaande, empirische convectiecorrelaties die in BES kunnen geïmplementeerd worden. Deze literatuurstudie brengt in het bijzonder de specificiteit van de correlaties aan het licht: de experimentopstelling zelf en de benadering om de correlaties af te leiden beperken de toepassingsmogelijkheden sterk. Vervolgens beschrijft dit werk de gevoeligheidsanalyse die nagaat in welke mate de voorspelde prestatie van nacht koeling in een kantoor in een gematigd klimaat (België) afhangt van de keuze van sommige van de besproken correlaties. Deze deelstudie geeft aan dat het modelleren van de convectieve warmteoverdracht zeker belangrijk is bij nachtkoeling, weliswaar alleen als mechanische koeling overdag ontbreekt. De keuze van de convectiecorrelaties kan zelfs de ontwerpbeslissingen veranderen.

Het volgende hoofdstuk tast aan de hand van experimenten af in hoeverre het kamer-/systeemontwerp in rekening moet gebracht worden bij het modelleren van gemengde convectieve warmteoverdracht. Eerst beschrijft het de uitgevoerde aanpassingen aan de gebruikte PASLINK-cel van het Wetenschappelijk en Technisch Centrum voor het Bouwbedrijf in Limelette (België). De nieuwe configuratie maakt het mogelijk te onderzoeken hoe de convectieve warmteoverdracht en het luchtstromingspatroon in een kleine gekoelde kamer afhangen van het convectieregime, de aanwezigheid van een thermisch massieve vloer en de locatie van de luchttoe-/afvoer. Vervolgens weidt het stuk uit over de integrale manier om de convectieve warmteflux aan de wanden af te leiden. De analyse steunt zoals de meeste voorgaande studies op temperatuurmetingen aan de binnenzijde en binnenin de wanden waarvan de (thermische) eigenschappen gekend zijn. Deze studie maakt echter gebruik van een snel geleidings-/stralingsprogramma om de convectieve warmteflux te bepalen. Dit leidt niet alleen tot een nauwkeuriger bepaling, maar laat ook toe experimenten met veranderende

randvoorwaarden te onderzoeken. De eigenlijke parameterstudie toont aan dat het kamer-/systeemontwerp duidelijk een invloed heeft op de gemengde convectieve warmteoverdracht en dat de bestaande convectiecorrelaties deze bijzonderheden niet in rekening kunnen brengen. Dergelijke nieuwe experimenten zouden heel wat bijbrengen, maar misschien zijn experimenten alleen niet de beste manier om de impact van nog meer parameters te onderzoeken – hoewel zij steeds nodig zullen zijn.

Numerieke stromingsmechanica (CFD) kan een waardevolle aanvulling zijn gezien het sneller meer complete resultaten oplevert, tegen een lagere prijs; weliswaar op voorwaarde dat de CFD-gebruiker zeker is dat de simulatietool toelaat om de werkelijkheid te benaderen en weet hoe de intrinsieke fouten te minimaliseren/kwantificeren. Daarom gaat deze deelstudie eerst in op de belangrijkste CFD-simulatieparameters: het grid, turbulentiemodellering en de beschrijving van de luchttoevoer. Deze literatuurstudie geeft aan dat veel onderzoekers het gebruik van veralgemeende Richardson extrapolatie verdedigen om de fout ten gevolge van het grid te schatten, maar de verschillende visies omtrent de veiligheidsfactor lopen nog steeds uiteen. Daarnaast wijst de literatuurstudie erop dat de keuze van een turbulentiemodel steeds een compromis tussen nauwkeurigheid en rekensnelheid inhoudt. Voor algemene binnentoepassingen schuiven verschillende CFD-gebruikers het RANS RNG k-ε model naar voren. Verder, van de vier mogelijke luchttoevoermodellen blijken slechts twee bruikbaar. Het impulsmodel krijgt doorgaans de voorkeur. Alleen jet-, spleet- en ventielroosters vereisen het boxmodel. Vervolgens beschrijft dit werk de gevoeligheidsanalyse die toont hoe de CFD-aanpak de voorspelde warmteoverdracht beïnvloedt. Deze studie beoordeelt in het bijzonder het grid, de turbulentiemodellering en de beschrijving van de luchttoevoer voor drie convectieregimes in een aangepaste 3-D Annex 20-testkamer. De resultaten geven voor de bestudeerde gevallen aan dat de beschrijving van de luchttoevoer veruit het belangrijkst is. Met andere woorden, CFD-gebruikers moeten een weloverwogen keuze maken uit de verschillende simulatiemogelijkheden, waaronder ook diegene die meer werk vergen.

Het voorlaatste hoofdstuk beschrijft de uitgebreide simulatiestudie die nagaat hoe het kamer-/systeemontwerp van een generiek nachtgekoeld landschapskantoor de convectieve warmteoverdracht beïnvloedt. Dit onderdeel legt eerst uit wat globale optimalisatie op basis van surrogaatmodellering (globale SBO) inhoudt en beschrijft waarom dit onderzoek een dergelijke methode toepast. Deze optimilisatieprocedure gaat iteratief de volledige ontwerpruimte af op zoek naar datapunten met de grootste informatiewinst en werkt het surrogaatmodel bij met de resultaten van de overeenstemmende simulaties. Op die manier verbetert deze procedure gelijktijdig de globale nauwkeurigheid van het surrogaatmodel en de nauwkeurigheid rond optima, aan de hand van een beperkter aantal simulaties dan bij klassieke procedures. Desondanks, het doel van globale SBO blijft optimalisatie; het surrogaatmodel is slechts een extraatje. Het tweede onderdeel van dit hoofdstuk beschrijft het experimenteel ontwerp. Het omvat een beschrijving van de configuratie van het experiment, een overzicht van hoe de geometrie-/gridgenerator, het numeriek stromingspakket en de

surrogaatmodelleringssoftware communiceren en details omtrent de CFD-aanpak en de surrogaatmodellering. De configuratie van het experiment is gebaseerd op het 2-D Annex 20-ontwerp. Dit referentiegeval laat toe om eenvoudig een aantal parameters te definiëren voor de globale SBO-studie. De onderzochte kamer-/systeemontwerpparameters zijn onderverdeeld in ventilatieconcept, thermische massaverdeling, geometrie en drijvende kracht voor de convectieve warmteoverdracht. Het hoofdstuk sluit af met een grondige bespreking van de simulatieresultaten. De analyse wijst uit dat de verdeling van de thermische massa eerder dan het ventilatieconcept de maximaal haalbare convectieve warmteflux bepaalt. Gevallen met een thermisch massieve vloer leiden tot duidelijk hogere convectieve warmtefluxen dan wanneer zich thermische massa aan het plafond bevindt. Daarnaast blijkt het doorgaans goed om de luchttoevoer bovenaan de wand te plaatsen. De positie van de afvoer is meestal van ondergeschikt belang. Alleen bij enkelzijdige ventilatie is de positie van de afvoer een kritieke parameter.

Het laatste hoofdstuk bevat een korte samenvatting en blikt vooruit op mogelijke toekomstige onderzoekspistes. In het bijzonder met de globale SBO-studie draagt dit werk bij tot een verbeterde BES-modellering. Enerzijds reiken de surrogaatmodellen optimale ontwerpoplossingen aan waarvoor nieuwe convectiecorrelaties kunnen afgeleid worden. Anderzijds kunnen afgeleide, meer globaal accurate surrogaatmodellen gekoppeld worden met BES.

Summary

Night cooling, especially in offices, attracts growing interest. For, it can improve the summer comfort and can lower the cooling need. However, the extent to which building designers succeed in finding an optimal night cooling design depends strongly on the simulation tool they use. Today, stand-alone building energy simulation (BES) programs are quite popular, but the way they model the convective heat transfer raises questions. They model the complex heat transfer in the boundary layer and the surrounding field by a convective heat transfer coefficient which relies primarily on case-specific experimental data. Therefore, this thesis evaluates whether this modelling approach suffices to accurately predict the night cooling performance and further investigates the impact of the room/system design on the convective heat transfer during night cooling.

First of all, this work exemplifies the aforementioned deficiency of BES. It starts with a review on existing empirically derived convective heat transfer correlations which are possibly suited for implementation in BES. This literature review brings especially to light the particularity of the correlations: the experimental setup itself and the approach to derive the correlations strongly limit the applicability of the correlations. Subsequently, this work describes the BES-based sensitivity analysis which evaluates the impact of some of the reviewed correlations on the predicted night cooling performance in an office room in a moderate climate (Belgium). This analysis reveals that for night cooled spaces, without mechanical cooling by day, the convective heat transfer modelling is important. The choice of the convection correlations can even alter the design decisions in a BES-based analysis.

The next chapter describes the experimental study which assesses to what extent it is necessary to include more room/system design parameters to model mixed convection heat transfer. It first describes the makeover of the used PASLINK cell at the Belgian Building Research Institute in Limelette (Belgium). The new setup enables to study how the convective heat transfer and the airflow pattern in a small cooled room relate to the convection regime, the presence of a floor with a high heat storage capacity and the position of the air supply/exhaust. Subsequently, this section dwells on the used integral way to derive the convective heat flux at the wall elements. The analysis relies like most earlier works on temperature measurements on the top and on the inside of the walls of which the (thermal) properties are known. However, this study deploys a fast-running conduction/radiation model to derive the convective heat flux. This enables a more accurate determination and allows to investigate experiments with changing boundary conditions. The actual parametric analysis shows that the room/system design significantly affects the mixed convection heat transfer and that existing convection correlations cannot take such particularities into account. To this end,

researchers can perform new experiments. However, experiments alone are perhaps not sufficient to study many parameters which apply to a wide range – even though they will always be needful.

Computational fluid dynamics (CFD) can be a valuable supplement to experiments as it provides much faster, more complete results, at a reduced financial cost; on condition that CFD users make sure that the simulation tool can accurately represent reality and know how to address the inherent error sources. Therefore, the next chapter first discusses the most important CFD simulation factors: the grid, turbulence modelling and the description of air supply diffusers. This literature review reveals that many researchers support the use of generalized Richardson extrapolation to estimate the error due to the grid, in spite of the many shortcomings. However, the various viewpoints on which safety factor to use have not converged yet. Next to it, the review indicated that the selection of a turbulence model is always a compromise between accuracy and computing effort. Many CFD users put forward the RANS k-ε model for general indoor airflow studies. Further, out of the four available diffuser modelling methods, only two seem useful. The momentum model usually gets preference. However, diffusers with complex mixing such as nozzle, slot and valve diffusers necessitate the box model. Subsequently, this work describes the CFD-based sensitivity analysis which assesses how the simulation approach influences the convective heat transfer. More specifically, this study evaluates the impact of the grid, turbulence modelling and the diffuser modelling approach for three convection regimes in a modified 3-D Annex 20 test room. The results indicate that, for the cases at hand, the diffuser modelling approach influences the predictions by far the most. In conclusion, CFD users have to consciously weigh up the simulation options for the case at hand, including the ones which take considerable effort to implement.

The last but one chapter of this work describes the extensive simulation study which evaluates how the room/system design affects the convective heat transfer in a generic night cooled landscape office. It first introduces the concept of global surrogate-based optimization (SBO) and explains why it is so useful for this study. This optimization procedure iteratively scans the complete design space for new data points which provide the greatest information gain and updates the surrogate model with the results of the corresponding simulations. This way, it enhances concurrently the global accuracy of the surrogate model and the accuracy near optima, through fewer simulations. Yet, the goal of global SBO remains optimization; the surrogate model is merely a bonus. The second section discloses the actual experimental design. It includes a description of the simulation experiment setup, an overview of how the geometry/grid generator, the CFD solver and the surrogate modelling software all fit together and details on both the CFD simulation approach and the surrogate modelling. The simulation experiment setup is based on the 2-D Annex 20 case. This simple reference case enables a straightforward parameterization for the global SBO study. The investigated room/system design parameters are subdivided into ventilation concept, thermal mass distribution, geometry and driving force for convective heat transfer. The chapter concludes with an in-depth discussion of the simulation results. The analysis reveals that the thermal mass distribution rather than the ventilation

concept determines the maximum attainable convective heat flux. Cases with thermal mass at the floor produce significantly higher convective heat fluxes than cases with a thermally massive ceiling. Next to it, it is usually not a bad choice to put the air supply at the top. The position of the exhaust is usually not that important, except in case of single sided ventilation.

The final chapter wraps up. First, it summarizes the most important conclusions and, then, brings up future research. In particular with the global SBO study, this work contributes to the advancement of BES modelling. On the one hand, they indicate profitable design solutions for which new convection correlations can be derived. Or derived more globally accurate surrogate models can be coupled with BES.

1

Introduction

This first chapter motivates this research effort and puts it into a larger perspective. The research topic is introduced by explaining the concept of night cooling and its relevance. Next, the study goes into the parameters influencing the night cooling performance. The second part of this chapter focuses on the state of the art in modelling heat transfer between indoor air and materials as this coupling greatly impacts upon the night cooling performance. The chapter concludes with a formulation of the research aim.

1.1 Background

1.1.1 Increasing cooling energy demand

What makes our planet fit for life? Is a mobile planet necessary for the birth of life or is life essential for important processes to emerge? Anyway, mankind is the first species which changes planet Earth, consciously. The IPCC-report states there is very high confidence that the global average net effect of human activities since 1750 has been one of warming [1]. That is, since the Industrial Revolution human activity has increased the concentration of greenhouse gases considerably. In particular burning massive amounts of fossil fuels tilts the scales. Unfortunately, fossil fuel resources – and especially oil – will remain the world's vital energy source for many years to come, even under the most optimistic assumptions about the pace of development and deployment of alternative technology [2]. Moreover, even though these resources can meet the demand until 2030, the cost to extract and deliver them is doubtful, increasing the energy prices. Preventing catastrophic scenarios, such as irreversible damage to the global climate or energy 'wars',

necessitates major policy action. The Kyoto protocol may serve as an example: in 1997 the developed countries committed themselves to reduce their collective emissions of six key greenhouse gases by 2008-2012 by 5.2% from the 1990 level [3]. Or the so-called 20-20-20 targets set by the EU: a reduction in EU greenhouse gas emissions of at least 20%, 20% of EU energy use to come from renewable resources and a 20% reduction in primary energy use, all to be met by 2020 [4].

According to the European Commission, buildings are responsible for about 40% of the total final energy demand throughout the projection period 1990-2030 [5]. Currently space heating and other heat uses dominate the final energy demand in most building types. However, in most European countries – even those located in cooler climates like in Central and Northern Europe – the air conditioned floor area is expected to double by 2020 in comparison with 2000 [6, 7]. And without doubt offices and commercial buildings will account for the largest share [8, 9]. Not only the increasing thermal insulation levels raise the cooling need, but also the higher internal and solar heat loads do [5]. And as if that is not enough the climate warming (e.g. [10-16]), the urban heat island effect [17-19] and higher comfort expectations [20-22] increase the cooling need too. Using only air conditioning systems to meet the increasing cooling demand will lead to a significantly higher energy use and will oblige the power generating industries to foresee additional power plants to satisfy the peak electricity demand. And this obviously increases even more the environmental and economical cost [10, 23]. Therefore, addressing successful solutions to counterbalance the effects of increasing cooling energy use in buildings is a necessary condition for the future.

1.1.2 Night cooling: a valuable alternative

At the level of the air conditioning systems, possible solutions include district cooling based on waste heat (e.g. [24, 25]) and more efficient air conditioning equipment. However, lowering the cooling demand may be as or even more effective. First of all, redesigning the urban environment influences the urban heat island effect. Secondly, adapting buildings to their specific environmental conditions – described as passive cooling by Santamouris and Assimakopoulos [26] – greatly contributes to a reduction of the cooling demand. These last-mentioned authors classified passive cooling into three categories. Solar and heat protection lower the heat load: e.g. solar shading, thermal insulation and occupant controlled lighting. Heat dissipation addresses an environmental heat sink: e.g. evaporative cooling and increased daytime ventilation. Heat modulation techniques use the thermal storage capacity of the inner building mass as a sink. Last-mentioned technique in conjunction with night cooling holds a significant potential for especially non-residential buildings like offices and commercial buildings, as experimentally shown by, amongst others, Ruud et al. [27], Allard et al. [28], Blondeau et al. [29], Zimmerman and Andersson [30] and Høseggen [31]. During cool nights, ventilation is applied to cool down the interior building fabric. The following day, the building elements with a high heat storage capacity – renamed to thermal mass – absorb the heat gains in the building by solar and infrared radiation and indoor air convection. As a result, night cooling reduces the peak air

temperatures and the operative temperatures and it creates a time lag between the occurrence of external and internal maximum temperatures [32-36]. By way of example, Figure 1.1 displays the frequency distribution of the daytime operative temperature T_{op} in a reference room and a similar room with night cooling, measured by Blondeau et al. [29]. There is a clear translation of the reference room curve to the low T_{op} values and a drop from 26.5°C to 25°C of the average T_{op}. This means that thanks to night cooling building users can enjoy an improved thermal comfort while clients can possibly build smaller mechanical cooling plants – or even leave them out – and can operate their buildings more efficiently. Also the reduction of the peak cooling demand would be of great interest to the power generating industries.

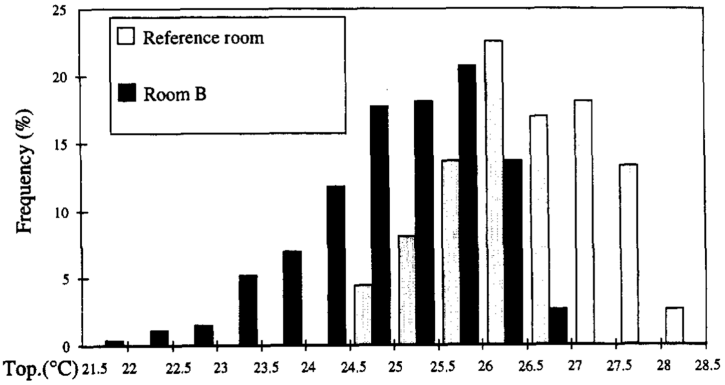

Figure 1.1: Operative temperature in a reference office room and a similar office room with night cooling [29]

1.1.3 Practical implementation of night cooling

Building designers who want to implement night cooling need to choose first and foremost whether or not fan power is used to move the air through the building. Saying that a building is mechanically ventilated means that fan power is used to supply and/or exhaust air. Natural ventilation indicates that the ventilation relies on the natural forces of wind and buoyancy. Mechanical systems generally offer a higher flexibility and are less weather dependent. However, they are more expensive to build, require extra operating energy and need more maintenance. Secondly, designers need to define the ventilation concept. Single-sided ventilation relies on one or more openings on one side only of the ventilated space. There is cross ventilation if ventilation openings are on both sides of the enclosure. The term stack ventilation is used to describe those ventilation concepts that utilise buoyancy to promote an outflow from the building, thereby drawing fresh cool air in via ventilation openings at a lower level. In case of under floor ventilation or ventilation via the ceiling air is supplied via one of the two horizontal surfaces of the space. Thirdly, the implementation of night cooling also comprises the determination of the air supply types. Natural ventilation devices include openable

windows, air bricks and ventilators. If the air supply is fan assisted it concerns one of the following different types: nozzle, valve, displacement, grille, slot, ceiling or vortex diffusers. Finally, building designers need to decide which building elements with a high heat storage capacity they make accessible: (parts of) the walls, the floor and/or the ceiling.

There are numerous examples of buildings with night cooling, of which some are textbook cases of integrated design. For example, the design of the police station of Schoten by Huiswerk Architecten is expressly tailored to the natural ventilation system, which is also used for night cooling (Figure 1.2). The building is organised around two atria which act as chimneys, exhausting hot air as it rises up through the atrium and out windows near the roof. The opening of the panels on top of the windows of the different zones and of the windows in the atria is automatically controlled by the indoor air quality during the heating season and additionally by the indoor temperature during summer. Moreover, during warm summer months the panels of the zones and the windows of the atria are completely open to achieve night cooling. The floors and the walls made out of concrete are intentionally left unfinished to make as much thermal mass as possible accessible. Another inspiring example is the courthouse of Antwerp by Richard Rogers. The building is designed with an eye to maximal use of natural light and natural ventilation: three wings on the right and the same number on the left, face to face, come together in the hall. The courtrooms, located under the expressive roof, are separated from the lower offices by a technical floor. During the winter and summer months the hygienic ventilation of the offices is fan assisted: floor diffusers in the raised floor supply (conditioned) air while exhaust ducts lead the indoor air back to the air handling unit (AHU). In mid-season single sided natural ventilation needs to guarantee a good indoor environment. During warm summer nights that same natural ventilation system is used to achieve primary night cooling. If daytime temperatures are so high that this natural night cooling would no longer be sufficient, mechanical night cooling takes over: outside air is supplied through the floor diffusers and the indoor air is exhausted through the ventilators. The concrete ceiling makes up the sole thermally massive element.

These two examples show only two combinations of the aforementioned design possibilities. Table 1.1 shows that there are many more. Some combinations even seem incompatible. For example, the offices of SD Worx (Kortrijk) and the police station in Schoten rely both on natural stack ventilation with air supply near the ceiling, but have accessible thermal mass at different locations, i.e. at the ceiling respectively at the floor. This indicates that there are different views on how to design a night cooled building.

Figure 1.2: Police station Schoten (Belgium) with natural night cooling (stack ventilation and air supply via windows)

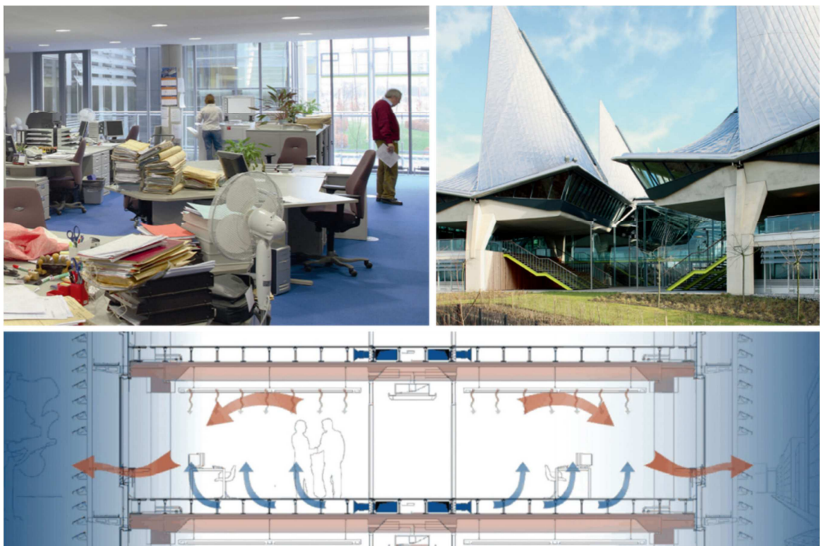

Figure 1.3: Courthouse Antwerp (Belgium) with mechanical night cooling (under floor ventilation and air supply via diffusers)

Table 1.1: Overview of choices made in the design of night cooling in some recently built office buildings in Belgium

Project	Driving force	Concept	Supply type	Thermal mass
IVEG (Hoboken)	Natural	Stack	Ventilators	Floor/ partly ceiling
SD Worx (Kortrijk)	Natural	Stack	Windows	Ceiling
Renson (Waregem)	Natural	Stack	Ventilators	Ceiling
Courthouse (Antwerp)	Natural/ mechanical supply	Single/ Floor	Ventilators/ diffusers	Ceiling
Unilin Flooring (Wielsbeke)	Natural	Cross	Ventilators	Floor
Port of Ghent (Gent)	Mechanical supply	Floor	Diffusers	Ceiling
Omega Pharma (Nazareth)	Mechanical exhaust	Cross	Ventilators	Ceiling
CIT Blaton (Schaarbeek)	Natural/ mechanical exhaust	Cross	Windows	Floor/ ceiling
Ufo (Gent)	Natural/ mechanical exhaust	Cross	Ventilators	Floor
Police station (Schoten)	Natural	Stack	Ventilators	Walls/ floor
Aéropolis II (Brussel)	Mechanical exhaust	Cross	Windows	Ceiling
Keppe Kouter (Aalst)	Natural/ mechanical exhaust	Cross	Ventilators	Partly ceiling

1.1.4 Parameters influencing night cooling performance

Numerous studies (e.g. [26, 34, 37]) identified the main parameters influencing night cooling performance. Although the typical classification states climate, building, system and occupancy, this introductory review goes back to the three basic elements of night cooling: the supply of cool air, the ability to store heat and the related heat transfer.

Supply of cool air

Introducing a larger change rate of cool air during the night increases the available heat sink. However, natural ventilation systems cannot supply ever increasing airflow rates. Meanwhile, in case of mechanical ventilation, higher rates necessitate supplementary fan energy, possibly counterbalancing the saved cooling demand [38]. Considering this, primarily the climate determines to what extent cool air is available. In general, the application of night cooling is more suitable in climates with large diurnal temperature differences. Especially in arid and desert regions the daytime outdoor temperature differs strongly from the relatively low night temperature. Further, moderate and cool climates have in general a low nighttime temperature. While early studies like Szokolay [39] proposed minimum requirements, more recent studies derived relations between the diurnal temperature range and the night cooling performance – defined by the increased thermal comfort [33] or the extra cooling capacity [40]. Meanwhile, authors like Givoni [34] and Van der Maas and Flourentzou [41] introduced an additional boundary condition: the daily mean temperature and relative humidity of the outside air during cooling season should be in the comfort range. Thus, because of a small diurnal temperature range and a high mean temperature and relative humidity, in warm, humid climates no benefit would be drawn from night cooling. However, plentiful researchers have demonstrated experimentally [42-44] or analytically [45, 46], that even in warm, humid climates night cooling in conjunction with thermal mass can be helpful. By recently mapping out the climate suitability for night cooling, authors like Axley and Emmerich [47] and Artmann et al. [48] went a step further. However, these maps have to be continuously updated, primarily because of the high variability of climatic conditions and the uncertain development of global warming – as demonstrated by, amongst others, Roaf et al.[49] and Eicker et al. [50].

Heat storage

As mentioned before, heat storage in the internal mass is necessary as the phase difference between heat transfer to and from the building structure has to be bridged. As reviewed by Goulart [42], numerous methods are available to quantify the heat storage capacity. A particularly popular method, developed by Loudon [51], defines the admittance as the ability of a building component to store and release energy over a daily periodic cycle. This parameter is actually defined as the ratio of heat flux variation to temperature variation during a 24-hour cycle. The higher the admittance, the larger the absorption caused by a fluctuating surface temperature. A large admittance requires large values of the volumetric specific heat capacity ρc and the thermal conductivity λ. The square root of these thermophysical properties defines the contact coefficient or effusivity b (Eq. (1.1)). The usage of heavy materials without insulating finishes to the inside environment, results in a high effusivity as well as a large admittance [52-54].

$$b = \sqrt{\rho \cdot c \cdot \lambda} \tag{1.1}$$

The same properties – rearranged as the thermal diffusivity a – determine, together with the period of temperature variation T, the depth δ that the diurnal wave reaches within the storage material (Eq. (1.2)). Materials with higher thermal diffusivity are more effective for cyclic heat storage at greater depth. For diurnal heat storage and release, the penetration depth equals five to ten centimetres in case of stone materials [55-57].

$$\delta = \sqrt{\frac{\lambda \cdot T}{\pi \cdot \rho \cdot c}} = \sqrt{\frac{a \cdot T}{\pi}} \tag{1.2}$$

Heat transfer

Obviously the convective heat transfer links the two previous elements, i.e. supply of cool air and heat storage. As a matter of fact, convective heat transfer occurs by virtue of a temperature difference between the air and the material surface. That same temperature difference, the fluid motion and the heat transfer surface area eventually determine the convective heat flow. Logically, increasing the temperature difference, enhancing the fluid motion and/or enlarging the heat transfer surface area result in a higher convective heat flow. However, in practice building designers also need to take into account extra requirements on acoustics, aesthetics and integration of high level services. For example, many building designers include a raised floor to hide cable networks, power cables, plumbing and heating systems. In such cases, they shield the thermally massive elements, which during daytime cannot cool the interior by radiation and, if the worst (that is, if the supply air does not pass through the void) by convection. Designing a well-performing night cooling system thus requires a well-considered analysis of the impact of the room/system design on the convective heat transfer, as put forward by many studies (e.g. [33, 35, 42, 58-60].

1.1.5 Convective heat transfer is a complex mechanism

To better explain what convective heat transfer is, this section discloses a well-elaborated example: a partly heated plate along which air flows (Figure 1.4(a)). This case involves a so-called turbulent boundary layer under equilibrium conditions, i.e. small (ideally zero) pressure gradients, a local equilibrium between generation and dissipation of turbulent energy and a constant (uniform) shear stress and heat flux in the near-wall region [61]. Just such conditions lead to a characteristic shape of the momentum and thermal boundary layer profiles. Figure 1.4(a) already reveals some basic features. The air near the solid boundary has zero velocity relative to the boundary (i.e. the no-slip condition). From there on, the velocity in the boundary layer increases until it reaches the outer flow velocity u_∞. Meanwhile, the local air temperature goes from the wall temperature T_w to the free stream temperature T_∞. Somewhat like the velocity profile, the temperature does not taper uniformly.

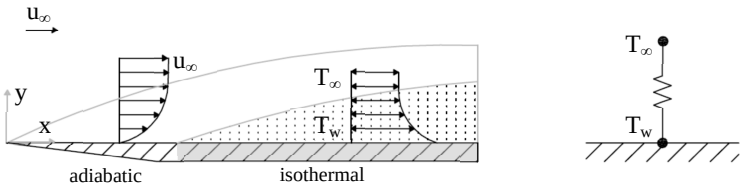

Figure 1.4: (a) Convective heat transfer for flow along a flat plate which is heated at a constant temperature T_w. Locating the heated part farther downstream of the leading edge enables to distinguish the momentum boundary layer (white area) from the thermal boundary layer (dotted area), (b) simplified way of representing convective heat transfer, i.e. by means of a thermal resistance and a temperature difference

Putting the dimensionless expressions of the velocity u^+ and the temperature T^+ against the dimensionless wall distance y^+ reveals a lot more (Figure 1.5). For that matter, Eq. (1.3)-(1.5) define these dimensionless quantities. Here, the parameter y is the distance normal to the wall, T(y) the temperature at y and q_{conv} the heat flux at the wall. Meanwhile, u_τ is the friction velocity at the wall, which on its turn depends on the wall shear stress τ_w and the fluid density ρ.

$$y^+ = \frac{u_\tau \cdot y}{\nu} \tag{1.3}$$

$$u^+ = \frac{u}{u_\tau} \tag{1.4}$$

$$T^+ = \frac{\rho \cdot c \cdot u_\tau \cdot [T_w - T(y)]}{q_{conv}} \quad where \; u_\tau = \sqrt{\frac{\tau_w}{\rho}} \tag{1.5}$$

Figure 1.5 indicates four regions, of which the first three are usually bundled into the so-called inner region. Closest to the wall, the viscous or laminar sublayer occurs. In this thin layer, momentum and heat transfer basically rely on diffusion (viscosity and thermal diffusivity) and, as a result, the velocity and the temperature depend linearly on the distance to the wall. On the other side of the inner region, inertia effects dominate and mainly turbulence transports momentum and heat. Here, logarithmic profiles apply to u^+ and T^+. In the buffer layer in between, neither law holds; the two laws basically blend. Outside the inner region, viscous effects induced by the wall are no longer of any importance. Now, the velocity-defect law prevails: the velocity and temperature are solely function of the boundary layer thickness and the free stream conditions. For more details, the reader is referred to the works of Cebecci and Bradshaw [62] and Schlichting and Gersten [63]. Note that boundary layer profiles for non-equilibrium flows, such as separated boundary layers, and for rough walls will be different from those presented in Figure 1.5.

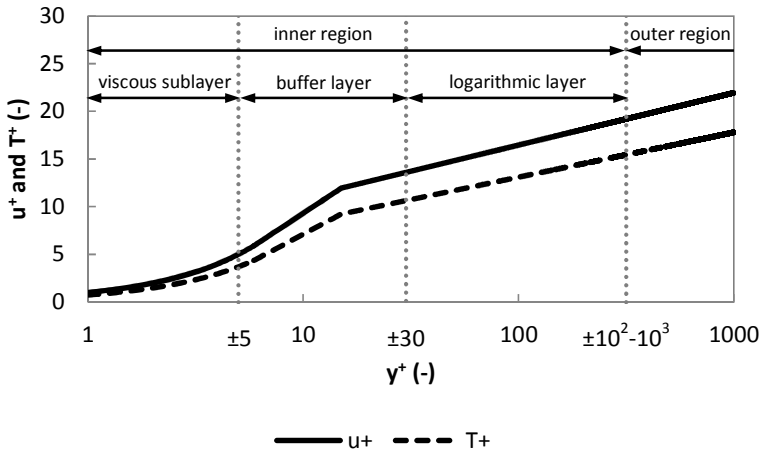

Figure 1.5: Dimensionless velocity ($u^{+)}$ and temperature (T^{+}) boundary layer profiles as a function of y^{+} (logarithmic scale)

Clearly, the convective heat transfer mechanism is far more complex than e.g. conduction; all the more so, because the driving force causing the air to flow affects the near-wall behaviour. Natural convection alludes to fluid motion as a result of density differences induced by heat transfer while fluid circulation produced by an external agent is forced convection. Saying that mixed convection occurs means that the fluid moves due to density differences as well as an external agent. Also the mechanism of fluid flow has a profound influence: chaotic movement of fluid particles in turbulent flow results in a higher convective heat transfer than laminar flow. Meanwhile, the driving force and the mechanism of fluid flow intertwine with, among other things, the operational state of the HVAC equipment, the surface orientation and its temperature, the temperature of the local air adjacent to the surface and the location of obstacles. Obviously, the extent to which building designers succeed in evaluating the impact of the room/system design on the convective heat transfer depends strongly on the simulation tool they use. Therefore, the next section reviews the state of the art in modelling.

1.2 State of the art in modelling

The 1970s energy crisis and the advent of information technology led to the development of computer-based building simulation. Now, substantial improvements in computing power, algorithms and physical data have made it possible to simulate physical processes at levels of detail and time scales, which were not feasible only a few years ago. Also modelling HVAC systems and associated (air)flow phenomena in the context of building design and building performance evaluation, is rapidly gaining more and more interest in both the building and environmental engineering communities [64]. Simulation-based information truly can improve quality, efficiency and productivity in the building industry as well as make innovation easier – as shown by, amongst others, Clarke [65]. First, modelling helps designers to decide among different concepts. Secondly, these tools enable architects and engineers to demonstrate code compliance [66]. Thirdly, they provide estimates of operation and maintenance costs – which is valuable for home builders and developers. Finally, by using modelling methods as a cost-effective alternative to experiments, researchers can improve the understanding on the performance of buildings related to thermal comfort and energy use [67].

The sophistication of an energy calculation procedure depends on the necessary detail of the energy process representation, and, thus, on the purpose. Allowing coarse distinctions, possible categories include: general or domain-specific, open-closed, stand-alone or integrated and sequential or simultaneous. However, the modelling community mostly suggests the distinction between (quasi-)steady-state and dynamic methods – or better analytical approaches versus numerical methods [64]. The difference lies in treating time as an independent variable. As a matter of fact, numerical methods model the time-dependent operation of equipment and variation in system capacity (which usually implies subhourly time steps) and the thermal storage itself. And precisely this feature appeals to a growing number of building designers [68]. Therefore, the following describes only the numerical methods in more detail, first in accordance with the classical breakdown, at a later stage according to a classification based on the approach to model convective heat transfer.

1.2.1 Classical breakdown

Building energy simulation

Today's building energy simulation programs (BES) not only include advanced heat transfer models such as ray-tracing for view factor calculation together with radiosity models [69, 70], but also enable to model other processes like illumination [71, 72] or moisture transport in fabric [73, 74]. However, there is a long history behind it.

The first dynamic numerical simulation methods appeared in the mid-1960s (e.g. [75, 76]). These early models, lumped together as the loads-systems-plant approach subdivide the problem into three sequential steps, because of limited and expensive computing resources. First they calculate the building's heating/cooling loads applicable to rather large time steps, then model the distribution systems of energy (e.g. fans, heating/cooling coils, air diffusers…) to ultimately place this energy demand on the plant's energy conversion systems (i.e. boilers/chillers) and related equipment (e.g. circulation pumps, cooling towers…). Obviously, the sequential nature neglects interactions between climate, building, systems, plant and occupants. Meanwhile, in 1967 Stephenson and Mitalas [77] pioneered with their response factor method. Their method made it possible to simulate transient phenomena (e.g. heat transfer through opaque fabric) by decomposing the complex nonlinear heat transfer system into a summation of responses of the component parts. Later, researchers expanded the response factor approach of Stephenson and Mitalas to calculating instantaneous space loads (i.e. the weighting factor or room surface factor method), which made the loads-systems-plant approach redundant [78]. Basically, the adopted air temperature weighting factors represent a transfer function that relates the indoor air temperature to the net energy load of the room. The weighting factors for a particular heat source are determined by introducing a unit pulse of energy from that source into the room's network. The network is a set of equations that represent a heat balance of the room. Yet, a more flexible alternative was the heat balance approach suggested by, amongst others, Kusuda [79]. It also applies the first law of thermodynamics for outside and inside surfaces and the inside air, but in a more fundamental way. A heat balance equation is written for each surface and one for the indoor air. Subsequently, this set of equations is solved for the unknown surface and air temperatures. Once the temperatures are known, they are used to calculate the corresponding heat fluxes. The importance of this heat balance approach lies in the fact that it leaves out some assumptions of linearity. For example, the convective coupling between air and surfaces can now respond to thermal states within the room, instead of being treated as a constant. Yet, these methods still applied the linear response factor method to calculate fabric transmission, until the late 1970s. Then, numerical discretisation techniques were increasingly used at the expense of the linear response factor method. Essentially, these techniques extent the concept of heat balances to all relevant building components. Having discretised enclosure elements into a finite number of nodes, energy balance equations provide information on e.g. the temperature inside each element. Finally, in the 1980s researchers like Mclean [80] and Tang [81] integrated more advanced models of HVAC systems.

Airflow modelling

Meanwhile, parallel work on airflow modelling has been ongoing. However, not until the mid-1980s, BES and airflow simulation started to converge (e.g. [82, 83]), considerably advancing predictions since then. These airflow simulation programs are either used stand-alone or are coupled with BES, supplying data on e.g. interzonal airflow rates or even convective heat transfer related to the airflow pattern. The available airflow simulation approaches include (multi)nodal, zonal and computational fluid dynamics (CFD) models (Figure 1.6).

The (multi)nodal approach represents a zone – possibly corresponding to several physical zones – by a single calculation node with uniform properties. In other words, the air in the zone is considered to be well-mixed. The term 'multi' points to modelling different interacting air nodes and is inherently coupled to today's understanding of BES programs – of which CAPSOL [84], ESP-r [69], EnergyPlus [70] and TRNSYS 16 [85] are well-known examples. These programs have been extended many times with airflow network models, which predict airflows between the zones and between the zones and the outside climate trough windows, cracks, doors, ducts… Multinodal models, such as CONTAM [86] and COMIS [87], fairly predict air infiltration and contaminant transport, at least under well-mixed conditions [88-91]. Zonal models (e.g. TRNSYS 17 [92]) on the other hand, divide one physical zone into a limited amount of calculation cells, which does allow for modelling distributions in a single space. Usually they use mass and energy conservation laws together with a 'degraded' equation for momentum to relate mass flow between the zones to the corresponding pressure differential [93, 94]. However, the representation of momentum conservation poorly predicts driving flows such as thermal plumes or jets and, thus, several authors [93, 95-97] introduced standard profiles of e.g. free jets and wall jets, which applied to a certain region in the computational domain – which necessitates prior knowledge. Finally, CFD models divide, like zonal models, a single zone into multiple calculation cells. However, they solve the complete set of mass, energy and momentum – or Navier-Stokes – equations. These equations can be solved with limited use of computational resources for laminar flow – i.e. when a fluid flows in parallel layers. In buildings, however, the flow is turbulent (i.e. characterized by chaotic, stochastic changes) and is harder to calculate. As a matter of fact, simulating all turbulent motions in building enclosures (i.e. direct numerical simulation or DNS) is unattainable for some time to come because of the large computational and economical costs [98]. DNS is only suitable for the study of simple problems using supercomputers. Therefore, in CFD the effects of turbulence are usually modelled, by time averaging the instantaneous Navier-Stokes equations (i.e. Reynolds averaged Navier-Stokes or RANS) or by calculating only the large scale turbulent motions (eddies), determined by filtering (i.e. large eddy simulation or LES), or by combining these approaches. Still, the above CFD approaches are significantly more demanding than zonal models, limiting a CFD analysis to a small number of zones in a building for only a limited period of physical time, as shown by e.g. Off et al. [99]. Nevertheless, CFD based on coarse grids can result in a higher accuracy than zonal models [100].

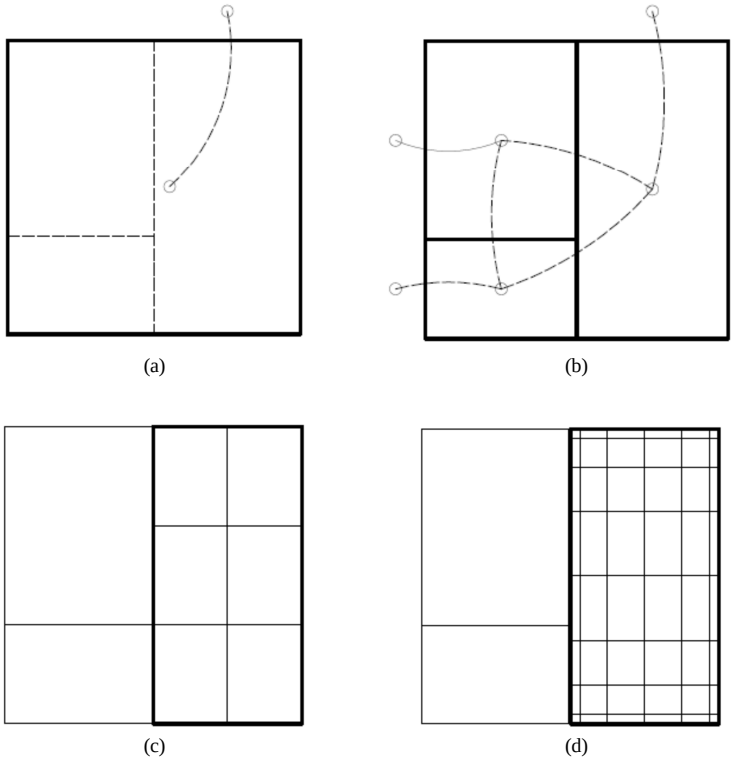

Figure 1.6: Schematic representation of airflow modelling techniques: (a) nodal, (b) multinodal, (c) zonal and (d) CFD approach

1.2.2 Alternative classification

Use of convective heat transfer coefficients

Multi(nodal) and zonal BES programs rely on Newton's law of cooling (Eq. (1.6)) to model the convective heat transfer. This relation is actually a discrete analogon of Fourier's first law (conduction). It presumes that the convective heat flux q_{conv} is proportional to the difference between the temperature at the wall T_w and a reference temperature T_{ref}. The constant rate of change stands for the so-called convective heat transfer coefficient h_{conv} (CHTC), which can be considered as the inverse of the 'virtual' thermal resistance of the boundary layer, as shown in Figure 1.4(b).

$$q_{conv} = h_{conv} \cdot \left(T_w - T_{ref}\right) \tag{1.6}$$

The CHTC is actually a simplified way to represent a complex heat transfer problem in the boundary layer and the surrounding flow field. The CHTC does not rely on known information on the wall boundary and, therefore, researchers have supplied a massive amount of primarily experimental data, altogether applicable to many situations. Thereby, the choice of the reference characteristic temperature proves delicate, especially for indoor air in buildings. As a matter of fact, while for flat plate flow the free stream temperature unambiguously acts as a reference, the inherent complexity of 3-D flows forces researchers to define an assumedly representative reference temperature. Also the choice of a characteristic dimension in case of 3-D enclosures leaves considerable room for interpretation.

Direct calculation of convective heat transfer

CFD on the other hand, can generate data on the convective heat transfer, for use in BES, perhaps in a dynamic coupling fashion when the convective heat transfer remains more or less constant during several time steps (e.g. [101-103]). Yet, the reliability of the convective heat transfer predictions by CFD depends to a large extent on the near-wall modelling. For example, not all RANS turbulence models are equally suited to predict flow near solid boundaries and, thus, the related convective heat transfer. High-Reynolds number (HRN) models such as the k-ε model are not apt for wall-bounded flow simply because they were originally developed for flow in regions somewhat far from walls (i.e. turbulent core flows). Therefore, CFD models can use semi-empirical, logarithmic wall functions to bridge the viscosity affected region between the wall and the fully-turbulent region (i.e. the viscous sublayer, buffer layer and part of the logarithmic layer). However, the wall function approach is inadequate when low-Reynolds number effects are pervasive in the flow domain and high three-dimensionality occurs: e.g. airflows inside buildings characterized by buoyancy effects, detachments zones… [104-109]. As a consequence, to accurately study the convective heat transfer in buildings, another approach is regarded necessary: solving the near-wall region by either a two-layer model or a low-Reynolds number (LRN) model. Basically, the two-layer model splits the domain up in a fully-turbulent region, which is resolved by a HRN model, and a viscosity-affected layer, where an adapted turbulence model comes in. When using a LRN model, the CFD software solves the entire domain with the same LRN model such as the k-ω model. Both options do necessitate a fine near-wall mesh, which obviously imposes a larger computational requirement.

1.3 Problem definition and aim

The above indicated that night cooling can improve the summer comfort and can lower the cooling need in buildings. This implies that a sufficient supply of cool air effectively cools down a considerable amount of accessible thermal mass. The limiting factor is usually the convective heat transfer. In principle, a high convective heat flow results from a high temperature difference, a vigorous fluid motion and/or a large heat transfer surface area. However, putting this in practice is, to put it mildly, not obvious. Building designers have to take into account many other requirements, which only complicates the design. And this while convective heat transfer is a complex mechanism. The extent to which building designers succeed in finding an optimal night cooling design depends strongly on the simulation tool they use. Nowadays stand-alone BES programs are quite popular. They include not only advanced heat transfer models, but also enable to model other processes like illumination or moisture transport in fabric. However, the way they model the convective heat transfer raises questions. The complex heat transfer in the boundary layer and the surrounding flow field is represented by a CHTC which relies primarily on experimental data. Each set of convection correlations applies to a specific situation.

Now the question is: does this current convective heat transfer modelling approach suffice to accurately predict the night cooling performance? Therefore, underlying work evaluates the current BES approach and further investigates the impact of the room/system design on the convective heat transfer during night cooling, experimentally as well as numerically. Chapter 2 exemplifies the limitations of convective heat transfer modelling in BES. To this end, it documents the literature review on existing convection correlations and the BES-based analysis which evaluates the impact of convection correlations on the predicted night cooling performance in an office room. Chapter 3 goes more deeply into the particularity of convection correlations. It describes the experimental study which assesses to what extent including more room/system design parameters is necessary to model mixed convection heat transfer. Chapter 4 discusses the most important CFD factors and reports on the sensitivity analysis which assesses how the CFD simulation approach influences the predicted convective heat transfer, in preparation for the extensive CFD simulation study described the next chapter. Chapter 5 discloses the simulation study which evaluates how the room/system design affects the convective heat transfer in a generic night cooled landscape office and which design solutions are most profitable. Chapter 6 summarizes the most important conclusions and brings up future research.

2

On the use of convective heat transfer coefficients

The underlying chapter exemplifies the limitations of convective heat transfer modelling in BES. First, it reports on the practicability of existing empirically derived CHTCs for use in BES. Secondly, it documents the BES-based sensitivity analysis which assesses the impact of convective heat transfer modelling on the predicted night cooling performance in an office room in a moderate climate (Belgium). This chapter was published in adapted form in the international journal Energy and Buildings [110].

2.1 Need for a critical review

A quick look at published convection correlations reveals a wide variety. However, the dimensionality of the respective research models throws up most of the reported data. The majority of the correlations, recommended by e.g. ASHRAE [111] and CEN [112], relies on data derived from experiments on isolated horizontal and vertical surfaces. These correlations do treat an important class of problems with many practical engineering applications. However, their suitability for building energy analysis is at best questionable. Neglecting the inherent three-dimensionality leaves out complexities in real building enclosures which significantly affect the flow pattern and, thus, the convective heat transfer [113]. Yet, there are still many convection correlations left which would apply to 3-D enclosures. These actually come in many different formulations, apply to distinct configurations and include various definitions of the reference variables. Authors like Khalifa [114] and Beausoleil-Morrison [102] already attempted to elucidate

this matter. However, their reviews may be missing recent contributions. Meanwhile, numerous researchers have shown the sensitivity of thermal predictions to the modelling of internal convection. For example, the worthy effort of the IEA Annex 21 [115], solely focussing on heating and free-floating conditions, acknowledged the dominant role of convective heat transfer in the building's energy balance. Other examples are the works of Beausoleil-Morrison [102], Delaforce [116] and Lomas [117]. Moreover, researchers like Clark [118], Givoni [58] and more recently Artmann et al. [119] have shown that the importance of convective heat transfer modelling increases in case of high ventilation rates. Unfortunately, last-mentioned authors based their investigations on arbitrary values of the CHTC, which to some extent limits their authority.

In response to aforementioned shortcomings, this chapter first extends the literature surveys of Khalifa [114] and Beausoleil-Morrison [102]. Also this review focuses on the most valuable convection correlations which assumedly apply to real building enclosures and are possibly apt for implementation in BES. It describes only the dimensional form of the correlations as adopted in BES. For each set of correlations, the experimental setup, the methodology used to derive the convective heat transfer and the practicability for use in BES are discussed. The definitions of the characteristic dimension and of the reference temperature receive special attention as these limit to a large extent the CHTCs' applicability. The review starts with correlations applicable to natural convection – which are function of a temperature difference – before elaborating on forced convection CHTCs. The latter CHTCs are dimensionally related with a term expressing the air velocity. Finally, mixed convection correlations (for which both external pressures and buoyancy forces are important) are described. Next to it, underlying chapter documents the BES-based sensitivity analysis (with TRNSYS 16) which assesses in the first place the impact of existing convection correlations (not arbitrary values) on the night cooling performance in an office room during summertime of a moderate climate (Belgium). In addition to this, several design parameters are varied to reveal the relative importance of the choice of convection algorithm.

2.2 Evaluation of convection correlations for use in BES

2.2.1 Correlations for natural convection

Alamdari and Hammond

Although Alamdari and Hammond [120] based their correlations on experimental data reported in literature for stand-alone surfaces, their work is worth mentioning. As a matter of fact, these authors reviewed correlations which span laminar and turbulent flow regimes for a wide range of temperature differences. Moreover, they included the surface's characteristic dimension, by which the correlations would apply to building applications. Using the local air temperature $T_{a,l}$ – defined as the free stream temperature – as a reference, Alamdari and Hammond converted the original correlations into 3-D forms applicable to respectively vertical surfaces, stably-stratified horizontal surfaces and buoyant flow from horizontal surfaces. By way of example, Eq. (2.1) shows that Alamdari and Hammond related the CHTC for a vertical wall to the temperature difference between the concerned air and the local air temperature, and this, for both the laminar and turbulent regime by using the blending function of Churchill and Usagi [121]:

$$h_{conv,nat} = \left\{ \left[1.5 \cdot \left(\frac{\left(T_w - T_{a,l}\right)}{H} \right)^{1/4} \right]^6 + \left[1.23 \cdot \left(T_w - T_{a,l}\right)^{1/3} \right]^6 \right\}^{1/6} \tag{2.1}$$

As the experiments were conducted on heated isolated plates, the correlations would only apply to purely buoyant flow, in particular where buoyancy is caused solely by a temperature difference between a surface and the surrounding air. However, Alamdari and Hammond expanded the application of the correlations to cooler surfaces – as commonly done in case of flat plate experiments. This means that e.g. the correlation valid for a heated floor also applies to a ceiling which is cooler than the adjacent air.

The choice of the local air temperature as a reference does not prohibit the use of the correlations in BES. Because of minor temperature variations, the local air temperature is expected to approximate the average indoor air temperature – as shown in the experimental study of Arnold et al. [122]. However, authors like Novoselac [103], Khalifa and Marshall [123] and Awbi and Hatton [124] reported that the Alamdari and Hammond equations predict a lower convective heat transfer than data collected within enclosures. As shown by Beausoleil-Morrison [102], this difference is, on the one hand, due to the fact that Alamdari and Hammond only included a characteristic dimension in the laminar part of the blending function, although even at small temperature differences turbulence dominates. On the other, this difference is also because Alamdari and Hammond neglected radiative heat transfer. Nevertheless, as building regulations promote building envelopes with increasing thermal resistances, the temperature difference between the air and the

surroundings diminishes, at least for natural convection regimes. Thus, according to the author of underlying literature survey, the relative impact of the possibly deviating Alamdari and Hammond correlations on the building's energy balance will decrease.

Khalifa and Marshall

Contrary to Alamdari and Hammond [120], Khalifa [125] and Khalifa and Marshall [123] derived their correlations from measurements in a single-size experimental chamber. The full-scale test cell actually consisted of two separate zones: a larger hot zone, used as the test compartment, and a cool room adjacent to one of the walls to simulate a cool outside environment. Nine of the most widely used heating configurations in buildings were covered by this study: heating hydronics, such as a radiator, in-floor heating – inducing natural convection – and fan assisted heaters – inducing mixed convection, were analysed, while varying the location of the heating system. Some configurations also included a window. Once steady-state conditions were obtained, the above authors derived the convective heat transfer from the heat balance at the internal surfaces (except for the heated surface), solely based on temperature measurements. Equally distributed triplets of thermocouples measured the interior and exterior surface temperatures, except for the floor. Assuming 1-D conduction and negligible radiation – as the surfaces were covered with aluminium sheets, the convective heat flux would come close to the heat loss by conduction. Subsequently, for all surfaces but the heated one, Khalifa developed a total of 36 correlations, using the average indoor air temperature as a reference. Khalifa and Marshall, conversely, combined similar correlations, obtained in the same experimental chamber, with the aforementioned equations to obtain more general correlations, resulting in a series of ten equations. Anyhow, both studies expressed the CHTC as a function of the temperature difference via a coefficient C and an exponent n.

The correlations developed by Khalifa and Khalifa and Marshall are suitable for rooms with a strong buoyant flow created by heating devices and for forced flow by fan assisted heaters. Unfortunately, their correlations probably produce a deviating convective heat transfer as the analysis did not take radiation explicitly into account. As put forward by Beausoleil-Morrison [102], especially the cases with large temperature differences will show a high error. More importantly, as the correlations do not include a length scale, the author of underlying survey believes that their applicability is limited to geometries similar to the experimental setup. Despite the aforementioned shortcomings, the work of Khalifa and Khalifa and Marshall proves to be valuable as, up to now, no alternative is available.

Awbi and Hatton

Awbi and Hatton [124] investigated natural convection from the heated surfaces themselves – as a valuable supplement to the work of Khalifa [125] and Khalifa and Marshall [123]. Additionally, they performed experiments in two enclosures of different size, admitting the assessment of scale effects. One room had a typical room size while the other was considerably smaller. Similar to the experiments of their predecessors, Awbi and Hatton built, adjacent to the test rooms, a cool chamber, which acted as a heat sink. To achieve an average air temperature in the test room of about 20°C, one surface in the test room, of which the convective heat flux was measured, was heated by electrical resistance heater panels. Like Khalifa [125] and Khalifa and Marshall [123], the convective heat transfer was derived primarily from temperature measurements. However, unlike last-mentioned authors, Awbi and Hatton corrected for the radiative heat flux – even though aluminium foils on the walls minimized the influence of radiation. The convective heat flow Q_{conv} from the heated plate equalled the power input Q_{panels} minus the conduction loss from the heated surface to the outside Q_{cond} and the radiative flow to the inside Q_{rad}.

To determine the CHTC, with the exception of the heated ceiling, Awbi and Hatton used as a reference the average temperature measured at twelve evenly distributed locations, at a distance of 0.1m from the heated surface. Given the assumption of a well-mixed model in BES, this could exclude the use of their equations. However, Awbi and Hatton observed that the air temperature varied little throughout the room. Only in case of a heated ceiling, a strong temperature stratification manifested itself. In that case, Awbi and Hatton used the air temperature in the centre of the room as a reference. Unfortunately, as they applied Newton's law of cooling to derive the CHTC, using this larger temperature difference led to a lower CHTC. As a result, the author of underlying review supposes, just as Beausoleil-Morrison [102], that adopting this convection correlation in BES leads to an underestimation of the convective heat transfer. Therefore, it is less suited for BES. Meanwhile, since their equations include the hydraulic diameter of the considered surface D_h, walls and floors of different dimensions can be represented by a single equation (Eq. (2.2)). So, the CHTC is only a function of the temperature difference (T_w-$T_{a,i}$), corrected for the surface dimensions using the hydraulic diameter D_h. This relation is defined by the coefficient C and the exponents n_1 and n_2, which are specific for respectively the wall correlation and the floor correlation:

$$h_{conv,nat} = \frac{C}{D_h^{n_1}} \cdot \left(T_w - T_{a,l}\right)^{n_2} \tag{2.2}$$

Awbi and Hatton only investigated heated surfaces to fill up the work of Khalifa [125] and Khalifa and Marshall [123] who considered all surfaces but the heated one in case of wall/floor heating. Meanwhile, the equations of Awbi and Hatton produce higher values than those of Alamdari and Hammond [120] – as indicated by Beausoleil-Morrison [102]. As previously mentioned, this is because Awbi and Hatton did not neglect the radiative heat transfer, but calculated it; and because they included a characteristic dimension.

2.2.2 Correlations for predominantly forced convection

Spitler et al.

Similar to Khalifa [125] and Khalifa and Marshall [123], Spitler et al. [126, 127] used a single-size experimental chamber. However, in this case, the heat loss by conduction through the envelope was minimized by enclosing the experimental chamber within a larger conditioned box. Meanwhile, well-integrated heated panels maintained the room surfaces at nearly isothermal conditions, thus minimizing the radiation component of the heat flux. The addition of a variable air ventilation system with two air supply openings – admitting to deliver air over a range of 2 to 100 air changes per hour – increased the flexibility of the facility to perform a wide range of convective heat transfer experiments. A total of 44 experimental tests were performed in which the flow rate, the air supply temperature and location, and the air supply area were varied. Four setups also included furniture. In each experiment the air delivered to the room was cooler than the surfaces. To deduce the convective heat flux q_{conv}, the calculated radiative heat flux q_{rad} was subtracted from the measured heat flux supplied to the room by the heated panels q_{panels}. Because of the linear relationship between the exhaust temperature and the volumetric rate, Spitler et al. chose to use the exhaust temperature as a reference to determine the convection coefficients. The CHTCs were correlated with the jet momentum number J using two empirically determined constants C_1 and C_2 – as shown in Eq. (2.3). Spitler et al. non-dimensionalized the jet momentum flux into the room by taking into account the air density ρ, the gravitational acceleration g and the room volume V. This way, the jet momentum number was actually a function of the air change rate n and the velocity of the supply air jet u_{sup}.

$$h_{conv,\,for} = C_1 + C_2 \cdot \sqrt{J} = C_1 + C_2 \cdot \sqrt{\frac{n \cdot u_{sup}}{g}} \tag{2.3}$$

Again, the author of underlying work marks that the extensibility of the correlations is limited because of the use of a single-size chamber. Moreover, the equations were derived for mainly forced convection cooling. As a matter of fact, Spitler et al. found that the data correlated well to a single parameter as long as the inertia forces dominated. More specifically, the Richardson number, defined by Eq. (2.4) with the maximum possible throw of the jet being L and the supply velocity being u, remained smaller than 0.3 and the lowest considered air change rate was $15h^{-1}$. Thus, the author of underlying survey concludes that for enclosures of similar size to the experimental setup, ventilated at relatively high air changes per hour, the correlations of Spitler et al. can be used in BES.

$$Ri = \frac{\beta \cdot g \cdot L \cdot \left(T_{exh} - T_{\sup}\right)}{u^2} \tag{2.4}$$

Fisher and Pederson

Fisher [128] extended the work of Spitler et al. [126, 127] using the same experimental setup and methodology to derive the convective heat transfer, this time for lower air change rates – i.e. from $3h^{-1}$ to $12\ h^{-1}$. In particular, the impact of two typical types of jets, i.e. radial ceiling jets and free horizontal jets, was investigated for cooling applications. For the majority of the experiments, the internal surfaces were held again isothermal, except for a measurement campaign in which one wall was cooled. However, these few non-isothermal experiments are not discussed because the investigated convection regime – in which the air supply temperature is in between the cool and warm surface temperatures – is not commonly encountered in buildings. Fisher considered the air supply temperature a better choice for normalizing the CHTCs – contrary to Spitler et al. [126, 127] who used the exhaust temperature. By this, not only smaller uncertainties in the CHTCs at low airflow rates occurred, but also the data correlated better. Following the work of Fisher, Fisher and Pedersen [127] analysed the same experimental data set using another functional form to prevent non-sensible values of the CHTC outside their range of validity, i.e. for air changes per hour lower than 3. In both cases, the dimensional form of the correlations was a function of the air change rate. However, both correlation sets produce substantially different convection coefficients, in particular for walls – as shown by Beausoleil-Morrison [102].

As the experimental campaign was performed analogous to the one of Spitler et al. [126, 127], similar remarks can be made regarding the validity of the convection coefficients. However, Fisher and Pedersen believed that the aforementioned correlations could also be used for heated rooms. For the ceiling jet, they found that the Coanda effect adhering to the ceiling and the walls exceeded the buoyancy forces of the cool jet. In case of heating, buoyancy forces would assist the jet to adhere to the ceiling.

2.2.3 Correlations for mixed convection

Awbi and Hatton

Following their experiments on natural convection, Awbi and Hatton [129] extended their work to mixed convection. In the same experimental setup they placed a fan box with an adjustable nozzle at one end of the surfaces, creating forced convection in addition to the natural convection due to the heated panels. Using as a reference the local air temperature defined in their previous study on natural convection – i.e. at twelve evenly distributed locations, 0.1m away from the surface, Awbi and Hatton developed correlations applicable to heated surfaces at which a jet is present. The CHTC for forced convection is expressed as a function of the width of the nozzle opening w and the velocity at the nozzle opening u_{sup} (Eq. (2.5)). Finally, to develop correlations for mixed convection, the data for natural convection found earlier – represented by $h_{conv,nat}$ – and the new data for forced convection from this study – defined by $h_{conv,for}$, were combined using the blending function (Eq. (2.6)) proposed by Neiswanger et al. [130]:

$$h_{conv,\,for} = C \cdot w^{n_1} \cdot u_{\mathrm{sup}}^{n_2} \tag{2.5}$$

$$h_{conv,mix} = \left(h_{conv,nat}^{3.2} + h_{conv,\,for}^{3.2}\right)^{1/3.2} \tag{2.6}$$

As Awbi and Hatton focused on heated surfaces, their correlations only apply to convective cooling applications. Additionally, Awbi and Hatton only varied the width of the supply jet while keeping the relatively small height constant. Therefore, according to the author of underlying survey, their correlations can only be applied to line-shaped diffusers. Besides, seemingly, Awbi and Hatton did not analyse the fitness of the correlations for implementation in BES. However, the jet induced by the fan would probably limit the difference between the local air temperature and the average indoor air temperature, especially at higher airflow rates. Anyhow, apart from the usability of the correlations for cooling applications, the work of Awbi and Hatton is useful because it provides a considerable insight into the distribution of local CHTCs under the influence of a jet.

Beausoleil-Morrison

As an alternative to the equations of Awbi and Hatton [129], the correlations of Beausoleil-Morrison [102] describe mixed convection. This author combined the correlations for natural convection of Alamdari and Hammond [120] and the forced convection equations of Fisher [128] – only for a radial ceiling diffuser – using a similar blending function as adopted by Awbi and Hatton [129]. However, next to using slightly differing exponents, Beausoleil-Morrison defined two distinct expressions (Eq. (2.7), Eq. (2.8)) for walls depending on the interaction of buoyancy and external forces. As the radial ceiling diffuser acts always downwards, this selection mechanism basically relies on comparing the surface temperature and the air temperature. For example, in case the surface temperature

is lower than the air temperature, the natural convection assists the forced convection induced by the radial ceiling diffuser, resulting in a higher CHTC.

$$h_{conv,mix,assisting} = \left(h_{conv,nat}^3 + h_{conv,for}^3\right)^{1/3} \tag{2.7}$$

$$h_{conv,mix,opposing} = \left|h_{conv,nat}^3 - h_{conv,for}^3\right|^{1/3} \tag{2.8}$$

Since the Fisher correlations use the air supply temperature as a reference, Beausoleil-Morrison found scaling to the indoor air temperature necessary for implementation in BES. Besides, the Fisher correlations limit the usability of the Beausoleil-Morrison CHTCs at the lower end to $3h^{-1}$. In addition, Beausoleil-Morrison only implemented in ESP-r the correlations for the case with a radial ceiling diffuser. Although he classified his equations as fit for mechanically ventilated rooms which are heated or cooled with air – without validation, further research is regarded necessary on lower air change rates, different diffuser types and their respective locations. This was partly done by the next author, Novoselac [103]. In the meantime, as no more detailed alternative is available, the author of underlying review suggests using the correlations of Beausoleil-Morrison in BES.

Novoselac

Novoselac [103] investigated the validity of existing correlations in an experimental chamber with typical room dimensions. As the test chamber included a window, Novoselac installed a climate chamber next to it to simulate external conditions. For cases for which the existing equations failed to predict the convective heat transfer, Novoselac conducted additional experiments to develop new correlations: a setup with displacement ventilation, forced convection induced by a high aspiration ceiling diffuser and/or radiant cooling ceiling panels, which occupied half of the ceiling surface. Similar to e.g. Awbi and Hatton [124, 129] and Spitler et al. [127], Novoselac did not measure the convective heat transfer directly, but calculated it from temperature measurements, using a heat balance at the internal surfaces. Different from aforementioned authors, the walls were not heated – approximating real building enclosures. For the forced convection correlation at floor surfaces with displacement ventilation, Novoselac proposed the air supply temperature as reference. In all other cases, he suggested the local air temperature measured at 0.1m from the surface.

As Novoselac used his correlations to improve the accuracy of thermal boundary conditions calculation in CFD simulations, his work proves valuable. However, when used in BES, the correlations can introduce large errors as the local air temperature is used as a reference for deriving the CHTCs. After all, the investigated configurations showed large temperature variations. As Novoselac explained comprehensively why the local air temperature should be used in deriving the correlations, similar remarks can be made concerning the implementation in BES.

2.2.4 Conclusions: particularity of convection correlations

Summarizing remarks

The above collection of convection correlations addresses many typical situations encountered in buildings. On the one hand, several sets together cover a considerable number of cases in which convective heat transfer originates from buoyancy forces. For example, the natural convection correlations of Awbi and Hatton [124] make it possible to assess the convective heat transfer at a hot window surface. On the other hand, the works of Spitler et al. [126, 127] and of Fisher and Pederson [128, 131] prove valuable for predominantly forced convection regimes such as night cooling applications for which a low Richardson number applies. Still, comprising all possible regimes encountered within buildings by only CHTCs is an unrealistic aim, just because of the particularity of each situation. After all, researchers can only account for a limited number of parameters: e.g. only a fan in the middle of a surface, mostly no furniture. As a result, to be able to use convection correlations in BES, a pragmatic approach urges itself: categorizing all situations into a discrete number of regimes for which specific correlations apply. For example, Beausoleil-Morrison defined five categories according to the type and cause of the driving force and implemented the corresponding correlations and selection mechanism in ESP-r [102]. This approach leaves the opportunity to assess the impact of e.g. a mechanical ventilation system indeed, yet it does not enable to investigate the influence of parameters other than the ones considered in the experimental setup on which the corresponding CHTCs rely (e.g. the instalment of multiple diffusers).

Next to this, the methodology used to derive the CHTCs further narrows the limits of application. For example, Khalifa [125] and Khalifa and Marshall [123] disregarded the radiative heat transfer, ending up with correlations unsuited for large temperature differences. Or most authors who included a characteristic dimension, agreed on making a distinction based on the mechanism of fluid flow: natural convection correlations link up with the dimensions of the considered surface and CHTCs for predominantly forced convection with a characteristic dimension of the external agent. However, the authors involved put forward divergent definitions: e.g. Awbi and Hatton [129] used the nozzle width of the fan while Spitler et al. [126, 127] included the room volume part of the so-called jet momentum number. Nevertheless, including a characteristic dimension only promotes the use of the corresponding CHTCs to dimensions other than the ones of the experiment. Finally, the choice of a reference temperature possibly precludes CHTCs for use in BES. Harmonizing CHTCs for rooms with (strong) temperature variations with the well-mixed assumption of BES troubles researchers and software developers. As a consequence, CHTCs applicable to e.g. displacement ventilation [103] are only fit for implementation in BES-zonal models.

Practicable correlations for the sensitivity analysis

Building on the previous literature review, the sensitivity analysis part of this chapter assesses the influence of some of the above convection correlations in particular on night cooling. However, these CHTCs, presumably apt for use in BES, are not necessarily valid for the convection regimes in the coming simulation model. During the day, natural convection – caused by a temperature difference between the surfaces and the air – plays a dominant role in transferring heat to the elements with a high heat storage capacity in the office room. The convective heat transfer is expected to stay limited because of the small temperature differences. On the other hand, during night cooling, the occurrence of larger temperature differences and a powerful jet results in a higher mixed convection heat transfer.

To introduce the sensitivity analysis to come, the underlying section presents the dimensional forms of the CHTCs as implemented by the author in TRNSYS 16. This overview starts with convection correlations which supposedly apply to natural convection, either because of their background or for the reason that they are only function of temperature. Two commonly used sets of correlations – not included in the previous literature review – act as a reference, i.e. the CHTCs described in NBN EN ISO 13791 [112] (Table 2.1) and the default TRNSYS 16 correlations [85] (Table 2.2). Together with the correlations of Alamdari and Hammond [120] (Table 2.3), these form a fist category of implemented natural convection correlations: based on experiments on isolated heated plates. Further, following recommendations of Beausoleil-Morrison [102], the CHTCs of Khalifa [125] and Awbi and Hatton [124] are combined (Table 2.4). The ceiling correlation of Awbi and Hatton would introduce a large error because of the badly chosen reference temperature – as discussed previously. Therefore, the author includes Khalifa's equation, which, unfortunately, lacks a characteristic dimension. In addition, similar to the approach used in flat plate experiments, the correlations valid for e.g. a disturbed air layer near the ceiling ($T_w<T_a$) are assumed to apply also to the floor in case the floor surface temperature exceeds the air temperature.

Table 2.1: Convection correlations for natural convection of NBN EN ISO 13791

Surface type	Mechanism	$h_{conv,nat}$ ($W.m^{-2}.K^{-1}$)
Vertical	Natural convection	2.5
Horizontal, heat flow upwards		5
Horizontal, heat downwards		0.7

Table 2.2: Convection correlations for natural convection of TRNSYS 16

Surface type	Mechanism	$h_{conv,nat}$ ($W.m^{-2}.K^{-1}$)
Vertical	Natural convection	$1.5 \cdot \Delta T^{0.25}$
Horizontal ($T_w>T_a$)		$2.11 \cdot \Delta T^{0.31}$
Horizontal ($T_w<T_a$)		$1.81 \cdot \Delta T^{0.25}$

With $\Delta T=|T_w-T_{a,l}|$, $T_{a,l}$ = free stream temperature

Table 2.3: Convection correlations for natural convection of Alamdari and Hammond

Surface type	Mechanism	$h_{conv,nat}$ ($W.m^{-2}.K^{-1}$)
Vertical	Natural convection	$\left\{\left[1.5 \cdot \left(\frac{\Delta T}{H}\right)^{1/4}\right]^6 + \left[1.23 \cdot \Delta T^{1/3}\right]^6\right\}^{1/6}$
Floor ($T_w>T_a$) Ceiling ($T_w<T_a$)		$\left\{\left[1.4 \cdot \left(\frac{\Delta T}{D_h}\right)^{1/4}\right]^6 + \left[1.63 \cdot \Delta T^{1/3}\right]^6\right\}^{1/6}$
Floor ($T_w<T_a$) Ceiling ($T_w>T_a$)		$0.6 \cdot \left(\frac{\Delta T}{D_h^2}\right)^{1/5}$

With $\Delta T=|T_w-T_{a,l}|$, $T_{a,l}$ = free stream temperature

Table 2.4: Convection correlations for natural convection of Awbi and Hatton, combined with Khalifa's natural convection algorithm

Surface type	Mechanism	$h_{conv,nat}$ ($W.m^{-2}.K^{-1}$)
Wall (Awbi and Hatton)	Natural convection	$\frac{1.823}{D_h^{0.121}} \cdot \Delta T^{0.293}$
Floor ($T_w>T_a$) Ceiling ($T_w<T_a$) (Awbi and Hatton)		$\frac{2.175}{D_h^{0.076}} \cdot \Delta T^{0.308}$
Floor ($T_w<T_a$) Ceiling ($T_w>T_a$) (Khalifa)		$2.72 \cdot \Delta T^{0.13}$

With for Awbi and Hatton: $\Delta T=|T_w-T_{a,l}|$, $T_{a,l}$ = free stream temperature
With for Khalifa: $\Delta T=|T_w-T_{a,i}|$, $T_{a,i}$ = indoor air temperature, averaged over multiple locations

The sensitivity analysis also comprises mixed convection correlations. Similar to their natural convection equivalent, the mixed convection correlations of Awbi and Hatton [129] are combined with Khalifa's natural convection correlation [125] (Table 2.5). Actually, only the correlation applicable to the ceiling alters as in the room configuration the jet is assumed to flow over the ceiling. Further, TRNSYS 16 is now equipped with Beausoleil-Morrison's correlations [102] (Table 2.6). Beausoleil-Morrison considered his correlations appropriate for mechanically ventilated rooms in general, even though the forced convection part of his correlations only applies to radial diffusers. However, the author of underlying study calls attention to the following. Beausoleil-Morrison introduced a scaling factor as the included forced convection algorithms of Fisher use the air supply temperature as a reference. As a result, even though the temperature difference between the surface and the indoor air is close to zero, the convective heat flux remains non-zero as long as the air supply temperature and the surface temperature differ (Figure 2.1 and Figure 2.2).

Table 2.5: Convection correlations for mixed convection of Awbi and Hatton, combined with Khalifa's natural convection algorithm

Surface type	Mechanism	$h_{conv,mix}$ ($W.m^{-2}.K^{-1}$)
Wall (Awbi and Hatton)	Mixed convection	$\frac{1.823}{D_h^{0.121}} \cdot \Delta T^{0.293}$
Floor ($T_w>T_a$) (Awbi and Hatton)		$\frac{2.175}{D_h^{0.076}} \cdot \Delta T^{0.308}$
Ceiling ($T_w<T_a$) (Awbi and Hatton)		$\left[\left(\frac{2.175}{D_h^{0.076}} \cdot \Delta T^{0.308}\right)^{3.2} + \left(4.25 \cdot W^{0.575} \cdot u_{sup}^{0.557}\right)^{3.2}\right]^{(1/3.2)}$
Floor ($T_w<T_a$) (Khalifa)		$2.72 \cdot \Delta T^{0.13}$
Ceiling ($T_w>T_a$) (Khalifa and Awbi and Hatton)		$\left[\left(2.72 \cdot \Delta T^{0.13}\right)^{3.2} + \left(1.35 \cdot W^{0.074} \cdot u_{sup}^{0.772}\right)^{3.2}\right]^{(1/3.2)}$

With for Awbi and Hatton: $\Delta T=|T_w-T_{a,l}|$, $T_{a,l}$ = free stream temperature
With for Khalifa: $\Delta T=|T_w-T_{a,i}|$, $T_{a,i}$ = indoor air temperature, averaged over multiple locations

Table 2.6: Convection correlations for mixed convection of Beausoleil-Morrison

Surface type		$h_{conv,mix}$ ($W.m^{-2}.K^{-1}$)
Wall	($T_w<T_a$)	$\left(\left\{ \left[1.5 \cdot \left(\frac{\Delta T}{H} \right)^{1/4} \right]^6 + \left[1.23 \cdot \Delta T^{1/3} \right]^6 \right\}^{3 \cdot 1/6} + \left\{ \left[\frac{T_w - T_{sup}}{\Delta T} \right] \cdot \left[-0.199 + 0.190 \cdot n^{0.8} \right] \right\}^3 \right)^{1/3}$
	($T_w>T_a$)	Maximum of $\left(\left\{ \left[1.5 \cdot \left(\frac{\Delta T}{H} \right)^{1/4} \right]^6 + \left[1.23 \cdot \Delta T^{1/3} \right]^6 \right\}^{3 \cdot 1/6} - \left\{ \left[\frac{T_w - T_{sup}}{\Delta T} \right] \cdot \left[-0.199 + 0.190 \cdot n^{0.8} \right] \right\}^3 \right)^{1/3}$ and $80\% \text{ of } \left\{ \left[1.5 \left(\frac{\Delta T}{H} \right)^{1/4} \right]^6 + \left[1.23 \cdot \Delta T^{1/3} \right]^6 \right\}^{1/6}$ and $80\% \text{ of } \left\{ \left[\frac{T_w - T_{sup}}{\Delta T} \right] \cdot \left[-0.199 + 0.190 \cdot n^{0.8} \right] \right\}$
Floor	($T_w>T_a$)	$\left(\left\{ \left[1.4 \cdot \left(\frac{\Delta T}{D_h} \right)^{1/4} \right]^6 + \left[1.63 \cdot \Delta T^{1/3} \right]^6 \right\}^{3 \cdot 1/6} + \left\{ \left[\frac{T_w - T_{sup}}{\Delta T} \right] \cdot \left[0.159 + 0.116 \cdot n^{0.8} \right] \right\}^3 \right)^{1/3}$
	($T_w<T_a$)	$\left(\left[0.6 \left(\frac{\Delta T}{D_h^2} \right)^{1/5} \right]^3 + \left\{ \left[\frac{T_w - T_{sup}}{\Delta T} \right] \cdot \left[0.159 + 0.116 \cdot n^{0.8} \right] \right\}^3 \right)^{1/3}$

Ceiling	(T_w<T_a)	$\left(\left\{\left[1.4\cdot\left(\frac{\Delta T}{D_h}\right)^{1/4}\right]^6+\left[1.63\cdot\Delta T^{1/3}\right]^6\right\}^{3\cdot 1/6}+\left\{\left[\frac{T_w-T_{sup}}{\Delta T}\right]\cdot\left[-0.166+0.484\cdot n^{0.8}\right]\right\}^3\right)^{1/3}$
	(T_w>T_a)	$\left(\left[0.6\cdot\left(\frac{\Delta T}{D_h^2}\right)^{1/5}\right]^3+\left\{\left[\frac{T_w-T_{sup}}{\Delta T}\right]\cdot\left[-0.166+0.484\cdot n^{0.8}\right]\right\}^3\right)^{1/3}$

With for Alamdari and Hammond: $\Delta T=|T_w-T_{a,l}|$, $T_{a,l}$ = free stream temperature
for Fisher: $\Delta T=|T_w-T_{a,i}|$, $T_{a,i}$ = indoor air temperature

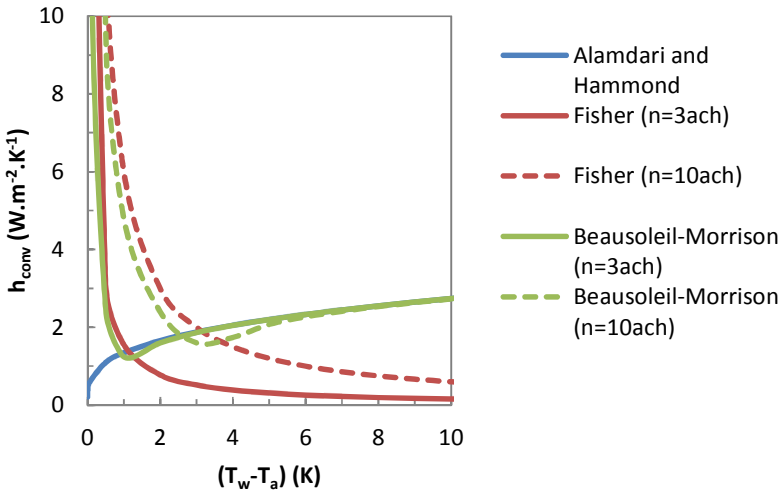

Figure 2.1: Comparison of correlations based on the predicted CHTC h_{conv} at a vertical wall (T_w=23°C and T_{sup}=17°C)

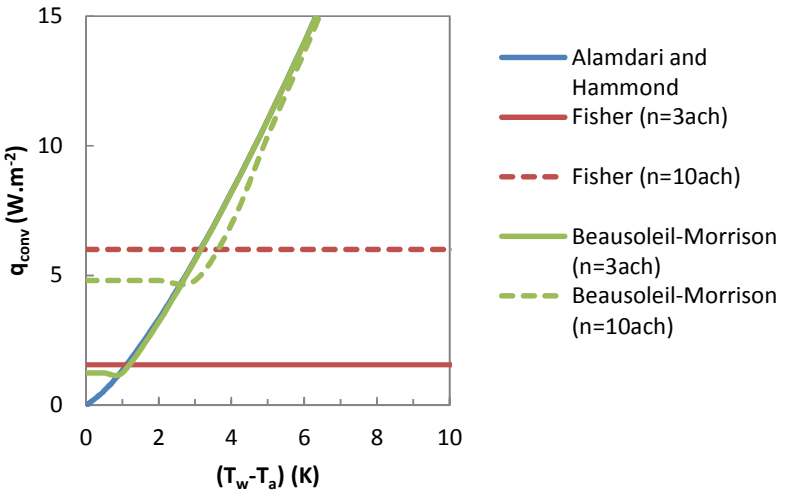

Figure 2.2: Comparison of correlations based on the predicted convective heat flux q_{conv} at a vertical wall (T_w=23°C and T_{sup}=17°C)

2.3 Sensitivity of the predicted night cooling performance to convection correlations

2.3.1 Materials and methods

Simulation model

The research model is a generic office room with night cooling. The sensitivity analysis takes into account several convection correlations, the most influential building characteristics, the relevant system controls as well as the building use – as identified by Breesch [37, 132]. The so-called one-at-a-time method is used: it evaluates the impact of each input factor in turn, but neglects the interactions between the respective input factors. This simple screening method is regarded sufficient as underlying study is intended only as a preliminary sensitivity analysis. Besides, more detailed and complete sensitivity analysis methods are impossible because the uncertainty bounds are not defined for all correlations.

Simulations are carried out in TRNSYS 16 simulation software. This implies that the research model is composed of several linked component models, of which TYPE 56 is used to model the thermal behaviour of the office room. The simulation interval is limited to the Belgian summer from May 21 to September 15, preceded by a three-week start-up. A 30s time step is selected. The choice of this small time step size is related to the specific implementation of the convection correlations in TRNSYS 16. As a matter of fact, to avoid convergence problems,

the following procedure is used. To adapt the value of the CHTC, the air and surface temperature of the previous time step are taken into account while the system controls, i.e. the air change rate and the air supply temperature, are part of the iterative sequence within the current time step. As the calculation of the CHTC relies on variables of the previous and the current time step, the time step size should be reasonably small. However, at the same time a sufficiently large time step should be chosen to limit the computational cost and to avoid an incorrect calculation of the conductive heat transfer in TRNSYS. As a matter of fact, small time steps can render the conduction transfer function method used in TYPE 56 unstable, especially in case of heavy constructions [133-135]. In response, the author performs two time convergence studies (with time step sizes of 15s, 30s, 60s, 900s and 1800s). The first one is intended to assess the impact of the time step size on the calculation of time-dependent variables like night cooling controls and variable CHTCs. For this purpose it relies on the original simulation model equipped with the mixed convection correlations of Awbi and Hatton, combined with Khalifa's natural convection algorithm. It reveals that a time step smaller than or equal to 30s does no longer significantly influence the predicted number of hours exceeding a PMV-value of 0.5 (TE(PMV>0.5)). The second time convergence study aims at ascertaining whether a time step of 30s does not lead to unstable conduction transfer function series. To this end it is based on a simplified research model which leaves the many time-dependent variables like night cooling controls and variable CHTCs out of account. Instead, it takes only heating/cooling to a variable set point temperature into consideration. The course of this set point temperature matches the one of the original simulation model. The different predicted total heat fluxes at the one exterior wall are similar, what was to be demonstrated.

Building characteristics

The examined room is based on the geometry described by Breesch [37, 132]. Figure 2.3 shows the floor plan respectively a section. In case of night cooling, the choice of dimensions – thus the amount of thermal mass – has a significant influence on the probability of good thermal comfort. However, assuming a lower thermal capacity provides a safe approximation. Therefore, this study takes into account the internal dimensions as laid down in the standard NBN EN ISO 13791 [112]. For that same reason furniture is not included.

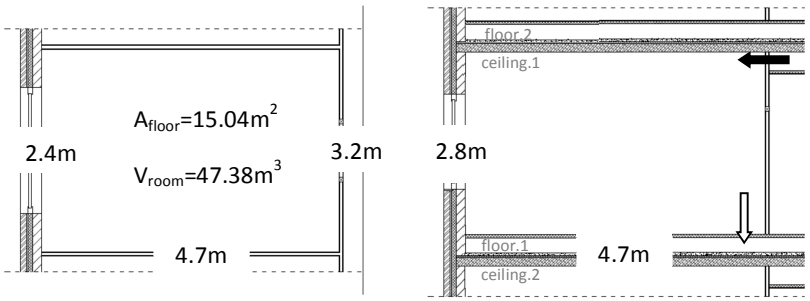

Figure 2.3: (a) Plan and (b) section of the office room

The basic office, west-oriented, includes an exposed concrete ceiling, a raised computer floor, a heavy façade including a window and light internal walls. Table 2.7 lists the wall composition, the solar absorptance a at the interior side of the wall and the thermal resistance R of the walls, based on the mean thermophysical properties for dry materials [136]. Breesch [132] lists the properties in more detail. The author of underlying study assumes uniform properties for all material layers, even for the hollow core concrete slabs, which constitute most of the internal mass in direct contact with the air. The rather high thermal conductivity of concrete partly justifies this simplification. The centre lines of the vertical internal walls are considered adiabatic. This way, only half of the wall is taken into account – gypsum board and half the insulation layer – which makes it possible to simulate an infinite sequence of identical rooms. However, this assumption fails for the horizontal dividing walls. Not only the composition of the floor is asymmetrical, on both sides also different boundary conditions may apply. Since TRNSYS 16 does not allow to connect two sides of a wall to one zone, a two-zone model, representing a recursive sequence of two floors, is set up in which the ceiling of the upper room 'ceiling.2' is connected to the floor of the bottom office 'floor.1' – as shown in Figure 2.3.

Table 2.7: Wall composition and thermal building data

Wall	Composition (from inside to outside)	α_{front} (-)	R ($m^2.K.W^{-1}$)
Floor/ceiling	Carpet, plywood, air cavity, light concrete, reinforced concrete, hollow core concrete slabs	0.72	0.58
Internal wall	Gypsum board, mineral wool, gypsum board	0.40	1.33
Heavy façade	Internal brick, mineral wool, air cavity, façade brick	0.49	2.51

Further, a constant leakage flow rate at 50Pa per area of external walls of $17.2 m^3.h^{-1}.m^{-2}$ is assumed, even though the rate of infiltration or exfiltration depends on the porosity of the building envelope and the magnitude of the natural driving forces of wind and temperature difference. This corresponds to an airflow rate at 50Pa divided by the volume, of $3.7\ h^{-1}$. This value ties in with the measured mean air tightness in nine new Belgian apartments [137] as well as to the results of a measurement campaign in 26 multi-family and 38 single-family dwellings [138, 139].

System characteristics

Mechanical ventilation is provided during office hours. A design flow rate of $36 m^3.h^{-1}$ of fresh air, with an air supply temperature of 16°C, is supposed to be supplied to the office near the ceiling and extracted from the floor – as shown in Figure 2.3. Moreover, a convective heating system with unlimited capacity is implemented to ensure good thermal comfort during midseason – i.e. at the beginning and the end of the simulation period, when low morning temperatures occur. The air temperature in the office is operated by a differential controller with dead band temperatures 20.5°C and 21.5°C. The heating is started up 1h before occupancy and stopped at the end of the working day. The original design is not equipped with mechanical cooling. However, to determine the saved cooling demand thanks to night cooling, additional simulations are performed on the office room which is then mechanically cooled – as explained in the section 'Performance indicators'.

To improve thermal comfort during summer, night cooling by mechanical ventilation, with an air change rate of $10 h^{-1}$, is used. Similar to the hygienic ventilation system, the cool air is supplied near the ceiling and extracted from the raised floor. Based on the work of Martin and Fletcher [140], an automatic on/off control system – shown in Table 2.8 – is proposed. Actually, the momentary temperature set points are controlled using a differential controller with a dead band interval of 1°C (nighttime activation requirement). Meanwhile, the temperature condition for the previous day, acts as an absolute set point (daytime activation requirement). Furthermore, contrary to aforementioned techniques, night cooling is active at weekends to remove excess heat during peak ambient conditions by the next working day.

Table 2.8: Basic conditions controlling night cooling by mechanical ventilation

Daytime activation requirement
$T_{a,i,max}$ > 23°C during previous day
Nighttime activation requirement
22h < time < 6h
$T_{w,ceiling}$ > 22°C [21.5-22.5] °C
$T_{a,i}$-$T_{a,e}$ > 2°C [1.5-2.5] °C
$T_{a,i}$ > 16°C [15.5-16.5] °C

Finally, to reduce the solar load on the window, movable exterior sunblinds are chosen. These are lowered when the internal air temperature exceeds 22°C – indicating that heating is off – and when the incident solar radiation exceeds 150W.m^{-2} [141]. They are pulled up when the solar radiation falls below 150W.m^{-2} or when the air temperature drops below 20°C, i.e. the heating set point temperature minus 1°C – primarily marking that the building is no longer occupied. Also at weekends the solar shading devices are controlled for limiting the possible peak temperatures of the next working day. Note that the distribution of the incoming solar radiation is modelled in a simplified way. More specifically, it is assumed that the floor absorbs 40% of the incoming solar radiation while the side walls and the back wall each account for 20%. A previous study [142] revealed that for the case at hand the modelling of the solar radiation distribution pales into insignificance compared to the choice of convection correlations.

Building use

In an office, people, lighting and office equipment emit heat. For non-dehumidified buildings, only sensible heat is important, of which 70% is assumed to be convective. CEN [112] , ISSO [141], CIBSE [60] and ASHRAE [111] list values for these internal heat gains. The heat production of people depends on the activity and characteristics of the indoor environment. In an office, during the cooling season, seated and light to moderate work is executed in light clothing. Meanwhile, the actual power use of office equipment is assumed to be equal to the total heat gain [111]. However, as not all computers, monitors, printers and lighting are in use all the time or are emitting their actual peak heat gain, the heat gains of the equipment are multiplied by a diversity factor [143]. High internal heat gains consistent with Breesch [37, 132] are assumed (Table 2.9); because this level leads to an appreciable number of overheating hours. The offices are occupied on weekdays from 8h to 17h (summer time).

Table 2.9 Internal heat gains

Source	Internal heat gain	Diversity factor
People	85W/pers	1.00
PC and screen	135W/pc	1.00
Lighting	10W.m^{-2}	1.00
Laser printer	130W/pc	0.40
Total (including diversity)	28.1W.m^{-2}	

Performance indicators

To assess the impact of the correlations, three performances are analysed: thermal comfort in free-floating conditions, cooling demand savings in case of mechanical cooling and operation time of the night cooling system. To evaluate the summer comfort, the temperature excess method [144], using a PMV-value of 0.5 as a limit, is chosen. To calculate the PMV-value, the operative temperature and the relative humidity are taken into account. Meanwhile, a constant metabolism of 1.2met and an air velocity of 0.1m/s are assumed. Finally, to take adaptation into

account, the clo-value is defined as a function of the running mean outdoor temperature T_{ORMT} which is calculated in accordance with van der Linden et al. [145] (Eq. (2.9), Eq. (2.10)). For intermediate running mean outdoor temperatures the clo-value is linearly interpolated. The temperature excess method states that a number of hours exceeding the limit during occupation less than 100h may be considered as an acceptable thermal comfort.

$$\text{clo}=0.5 \text{ when } T_{ORMT} > 15°C \tag{2.9}$$

$$\text{clo}=0.8 \text{ when } T_{ORMT} < 10°C \tag{2.10}$$

To determine the profitability of the night cooling two criteria are chosen. First, the cooling demand savings as a result of the operation of night cooling is used as an indicator. Therefore, additional simulations are performed on the office room which is then mechanically cooled, both in the case with and without night cooling. A comfort level B as defined by the adaptive temperature limits indicator [145], is used as the set point for mechanical cooling during office hours. This adaptive temperature limits indicator defines comfort limits on the indoor operative temperature based on the outdoor temperature of the preceding days. The cooling system is modelled 100% convective, ideally controlled and is assumed to have unlimited capacity. Secondly, for the case without mechanical cooling, the operation time of the night cooling system is considered, as, in case of night cooling by mechanical ventilation, even large mechanical cooling energy savings can be counterbalanced by the electrical energy use of the fans. The author defines the operation time percentage as the ratio of the time night cooling is activated $t_{NV,act}$ to the maximum possible operation time $t_{NV,max}$ – i.e. from 22h to 6h.

2.3.2 Results

Preliminary comparison of correlations

To facilitate the understanding of the simulation results, this section describes a preliminary comparison of the convection correlations. Contrary to previous works which focused on the predicted CHTC, this study analyses the convective heat flux – which is regarded more comprehensible. Moreover, the author discusses only the ceiling correlations in detail – even though both the ceiling and the façade wall are the primary elements with a high heat storage capacity in the office room. As a matter of fact, the ceiling surface temperature acts as a control parameter of the night cooling system while the correlations for a vertical wall produce similar results, during the day as well as during night cooling – as shown in Figure 2.4 and Figure 2.5.

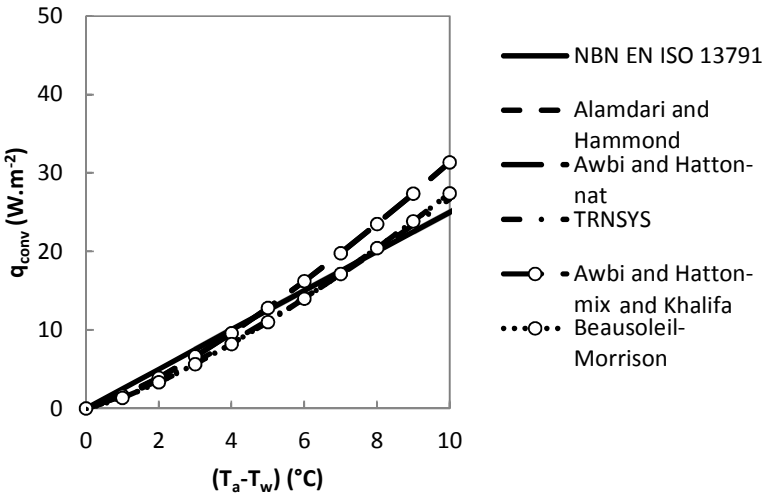

Figure 2.4: Comparison of correlations based on the predicted convective heat flux q_{conv} at the façade wall for a summer day (T_w=20°C, T_a>T_w, n=0.76h^{-1} and T_{sup}=22°C)

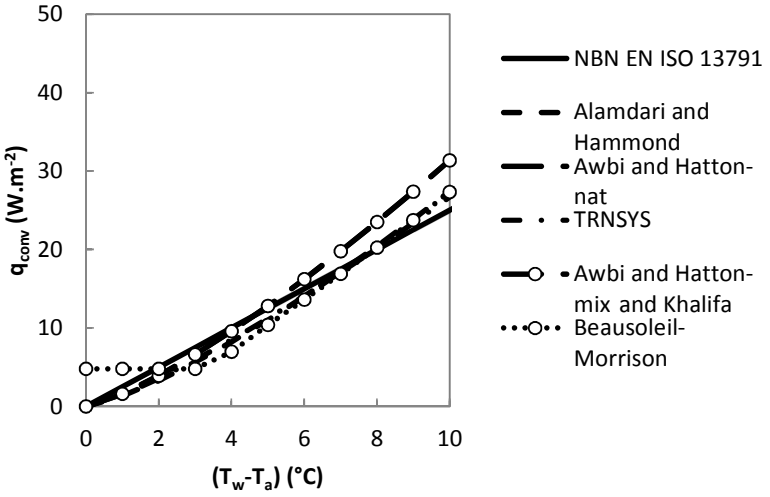

Figure 2.5: Comparison of correlations based on the predicted convective heat flux q_{conv} at the façade wall for a summer night with night cooling (T_w=23°C, T_w>T_a, n=10.00h^{-1} and T_{sup}=17°C)

Figure 2.6 shows the predicted convective heat flux during the day as a function of the temperature difference between the ceiling surface and the indoor air. As the standard NBN EN ISO 13791 proposes convection coefficients independent of a temperature difference, the predicted heat flux stands out, in particular at low temperature differences. Meanwhile, as natural convection dominates, the mixed convection correlations approximate their respective natural convection values. Awbi and Hatton-mix and Khalifa produces only slightly higher fluxes than Awbi and Hatton-nat and Khalifa. The Beausoleil-Morrison correlation equals the one of Alamdari and Hammond. Also the TRNSYS 16 correlation comes close to these last-mentioned correlations. However, contrary to the other algorithms, TRNSYS 16 only considers the temperature difference between the surface and the air without taking into account the direction of the heat flux. Moreover, similar to the correlations of NBN EN ISO 13791 and of Khalifa, used in conjunction with Awbi and Hatton, the TRNSYS 16 correlations include no characteristic dimension. Meanwhile, the background of these algorithms is unknown, which limits their applicability. Revising this set of correlations for the day regime, only the ones of Alamdari and Hammond and Beausoleil-Morrison are a valuable alternative.

During night cooling, the convective heat flux predicted by the respective convection correlations shows a larger spread (Figure 2.7). Obviously, the mixed convection correlations, taking into account the operation of the night cooling system, predict, together with the TRNSYS 16 correlations, the largest convective heat transfer: i.e. Awbi and Hatton-mix and Khalifa and Beausoleil-Morrison. However, again, the absence of a characteristic dimension and/or the unknown background, limit the authority of the TRNSYS 16 and Awbi and Hatton-mix and Khalifa correlations. Furthermore, the Beausoleil-Morrison convection correlation predicts a higher convective heat transfer at small temperature differences, compared with the other correlations. As previously mentioned, this is due to the scaling factor for the forced convection correlations of Fisher. This discrepancy may not be disregarded as small temperature differences are common during the night cooling regime – which can be derived from Figure 2.8 and Figure 2.9. These two last figures depict the course of both the simulated indoor air and ceiling surface temperature in the generic office room for a typical 72h period. The grey zones indicate the maximum possible operation time of night cooling – i.e. from 22h to 6h. Meanwhile, the grey dotted lines in Figure 2.9 mark the control band of the ceiling surface temperature, i.e. $T_{w,ceiling}$>22°C [21.5°C-22.5°C].

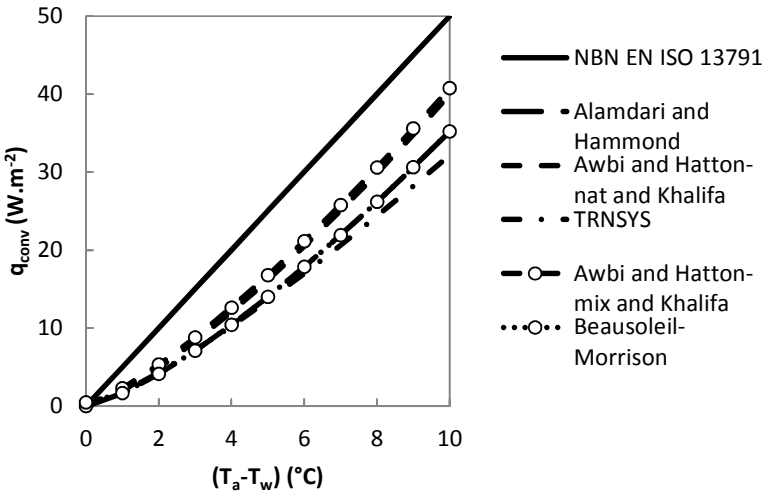

Figure 2.6: Comparison of correlations based on the predicted convective heat flux q_{conv} at the ceiling for a summer day (T_w=20°C, T_a>T_w, n=0.76h^{-1} and T_{sup}=22°C)

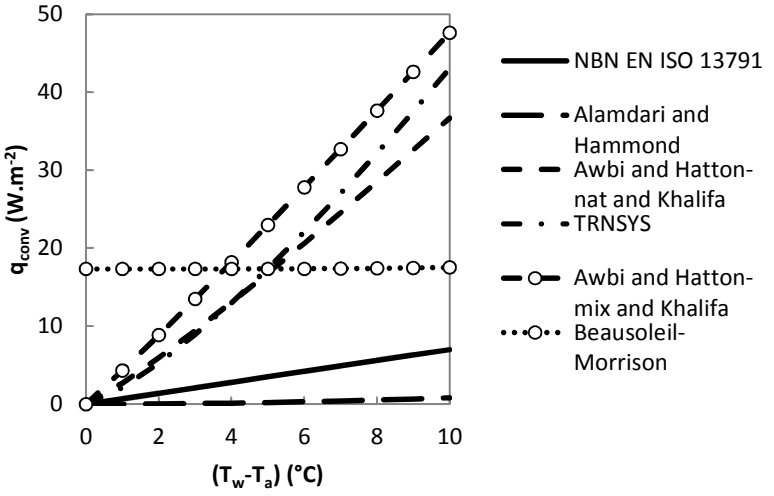

Figure 2.7: Comparison of correlations based on the predicted convective heat flux q_{conv} at the ceiling for a summer night with night cooling (T_w=23°C, T_w>T_a, n=10.00h^{-1} and T_{sup}=17°C)

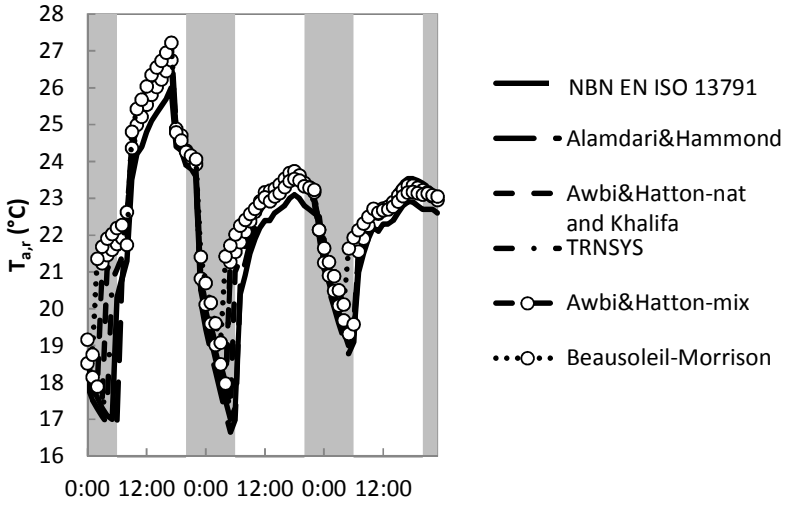

Figure 2.8: Indoor air temperature in the night cooled office for two summer days

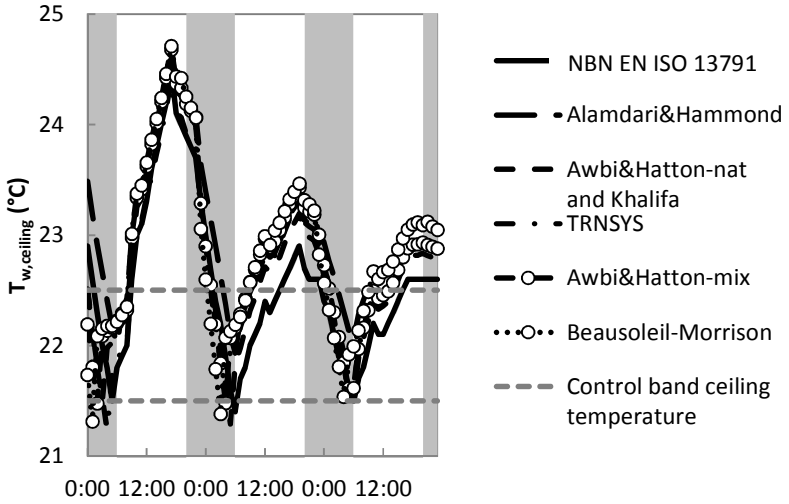

Figure 2.9: Ceiling surface temperature in the night cooled office for two summer days

Impact of convection correlations on predicted night cooling performance

Table 2.10 compares the building simulation results of the office model for different CHTC correlations. The simulation results are both given in absolute values and relative (italic) to the results using the correlations of NBN EN ISO 13791, except for the operation time percentage – which expresses the actual operation time of the night cooling to the maximum possible operation time – i.e. from 22h to 6h. Apparently, the cooling demand is similar for all correlations if no night cooling is applied (MC). Thus, the choice of the convection correlation has only a minor impact. The mechanical cooling, which is ideally controlled and has unlimited capacity, actually limits the temperature difference between the surfaces with high heat storage capacity and the air. The absolute temperature differences are smaller than 1°C for 85% to 97% of the time. As shown in Figure 2.4 and Figure 2.6, the correlations are alike at such small temperature differences. On the other hand, in case the office is night cooled, a larger scatter is noticeable, just because larger temperature differences occur. In particular, if both mechanical and night cooling are used (NV+MC), the yearly cooling demand for NBN EN ISO 13791 strongly deviates from the other correlations. As for the summer comfort in case of only night cooling (NV), the Alamdari and Hammond correlations show a small overheating risk. Meanwhile, the remaining natural convection algorithms, NBN EN ISO 13791, Awbi and Hatton-nat and Khalifa and TRNSYS 16, provide a similar or even better comfort compared with the mixed convection correlations. Conversely, Awbi and Hatton-mix and Beausoleil-Morrison limit the operation time compared with the natural convection correlations: the higher the convective heat transfer at the ceiling during night cooling, the shorter the operation time. In the following, the performance of the different correlations is discussed in more detail to explain the above observations.

At first, the simulation results based on NBN EN ISO 13791 stand out, showing the least overheating hours and mechanical cooling demand. However, the operation time is quite long – limiting the profitability in case of night cooling by mechanical ventilation. This can be explained as follows. During the day, a lot of heat is absorbed by the ceiling because of the high constant CHTC – as shown in Figure 2.6. At night, however, the heat flux at the ceiling is limited as the heat flux direction is altered (Figure 2.7) – prolonging the operation time of the night cooling. Meanwhile, the façade wall gets firmly cooled down because of the same high CHTC as during the day (Figure 2.4, Figure 2.5) – providing a considerable heat sink. Given this, the peak indoor air temperatures are reduced – impacting upon the summer comfort and the mechanical cooling demand. As observed in Figure 2.9, the ceiling surface temperature does not act as a control parameter for night cooling as it mostly does not approach 21.5°C – i.e. the lower dead band temperature of the night cooling differential controller. Figure 2.6 and Figure 2.7 show for the correlations of Alamdari and Hammond a tendency similar to NBN EN ISO 13791. However, the predicted convective heat fluxes at the ceiling are, for both day and night regime, much smaller while a similar convective heat transfer occurs at the façade wall. In conjunction with a higher indoor air temperature (Figure 2.8), this explains the poor summer comfort and the long

operation time. The remaining natural convection algorithms, Awbi and Hatton-nat and Khalifa and TRNSYS 16, predict a better performance, mainly because of the higher convective heat flux during the night – as shown in Figure 2.7. Finally, introducing the impact of the night cooling system into the correlations, further improves the predicted performance. In case of the algorithms of Beausoleil-Morrison, the operation time of the night cooling is the shortest and, thus, both the ceiling and the heavy façade wall cool down less. As a result, the overheating risk is slightly higher than in the case of the mixed convection correlations of Awbi and Hatton and Khalifa.

Table 2.10 Impact of convection correlations on the predicted night cooling performance

Correlation	TE(PMV>0.5) (h)	Q_{cool} ($kWh.m^{-2}$)		$t_{NV,act}.t_{NV,max}^{-1}$ (%)
Operating systems	NC	NC+MC	MC	NC
NBN EN ISO 13791	54	2.45	14.55	52
Alamdari and Hammond	101 *(187%)*	5.18 *(211%)*	14.00 *(96%)*	54
Awbi and Hatton-nat and Khalifa	69 *(128%)*	4.43 *(181%)*	14.11 *(97%)*	49
TRNSYS	81 *(150%)*	4.88 (199%)	14.13 (97%)	49
Awbi and Hatton-mix and Khalifa	66 *(122%)*	4.50 *(183%)*	14.10 *(97%)*	47
Beausoleil-Morrison	77 *(143%)*	5.63 *(229%)*	14.42 *(99%)*	39

Sensitivity analysis

This study takes into account a set of the most influential parameters (Table 2.11), based on Breesch [37, 132]. The list includes the building use – defined by the internal heat gains, building characteristics – such as the air tightness expressed by the v_{50}-value and the solar heat gain coefficient of the sunblinds g – and some system characteristics of night cooling and solar shading. In this case, the effect of the CHTCs on the night cooling performance is compared with the effect of the other parameters. To reduce the number of simulations, the author chooses three significantly different correlations: the natural convection algorithms of NBN EN ISO 13791 and Alamdari and Hammond, and Beausoleil-Morrison's correlations applicable to mixed convection. Since the cooling demand as an indicator only showed minor differences in the above study, this sensitivity analysis only uses the temperature excess method and the operation time.

Figure 2.10 shows the temperature excess hours for each scenario. The predicted performance is expressed absolute and relative to the base case, given the application of the same CHTC correlation. Meanwhile, Figure 2.11 gives an overview of the actual time night cooling is activated $t_{NV,act}$ relative to the maximum possible operation time $t_{NV,max}$ – i.e. the operation time percentage. As in the base case, a strong relation between the applied convection algorithm and the

night cooling performance is clear. In addition, the choice of the correlation is of the same importance as the choice of e.g. internal heat gains or sunblind control. To explain the differences, a distinction is made between the parameters primarily impacting upon the heat-balance ratio of gains to losses during the day – parameters 2, 3, 4 and 5 – and the cases which mainly influence the night cooling operation – parameters 6, 7 and 8. Focusing on the first-mentioned group, the author makes the following observation: the higher the ratio of gains to losses during the day, the higher the temperature excess hours and the night cooling operation time. Meanwhile, no distinct behaviour can be discerned between the two natural convection correlations, showing respectively relative difference ranges of 33%-172% and 44%-177%. This contrasts with the mixed convection CHTCs of Beausoleil-Morrison. These correlations produce a relatively higher mean operative temperature during the day approaching the limit value for overheating – as can be derived from Figure 2.8 and Figure 2.9 – and are, therefore, more sensitive. Besides, as night cooling in case of Beausoleil-Morrison, when started, does not necessarily stay active until the morning – because of a large convective heat flux (Figure 2.7), the operation time is more strongly influenced. Also in case of parameter 8, i.e. lowering the night cooling air change rate, the results with Beausoleil-Morrison are the most sensitive to this parameter. Because these correlations take the air change rate into account, the operation time is strongly influenced. However, as the time restraint does not necessarily limit the night cooling operation, the thermal comfort does not aggravate as much as in the case of the natural convection algorithms. A similar rationale explains why in case of parameters 6 and 7, the results on the temperature excess hours for Beausoleil-Morrison are quite insensitive to the night cooling control algorithm: because of the short operation time, the indoor air temperature stays relatively high.

Table 2.11 Overview of parameters for sensitivity analysis

Parameter	Quantity	Original	Adapted
1	Base case	-	-
2	Internal heat gains ($W.m^{-2}$)	28.1	21.7
3	Air tightness v_{50} ($m^3.h^{-1}.m^{-2}$)	17.2	4.2
4	$g_{sunblinds}$ (-)	0.17	0.3
5	Condition controlling sunblinds	150	300
6	Condition controlling night cooling; during operation time: $T_{a,i}$-$T_{a,e}$ > x (°C)	2	3
7	Condition controlling night cooling; during operation time: $T_{a,i}$ > x (°C)	-	18
8	Air change rate during night cooling (h^{-1})	10	6

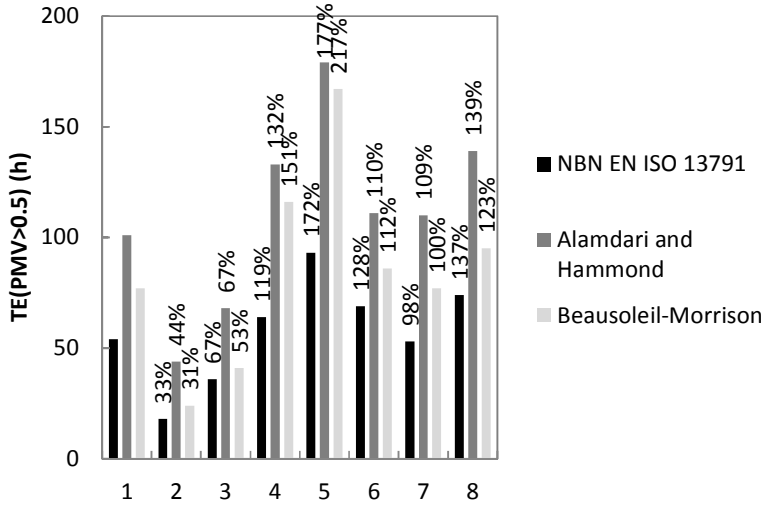

Figure 2.10: Temperature excess hours of the sensitivity analysis

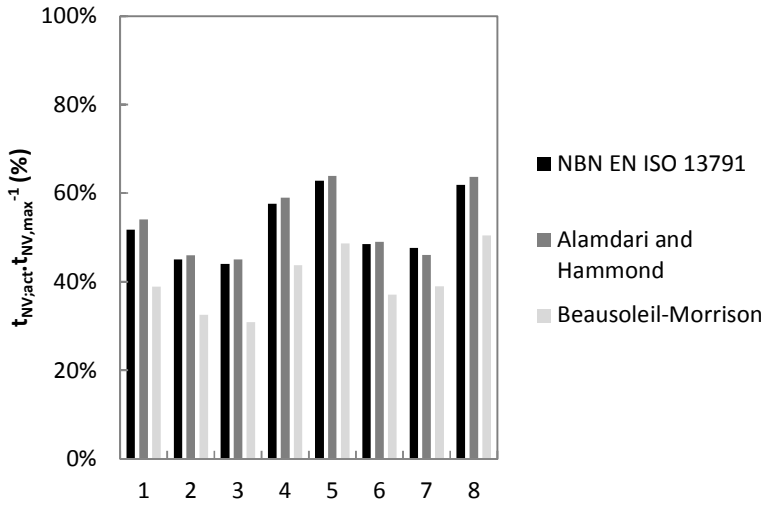

Figure 2.11: Operation time percentage of the sensitivity analysis

2.3.3 Conclusions: need for accurate convective heat transfer modelling in BES

The above sensitivity analysis revealed that for night cooled spaces, without mechanical cooling, the convective heat transfer modelling is important. The proof lies in the large spread of predicted performances. The operation time mainly depends on the convective heat transfer during the night. The temperature excess hours and the cooling demand depend to a larger extent on the ability to store heat during the day. Logically, correlations producing overall high convective heat fluxes, provide a good overall performance. However, not necessarily mixed convection correlations lead to the best performance. Moreover, the choice of the CHTC can alter the design decisions drawn from a BES-based analysis. After all, the sensitivity analysis revealed that the choice of convection correlations is of the same importance as the choice of design parameters. So, categorizing all situations into a discrete number of regimes for which specific correlations apply – as already suggested by e.g. Beausoleil-Morrison – is no luxury. However, now the question is whether the current BES approach is enough to accurately model night cooling. This is answered in the next chapter.

3

Experimental investigation of the impact of room/system design

This chapter documents the experimental campaign held in a PASLINK cell. The aim is to show experimentally the impact of the room and system design on the mixed convection heat transfer. This chapter starts with justifying the realization of such an experiment. Hereafter, the study dilates on the experimental setup: it describes the test room setup, the test equipment and the test procedure. Then it explains the preferred way of deriving the convective heat transfer, before it goes into the results of both the steady-state and the dynamic experimental runs. The lion's share of this chapter was published in the international journal Energy and Buildings [146].

3.1 Grasping the essentials

The literature review in the previous chapter revealed that a limited number of convection correlations are suited for implementation in BES and that they apply only to specific cases, determined by flow regime, driving force for convective heat transfer and geometry. Actually the researchers in question successively filled the major gaps: they developed convection correlations for distinct cases which had not been studied yet. For example, Awbi and Hatton [105] investigated the natural convection heat transfer only at heated surfaces to fill up the work of Khalifa [125] and Khalifa and Marshall [123]. Or in the early 1990s Spitler et al. [126, 127] questioned the applicability of the available natural convection correlations under ventilative cooling conditions and, as a consequence, developed correlations for predominantly forced convection. Putting several of such

convection correlations together in BES, as done by e.g. Beausoleil-Morrison [102], improves the convective heat transfer modelling indeed, yet it provides only a rough estimate. In response, recently researchers started to investigate whether or not today's correlations need to be refined. For example, Peeters et al. [147] experimentally tested the robustness of existing convection correlations. They looked into, among other things, the impact of intermittent operation of fans and of internal obstructions and concluded that more research is required on specific but common situations in indoor environments. Or Artmann et al. [148] investigated for several convection regimes how two ventilation modes (mixing and displacement ventilation) influenced the mixed convection heat transfer during night cooling. They left the thermal mass distribution unchanged ('thermally heavy' gypsum boards at the ceiling) and measured only the response to a step in the airflow rate for at least 12h. Their experiments revealed a distinct impact of the ventilation mode on the convective heat transfer distribution. So most likely new correlations are necessary should BES users want to calculate such a specific case.

To further substantiate this, underlying study investigates to what extent the air supply/exhaust configuration (only mixed ventilation mode) and thermal mass impact upon the convective heat transfer during two typical mixed convection cooling regimes (a typical day regime and a regime resembling night cooling, which in some cases come one after another). To this end, a PASLINK cell was made over. A new geometrically simple test room was created by installing a new wall, which actually included multiple air supply/exhaust openings. Also a heat source was installed and some (dynamic) experimental runs included two layers of concrete tiles on the floor. The convective heat transfer at the walls was derived from temperature measurements in these walls while thermocouples and omnidirectional anemometers measured the temperature/velocity distribution inside the test room. This study was done in collaboration with the Belgian Building Research Institute (BBRI). This private research institute made a PASLINK cell available, made the adjustments to the cell and performed the tests.

3.2 Experimental design

3.2.1 Test room setup

An outdoor climate chamber, the PASLINK cell at the BBRI in Limelette (Belgium), accommodated the experiments. The development of this type of highly standardized test cell started with the PASSYS Project which began in 1985. The researchers involved attempted to increase confidence in energy conscious and passive solar building products and evaluation techniques. To this end, they built test cells that enabled to define the thermal performance of building components exposed to real climate conditions. Such a test cell was constructed as a prefabricated, well-insulated structure comprising a test room and a service room. The test room basically acted as a calorimeter: it allowed for measurements of heat transfer through all enclosure surfaces. To guarantee well-mixed indoor conditions,

an AHU, placed within the test room, circulated heated/cooled air via two distribution hoses. The service room, next to it, was used as a space for control and measuring equipment, a cooling unit and a small wall heater, which kept its own indoor conditions at a desired temperature. Wouters et al. [149] and Vandaele and Wouters [150] describe in detail the test facility. Later, as part of the COMPASS project, the PASSYS test cells were updated to improve the test cell performance and measurement accuracy. A calorimetric layer, called the pseudo-adiabatic shell (PAS), was added, having a threefold purpose: to decrease the thermal inertia of the system, to minimize the heat fluxes through the test cell envelope and to measure the temperature difference across the test cell envelope with increased accuracy. The BBRI added twenty panels to the test room of each PASSYS test cell: four to the floor, four to the ceiling and four to each of the long side walls and two to each of the short side walls. Each PAS panel consisted of an electric heating foil and a sequence of insulating and conductive materials on the interior side. Readers interested in more details on the PAS are referred to Maldonado [151] and Hahne and Pfluger [152]. A last large-scale application of the test facilities was the PASLINK project – determining the current name of the test cells. This project did not make changes to the test facilities as it focussed on the dynamic analysis and test methodology for building component evaluation under real outdoor conditions. In conclusion, the advantages of this type of test cell lied in the well-controlled, real room sized environment and the absence of occupancy effects. Besides, the presence of the PAS panels enabled to determine more accurately the conductive heat flux and, thus, the convective heat flux. Therefore, the test cell was found adequate to investigate convective heat transfer.

Yet, the test cell still needed modifications. First, the measurement bay which was originally used for adding building components, was filled with a copy of the current side walls. Further, a separation wall made of 0.20m expanded polystyrene (EPS) was installed in the test room to isolate the AHU in a second service room. This created a new geometrically simple test room, having internal dimensions of 3.75m in length, 2.51m in width and 2.50m in height (Figure 3.1).

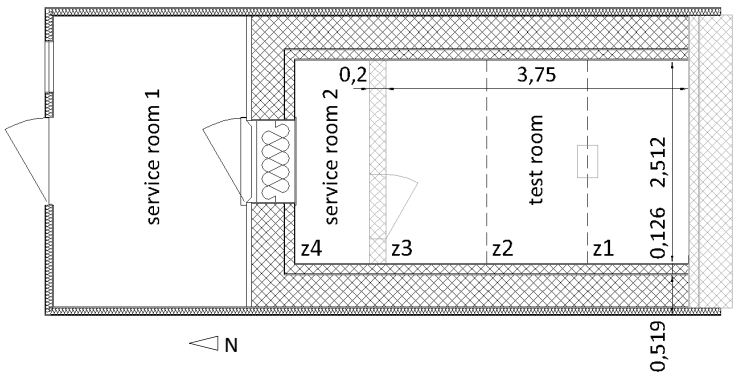

Figure 3.1: Plan of the PASLINK (black) with modifications (grey) (dimensions in meters)

In the upper part of this new separation wall, at 0.20m from the ceiling, two openings were foreseen: one in the symmetry plane and one at 0.20m from the east side wall. At the lower part, one opening was located in the symmetry plane at 0.20m above the floor (Figure 3.2, Figure 3.3(a)). Each opening could be used to exhaust or supply air to the test room or could simply be closed. For use as an exhaust, the opening linked the test room directly with the second service room, which was depressurized by the AHU. In case of an air supply, a grille diffuser, Trox Type AT 100mm x 200mm [153], was installed in the opening. In that case, a flow straightener consisting of three wire meshes was installed between the duct of the AHU and the grille.

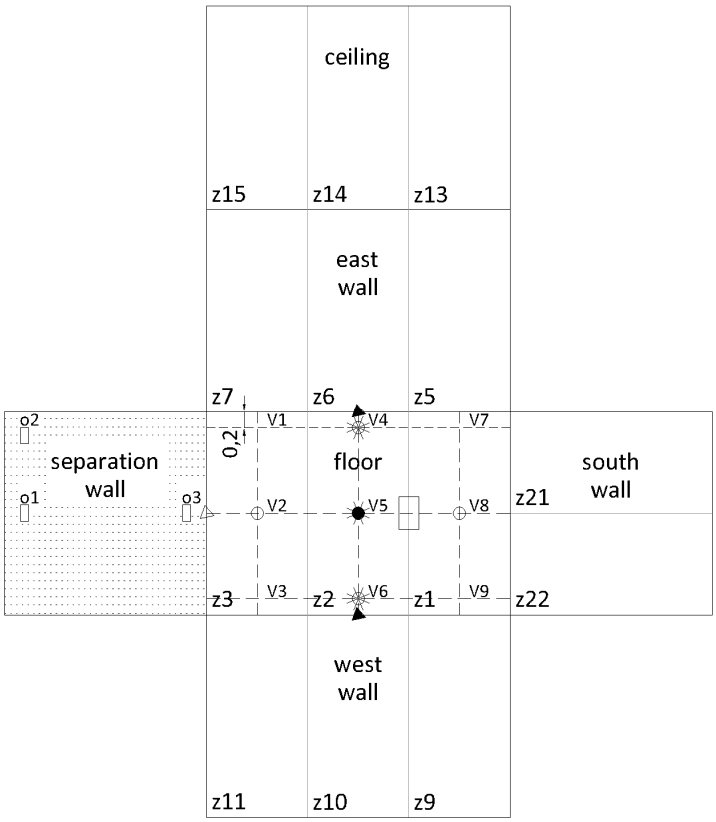

Figure 3.2: PAS panel distribution and measurement locations in the new test room: a) intersection of striped lines: air temperature at 0.20m, 1.25m and 2.30m height, b) ✳: air temperature at 0.02m, 0.04m, 0.10m, 0.20m, 1.25m, 2.30m, 2.40m, 2.46m and 2.48m height, c) ○: velocity measurement at 1.25m height, d) ●: air velocity at 0.20m, 1.25m and 2.30m height, e) △: surface temperature at 1.25m height, f) ▲: surface temperature at 0.20m, 1.25m and 2.30m height, g) heat flux sensors on the floor near v2, v5 and v8

Next to it, a heat source, which could be activated, was located between zone 1 and zone 2 (grey rectangular in Figure 3.1 and Figure 3.2; Figure 3.3(b)). The design of this heat source was based on DIN 4715 [154], which sets guidelines for chilled beams testing, and on recommendations by Zukowska and Melikov [155]. It was a closed aluminium box having dimensions of 0.40m in length, 0.25m in width and 1.00m in height, supported by 0.10m high legs. Its outside was finished with a paint similar to the one of the enclosure surfaces. At the inside, three electrical bulbs could produce a heat load of 77.2W while two fans (2 x 1.4W) guaranteed a uniform temperature distribution. Finally, in some experimental runs there was a double layer of common concrete tiles placed on the floor of the PASLINK test room.

(a) (b)

Figure 3.3: Inside view of (a) the test room and (b) the convective heat source

3.2.2 Test equipment

As mentioned before, the PAS panels (Figure 3.4) acted as large heat flux sensors. The electric heating foil in each panel was located in between the original outside envelope and a 0.10m EPS layer. The aluminium layers on either side of this 0.10m EPS layer created isothermal planes and each one of them was equipped with a set of eight thermocouples (copper-constantan). The accuracy of one such thermocouple was ±0.19°C. This value was derived from prior measurements by the BBRI. Several thermocouples which were configured in the PASLINK cell and a Pt100 sensor (Burns 12001) were put in a thermostatic bath of which the temperature was increased in steps and the absolute differences between the thermocouple readings and the corresponding temperature measured by the Pt100 sensor were set down. The 95th percentile of these absolute differences determined

the quoted accuracy. Originally, the two sets of eight thermocouples acted as a thermopile (i.e. thermocouples connected in series), for which the output voltage is proportional to the temperature gradient. This thermopile signal controlled the heating foil in such a way that the resulting heat flux approximated zero. However, for this study the thermocouples were rewired so that the two sets of eight thermocouples each measured the temperature at the corresponding aluminium layer. In addition, the heating foil was then controlled by the temperature set at the outer aluminium plate: when the average temperature registered by the eight thermocouples at the outer aluminium plate equalled the set point temperature minus 0.5°C the heating foil became active and kept on heating until the set point was reached. Altering the wiring left opportunity to derive the conductive heat flux through the PAS and to determine the radiative heat flux at the surface and, thus by extension, the convective heat flux at the interior surface. To determine the conductive heat flux through the concrete tiles three heat flux sensors TNO WS 31S [156] were fixed on the interior surface of the tiles, near locations v2, v5 and v8 (Figure 3.2). Those same heat flux sensors were also present in experimental runs without tiles.

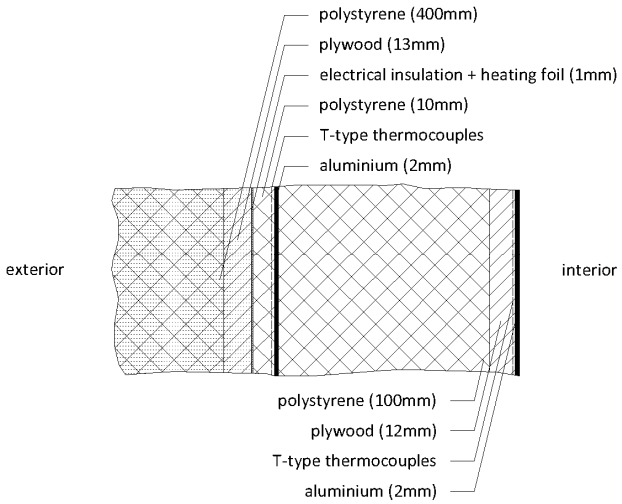

Figure 3.4: Structure of the PAS and a part of the original envelope (shaded)

The interior of the test room was also equipped with T-type thermocouples (Figure 3.2). First of all, at the same locations of the three heat flux sensors, thermocouples were installed on top of and between the two layers of concrete tiles. Further, thermocouples fixed to the interior side of the inner aluminium layers of PAS panels z6 and z10 measured the local surface temperature at 0.20m, 1.25m and 2.30m height. These enabled to check whether the highly conductive aluminium sheets guaranteed a uniform temperature distribution. Next to it, thermocouples fixed to the centre of the EPS separation wall and of the respective

five surfaces of the heat source measured the surface temperature. Besides, locating thermocouples in the air supply and exhaust openings would allow determining the global system performance. Furthermore, more thermocouples, fixed to nine vertical ropes measured every minute the temperature distribution in the room. In general, the air temperature was monitored at three heights (0.20m, 1.25m and 2.30m). However, at positions v4, v5 and v6, additional sensors at smaller distances (0.02m, 0.04m and 0.10m) from the horizontal surfaces recorded the local air distribution. To perturb the airflow as little as possible, the original radiation shields around the thermocouples were removed. In this experimental setup, radiation introduced an error in measurement which was smaller than the thermocouple accuracy. The following reasoning justifies this statement.

Due to the high thermal diffusivity of the thermocouple and assumedly negligible conduction effects, only convection and radiation determine the heat balance and, thus, the thermocouple reading. Such a heat balance based on the linear relationships for heat transfer (i.e. the heat flux equals the product of a heat transfer coefficient and a (small) temperature difference), indicates that the temperature registered by the thermocouple T_{TC} depends on the weighted average of the local air temperature $T_{a,l}$ and the mean surface temperature $T_{w,avg}$ of the surroundings, defined by the convective heat transfer coefficient h_{conv} and the radiative heat transfer coefficient h_{rad} (Eq. (3.1)). Reworking last-mentioned equation leads to an expression of the local air temperature (Eq. (3.2)). Setting this calculated local air temperature against the thermocouple reading offers the opportunity to assess the impact of radiation on the reading. This type of analysis is only possible at seven locations, i.e. where both temperature and velocity are measured.

$$T_{TC} = \frac{h_{conv} \cdot T_{a,l} + h_{rad} \cdot T_{w,avg}}{\left(h_{conv} + h_{rad}\right)} \tag{3.1}$$

$$T_{a,l} = \frac{\left(h_{conv} + h_{rad}\right) \cdot T_{TC} - h_{rad} \cdot T_{w,avg}}{h_{conv}} \tag{3.2}$$

The estimate of the radiative heat transfer coefficient relies on Annex A of NBN ISO 6946 [157]. This standard expresses the radiative heat transfer coefficient h_{rad} as a function of the emissivity ε and the radiative coefficient for a black-body surface h_{ro}:

$$h_{rad} = \varepsilon \cdot h_{r0} \tag{3.3}$$

The emissivity of the thermocouple used in the PASLINK test cell assumedly equals 0.20 in accordance with Siegel and Howell [158]. The radiative coefficient for a black-body surface depends on the mean surface temperature, as laid down in aforementioned standard. The weighting function to determine this mean surface temperature relies on view factor calculation. To derive the convective heat

transfer coefficient this analysis relates the convective heat transfer to crossflow over a circular cylinder, as investigated by, e.g. Zukauskas and Ziugdza [159], Morgan [160] and Wang and Trávníček [161]. In particular last-mentioned authors successfully developed forced convection heat transfer correlations for low-Reynolds number flows (i.e. when viscous forces are dominant. They found that the Nusselt number Nu, i.e. the ratio of convective to conductive heat transfer, depends linearly on a redefined representative Reynolds number Re_{rep} (Eq. (3.4)), for which the kinematic viscosity $\nu(T_{rep})$ is function of some ratio of the cylinder surface temperature T_w and the free stream temperature T_∞ (Eq. (3.5)).

$$Nu = 0.502 + 0.434 \cdot \sqrt{\mathrm{Re}_{rep}} \tag{3.4}$$

$$\frac{T_{rep}}{T_\infty} = 1 + 0.36 \cdot \frac{T_w - T_\infty}{T_\infty} \tag{3.5}$$

Because of the relatively low indoor air velocities (0.05 to 1.5m/s) measured during the experimental runs in the PASLINK test cell and the small diameter of the thermocouple (≈0.001m), a low-Reynolds flow applies. None of the velocity readings results in a redefined effective Reynolds number Re_{eff} (for which the kinematic viscosity $\nu(T_{eff})$ relies on Eq (3.6)) higher than 46.8.

$$\frac{T_{eff}}{T_\infty} = 1 + 0.28 \cdot \frac{T_w - T_\infty}{T_\infty} \tag{3.6}$$

Besides, even when the boundary conditions change, this passes gradually, inducing only forced convection. The readings actually fulfil different criteria in literature to determine the forced convection region: $Gr.Re^{-1.8}<0.62$, $Ri<0.5$ and $Gr.Re^{-2.39}<0.1$ (according to Sharma and Sukhatme [162], Morgan [163] and Hatton et al. [164], respectively). As a result, the above linear relation (Eq. (3.4)) can be used to determine the convective heat transfer coefficient. Roughness – e.g. interwoven wires, corrosion, possibly increasing the heat transfer, is neglected. For that matter, Eq. (3.2) relies on ten minute-averages of the terms and necessitates an iterative calculation procedure. By way of example, Figure 3.5 depicts the difference between the thermocouple readings and the corresponding derived air temperatures during dynamic experimental run 3 (N;c;T). All but the temperature difference on vertical v2 reveal a similar course. During the night period with night cooling the differences equal -0.05°C at the beginning and diminish gradually while by day they approximate 0. The differing course of the temperature difference on vertical v2, especially by day (which is at most 0.07°C), is due to the fact that this thermocouple is within the cool jet. Overall, in this experimental setup, radiation introduces an error in measurement which is smaller than the thermocouple accuracy (±0.19°C). Yet, putting forward the related uncertainty for all thermocouples in the test room is impossible as only at seven locations both the temperature and the velocity are available.

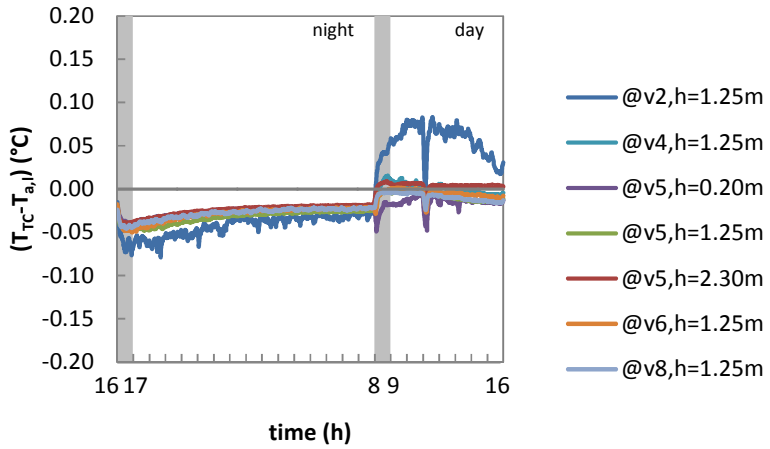

Figure 3.5: Comparison of thermocouple reading and derived air temperature during the last 24h of dynamic experimental run 3 (N;c;T)

Furthermore, omnidirectional thermal anemometers (TSI 8475 [165]) measured every minute the air velocity at seven points (Figure 3.2). The measurement accuracy was limited to ±3.0% of the recording ±1.0% of the selected measurement range (0.05m.s^{-1} to 2.5m.s^{-1}). By the way, prior to the actual measurement campaign, using the same anemometers, multiple detailed velocity profiles near the diffuser were obtained in accordance with the method described in ASHRAE Standard 70-2006 [166]. First, smoke visualization allowed defining the adequate measuring planes and determining the flow direction. On the one hand, a measurement plane is preferably located in the fully-developed jet region where velocity and temperature profiles are self-similar, i.e. can be described by non-dimensional equations. On the other, the plane should be near the air supply to avoid the interaction of the jet with recirculation flows and thermal plumes. Then, having deduced two assumedly proper planes, the seven anemometers, fixed to a stand, measured under isothermal conditions the air velocity at seven locations on a horizontal (Figure 3.3(a)). This procedure was repeated at four other heights, ending up with a 7x5 grid. The recording frequency was significantly increased from once a minute to twenty measurements per second.

3.2.3 Test procedure

The following parameters were varied in the steady-state experiments: the volumetric flow rate $n \cdot V$, the air supply temperature T_{sup}, the temperature measured at the aluminium layer at the exterior side of the PAS TC_{outer}, the operation of the heat source and the locations of the air supply/exhaust. The dynamic experiments could additionally include two layers of concrete tiles on the floor. The parameters were tuned in such a way that the experiments imitated two typical mixed convection regimes, possibly coming one after another. The first one resembled a typical day regime, with a moderate ventilative cooling rate and an active heat source. The second one imitated night cooling, with a considerable ventilative cooling rate and an inactive heat source (from now on called night regime). The imposed temperatures are loosely based on measurements by Blondeau et al. [29], the air flow rates partly rely on EN 13779 and the power of the active heat source corresponds to the medium level defined by Breesch [37].

During the day regime, the AHU supplied $36.0 m^3.h^{-1}$ of air at 23.7°C while the heat source of 80.0W was active. TC_{outer} was set to 30°C so that the difference between the temperature of the inner aluminium layer and the one of the supplied air equalled 6°C. During the night regime, the ventilative cooling rate was higher ($n \cdot V = 188 m^3.h^{-1}$ and T_{sup}=16.5°C) and the heat source was inactive. TC_{outer} equalled 45°C to obtain the same temperature difference between the inner aluminium layer and the supplied air as during the day regime. These two convection regimes were combined with two air supply/exhaust configurations: o1/o3 and o2/o3, which resulted in a total of four steady-state experimental runs. Each steady-state experiment lasted at least five days, as it took some time to achieve approximately steady-state conditions.

Table 3.1: Parameter values for steady-state experiments

	Day regime	Night regime
TC_{outer} (°C)	30.0	45.0
$n \cdot V$ ($m^3.h^{-1}$)	36.0	188.0
T_{sup} (°C)	23.7	16.5
Q_{source} (W)	80.0	0
Air supply/exhaust (Figure 3.2)	o1/o3; o2/o3	

The second experimental series were designed to study the response to stepwise changes of the convection regimes. These dynamic experiments imitated a 24h cycle which comprised two distinct convection regimes as shown in Figure 3.6. From 8h until 16h the boundary conditions led to a convection regime similar to the day regime of the steady-state experiments. The AHU supplied $36.0 m^3.h^{-1}$ of air at 23.5°C and the heat source of 80.0W was activated. During the following period, i.e. from 16h until 8h, everything but the heating by foils could be shut down or night cooling could be imitated ($n \cdot V = 188 m^3.h^{-1}$ and T_{sup}=16.5°C, inactive heat source). These two possible sequences were combined with two different amounts of thermal mass (with and without concrete tiles on the floor) and with

two air supply/exhaust configurations (o1/o3 and o3/o1), which resulted in a total of eight dynamic experimental runs as shown in Figure 3.7. Each run lasted about six days. Note in Figure 3.7 the codes of the respective runs: the capital letters N, C and T indicate that night cooling was applied, concrete tiles were present respectively the air supply was located at the top. Regular letters represent the other possibilities. Further note that the results of the period of time in which the AHU and the heat source were switched off, are usually omitted in the analyses to come.

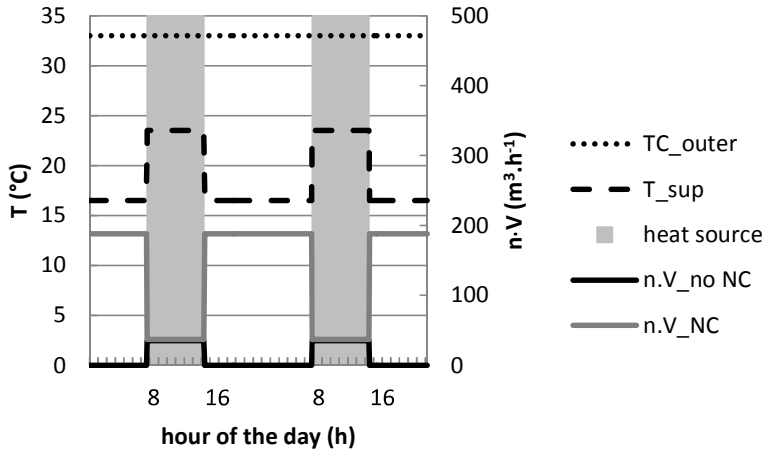

Figure 3.6: Boundary conditions for dynamic experiments

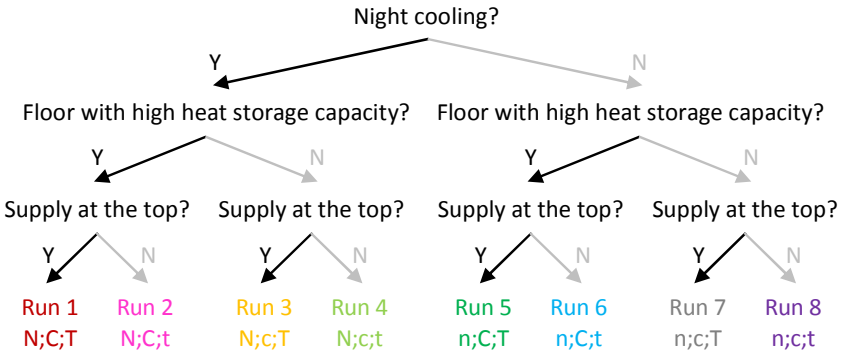

Figure 3.7: Tree diagram of dynamic experiments

3.3 Analysis method

3.3.1 Conduction/radiation model

This study derives the convective heat flux from temperature measurements, like many previous studies [103, 123-125, 129] (see Chapter 2). However, the derivation approach differs in one or more aspects. First, this study does not always aim at steady-state boundary conditions. It also investigates the transient response of a room induced by step changes. As a consequence, a transient thermal analysis is necessary to derive the time-varying heat flux. Secondly, no surface inside the adapted PASLINK cell has a reflective finish and, thus, it is primordial to take radiation into account. For these reasons, this study deploys a conduction/radiation model which solves a heat balance at a given PAS panel (Eq. (3.7)). The reason why this in-house conduction/radiation model is used is because it runs faster in comparison with commercial alternatives. With this, this study follows the approach suggested by Artmann et al. [148].

$$q_{conv}(t) = q_{cond}(t) - q_{rad}(t) \tag{3.7}$$

A 1-D finite volume model, with Crank-Nicholson time stepping (which assumes a linear temperature-time relation), calculates the transient conductive heat flux through a PAS panel. Assuming uniform conductivity and uniform grid spacing, the used discretised heat conduction equation comes down to Eq. (3.8). This equation is used to predict the temperature at point i at time m [167].

$$\begin{aligned}\rho \cdot c \cdot \frac{\Delta x}{\Delta t} \cdot \left(T_i^m - T_i^{m-1}\right) = 0.5 \cdot \left[\frac{\lambda \cdot \left(T_{i-1}^m - T_i^m\right)}{\Delta x} - \frac{\lambda \cdot \left(T_i^m - T_{i+1}^m\right)}{\Delta x}\right] \\ + 0.5 \cdot \left[\frac{\lambda \cdot \left(T_{i-1}^{m-1} - T_i^{m-1}\right)}{\Delta x} - \frac{\lambda \cdot \left(T_i^{m-1} - T_{i+1}^{m-1}\right)}{\Delta x}\right]\end{aligned} \tag{3.8}$$

The temperature measured at the inner aluminium layer and the one at the exterior side of each PAS panel act as input to the conduction model. Therefore, the model (certainly) comprises the three PAS layers between these two measurement planes. Table 3.2 lists their respective thickness d, thermal conductivity λ and volumetric heat capacity ρc. However, there is also a virtual layer included. This 0.0001m thick layer, with a negligible thermal resistance (1.10^{-8}m.K.W^{-1}) and a small volumetric heat capacity (0.01kJ.m^{-3}.K^{-1}), is located closest to the interior of the PASLINK cell. Split into parts, this very thin layer with a high thermal diffusivity enables to accurately determine the conductive heat flux to the interior aluminium layer without significantly increasing the computational time; also in the grid convergence study to come, in which the discretisation level of the PAS layers is varied. Actually, to determine the conductive heat flux to the interior, Fourier's law of conduction is applied to the two computing nodes in the virtual layer closest to the interior, which are at a small fixed distance from each other (Eq. (3.9)).

$$q_{cond} = \frac{\lambda \cdot (T_{i-1} - T_i)}{\Delta x} \tag{3.9}$$

Table 3.2: Mean properties and uncertainties (95%) of the considered PAS layers

Layer	d (m)	λ (W.m^{-1}.K^{-1})	ρc (kJ.m^{-3}.K^{-1})
Outer aluminium	0.002 ±10%	230 ±2%	2430 ±5%
EPS	0.100 ±0.002	0.033 ±0.002	26 ±10%
Plywood	0.012 ±5%	0.108 ±0.014	1400 ±5%

Aforementioned conduction model is not only verified against the commercial software VOLTRA [168], it is also validated against the measured heat fluxes at PAS panels z1, z2 and z3. By way of example, Figure 3.8 shows that the predicted conductive heat fluxes correspond to the values measured by the heat flux sensors. For that matter, validation against the total convective heat flow removed by the AHU could be another possibility, were it not that the determination of the airflow rate introduces a quite large uncertainty.

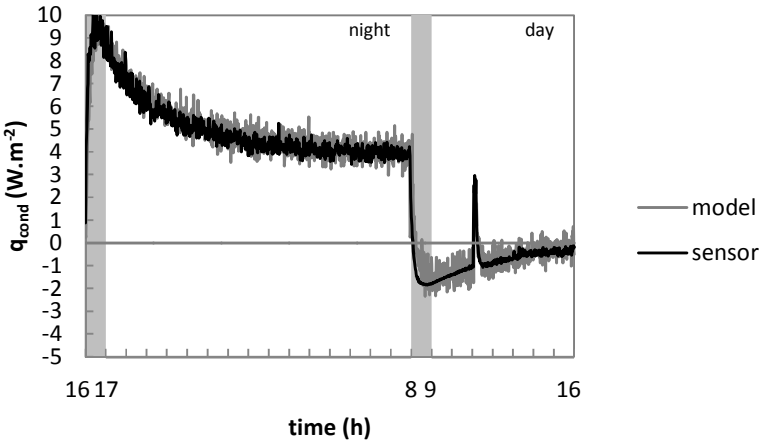

Figure 3.8: Conductive heat flux at PAS panel z1 during the last 24h of dynamic experimental run 3 (N;c;T) (estimated uncertainty in heat flux sensor = ±5%)

This conduction model is complemented with the ability to calculate radiant heat transfer, in conjunction with view factor calculation, for the twenty surfaces considered (i.e. fourteen PAS panels, one EPS separation wall and five surfaces of the heat source). This model assumes diffuse-grey surfaces with a non-participating medium in between (that is, air). At each time step, it solves, with the aid of Gaussian elimination, Eq. (3.10) for the unknown radiosity J_i of each surface in the room (i.e. the total radiation that leaves the surface per unit time and per unit

area). The net radiant flux $q_{rad,i}$ lost by surface i then comes from Eq. (3.11), i.e. the difference between the radiosity J_i and the irradiation G_i (i.e. total radiation incident on the surface per unit time and per unit area).

$$J_i = \varepsilon_i \cdot \sigma \cdot T_i^4 + (1-\varepsilon_i) \sum_{j=1}^{n} F_{ij} \cdot J_j \tag{3.10}$$

$$q_{rad,i} = J_i - G_i = J_i - \sum_{j=1}^{n} F_{ij} \cdot J_j \tag{3.11}$$

Here, the parameter σ represents the Stefan-Boltzmann constant and F_{ij} is the view factor from surface i to surface j. Further, ε_i stands for the emissivity of each one of the surfaces i. The BBRI indicated that almost all surfaces have an emissivity of 0.88. Only the concrete tiles have a higher emissivity of 0.95. Finally, T_i equals the temperature of each one of the surfaces i. In case of a PAS panel, this corresponds to the average of the thermocouple readings at the inner part. On the other hand, in case of the EPS separation wall and the surfaces of the heat sources, the temperature T_i comes from one thermocouple reading. This radiation model was verified against the radiation model available in the commercial software VOLTRA, confirming its precision.

Each simulation covers 3.5 days singled out of the respective experimental campaigns. The first 2.5 days account for the unknown initial temperature distribution in the PAS; the remaining period of one day is used for analysis. By way of example, Figure 3.9 shows the results of the transient analysis at PAS panel z6, one of the ceiling panels, during the last 24h of run 3 (N;c;T). This graph depicts the predicted convective heat flux and the surface temperature at PAS panel z6, the local air temperature $T_{a,l}$ on v8 at 2.30m height and the air supply temperature T_{sup}. The two distinct operating conditions catch the eye: the day regime and the night regime with night cooling. Next to this, each regime comprises two behaviours: a stepwise change leads to an initial steep transition of the convective heat flux followed by a quasi-exponential increase/decrease to the steady-state level (quasi-exponential because of the changing heat transfer and the time constant of the indoor air). The steep changes originate from the delayed change of the air supply temperature and the time constant of the indoor air. Therefore, further analyses of the dynamic experiments exclude the first hour of each regime (indicated by the grey zones). In addition, this enables to calculate low-order polynomial regressions of the convective heat flux q_{regr}, on which the bulk of the following analyses build. Obviously, this fit corresponds to the average flux in case of the steady-state experiments.

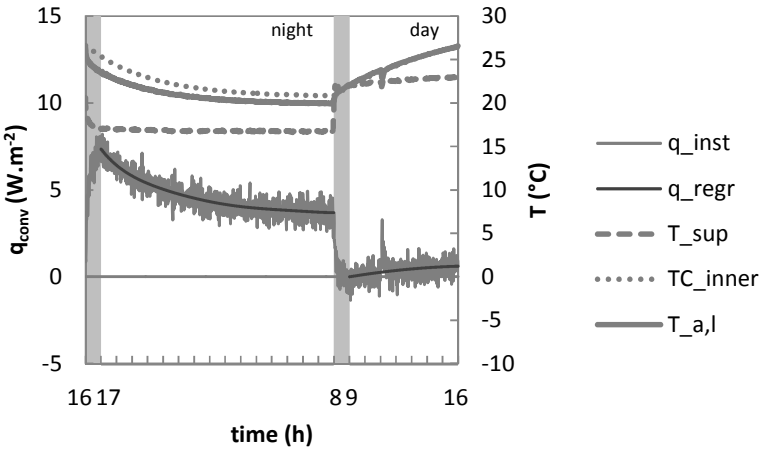

Figure 3.9: Convective heat flux and temperatures at PAS panel z6 during the last 24h of dynamic experimental run 3 (N;c;T)

3.3.2 Uncertainty analysis

Even though the conduction/radiation model is verified against commercial software and partly validated, the calculated heat fluxes are of course not free of error. First of all, as any numerical simulation, this model introduces a space and time discretisation error. Yet, performing multiple simulations, of which each one has a different discretisation level, enables to investigate whether the discretisation error is sufficiently small. First, underlying study checks upon the grid resolution of the three PAS layers. The originally used non-uniform grid size Δd_{ori}, i.e. 0.005m for the EPS layer and 0.0005m in case of plywood and aluminium, is refined two, four and eight times. Next to it, this study investigates multiple time step sizes: 60s, 30s, 10s and 5s. Starting from the measuring interval, i.e. 60s, this study applies Shepard's method [169] to derive the inner and outer temperatures at intermediate time steps. This simple form of interpolation uses a weighting function which depends on the distance from the scatter point to the interpolation point. In both convergence analyses the finest resolution acts as a reference. The difference in output between such high-res simulation and a coarser one assumedly reflects the discretisation error. Note that this approach is just one of several possibilities; however, the fast-running conduction/radiation model enables to test a fairly fine discretisation level which is assumed to introduce no discretisation error. The aforementioned outcome is either the instantaneous convective heat flux or the corresponding polynomial regression. Further, these analyses consider the steady-state experiments ('day/night, o1/o3') and the dynamic experimental run 3 (N;c;T) because these comprise two distinct sets of boundary conditions: a day regime and a night regime with night cooling. However, the following figures only depict the results belonging to the dynamic experiment. After all, the stepwise

changes of the boundary conditions make the simulations more sensitive to discretisation errors. Figure 3.10 and Figure 3.11 show for the day respectively night regime with night cooling the boxplots of the differences between the (a) instantaneous/(b) regressed convective heat fluxes for different grids and the ones obtained with the finest resolution, i.e. $\Delta d=\Delta d_{ori}.8^{-1}$. Figure 3.12 and Figure 3.13 do the same for the time discretisation error. In this case, similar to the grid convergence study, the results obtained with the finest resolution, now $\Delta t=5s$, are assumed to be equal to the continuous solutions. Note that the lower and upper quartiles tie in with the 2.5^{th} and 97.5^{th} percentile. This adaptation facilitates the comparison of the space/time discretisation error with the other errors, all having a 95% confidence interval. For this study, the main advantage of using boxplots lies in their ability to distinguish absolute from cumulative errors. The median indicates – better than the mean in the presence of outlier values – whether the error accumulates. Secondly, the spacings between the different parts of the box help indicating the degree of spread and skew in the data, and help identifying outliers. Underlying figures indicate that the median approximates zero in all cases. In other words, the cumulative error due to space/time discretisation is non-existent. Beside it, the large spread and significant outliers in case of instantaneous convective heat fluxes stand out (Figure 3.10(a), Figure 3.12(a)): eddies produce (fast-)changing fluxes and also the limited resolution of the thermocouples is involved. However, the focus of this study lies on polynomial regressions of the convective heat fluxes, to which smaller space and time discretisation errors apply. Figure 3.10(b) and Figure 3.11 show that increasing the grid resolution does not significantly improve the predictions (mind the smaller y-axis scale). After all, the results obtained with the original grid approximate the ones of the finest grid. As shown in Figure 3.12(b) and Figure 3.13, the time step size influences more but still to a limited extent the predicted convective heat fluxes. The fluxes at all PAS panels but one based on a time step of 60s differ from their finest resolution results by at most $0.005W.m^{-2}$. The fluxes at PAS panel z21 exhibit a larger spread ($0.03W.m^{-2}$); because of the many unsolicited starts/stops of the heating foil in the PAS panel in question. Nevertheless, looking ahead at the other uncertainties, the space/time discretisation error is negligible. Therefore, the rest of this study relies on the original discretisation resolutions and leaves out the space/time discretisation errors.

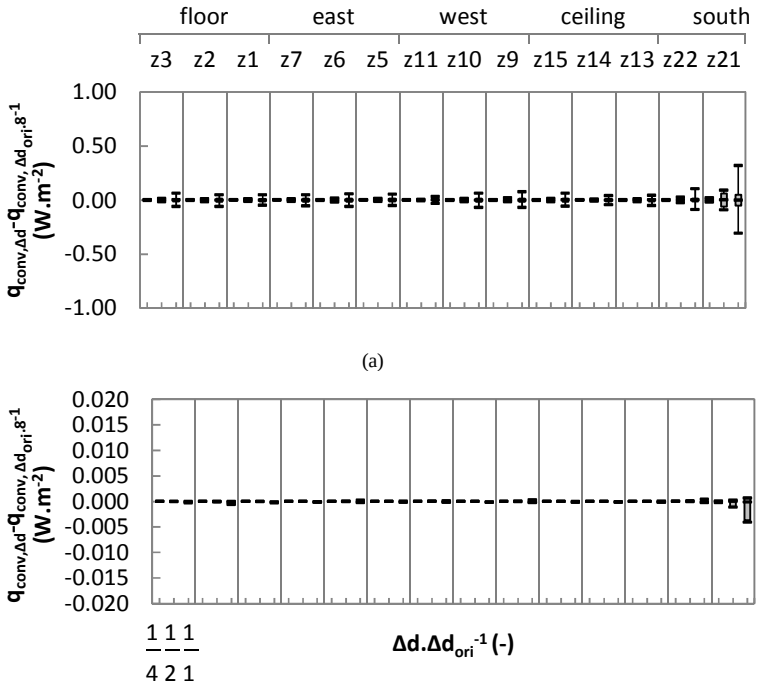

Figure 3.10: Boxplots (min, 2. 5%, median, 97.5%, max) of differences between (a) actual/(b) fitted convective heat fluxes for different grids (day regime of run3(N;c;T))

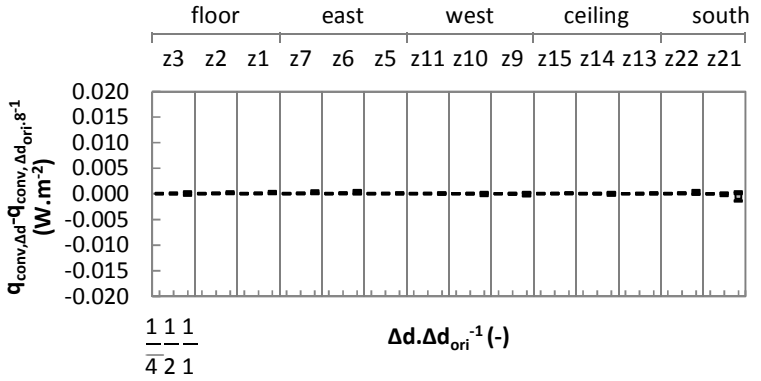

Figure 3.11: Boxplots (min, 2.5%, median, 97.5%, max) of differences between fitted convective heat fluxes for different grids (night regime of run3(N;c;T))

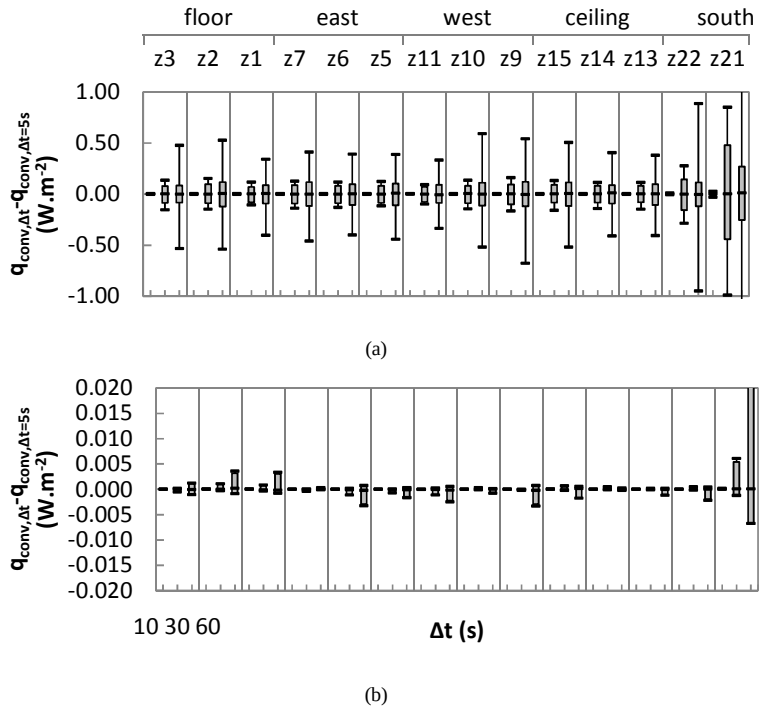

Figure 3.12: Boxplots (min, 2.5%, median, 97.5%, max) of differences between (a) actual/(b) fitted convective heat fluxes for different time steps (day regime of run3(N;c;T))

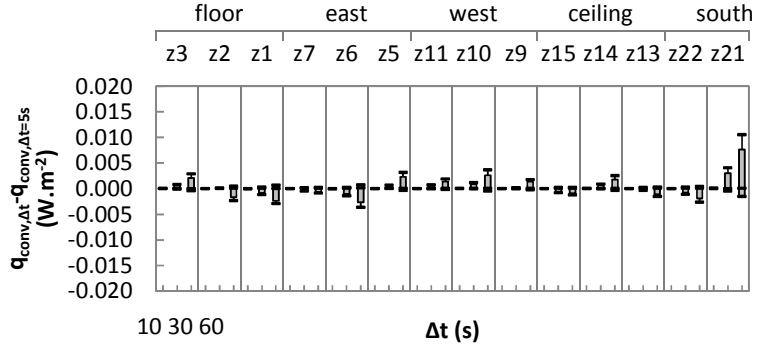

Figure 3.13: Boxplots (min, 2.5%, median, 97.5%, max) of differences between fitted convective heat fluxes for different time steps (night regime of run3(N;c;T))

Further, regardless of whether model inputs are measured experimentally or obtained from literature, they cannot be assumed to be free of error. To determine how these input uncertainties impact upon the convective heat fluxes derived from the measured temperatures, this study relies on Monte Carlo analysis. This method incorporates the influence of the whole range of variation and distribution of the input parameters and evaluates the effect of one parameter while all other parameters are varied as well [170]. This way, the uncertainty analysis provides the range and probability density for specific confidence intervals (typically 95%). The analysis takes into account the uncertainties in the following input variables: the thickness, the thermal conductivity and the volumetric heat capacity of the considered PAS layers, the emissivity of the inner surfaces and the thermocouple readings at the inner and outer part of the considered layers – in this study all classified under setup error. The actual procedure starts with selecting a distribution and range for each input parameter. Aforementioned input variables are assumed to be normally distributed, having a confidence interval of 95%. Table 3.2 shows the mean value and associated uncertainty of the properties of the considered PAS layers. The thickness of the layers corresponds to the product specifications. The related uncertainties are based on Bowler et al. [171] (aluminium), EN 13163 [172] (EPS) and BS EN 315 [173] (plywood). The thermal conductivities are measured with a guarded hot plate on material samples from the PAS. The associated uncertainties account for the accuracy of the prior conductivity measurements (±2%) and the temperature dependency of the material involved (ISO 10456 [174], ΔT assumed to be 10 to 15°C). The volumetric heat capacity of the materials mainly corresponds to product specifications. Only the density of EPS was measured on material samples from the PAS. The related uncertainties are based on, amongst others, MacDonald [175] and BS EN 1602 [176]. The emissivity of the inner surfaces of the PAS is set to 0.88±0.05 while 0.95±0.05 applies to the concrete tiles. The emissivities are provided by the BBRI while the uncertainties are based on measurements by Willockx [177]. Finally, the uncertainty of the thermocouple reading at the inner/outer part of each PAS panel equals ±0.07°C, which is smaller than the aforementioned uncertainty for one thermocouple, i.e. ±0.19°C. This is based on the following (optimistic) reasoning. The stored temperature equals the arithmetic mean of eight thermocouple recordings, of which each covers an identical area. Highly conductive aluminium sheets guarantee a uniform temperature distribution and, thus, each thermocouple measures the same temperature. So, on the assumption that the cold junction compensation error is negligibly small, the uncertainties related to the voltage readings are independent (not constant over time) and a high-order calibration curve excludes the error due to the different compositions of the alloys [178], the error of eight thermocouple recordings reduces by a factor 2.8 according to theory of error propagation: [8·(0.19)2]0.5/8. The uncertainty analysis continues by generating a sample from these distributions. For simplicity, this study uses the method of random sampling to select a sufficiently large sample. Then, the conduction/radiation model calculates the impact for each element of this sample, before finally deriving the uncertainty bounds. How to determine these uncertainty bounds is explained in the following. To facilitate reading comprehension, Figure

3.14 displays a schematic overview of the methodology used. Starting with the measured temperatures at time steps T_1, T_2, …, T_m (where m=5250), simulations including different combinations of setup uncertainties E_1, E_2, …, E_n (where n=300) enable to determine the standard deviation of the resulting regressed 300 fluxes for each time step $\sigma(q_{1,regr\ j})$, $\sigma(q_{2,regr\ j})$, $\sigma(\ldots)$,$\sigma(q_{m,regr\ j})$. For steady-state experiments, the quoted standard deviation equals the average of the values at the respective time steps. Obviously, multiplied by ±1.96, this standard deviation defines the 95% confidence interval. Mind that this uncertainty neglects the (small) error introduced by the regression of the actual heat fluxes $q_{1,j}$, $q_{2,j}$, …, $q_{m,j}$.

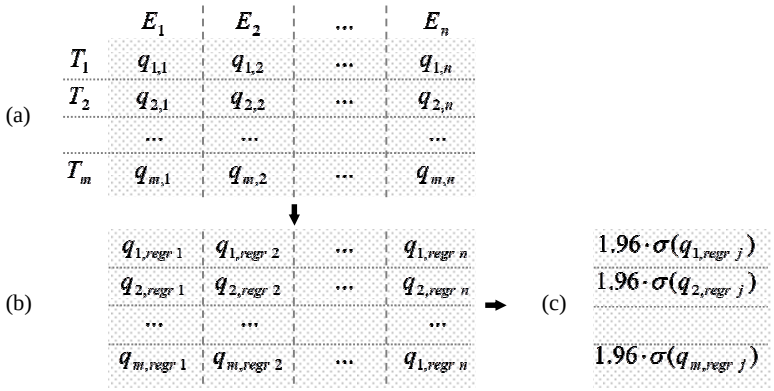

Figure 3.14: (a) input and simulation, (b) regression and (c) uncertainty estimate

Figure 3.15 demonstrates how the uncertainties in the convective heat fluxes at the respective PAS panels relate to each other during the steady-state runs of the (a) day respectively (b) night regime of air supply/exhaust configuration o1/o3. The left y-axis zooms in on the uncertainties while the right y-axis shows the convective heat fluxes at the respective panels together with their uncertainties. The uncertainty due to the setup is only slightly sensitive to the PAS panel and the convection regime (day/night). On average, the 95% confidence interval spans ±0.5W.m^{-2}. However, this is not the case for the convective heat fluxes. The heat fluxes during the night regime are considerably larger and show a larger spread than in case of the day regime. Setting the convective heat fluxes and the associated uncertainties against each other reveals that assessing the heat flux distribution is only possible for the night regime. However, the considerable uncertainty bounds do not interfere in assessing the room/system design impact for each panel separately: the setup properties stay assumedly the same during the considered measurement periods or, in other words, the setup uncertainty is systematic. Similar remarks apply to the uncertainties obtained for dynamic experimental runs with this distinction that the uncertainties vary over time, as shown in Figure 3.16. Last-mentioned figure depicts boxplots of the convective heat fluxes at all PAS panels (right y-axis) and of the related uncertainties (left y-

axis) during dynamic experimental run 3 (N;c;T). The uncertainties reach a maximum after each stepwise change and then decrease exponentially towards the level observed during the steady-state experiments. Apparently, one or more input variables introduce a larger uncertainty when heat fluxes change rapidly. Unfortunately, the above uncertainty analysis cannot specify the uncertainty sources.

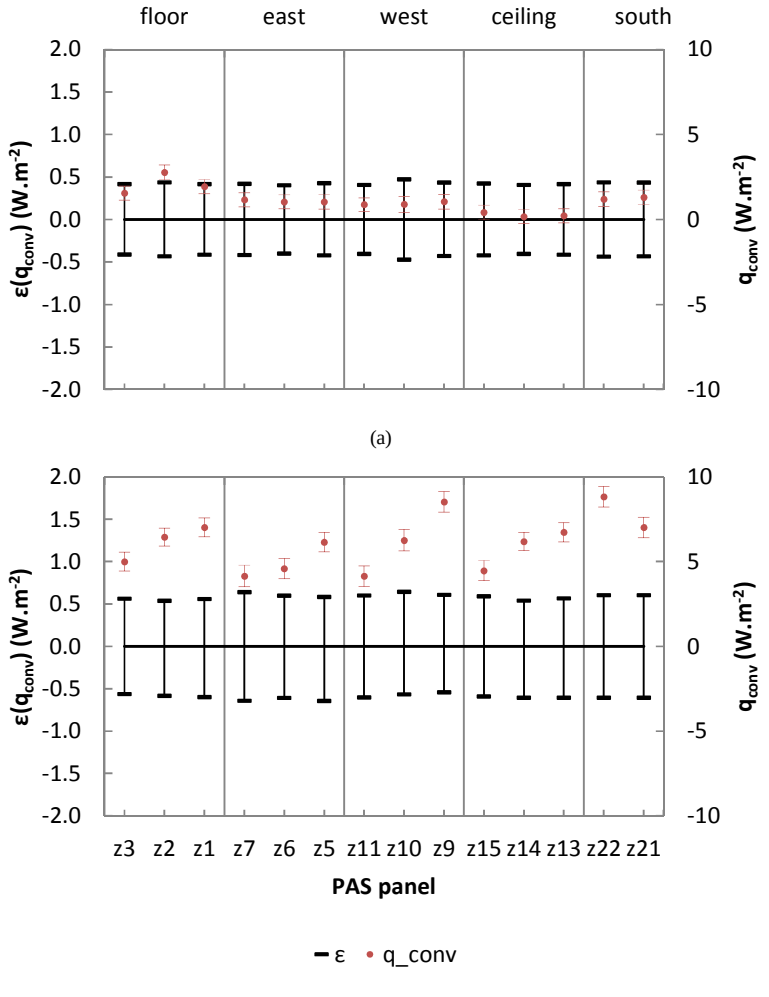

Figure 3.15: Uncertainties in the convective heat flux at respective PAS panels during steady-state experiments: (a) 'day regime, o1/o3' and (b) 'night regime, o1/o3'

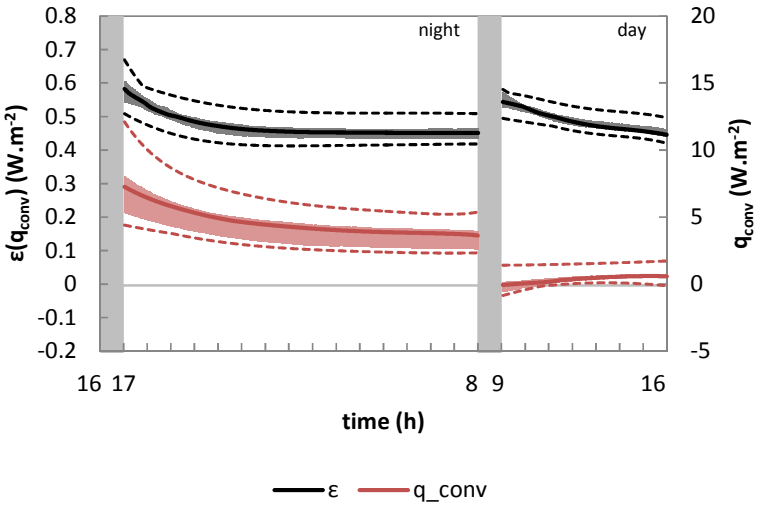

Figure 3.16: Boxplots (min, 2.5%, median, 97.5%, max) of the uncertainties in the convective heat flux at PAS panels during dynamic experimental run 3 (N;c;T)

Furthermore, the resulting heat fluxes rely on an imperfect system control and inherently present eddies, which introduce another source of uncertainty. For example, in case of the night regime, the cooling unit switches on and off more often because of the higher overall convective heat flux. Unfortunately, determining the related uncertainty is impossible: the airflow behaviour and the system responses interdepend. Nevertheless, to get an idea of the possible impact, this study incorporates a finger exercise on the steady-state experimental runs (a) 'day regime, o1/o3' and (b) 'night regime, o1/o3'. Now, a similar Monte Carlo analysis starts from multiple sinusoidal variations of the average inner/outer temperatures. The amplitudes are limited to the 2.5th and 97.5th percentiles of the respective registered inner/outer temperatures. The angular frequencies, on the other hand, are based on the observed range of periods. For the outer temperature a minimum period of 4 minutes applies which can go up to five hours while the period of the inner temperature varies between five hours and twelve days. This analysis shows that the related uncertainty bounds exceed the setup uncertainty limits at most by an inappreciable percentage of 4%. This partly refutes the criticism that an outdoor test facility like the PASLINK cell would be unsuited for this kind of study. For, the heating foils guarantee a quasi-steady-state temperature boundary condition while the ventilation system turns out to control the indoor conditions reasonably well. For that matter, even box-in-box cells show similar unstable behaviour (e.g. [179]).

3.3.3 Sensitivity analysis

The above uncertainty analyses indicate that the setup uncertainty is most important. Unfortunately, they cannot further point out the uncertainty sources – as previously mentioned. However, bearing similar future experiments in mind, indicating weak links in the setup proves valuable. Therefore, this study includes a sensitivity analysis. This determines the contribution of the uncertainties in the individual input variables to the calculated heat flux uncertainty [180]. This study only aims at identifying and ranking qualitatively the factors that control most of the output variability. Therefore, it does not go beyond an economical screening method such as the one-at-a-time method. This approach evaluates in turn the impact of changing values of each input parameter. For each parameter, two extreme values are selected on both sides (higher '+' or lower '-') of the standard value – in this case corresponding to the 95% confidence limits. The major limitation is that interactions between input factors cannot be determined.

Figure 3.17 displays the sensitivity of the convective heat fluxes to the setup variables for the steady-state experiments (a) 'day, o1/o3' and (b) 'night, o1/o3'. The difference between the results obtained with the respective extreme values is used to indicate the sensitivity: a positive difference indicates that the convective heat flux obtained with the upper value of the considered input variable is higher than the one obtained with the lower value and vice versa. Furthermore, the box plots contain the respective sensitivities in the convective heat fluxes at all PAS panels. According to Figure 3.17(a), the convective heat flux is most sensitive to the thermocouple reading at the inner aluminium sheet. After all, large temperature differences between the heat source surfaces and the PAS panels result in a high radiative flux. During the night regime (Figure 3.17(b)), however, the thermocouple reading accuracy at the inner aluminium sheets is just as important as the thermal conductivity of the EPS layer. Note that also the thickness of that same EPS layer has become important. After all, the heat source is inactive while the ventilation system induces a higher convective and, thus conductive heat flux. Furthermore, in both experimental runs the impact of the emissivity depends heavily on the considered PAS panel, even though all panels have assumedly the same emissivity. However, the strongly differing view factors explain this finding. For example, an altered emissivity logically influences more panel z21 than z3 during the day regime as z21 stands in front of the heat source. Finally, for both regimes, the thermal capacity is of no account as these results rely on nearly steady-state boundary conditions. Conversely, no doubt the thermal capacity of in particular the material layers on the inside will come into play during dynamic experiments.

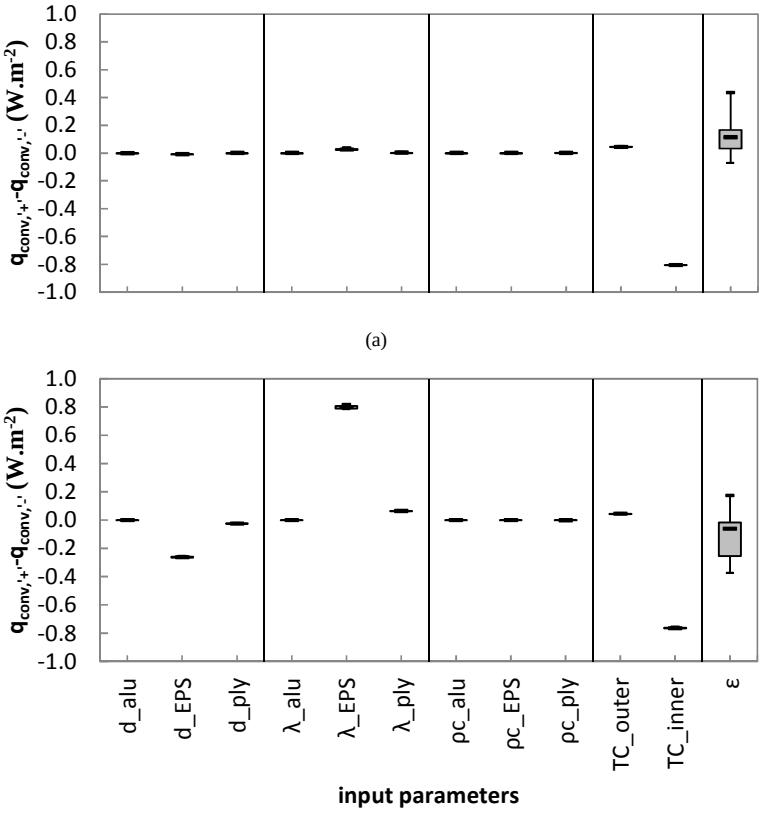

Figure 3.17: Sensitivity of the convective heat flux at PAS panels for (a) 'day regime, o1/o3' and (b) 'night regime, o1/o3' (boxplot; min, 2.5%, median, 97.5%, max)

Figure 3.18 depicts the result of a similar sensitivity analysis performed on dynamic experimental run 3 (N;c;T). Now the boxplots are plotted as a function of time and comprise only the six most influential factors. As during the steady-state experiments, improving the inner temperature measurement accuracy would reduce the uncertainty the most. Also the thickness and the thermal conductivity of the EPS layer and the emissivity of the panels are again involved. In addition, two new foreseen parameters are the thickness and the thermal capacity of the plywood. All parameters approach an asymptotic value after each step change, one faster than the other. This clearly explains the varying uncertainty bounds observed in Figure 3.16. As a matter of fact, the sensitivities transgress from one steady-state level to another. For example, the importance of the thickness and the thermal conductivity of the EPS layer increases during the night regime with night cooling and vice versa during the day. The impact of the two 'new' parameters, on the

other hand, is significant near step changes but decreases rapidly over time to a marginal level – especially during the night regime with night cooling. This is because, during quasi-steady-state conditions, the thermal resistance of the plywood is nothing compared with e.g. the one of the EPS layer while the thermal capacity is of little account. Furthermore, the emissivity shows the largest dispersion among the PAS panels – as in the steady-state experiments. Also the impact of the thickness and of the thermal capacity of the plywood of the respective PAS panels differs, but only near a step change. This differing behaviour originates from the different magnitudes of the convective heat fluxes. In conclusion, the above sensitivity analyses clearly indicate the points of improvement. Overall, improving the inner temperature measurement is the most worthwhile intervention. Furthermore, a better knowledge of the properties of the material layer(s) on the inside of the test cell would be particularly helpful in dynamic experiments. Finally, the thermal conductivity of insulating materials, even those further away from the inside, proves to be a point of attention.

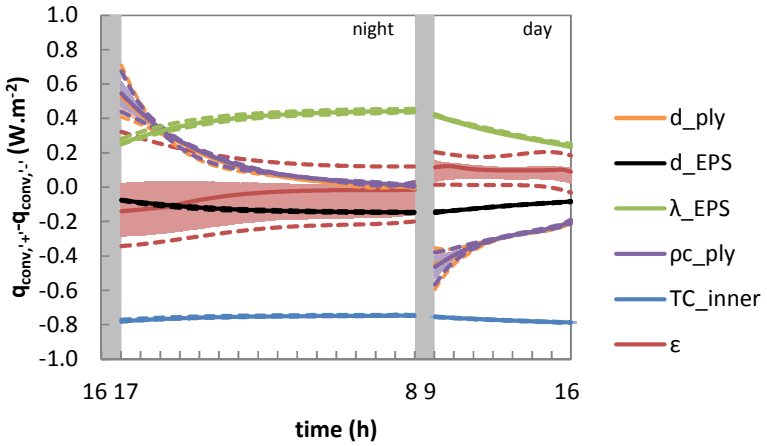

Figure 3.18: Sensitivity of the convective heat flux at PAS panels for dynamic experimental run 3 (N;c;T) (boxplot: min, 2.5%, median, 97.5%, max)

3.4 Results

3.4.1 Steady-state experimental runs

The analysis of the impact of the room/system design on the mixed convection heat transfer starts with the steady-state experiments. The set of graphs in Figure 3.19 pretty much sums it all up. The first two show the (a) convective respectively (b) radiative heat flux at each PAS panel for each experimental run. The

accompanying uncertainties correspond to the ones originating from the setup. Figure 3.19(c) helps to interpret the tendencies observed in these graphs. It depicts the averages of the indoor air temperatures (i.e. of the averages of the air temperatures at 0.20m, 1.25m and 2.30m height on all verticals) and detailed surface temperature distributions. The accompanying uncertainties are now left out, not to obscure the graph. Anyhow, the 95% limit value of the random and bias error of the average indoor air temperature equals at most 0.08°C while the maximum uncertainty of the surface temperature at the PAS panels is 0.22°C. Furthermore, note that the quantities in all graphs of Figure 3.19 are discrete. So the connecting lines are only meant to make the tendencies more clear. First, Figure 3.19 shows the unmistakable impact of increasing the ventilative cooling rate during the night regimes. The convective heat fluxes during the night regimes are at least three times as high as the corresponding ones during the day regimes. Especially the convective heat fluxes at the ceiling and those at the opposite south wall increase significantly. What's more, during the night regimes, the convective heat flux at the respective surfaces culminates at PAS panels farthest away from the air supply whereas during the day regimes the highest convective fluxes occur at the middle panel of the floor and in case of o2/o3 also at panel z6 at the east side. Also the ratio of convection to radiation differs significantly because of the convection regime. During the day regimes the absolute values of the convective and radiative fluxes are alike (the active heat source accounts for the opposite sign). However, during the night regimes, the convective fluxes are significantly higher. Yet, the convective heat flux distribution always connects closely with the one of the radiative fluxes: a low convective heat flux coincides with a high radiative heat flux and vice versa. Moreover, locating the air supply near the east wall results in a 30% higher convective heat transfer at panels z5, z6, z7 and z21. By contrast, during the night regime, o1/o3 creates unexpectedly at the west wall a higher convective heat flux than at the east wall. After all, the asymmetric velocity profile of the jet would indicate otherwise (Figure 3.21). The above findings are explained as follows. During the day regimes, the jet falls quickly to the ground upon entering the test room, causing the highest convective heat fluxes at the floor. In that case, buoyancy prevails over the jet momentum and, thus, mixed convection with strong buoyancy induces an overall low convective heat flux. During the night regime, however, as the stronger jet spreads, it adheres due to the Coanda effect to the nearest surface, i.e. the ceiling, and penetrates to the back of the room. Figure 3.20 which depicts the smoke visualisations of the jet during the (a) day and (b) night regime of o1/o3, clearly confirms this observation. Why the convective heat fluxes are connected with the radiative heat fluxes is because a low convective heat flux leads to a high surface temperature and, thus, more radiation. Finally, the reason for the high convective heat fluxes at the east wall in case of o2/o3 is obvious: the jet supplies cool air at a significant speed near that surface. However, explaining why o1/o3 leads to particularly high convective heat fluxes at the west wall during the night regime needs more thinking: the omnidirectional thermal anemometers cannot determine the flow direction, but fortunately the smoke visualisations can. Apparently, the jet directs itself towards the west side, which is probably because of the flexible tube connecting the AHU with the grille.

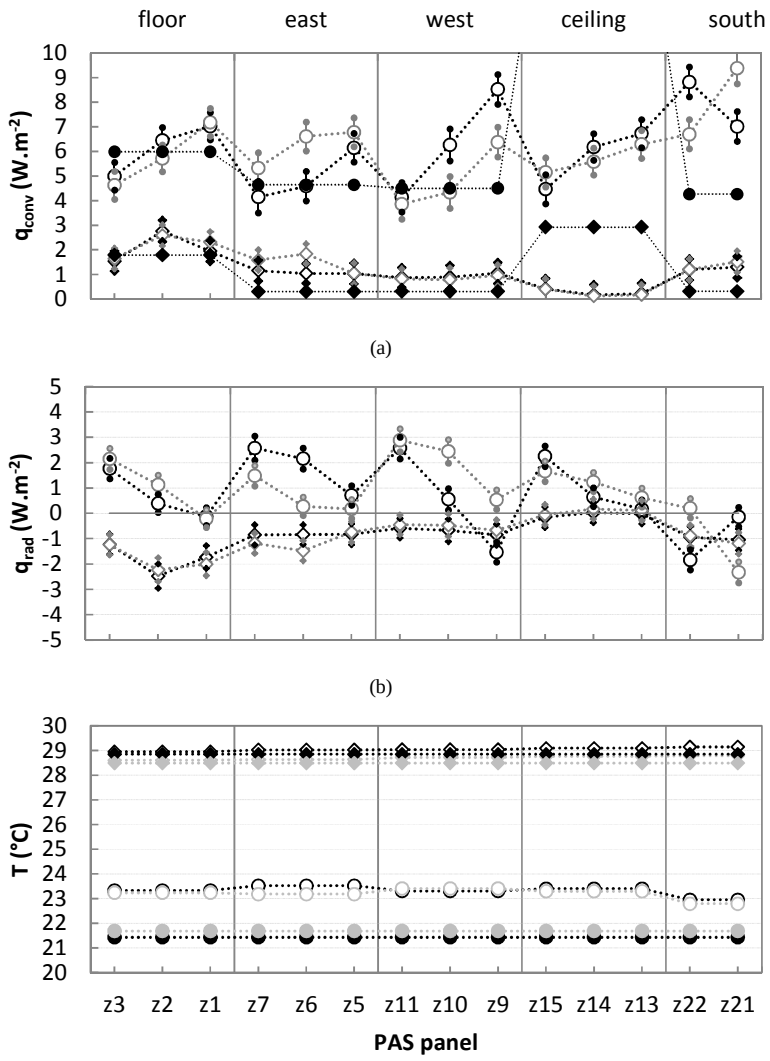

Figure 3.19: Average (a) convective heat flux,(b) radiative heat flux and (c) surface temperature at respective PAS panels and average indoor air temperature for all steady-state experimental runs

(a) (b)

Figure 3.20: Smoke visualisation of the jet during steady-state runs (a)'day regime, o1/o3' and (b)'night regime, o1/o3'

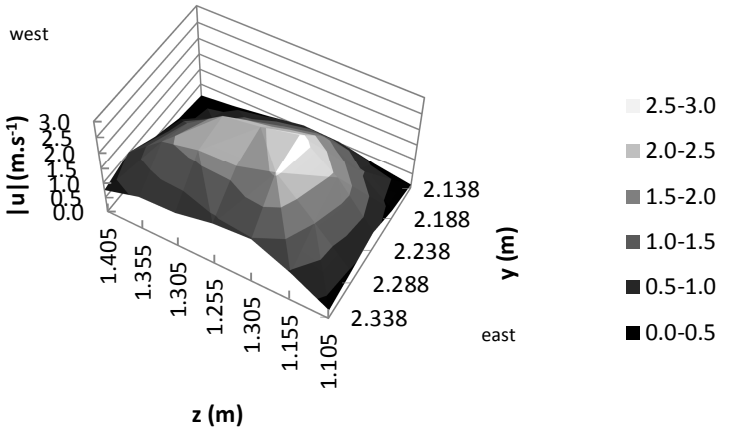

Figure 3.21: Velocity profile 0.60m away from the jet during steady-state experimental run 'night regime, o1/o3'

To further explain the above observations, the distribution of the temperature and air velocity recordings can prove useful – even though the limited number prohibits a complete figure. For example, Figure 3.22 shows the time-averaged temperature distribution on verticals v4, v5 and v6 during the night runs of both the investigated air supply/exhaust configurations. Each series only includes seven recordings, but for better understanding lines connect the separate values. The associated uncertainties include a random and a bias error, which are considered to be independent. The uncertainty due to the random error spans the 95% confidence interval of the respective recordings. The bias error corresponds to the measurement accuracy of the thermocouples, i.e. ±0.19°C. First, Figure 3.22(a) confirms the asymmetrical flow pattern. The temperatures at the west side, i.e. v6, are lower than the ones at the opposite side. Next to this, both graphs reveal the position of the air supply. Locating the air supply in the symmetry plane (o1/o3) lowers the temperature at the top of vertical v5 while air supply/exhaust

configuration o2/o3 does this on vertical v4. Unfortunately, further in-depth analysis of the temperature distribution at the displayed and other verticals is impossible because of the limited thermocouple accuracy. This also applies to the air velocity recordings and derived global performance indicators such as the temperature efficiency or the total convective heat transfer. Then again, the investigated configurations do not differ that much. After all, quasi-steady-state conditions prevail, the air supply is always located near the ceiling and each heating foil keeps its adjacent outer aluminium sheet at the same temperature. However, the dynamic runs discussed in the next section tell a different story.

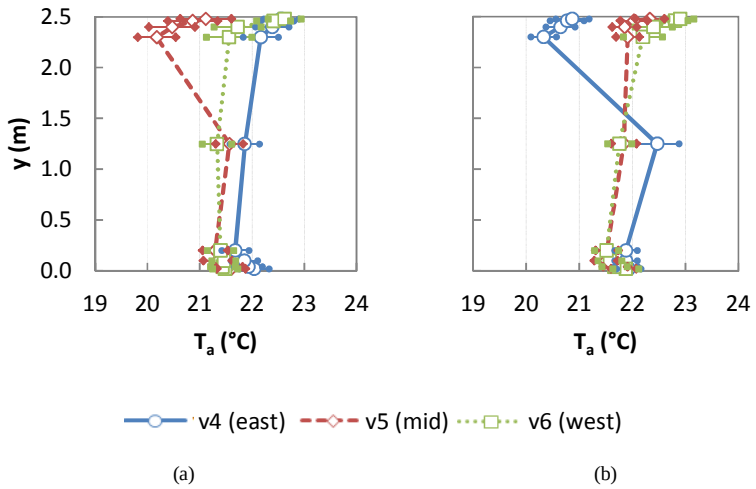

Figure 3.22: Temperature profiles on verticals v4, v5 and v6 during steady-state experimental runs (a) 'night regime, o1/o3' and (b) 'night regime, o2/o3'

Finally, this section assesses the applicability of existing convection correlations. To this end, it compares for two steady-state experimental runs (i.e. 'day regime, o1/o3' and 'night regime, o1/o3') the convective heat fluxes predicted by correlations to the ones derived from the measurements. To determine which correlations would apply to the cases at hand, the author relies on the classification of flow regimes and associated correlations suggested by Beausoleil-Morrison [102]. In all experiments mechanical forces are caused by an AHU delivering heated/cooled air through wall-mounted diffusers and buoyancy forces by surface-to-air temperature differences and, thus, the mixed convection correlations of that same Beausoleil-Morrison would apply. However, note that in principle Beausoleil-Morrison's correlations apply merely to cases with one central radial ceiling jet and air change rates higher than $3h^{-1}$. The correlations take into account the indoor air temperature (in this case, the average of the readings at 0.20m, 1.25m and 2.30m height on all verticals), the surface temperature of the respective enclosure surfaces (in this case, the average of the readings at the floor, ceiling…), the air supply temperature and the air change rate. Figure 3.19(a) shows that during

the day regime Beausoleil-Morrison's correlations usually underestimate the convective heat transfer by a factor of three to four. Only at the ceiling, the correlations predict a significantly higher convective heat flux. Somewhat similar appreciations apply to the night regime. However, the differences are less distinct and, what's more, now the measured convective heat flux at the south wall is also significantly higher than the prediction. As a matter of fact, in the PASLINK cell, the grille, located in the separation wall at 0.20m from the ceiling produces a jet which covers only part of the ceiling. In case buoyancy forces prevail, the jet soon falls to the ground while during the night regime, the jet reaches the back of the room indeed, yet its spreads is limited. All this obviously contrasts with the experimental setup on which Beausoleil-Morrison's correlations rely. As previously mentioned, the forced convection components were derived for a case with one central radial ceiling jet, which induced the highest convective heat flux at the ceiling. In other words, the available correlations only provide a rough estimate; they cannot account for the particularity of the cases at hand.

3.4.2 Dynamic experimental runs

To introduce the dynamic experimental runs, Figure 3.23 depicts the (a) temperature respectively (b) velocity magnitude courses at the middle floor panel z2. The label 'w,PAS' indicates the inner surface of the PAS panel, 'w,concr' the inner surface of the concrete tiles at vertical v5 and 'a,l' the measuring position at 0.20m above the floor on that same vertical v5. The uncertainty in $T_{w,concr}$ and $T_{a,l}$ equals ±0.19°C, the one in $T_{w,PAS}$ ±0.07°C and the relative uncertainty in $u_{a,l}$ is ±3% of the reading ± 1% of the measuring range 0 to 2.5m.s^{-1}. Yet, they are left out of the graph. Runs 5 to 8 (without night cooling) exhibit high, almost constant and similar local air and surface temperatures and a moderate, almost constant local air velocity. Most likely, these runs will have limited or no cooling capacity during the day regime. Runs 1 to 4 (with night cooling), on the other hand, have different, changing temperatures. At the onset of a new convection regime, the local air temperature decreases/increases steeply and then gradually follows the exponential decrease/increase of the surface temperature. The local air velocity usually reaches almost instantly its on average constant value. Only during the day regime of run 2 (N;C;t) and run 4 (N;c;t) it first increases for then to decrease. Night cooling (low air temperature, high velocity) effectively cools down the surrounding materials which can absorb heat during the following day regime, at least at the start. Ultimately, every surface temperature would increase above the local air temperature in such cooling cases. However, thermal mass slows down the congruence of the local air temperature and the surface temperature. Because of this, higher temperature differences occur for a longer period of time and more energy is stored/released. Locating the air supply near the one thermally massive surface (as in run 2 (N;C;t)) leads to the lowest local air temperature and the highest local air velocity and, thus, most likely the highest convective heat transfer. The jet in run 1 (N;C;T), on the other hand, is broken down for the most part until it hits the concrete tiles (higher local air temperature and lower local air velocity).

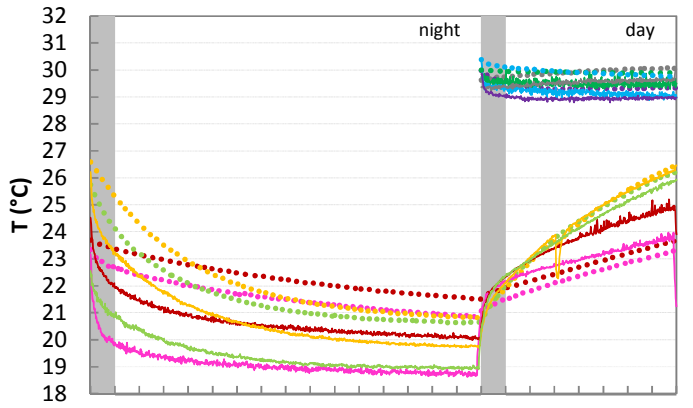

(a)

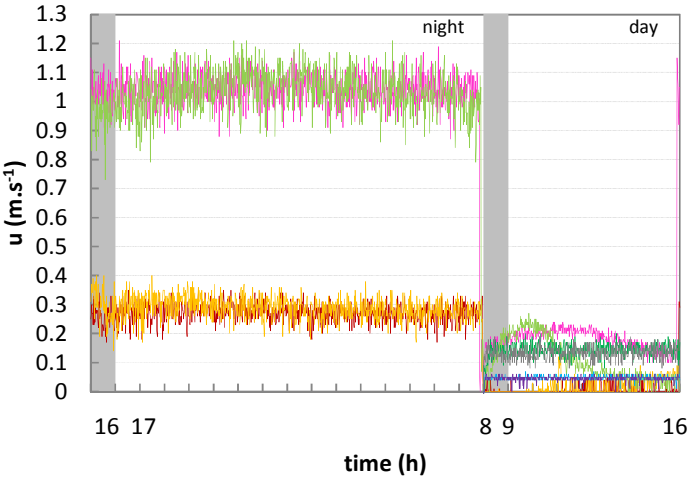

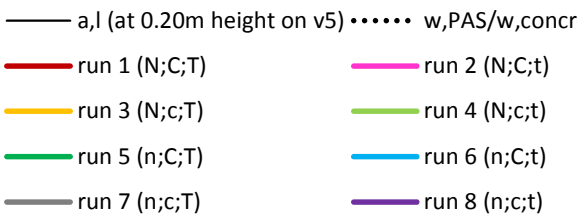

(b)

Figure 3.23: (a) Temperature and (b) velocity magnitude measured near z2 during dynamic experimental runs (uncertainty in $T_{w,concr}$ and $T_{a,l}$=±0.19°C, uncertainty in $T_{w,PAS}$=±0.07°C, relative uncertainty in $u_{a,l}$=±3% of reading ±1% of measuring range)

Figure 3.24 confirms that the above predictions are true for the total ventilative cooling performance of the respective runs. It shows the total convective heat flow $Q_{conv,tot}$, i.e. the sum of the convective heat flows at all PAS panels and, when present, concrete tiles, as a function of time. A positive $Q_{conv,tot}$ indicates that the surfaces release heat, a negative one the opposite. The uncertainties are rather small (4.94W to 7.42W) and are therefore left out of the graph. First of all, the impact of the operating conditions on the total convective heat flow catches the eye: the total convective heat flows are usually lower during the day regime than the ones during the night regime. Yet, every total convective heat flow approaches quasi-asymptotically its steady-state level. Next to this, the runs with night cooling show an unmistakably different behaviour: runs 1 to 4 (with night cooling) exhibit a rather low total convective heat flow during the day regime. Run 1 (N;C;T) and run 2 (N;C;t) (with night cooling in conjunction with thermal mass) even have an overall negative $Q_{conv,tot}$ during the day regime: apparently one or more surfaces absorb heat for the whole period. Moreover, these night cooled runs with thermal mass show a much smaller rate of change of the total convective heat flow than the light equivalent runs do. In addition to this, these cases are particularly sensitive to the air supply/exhaust configuration. In this case, locating the air supply near the concrete tiles on the floor pays off: the total convective heat flow during the day regime is in run 2 (N;C;t) four times as high as the one in run 1 (N;C;T).

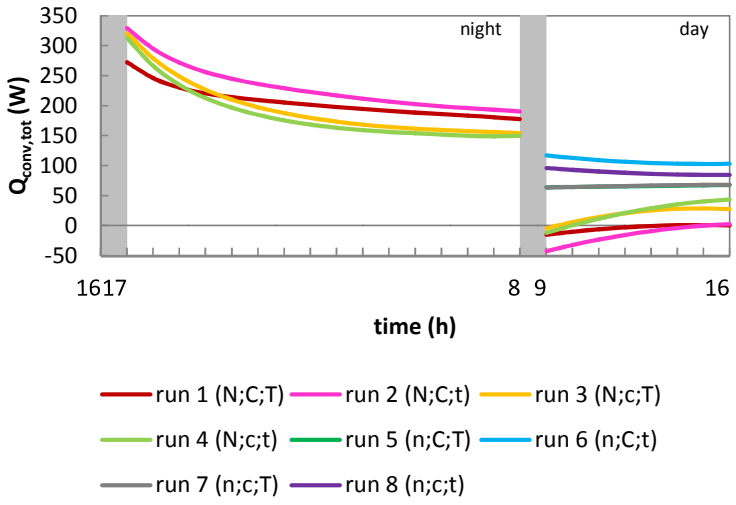

Figure 3.24: Total convective heat flow (uncertainties range from ±4.94W to ±7.42W)

To compare the respective convection regimes, Figure 3.25 sets the area-weighted convective heat flux at all PAS panels and, when present, concrete tiles $q_{conv,avg}$ against the difference between the corresponding area-weighted surface temperature $T_{w,avg}$ and the air supply temperature T_{sup}. A positive $q_{conv,avg}$ indicates that the surfaces release heat, a negative one the opposite. The uncertainty in $(T_{w,avg}-T_{sup})$ equals ±0.19°C and the uncertainties in $q_{conv,avg}$ range from ±0.11W.m^{-2} to ±0.17W.m^{-2}. This actually copies the approach used by Artmann et al. [148] to investigate the convective heat transfer during night cooling. The gradients were interpreted as average heat transfer coefficients $h_{conv,avg}=q_{conv,avg}\cdot(T_{w,avg}-T_{sup})^{-1}$. Such an interpretation also applies to most of the results of underlying study. The aforementioned assumption holds for the runs without concrete tiles on the floor. Like this, an average heat transfer coefficient of 0.88W.m^{-2}.K^{-1} applies to the results of the night regime of run 3 (N;c;T) and run 4 (N;c;t). A lower value of about 0.24W.m^{-2}.K^{-1} characterizes the convective heat transfer during the day regime of run 3 (N;c;T), run 4 (N;c;t), run 7 (n;c;T) and run 8 (n;c;t). It appears that in these cases with a limited amount of thermal mass the convective heat transfer is insensitive to the air supply/exhaust configuration – which was also found by Artmann et al. However, all this does not hold for the cases with concrete tiles on the floor. Deriving an average heat transfer coefficient is less obvious and the air supply/exhaust configuration does matter. As previously mentioned, locating the air supply near the concrete tiles (as in run 2 (N;C;t)) leads to a higher convective heat flux during the night regime by which during the following day regime a lower negative $q_{conv,avg}$ applies.

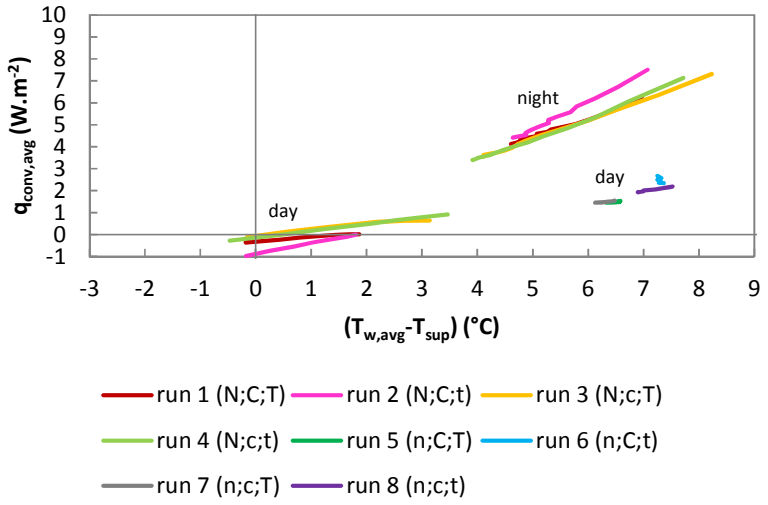

Figure 3.25: Average convective heat flux as a function of the difference between the average surface temperature and the air supply temperature (uncertainty in $(T_{w,avg}-T_{sup})$ is ±0.19°C, uncertainties in $q_{conv,avg}$ range from ±0.11W.m^{-2} to ±0.17W.m^{-2})

Next, this section sets the convective heat fluxes derived from the temperature measurements against the predictions by existing convection correlations. Just as with the steady-state experimental runs, the mixed convection correlations of Beausoleil-Morrison act as a reference. Figure 3.26 uses an interpretation somewhat similar to the previous graph. However, it takes into account the average indoor air temperature (i.e. the average of the readings at 0.20m, 1.25m and 2.30m height on all verticals) instead of the air supply temperature, in line with the approach used in BES. The uncertainty in $(T_{w,avg}-T_{a,avg})$ is ±0.19°C. The uncertainties in $q_{conv,avg}$ obviously range again from ±0.11W.m^{-2} to ±0.17W.m^{-2}. Using the average indoor air temperature to determine the temperature difference complicates the interpretation. After all, the indoor air is not well-mixed. Especially the runs with the air supply at the bottom exhibit an inhomogeneous temperature distribution. A larger $(T_{w,avg}-T_{a,avg})$ usually applies to these cases. Because of this, the air supply/exhaust configuration seems to matter now. Nevertheless, the graph reveals that the convection correlations overestimate the average convective heat flux during the night regime. The difference between them varies from 0.07W.m^{-2} to 2.17W.m^{-2}. During the day regime the correlations usually underestimate the average convective heat flux with at most 1.60W.m^{-2}, which is large in comparison to the measured fluxes.

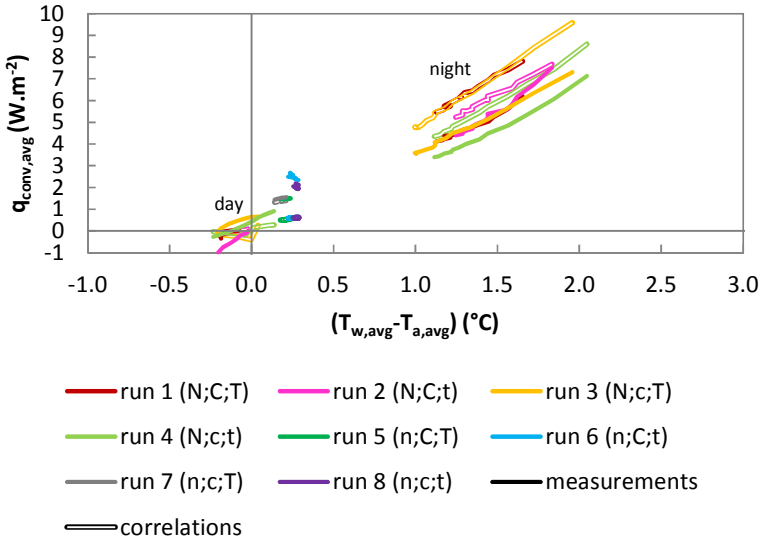

Figure 3.26: Average convective heat flux as a function of the difference between the average surface temperature and the average indoor air temperature (uncertainty in $(T_{w,avg}-T_{a,avg})$ is ±0.19°C, uncertainties in $q_{conv,avg}$ range from ±0.11W.m^{-2} to ±0.17W.m^{-2})

A look at the convective heat fluxes at some surfaces demonstrates why the measured average convective heat fluxes relate to the overall predictions by convection correlations in such a way. Figure 3.27 and Figure 3.28 depict for the night regime respectively the day regime the convective heat flux q_{conv} at (a) the ceiling, (b) the floor and (c) the south wall as a function of the difference between the surface temperature T_w (that is, floor, ceiling…) and the average indoor air temperature $T_{a,avg}$ (i.e. the average of the readings at 0.20m, 1.25m and 2.30m height on all verticals). The uncertainty in $(T_w-T_{a,avg})$ equals ±0.08°C in case of a PAS panel and ±0.13°C in case of concrete tiles. The uncertainties in the convective heat flux derived from the temperature measurements range from $\pm 0.24 W.m^{-2}$ to $\pm 0.52 W.m^{-2}$. During the night regime, the predictions by convection correlations differ the most from the measured convective heat fluxes at the ceiling and in run 2 (N;C;t) and run 4 (N;c;t) from the ones at the floor. At the ceiling, Beausoleil-Morrison's correlations predict for all runs convective heat fluxes which are three to fourteen times as high as the measured ones. What's more, the cases with the air supply at the bottom show a different course: the higher the temperature difference, the lower the measured convective heat flux. At the floor, on the other hand, the convection correlations underestimate the convective heat flux in run 2 (N;C;t) and run 4 (N;c;t) by 50 to 70%. The results and the predictions of the other two runs correspond reasonably well. At the south wall, the correlations approximate the measured convective heat fluxes in the runs with the air supply at the bottom, i.e. run 2 (N;C;t) and run 4 (N;c;t). Run 1 (N;C;T) and run 3 (N;c;T) exhibit convective heat fluxes which are at most 75% higher than the predictions by correlations. Further note that runs with thermal mass can show an ambiguous relation between the convective heat flux and the temperature difference (e.g. at the floor in run 2 (N;C;t)). During the day regime, again the results at the ceiling and the floor show the largest differences. At the ceiling, the convection correlations usually overestimate the convective heat flux. Moreover, the predictions by correlations do not always exhibit the expected behaviour: e.g. unreasonably high convective heat fluxes at small temperature differences as in run 3 (N;c;T) and run 4 (N;c;t), or the predictions for runs 5 to 8 are significantly higher than the ones of runs 1 to 4. At the floor, most convection correlations predict negative convective heat fluxes as the temperature difference is negative. However, the corresponding measured convective heat fluxes are usually positive, indicating that the floor releases heat. Only the results of run 1 (N;C;T) and run 7 (n;c;T) show a rough correspondence. Further, the predictions and the measurements at the floor generally differ the most in case the air supply is located near the floor. At the south wall, the predictions by correlations for runs 1 to 4 are within the uncertainty bounds of the measured convective heat fluxes. The predicted fluxes for run 5 to 8, on the other hand, are clearly lower than the measured ones.

Most of the above discrepancies are caused by the difference in configuration. As previously mentioned, Beausoleil-Morrison's correlations apply basically to cases with one central radial ceiling jet. This jet produces a particularly high convective heat flux at the ceiling and lower ones at the other enclosure surfaces. By contrast, in the PASLINK cell, the jet is only able to cover a part of the ceiling during the night regime of cases with the air supply at the top. So it is self-evident that the predicted convective heat fluxes at the ceiling are significantly higher than the measured ones, certainly when the air supply is at the bottom. A similar reasoning explains why predictions at the floor are nowhere close to the measurements in case the air supply is located at the bottom. The influence of a central ceiling jet on the air near the floor is obviously far less than that of a jet at the bottom. The usually positive measured convective heat flux at the floor during the day regime in spite of a negative (T_w-$T_{a,avg}$) is because the (falling) jet locally produces a positive temperature difference. Why the predicted fluxes at the south wall during the night regime of run 1 (N;C;T) and run 3 (N;c;T) are lower than the measured ones is because only then the jet in the PASLINK cell hits the south wall frontally. The several – at first – ambiguous relations are explained as follows. The inverse relationship between the measured convective heat flux and the temperature difference during the night regime of run 2 (N;C;t) and run 4 (N;c;t) is because as time goes by the indoor air stratification diminishes and, thus, the difference between the surface temperature and the average indoor air increases. The inhomogeneous temperature distribution also explains the curved relationships of some predictions/measurements. For example, at the beginning of the night regime of run 2 (N;C;t) the measured convective flux at the floor peaks, but the average indoor air temperature lags. The different predicted convective heat fluxes for the same temperature differences, on the other hand, occur because Beausoleil-Morrison's correlations include the surface temperature, the average air temperature and the air supply temperature. As a matter of fact, the scaling factor $(T_w\text{-}T_{sup}).|T_w\text{-}T_{a,avg}|^{-1}$ part of the forced convection component leads to higher convective heat fluxes when the surface temperature differs more from the air supply temperature, as is usually the case in runs 5 to 8. That same scaling factor also causes the unreasonably high convective heat fluxes at small temperature differences (remember the prediction at the ceiling during the day regime of run 3 (N;c;T) and run 4 (N;c;t)). The above comparison of the convective heat fluxes predicted by assumedly apt convection correlations to the measured ones obtained from dynamic experimental runs once again confirms the particularity of the available convection correlations.

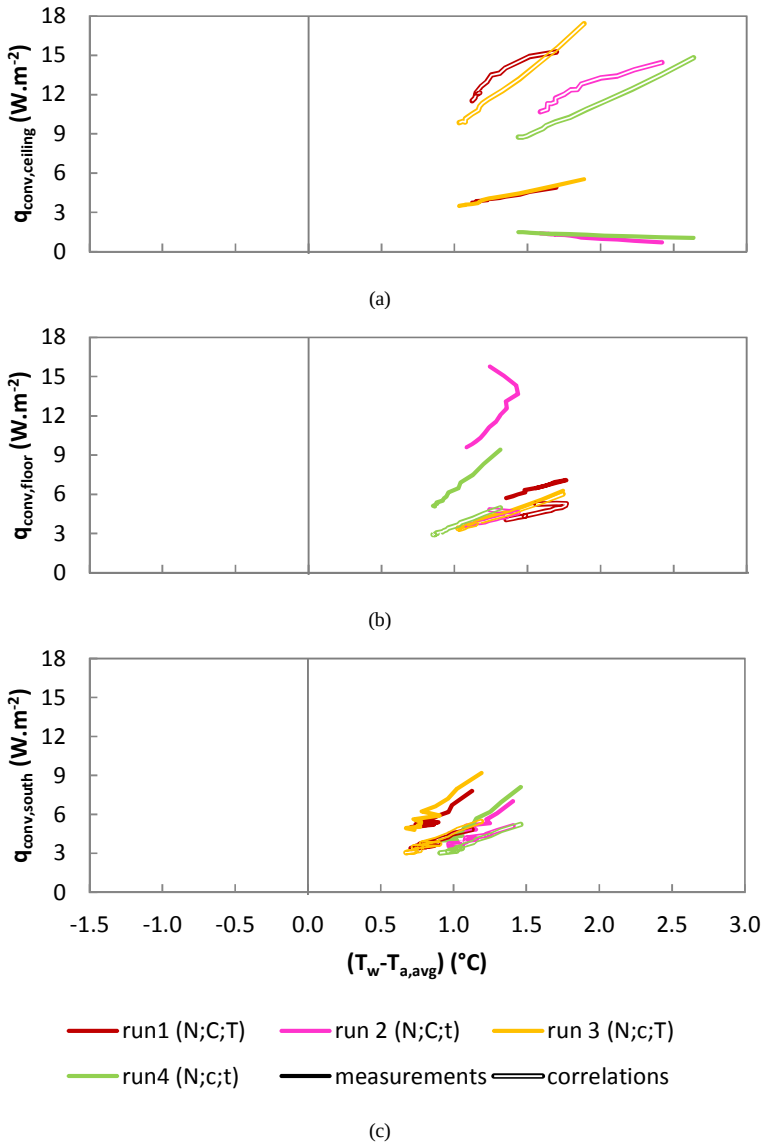

Figure 3.27: Convective heat flux at (a) the ceiling, (b) the floor and (c) the south wall during the night regime as a function of the temperature difference between the respective surface and the average indoor air temperature (uncertainty in (T_w-$T_{a,avg}$) is ±0.08°C (PAS) or ±0.13°C (concrete), uncertainties in q_{conv} range from ±0.24W.m^{-2} to ±0.52W.m^{-2})

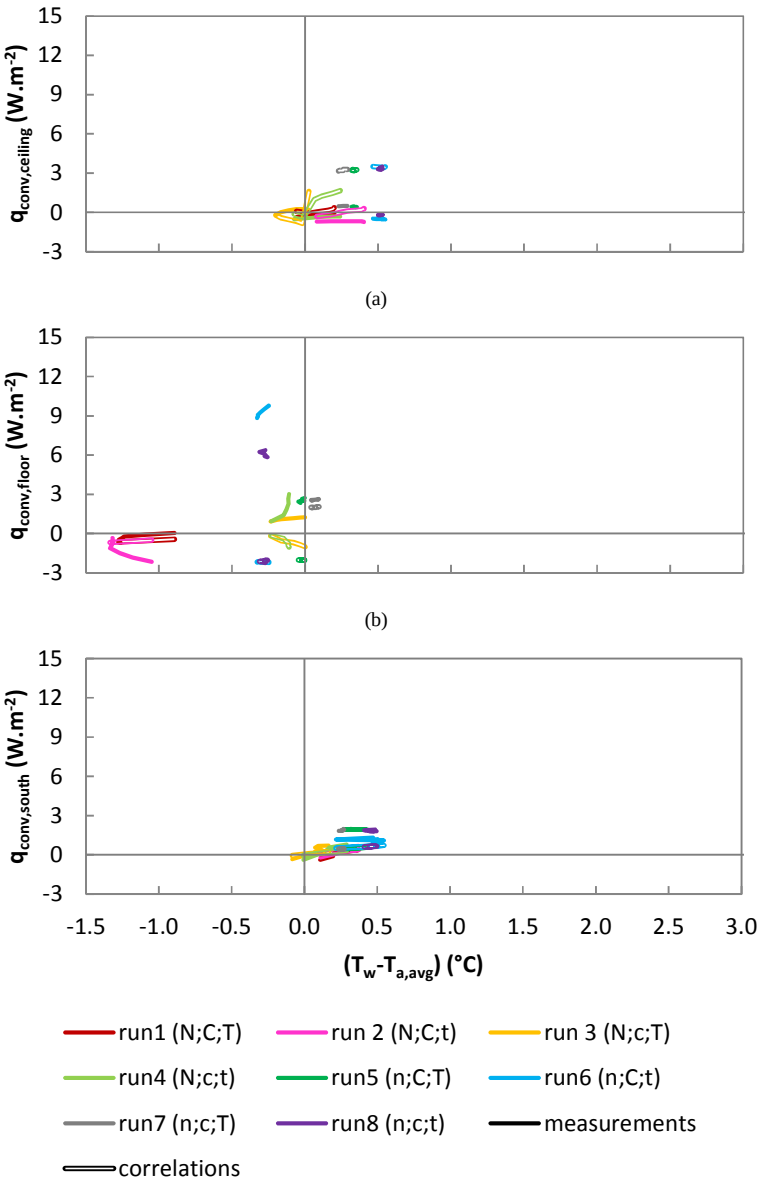

Figure 3.28: Convective heat flux at (a) the ceiling, (b) the floor and (c) the south wall during the day regime as a function of the temperature difference between the respective surface and the average indoor air temperature (uncertainty in $(T_w-T_{a,avg})$ is ±0.08°C (PAS) or ±0.13°C (concrete), uncertainties in q_{conv} range from ±0.24W.m^{-2} to ±0.52W.m^{-2})

3.5 Conclusions: room/system design matters

Above experimental effort is surely no isolated case. However, the suggested approach to derive the convective heat flux and the subsequent uncertainty and sensitivity analyses might be a step forward. The use of a dynamic conduction/radiation model to calculate the convective heat flux introduces without doubt some benefits. First, it enables a more accurate determination and allows to investigate experiments with changing boundary conditions. Secondly, the model enables in conjunction with a sensitivity analysis method to pinpoint difficulties in the setup – which is valuable for future similar experiments. Such sensitivity analysis on the PASLINK cell revealed that the thermocouple reading accuracy at the inside of the panels and the determination of the thermal resistance of insulating materials of the PAS and of the emissivity of the interior are special points of interest. Next to this, the material properties of the inner layer(s) turned out to be equally important in case of significant sudden changes of the boundary conditions. However, the accompanying uncertainty analysis showed that the uncertainties in the derived convective heat fluxes due to the experimental setup did not prohibit a thorough comparison of the experimental runs.

The actual parametric analysis aimed at identifying the impact of the air supply/exhaust configuration and thermal mass on the convective heat transfer during two typical mixed convection regimes. The results revealed that the air supply/exhaust configuration is particularly important in case of heterogeneously distributed thermal mass. For example, locating the air supply near the concrete tiles instead of near the ceiling resulted in an 11% increase of the heat released during night cooling and a 410% increase of heat absorbed during the following day period. The accompanying study on the applicability of existing convection correlations showed that correlations should not be used when the setup and the convection regime differ a lot from those of the corresponding experiments. For example, the assumedly apt correlations of Beausoleil-Morrison predicted at the ceiling convective heat fluxes which were three to fourteen times as high as the measured ones. In other words, it is necessary to further investigate in detail how interrelated room/system parameters affect the mixed convection heat transfer. The number of design parameters that can be taken into account depends heavily on the available resources and the state-of-the-art. Yet, primary design parameters like e.g. the ventilation concept and the air supply position should definitely be part of the analysis. To this end, researchers can perform more experiments. However, experiments alone are perhaps not sufficient to study many parameters which apply to a wide range – even though they will always be needful, if only to validate simulation models. As a matter of fact, CFD can be a valuable supplement to experiments as it provides much faster, more complete results, at a reduced financial cost. Obviously this view fits into the global movement of experimenters turning to mathematical models [181]. Yet, before such a simulation study is started, the proper CFD simulation approach needs to be determined. This is the subject of the next chapter.

4

Modelling convective heat transfer with CFD

The following describes the research effort on advisable CFD simulation approaches to predict the convective heat transfer. This chapter begins by revealing the need for such an undertaking. Subsequently, it discusses the literature review on the most important simulation factors: the grid, turbulence modelling and the description of air supply diffusers. The final section describes the CFD study which evaluates how the above points of interest influence the predicted convective heat transfer.

4.1 Exploring the capabilities

Since Nielsen [182] introduced CFD in building research and design, the popularity of CFD boomed, in particular because of its versatility. For example, today's (commercial) CFD software enables researchers and building designers to optimize natural ventilation systems [183] or to quantify the indoor comfort [184]. More complicated applications include other heat transfer mechanisms: e.g. smoke movement calculation including radiation [185]. Or some deal with heat and mass transfer in building materials: e.g. studies on local hygrothermal interaction between airflow and porous materials [186, 187]. Finally, CFD goes hand in hand with other simulation tools, such as BES (e.g. [101-103]). Unmistakably, CFD will play an increasingly important role in the design, analysis and optimization of engineering systems [188, 189]. However, CFD does not necessarily provide reliable results. At best the CFD results are as good as the physics; at worst as good as its operator. Inexperienced users can easily turn CFD into Coloured Fluid

Dynamics, presenting merely colourful images instead of advancing building science and design. In other words, users need to make sure that the simulation tool can accurately represent reality and, secondly, they need to know how to address the inherent error sources.

The prediction of indoor airflow by CFD usually relies on the following fundamental equations [190]: the equation of continuity (Eq. (4.1)), one momentum equation for each coordinate direction (Eq. (4.2-(4.4)) and the energy equation (Eq. (4.5)). Note that the shown equations apply to incompressible flow [191]. After all, air – a compressible medium indeed – behaves like an incompressible fluid at low speeds or more specifically at Mach < 0.3 (i.e. the fluid velocity remains smaller than 0.3 times the speed of sound in the fluid). Moreover, these equations are much alike. The many commonalities between the various equations enable to define one generalized form, the so-called transport equation for property ϕ (Eq. (4.6)). Most conveniently, this general form highlights the various processes and, what's more, it acts as a starting point for numerical procedures. Replacing ϕ by the relevant quantities and selecting appropriate values for the diffusion coefficient Γ and the source terms leads to the specific forms of Eq. (4.1)-(4.5).

$$div(\vec{u}) = 0 \tag{4.1}$$

$$\frac{\partial(\rho u)}{\partial t} + div(\rho u\vec{u}) = -\frac{\partial p}{\partial x} + div(\mu\ grad\ u) + S_{Mx} \tag{4.2}$$

$$\frac{\partial(\rho v)}{\partial t} + div(\rho v\vec{u}) = -\frac{\partial p}{\partial y} + div(\mu\ grad\ v) + S_{My} \tag{4.3}$$

$$\frac{\partial(\rho w)}{\partial t} + div(\rho w\vec{u}) = -\frac{\partial p}{\partial z} + div(\mu\ grad\ w) + S_{Mz} \tag{4.4}$$

$$\frac{\partial(\rho cT)}{\partial t} + div(\rho cT\vec{u}) = div(\lambda\ grad\ T) + S_T \tag{4.5}$$

$$\frac{\partial(\rho\phi)}{\partial t} + div(\rho\phi\vec{u}) = div(\Gamma\ grad\ \phi) + S_\phi \tag{4.6}$$

term 1: rate of increase of ϕ of fluid element	+	term 2: net convective flow rate of ϕ out of fluid element	=	term 3 rate of increase of ϕ due to diffusion	+	term 4 rate of generation of ϕ due to sources

The solution of the above differential equations of mass, momentum, energy (and other scalars) poses two problems. First of all, the convective terms of the momentum equations contain nonlinear quantities. In the second place, the equations are coupled: the velocity components appear in every equation. Because of this, an approximating numerical method is necessary. This starts with a mathematical model and comprises, among other things, a discretisation technique (e.g. finite difference, finite volume, finite element), a numerical grid (e.g. structured, block-structured, unstructured), finite approximations (e.g. in a finite volume method the methods of approximating surface and volume integrals), a solution method (usually iterative techniques) and convergence criteria for the iterative method. Numerical errors originate from the numerical solution of the mathematical equations: i.e. programming mistakes, computer round-off, iterative convergence and spatial and temporal discretisation and are usually the subject of a verification procedure. The largest contributor to numerical solution error is the one caused by inadequate grid resolution [61, 192, 193]. Meanwhile, for many phenomena (e.g. turbulence, combustion and multiphase flow) the exact equations are either unavailable or a numerical solution is not feasible – necessitating the introduction of simplified models. As a result, assumptions and approximations in the mathematical representation of the physical problem (e.g. geometry, turbulence models, boundary conditions) and incorporation of previous data (e.g. fluid properties) introduce the so-called modelling errors and corresponding uncertainties. In response, a validation process enables to identify and eliminate modelling errors. For all that, previous studies, such as the IEA Annex 20 project [194], identified as key modelling error sources turbulence modelling and the description of the air supply opening(s).

The computational domain, e.g. a room, is divided into discrete parts – altogether constituting the grid – while the differential equations are transformed into discretised equations formulated around each grid entity. In theory, the discretisation error approaches zero as the grid resolution reaches infinity. However, this is at the expense of computational cost. Therefore, CFD operators aim for the 'necessary' resolution. Numerical discretisation schemes – i.e. assumptions about how the variable varies between the grid points – help to economize on grid resolution, but cannot bridge ever increasing dimensions. As a consequence, CFD users preferably demonstrate that the discretisation error is sufficiently small – at least for the investigated variable. Unfortunately, there is no formal way of estimating errors introduced by inadequate grid design for a general flow, despite of ambitious initiatives of e.g. Casey and Wintergerste [193] and Franke et al. [61]. An even bigger challenge – for both software developers and users – is turbulence modelling. LES, which simulates the large motion scales, is in principle superior to RANS modelling wherein transport terms are treated empirically. However, looking ahead at (extensive) parameter studies in research and rapid building design, RANS takes advantage of its faster execution. Moreover, interest of building research and design usually lies more in mean properties, as in RANS, rather than instantaneous airflow information provided by LES [195]. Unfortunately, only few RANS turbulence models apply to an enclosed environment [195]. As a result, many studies evaluated the generality and

robustness of turbulence models for various indoor airflow scenarios (e.g. [194, 196, 197]). Besides, not all turbulence models are equally suited to predict flow near solid boundaries – as discussed in the introductory chapter of underlying work. This connects with the final important source of error: that is, the description of the boundary conditions. It is not an easy task to handle all the boundary conditions with a high level of accuracy. Especially the air supply opening(s) may cause problems. Directly simulating all details in the diffuser design demands a high grid resolution, augmenting the computational cost significantly. Nevertheless, simulating air terminal devices accurately takes priority. After all, the momentum flow from the air supply often dominates the indoor airflow – particularly in case of night cooling. Consequently, numerous researchers intensively looked for apt approximations and simplifications of air supply geometries. Going on these foregoing studies, works like [61, 193, 198] put forward absolutely necessary guidelines.

Unfortunately, as most studies looked at point variables, these general recommendations do not necessarily apply to other (integral) variables, such as the convective heat flux. For example, in validating simplified diffuser modelling methods, Srebric [199] relied solely on velocity, temperature and concentration profiles. In response, underlying chapter intends to verify the impact of the CFD simulation approach on the predicted convective heat flux. This is considered necessary, before analysing by means of CFD the relation between room/system design and night cooling performance – as discussed in the next chapter. This chapter starts with a literature survey which goes into detail on aforementioned sources of error and uncertainty. This review actually attempts to distil the advisable simulation approaches – at least for the finite volume method on which most commercial CFD software packages rely. The subsequent CFD study tries out the various approaches, mainly looking at the effect on the predicted convective heat transfer. Readers interested in more on numerical methods are referred to Ferziger and Perić [200]. Next to this, the work of Patankar [167] proves particularly helpful to novices: it explains several numerical techniques from a physical point of view. Finally, the text book of Versteeg and Malalasekera [190] acts as a reference for underlying study. For, it studies the finite volume method on which Fluent [201], i.e. the software used in this study, builds.

4.2 On the simulation approach

4.2.1 Grid resolution and quality

Prior reduction of all other numerical errors

On the assumption that software developers verified their codes and, thus, make high-quality software available, the responsibility for solution verification of every simulation is left with CFD users. Next to this, users should be able to enter input data and extract output correctly. Consequently, solution verification focuses on limiting the remaining numerical errors: i.e. errors due to computer round-off,

incomplete iterative convergence and space/time discretisation. First of all, choosing double precision calculation reduces the round-off error. To put it another way, doubling the number of bits of memory for each number (64 instead of 32) sharply improves the accuracy. Moreover, double precision calculation results in a possibly lower level out of the residuals (i.e. changes over successive iterations) or of the mass/heat/concentration imbalance in each cell, which are helpful in judging qualitatively iterative convergence – a second source of numerical solution error.

As directly solving the nonlinear algebraic system of equations is too costly, CFD relies on iterative methods. Consequently, stopping the iteration process too soon introduces a significant iterative convergence error. Often this concurs with high residuals/imbalances. Studies like [202, 203] confirm that the residual reduction tracks well with the actual iterative error for a wide range of nonlinear problems in fluid mechanics, but the residual definitions and suggested bounds can be misleading for some cases. For example, starting from a good initial guess of the flow field may lead to a large scaled residual for the continuity equation: after all, the initial continuity which is used for scaling, is very small [201]. Or small time steps and/or relaxation factors possibly result in small solution residuals while the iterative error is large [200]. Therefore, it is good practice to check also property conservation. Fluent [201] postulates that the net imbalance should be less than 1% of the smallest flux through domain boundary. However, experience indicates that this goal can be too severe: e.g. the convective heat flux at the ceiling of a room with strong thermal stratification is negligibly small and is, therefore, of no account. Furthermore, it is requisite to judge convergence of physical (integrated) target quantities with iteration or time, such as the convective heat transfer at a surface. This convergence error and uncertainty estimate relies on graphical or theoretical approaches and depends on the type of iterative convergence: oscillatory, convergent or mixed oscillatory/convergent. In particular Stern et al. [204] lucidly explain the graphical methods. For oscillatory convergence, the maximum and minimum values – divided by two – provide an uncertainty estimate. For convergent iterative convergence, the difference between the value and an exponential curve-fit for a large iteration number applies. Finally, mixed oscillatory/convergent iterative convergence necessitates the determination of the amplitude of the solution envelope. Theoretical estimates of the iterative error are presented in e.g. Ferziger and Perić [200, 205] and involve estimation of the principal eigenvalue of the iteration matrix – a procedure which is not necessarily straightforward. Nevertheless, only when the computer round-off is reduced and the iterative convergence level is satisfactory, CFD users can assess the final and most important sources of numerical error: spatial and temporal discretisation [61, 193].

Variety of grid convergence assessment procedures

Last-mentioned errors correspond to the difference between the exact solution of the basic partial differential equations and the numerical solution obtained with finite space and time discretisation. Actually three errors make up each discretisation error [206]. The truncation error – which gets often mixed up with the discretisation error – is the difference between the partial differential equation and the discretized equation. Further, the dispersive error terms cause oscillations in the solution while dissipation error terms smooth out gradients. Steady-state simulations suffer from the spatial discretisation error alone while for transient ones, the governing equations must be discretised in both space and time. Note that especially for time-dependent flows the time step size is strongly coupled with the grid size: finer grids necessitate smaller time steps or higher-order discretisation schemes [193, 207]. Yet, in principle, both space and time discretisation errors are part of every indoor airflow simulation. After all, indoor airflows are physically time-dependent – but possibly statistically steady-state – and, as a consequence, necessitate time-dependent simulations [193]. Steady-state or even transient simulations with a large time step size often fail to capture important flow features and, therefore, mimic unphysical steady behaviour. Activating time dependence is also particularly useful when attempting to solve steady-state problems which tend towards instability (e.g. natural convection problem in which the Rayleigh number gives the strength of the buoyancy-induced flow, is close to the transition region [201]). Overall, similar directions apply to both space and time discretisation; even the same error estimation techniques can be used. However, in particular the space discretisation error relies on an additional parameter: the grid quality, which includes the topology of the grid cells and the distribution of them. Because of this extra parameter, discretising the computational space into a suitable grid requires substantially more effort than just looking for an apt time step size [191]. Therefore, the following discussion focuses on the error introduced by the grid. Where relevant, the text refers to the time discretisation error.

A grid which does not introduce too large errors starts with a high grid quality. After all, optimizing the grid with a given number of grid points can lead to a similar or even higher accuracy than systematically refining a non-optimal grid. As a matter of fact, the performance of the discretisation schemes heavily depends on the topology of the cells, in particular the cell type, the skew and the aspect ratio. For example, maximum accuracy of the diffusive flux is only possible when the line connecting two neighbouring control volume centres is orthogonal to the cell face and passes through the cell-face centre: orthogonality increases the accuracy of the central-difference approximation used [200]. This partly explains why works like [193, 200, 208] suggest using quadrilateral/hexahedral (2-D/3-D) cells near boundaries – i.e. where diffusion becomes important. The ability of this type of cells to easily adjust in accordance with the near-wall turbulence model requirements only confirms their superiority near walls. Also prismatic cells possess these features and, as a consequence, are allowed near boundaries in case tetrahedral cells make up the rest of the 3-D grid [209]. However, even farther away from boundaries, quadrilateral/hexahedral cells perform well – even though

such grids require far more cells than an equivalent with triangular/tetrahedral cells [201, 210]. Not only they introduce smaller truncation errors, they also induce a better iterative convergence [193, 211]. Once CFD users have defined the type of cells in the computational domain, they should keep the skew and the aspect ratio of the cells within bounds and avoid rapid changes in cell volume between adjacent cells [61, 193, 201]. In general: aspect ratios should be lower than 5:1, optimal quad/hex cells have bounded angles of 90° and tri/tet cells are preferably equilateral. Further, the expansion ratio between two consecutive cells should usually stay below 1.2-1.3 [212, 213] – except when higher-order numerical schemes are used [214]. Fortunately, these recommendations are not equally stringent throughout the computational domain, which helps to economize on the grid resolution. For example, cells with a high aspect ratio can be tolerated in benign flow regions but can be very damaging in regions with strong flow gradients (e.g. shear, mixing) – except for boundary layers. The drawback is that – as previously mentioned – coming up with an apt distribution can make grid generation alone time-consuming.

What are obviously missing are recommendations for the necessary grid resolution – just as for the time step size. As a matter of fact, putting forward a proper resolution, in advance, everywhere, is impossible, as it depends on the flow problem set [215, 216]. Only for the grid resolution near walls, some rough estimates are available. These are particularly helpful to judge whether or not the near-wall grid resolution is enough to resolve entirely the boundary layer – i.e. the way to go in predicting convective heat transfer [104-109] (see introductory chapter of this work). First, the dimensionless distance of the wall-adjacent cells to the walls y^+ enables to check the location of the first node away from the wall. This y^+ value is preferably in the order of one. However, higher values up to four or five are acceptable: the first node is still well inside the viscous sublayer. Secondly, the turbulent Reynolds number Re_y (Eq. (4.7)), function of the distance to the wall y, the turbulence kinetic energy k and the kinematic viscosity ν, indicates whether the flow in the wall-adjacent cells is in the viscosity-affected region or in the fully-turbulent region. This Re_y should not exceed 200. Only then, at least ten cells are found in the viscosity-affected near-wall region, which enables the CFD program to resolve correctly the mean velocity and turbulent quantities in that region.

$$\mathrm{Re}_y = \frac{y \cdot \sqrt{k}}{\nu} \tag{4.7}$$

Because of aforementioned hiatus, CFD users preferably rely on time/grid convergence studies which enable to estimate the uncertainty due to the discretisation error in retrospect. As a consequence, researchers (have) put a lot of effort in (re)developing so-called a posteriori methods. In particular extrapolation-based error estimators receive attention as this group equally applies to different discretisation techniques (finite-difference, finite-volume, finite-element). For this reason, they replace another important set of a posteriori methods, i.e. finite-element-based estimators. After all, only by considerable additional effort, last-

mentioned group of error estimators apply to discretisation techniques other than finite-element (e.g. [217]). The work of Roy [215] presents a more detailed discussion on examples of finite-element-based estimators. Another advantage of extrapolation-based error estimators is that they apply not only to local flow variables (e.g. point-by-point velocity) but also to derived integral quantities (e.g. convective heat flow). Supporting the above view, underlying work intends to cover only extrapolation-based error estimators. Literature actually indicates two approaches: order extrapolation (p-extrapolation) and Richardson extrapolation (h-extrapolation). The first method requires numerical solutions for the same discretisation level (time step size/grid resolution) but with discretisation schemes having a different formal order of accuracy to obtain a higher-order estimate of target quantities. Setting this estimate against the values obtained from the numerical solutions leads to an error estimate for the respective grids. Unfortunately, order extrapolation necessitates advanced solution algorithms to obtain higher-order numerical schemes, which is difficult to code and expensive to run [215]. Therefore, most popular approaches rely on comparing numerical solutions of different discretisation level, i.e. Richardson extrapolation (RE) [218, 219]. The idea behind (standard) RE is to combine two separate discrete solutions on two different grids, so as to obtain an error estimate. The discretisation scheme is typically second-order accurate and the mesh is refined or coarsened twice. Contrary to this, the so-called generalized RE, on which the bulk of the currently used approaches build, incorporates higher-order accurate schemes with solutions on meshes which are not necessarily different by a factor of two.

RE comes about as follows. For a smooth function, i.e. one with derivatives of all orders, a Taylor series expansion relates the solution to the discretised equations f_k and the solution to the original partial differential equations f_{exact} (Eq. (4.8)):

$$f_k = f_{exact} + g_p \cdot h_k^p + O\left(h_k^{p+1}\right) \tag{4.8}$$

where h_k is a linear measure of the time step/grid element size of discretisation level k, p is the order of accuracy and g_p equals the coefficient of the p^{th} order error term. The big-O notation indicates that the higher-order terms are insignificant and, thus, the numerical solution is in the so-called asymptotic range. This means that h_k is sufficiently small so that p and g_p are virtually independent of h_k. However, in reality CFD users have to be satisfied with solutions near the asymptotic range. This implies that the observed order of accuracy of the solution is not necessarily equal to the formal (theoretical) one of the used discretisation scheme and, thus, this p needs to be estimated alongside f_{exact} and g_p. Therefore, at least three solutions of different discretisation level are necessary. These discretisation levels, designated fine (k=1), medium (k=2) and coarse (k=3), relate to each other by a so-called refinement ratio r (Eq. (4.9)).

$$r_{21} = \frac{h_2}{h_1}, r_{32} = \frac{h_3}{h_2} \tag{4.9}$$

Now, expressions similar to Eq. (4.8) for the three solutions yield the absolute discretisation error ε_D of the respective levels (Eq. (4.10)-(4.12)) and the estimated order of accuracy p (Eq. (4.13)). Readers interested in the formula deduction are referred to the work of Franke et al. [61]. Note that the emphasis lies on the error, not on the estimated exact value. After all, the extrapolated solution is not conservative in the sense of maintaining conservation properties [220].

$$\varepsilon_{D,1} = f_1 - f_{exact} \cong \frac{f_2 - f_1}{r_{21}^p - 1} \tag{4.10}$$

$$\varepsilon_{D,2} = f_2 - f_{exact} \cong \frac{r_{21}^p \cdot (f_2 - f_1)}{r_{21}^p - 1} = r_{21}^p \cdot \varepsilon_{D,1} \tag{4.11}$$

$$\varepsilon_{D,3} = f_3 - f_{exact} \cong \frac{r_{32}^p \cdot r_{21}^p \cdot (f_2 - f_1)}{r_{21}^p - 1} = r_{32}^p \cdot r_{21}^p \cdot \varepsilon_{D,1} \tag{4.12}$$

$$p = \frac{\ln\left[(f_3 - f_2)/(f_2 - f_1)\right]}{\ln(r_{21})} - \frac{1}{\ln(r_{21})} \cdot \left[\ln\left(r_{32}^p - 1\right) - \ln\left(r_{21}^p - 1\right)\right] \tag{4.13}$$

$$\varepsilon_{D,1} = \frac{\varepsilon_{D,2}}{r_{21}^p} = \frac{\varepsilon_{D,3}}{(r_{32} \cdot r_{21})^p} \tag{4.14}$$

Eq. (4.14), which relies on the first three of the above equations, enables to check whether the solutions are in the asymptotic range. Another more stringent condition to apply RE is that the solutions should be monotonically convergent. As a matter of fact, the ratio of the solution changes $R=(f_2-f_1).(f_3-f_2)^{-1}$ discerns three behaviours: monotonic convergence, oscillatory behaviour and divergence. For better understanding Figure 4.1 explains the subject matter graphically. Here, it is assumed that the exact solution is known and a constant refinement ratio applies. Starting from the numerical solutions on the fine and medium discretisation level, the figure indicates the intervals of the numerical solution on the coarse level corresponding to different solution behaviours. Divergent behaviour simply shuts the door on error estimation and indicates that an improved simulation approach is necessary (e.g. prolongation of the iterative calculation, higher grid resolution). For oscillatory behaviour, the solutions display oscillations which may be erroneously identified as monotonic convergence or divergence. In particular Coleman et al. [221] put – at Celik and Karatekin's suggestion [222] – a caveat against this inconvenience, but suggest in another work [204] how to get round it. The upper and lower bounds of solution oscillation, which are derived on more than three grids, are assumed to provide a rough uncertainty estimate. This estimate of uncertainty then equals half of the solution range, which is defined by the upper and lower solution.

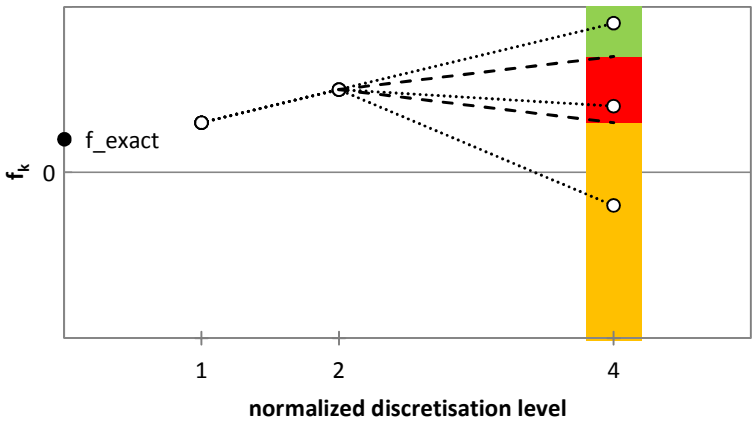

	Interval	Behaviour	Fill
$R=\frac{(f_2-f_1)}{(f_3-f_2)}$	$0 < R < 1$	monotonic convergence	
	$\lvert R\rvert > 1$	divergence	
	$R < 0$	oscillatory behaviour	

Figure 4.1: Fundamentals of solution behaviour

The above discussion already revealed some of the far-reaching limitations of generalized RE, which may be criticized. First, other sources of error like round-off or incomplete iterative convergence really need to be small as the extrapolation tends to amplify them [220]. Secondly, Oberkampf [223, 224], amongst others, casted doubt on the assumption of smoothness. Singularities, discontinuities and buckling are common in complex models, where multiple space and time scales may be important and strong nonlinearities may be present. The question how these possibly insufficiently resolved regions impact upon the discretisation error in more accurately resolved parts of the computational domain keeps researchers busy (e.g. Babuska et al. [225], Oden et al. [226]). Thirdly, having all three grids close to the asymptotic range requires large computational resources [220, 223, 224]. After all, it happens more often than one might expect that only a single grid resolution at the limit of the available resources is able to resolve an important flow structure. An error estimate is then impossible. However, an alternative refinement ratio can sometimes offer a way out. Unfortunately, the researchers in question are at sixes and sevens on this subject. A refinement ratio approximating unity renders too small solution changes while a large ratio requires unrealistically high grid resolutions. Ideally, the refinement ratio equals two. This is the lowest value which does not require interpolation, but it is often too demanding. Ferziger and Perić [200] suggested a minimum increase of 50% in each coordinate direction. Stern et al. [204] stated $r=2^{0.5}$ while Roache [220] has proven that even 1.1 suffices for

simple grids. Further, using only two grids to get round the condition that the numerical solutions need to be in the asymptotic range appears to be empty talk. After all, the observed order of accuracy of the solution usually differs from the formal order of the discretisation scheme for a variety of reasons – as discussed in detail by e.g. Roache [220], Ferziger and Perić [200] and Oberkampf and Trucano [227]: e.g. non-uniform grid distribution [223], issues with smoothness, solutions still out of the asymptotic range [204]. Moreover, the procedure fails in case of small differences between the solutions on the respective grids. This might then be an indication of oscillatory convergence or, in rare situations, it may indicate that the exact solution is approximated [228]. In short, it is not wrong to say that generalized RE is far from perfect.

To account for the uncertainty due to the above factors, Roache [229] multiplied the Richardson-based relative error estimate for discretisation level k $\varepsilon_{rD,k}$ by a safety factor F_s, which resulted in the so-called grid convergence index (GCI) (Eq. (4.15)). As such the GCI is not an error estimator, but rather – in the words of Roache – 'an error band in a loose statistical sense'.

$$GCI_k = F_s \cdot \left|\varepsilon_{rD,k}\right| \tag{4.15}$$

Originally, Roache recommended F_s=3 as this value apparently had the advantage of relating any grid convergence study (any r and p) to one with a grid doubling and a second-order method (r=2, p=2). However, following several applications described in Johnson and Hughes [230], Roache [220] needed to readjust his safety factor. A modest value of F_s=1.25 appeared to be adequately conservative for scrupulously performed grid convergence studies with three solutions. On the other hand, for high-quality studies on two grids and low-quality studies on three grids, Roache retained F_s=3. The aforementioned quality labelling of such studies depends on how good the observed order of accuracy matches the formal one.

Further, Stern et al. [204] sought to broaden the applicability of generalized RE. They had difficulty with Roache not stating a confidence interval for his GCI. But, more importantly, analytical benchmarks revealed that Eq. (4.10)-(4.12) have the correct form, but Eq. (4.13) estimates poorly the order of accuracy outside the asymptotic range. As a matter of fact, the estimated order p approaches the formal one q in an oscillatory fashion with a large range of values. As achieving the asymptotic range for practical geometries and conditions is usually impossible and more than three solutions from a resources point of view is undesirable, Stern and colleagues came up with a correction factor which accounts for the effects of higher-order terms outside the asymptotic range. In [231] they explain why they do not rely on other approaches like the least square method of Eça and Hoekstra [232]. Issues of this last-mentioned alternative to safety factors are the conflicting requirement of solutions in the asymptotic range and the inability to distinguish convergence from divergence. So, similar to Roache's GCI, Stern et al. set the uncertainty equal to the Richardson-based error estimate times a now variable factor $F_s(C)$ (Eq. (4.16)). They actually refined Roache's rough classification of low- and high-quality grids. The correction factor C, which determines the safety

factor F_s, indicates how good the estimated order of accuracy approximates the formal order, and, thus, how close the solutions are to the asymptotic range. Eq. (4.17) expresses this relation for the fine grid solution.

$$\varepsilon_{k,C} = F_s(C) \cdot \left| \varepsilon_{rD,k} \right| \tag{4.16}$$

$$C = \frac{r_{21}^{p} - 1}{r_{21}^{q} - 1} \tag{4.17}$$

However, since Stern and colleagues launched this concept, they worked over the definition of the variable safety factor several times – often in response to criticism of Roache (see e.g. discussions in [233, 234]). In 2002, Wilson and Stern [235] corrected themselves the ill behaviour of their correction factor. For C≤1 the original definition would only provide a 50% confidence level. They also introduced a safety factor of 10% in the limit C=1. As a result, the factor of safety equals 1.1 in the limit while, farther away, it linearly increases up to the low-quality level of Roache (Eq. (4.18) and Eq. (4.19), Figure 4.2).

$$F_s = 9.6 \cdot (1 - C)^2 + 1.1 \;\; if \;\; |1 - C| < 0.125 \tag{4.18}$$

$$F_s = 2 \cdot |1 - C| + 1. \;\; if \;\; |1 - C| \geq 0.125 \tag{4.19}$$

Later on, Xing and Stern [231] readjusted the safety factor so that an overall 95% confidence interval assumedly applies. The definition of Wilson and Stern [235] provided an unreasonably small uncertainty estimate when C>1, compared with those with the same distance to the asymptotic range for C<1. Therefore, the safety factor of Xing and Stern increases more rapidly when the estimated order of accuracy exceeds the formal one (Eq. (4.20) and Eq. (4.21), Figure 4.2).

$$F_s = 2 - 0.75 \cdot C \; if \;\; 0 < C \leq 1 \tag{4.20}$$

$$F_s = \frac{C \cdot (0.5 + 0.75 \cdot C)}{2 - C} \;\; if \;\; 1 < C < 2 \tag{4.21}$$

In the meantime, Logan and Nitta [236] showed that when the estimated order p exceeds the formal one q, Roache's F_s=1.25 is closer to the 68% confidence interval than the preferred 95% and, as a consequence, put forward another variable safety factor definition (Eq. (4.20) and Eq. (4.21), Figure 4.2).

$$F_s = 1.25 if \;\; C \leq 1 \tag{4.22}$$

$$F_s = 1.25 \cdot C \;\; if \;\; C > 1 \tag{4.23}$$

Comparing aforementioned suggestions of the safety factor, reveals a large spread and, thus, the strongly conflicting opinions among specialists. In particular the question which factor of safety provides 95% confidence, remains a point of debate. However, going more into detail on the approaches is out of scope here.

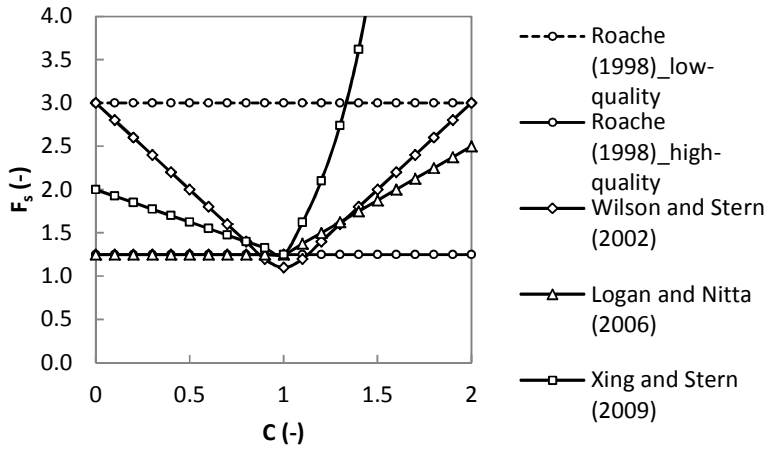

Figure 4.2: Safety factors

4.2.2 Turbulence modelling

Closing the gap

In 1895 Reynolds made the first step towards the well-known Reynolds-averaged (RANS) approach [237]. He suggested decomposing each instantaneous scalar and vector flow variable into a statistically averaged value and superimposing a turbulent fluctuation thereon. For example, the velocity u falls into the time-averaged velocity ū and the fluctuating velocity u' (Eq. (4.24)).

$$u = \bar{u} + u' \tag{4.24}$$

Substituting this redefined velocity into the instantaneous x-momentum equation (Eq. (4.3)) and taking the time-average, results in the so-called Reynolds-averaged x-momentum equation (Eq. (4.25)). This equation consists of the terms of its instantaneous equivalent and an additional term, the Reynolds stresses ($-\rho\overline{u}\,\overline{u}$).

$$\frac{\partial(\rho\bar{u})}{\partial t} + div\left(\rho\bar{u}\bar{\vec{u}}\right) = -\frac{\partial\bar{p}}{\partial x} + div(\mu\ grad\ \bar{u}) + S_{Mx} + div\left(-\rho\overline{u'\vec{u}'}\right) \tag{4.25}$$

This extra term makes up the convective momentum transfer due to velocity fluctuations – or, better, turbulence. Obviously, similar equations apply to the y- and z-momentum. Meanwhile, deriving the time-average transport equation for an arbitrary scalar quantity produces similar extra turbulent transport terms. Unfortunately, because of these time-averaging operations, the new set of equations describing the flow is no longer closed and this is where turbulence modelling comes in. In other words, a turbulence model is a computational procedure to close the system of mean flow equations. Expressions for the Reynolds stresses and the turbulent scalar transport terms account for the effects of turbulence on the mean flow. Incited by the early but important attempt of Boussinesq [238] to mathematically describe the turbulent stresses, many researchers have come up with new turbulence models or improvements. These RANS turbulence models are usually classified as either eddy viscosity models or Reynolds stress models.

The eddy viscosity models build on a proposal of that very same Boussinesq, his so-called eddy viscosity hypothesis [238]. This presumes that turbulent stresses relate – whether or not linearly – to the mean velocity gradients, just as viscous stresses do in laminar flows. Eq. (4.26), in so-called suffix notation (i.e. i or j=1 corresponds to the x-direction, i or j=2 to the y-direction and i or j=3 to the z-direction), depicts such a linear eddy viscosity model, for incompressible flows:

$$-\rho\overline{u_i'u_j'} = \mu_t\left(\frac{\partial(\overline{u}_i)}{\partial x_j}+\frac{\partial(\overline{u}_j)}{\partial x_i}\right)-\frac{2}{3}\rho k\delta_{ij} \quad where\ k=\frac{1}{2}\overline{u_i'u_i'} \tag{4.26}$$

Here, μ_t stands for the turbulent or eddy viscosity, which, in contrast to the molecular viscosity, is not a fluid property. Rather, it depends on the state of turbulence, which varies from point to point, from flow to flow. The last term involving the Kronecker delta δ_{ij} (equal to unity for i=j and zero for i≠j) is necessary to make sure that the sum of the three normal stresses matches twice the turbulent kinetic energy k (i.e. the total amount of turbulent energy in the flow). Allocating an equal third implies an isotropic assumption for the normal Reynolds stresses. Next to this, there is a parallel between turbulent transport of momentum and turbulent transport of a scalar, such as heat. Now, a similar turbulent or eddy diffusivity Γ_t relates the turbulent scalar transport terms to the gradient of the transported scalar, forming an eddy diffusivity model. The specific name of this eddy diffusivity depends on the scalar in question: e.g. eddy temperature diffusivity α_t in case of heat. Like the eddy viscosity, the eddy diffusivity depends on the state of turbulence. Because of this, the main question in turbulence modelling shifts to the determination of μ_t and Γ_t, at least at first. As a matter of fact, most turbulence models rely for e.g. thermal transport on the Reynolds analogy. This implies that the eddy temperature diffusivity α_t assumedly relates to the kinematic eddy viscosity ν_t via the so-called turbulent Prandtl number Pr_t (Eq. (4.27)). After all, the same eddy mixing transports both momentum and e.g. heat. Obviously, similar assumptions apply to other scalar quantities. As a result, an eddy viscosity model only involves expressions estimating the kinematic eddy

viscosity. The commonly accepted idea is to relate the kinematic eddy viscosity ν_t to the product of a turbulence velocity scale ϑ and some turbulence length scale ℓ (Eq. (4.28); cf dimension of ν_t is $m^2.s^{-1}$).

$$\mathrm{Pr}_t = \frac{\nu_t}{\alpha_t} = \frac{\mu_t}{\rho \cdot \alpha_t} \tag{4.27}$$

$$\nu_t = \frac{\mu_t}{\rho} = \vartheta \cdot \ell \tag{4.28}$$

The number of transport equations that are solved for turbulence determines the complexity and, at the same time, a clear-cut classification of the linear eddy viscosity models: zero-equation models – or algebraic models – (e.g. Prandtl's mixing length model [239]), one-equation models (e.g. Spalart-Allmaras model [240]) and two-equation models (e.g. standard k-ε model [241], standard k-ω model [242]). Nonlinear eddy viscosity models extend the description of the eddy viscosity with one or more terms that involve higher-order flow parameters (e.g. cubic k-ε model of Merci et al. [243]) and v^2-f models (e.g. k-ε υ^2 model of Durbin [244]). Such models are, in contrast to linear eddy viscosity models, able to predict anisotropy, but are usually not available in commercial software like Fluent [201]. Yet, the eddy viscosity models suffer from some major limitations. First of all, because the turbulent viscosity relies on flow-specific theoretical or empirical relations, there is no universally valid turbulence model which performs well for all classes of flows. In the second place, most turbulence models apply to high-Reynolds number turbulent flows. In other words, to be valid in the near-wall region where low-Reynolds numbers are pervasive, such models require modifications (see introductory chapter of this work). Finally, the linear eddy viscosity models assume the turbulent viscosity and, thus, turbulence to be isotropic, which is usually not the case.

More advanced RANS turbulence models which automatically account for turbulence anisotropy are the Reynolds stress models, also known as second-order or second-moment closure models [245]. Basically, such a model closes the Reynolds-averaged Navier-Stokes equations by solving transport equations for the Reynolds stresses, together with an equation for the turbulence dissipation rate. Thereby, it promises to give more accurate predictions for complex flows, including strong streamline curvature, rotation, swirl and rapid changes in strain rate. However, because of the still uncertain enclosed assumptions and its considerable additional computational expense, it prices itself out of the market, certainly for building applications such as the studies part of this thesis. Only when the flow features of interest result from the anisotropy in the Reynolds stresses, the use of a Reynolds stress model justifies the extra computational cost: e.g. cyclone flows, highly swirling flows in combustors.

Different flavours of two-equation eddy viscosity models

The two-equation eddy viscosity models are the most popular RANS models in building design, and by extension engineering applications. After all, such turbulence models balance computation effort with solution accuracy. Two-equation models require more computation effort than algebraic and one-equation models do, but they do not use an algebraic expression based on geometrical conditions to compute the eddy viscosity [246]. Instead, they relate the kinematic eddy viscosity ν_t ($m^2.s^{-1}$) to the turbulent kinetic energy k ($m^2.s.^{-2}$) (which gives the turbulence velocity scale ϑ) and some second turbulent quantity (which provides the turbulence length scale ℓ, either direct or in combination with k). Precisely the definition of this last-mentioned quantity subdivides the two-equation models. Most models use either the turbulent dissipation rate ε ($m^2.s^{-3}$) (Eq. (4.29)) or the specific turbulent dissipation rate ω (s^{-1}) (Eq. (4.30)), also known as turbulence frequency. The ε-equation is usually derived from the modelled k-equation by dimensionally mapping ε onto it (with added constants and damping functions). Deriving an equation for ω is done based on reasoning from the ε-equation. ω is then thought of as the ratio of ε to k [246].

$$\nu_t \sim \frac{k^2}{\varepsilon} \tag{4.29}$$

$$\nu_t \sim \frac{k}{\omega} \tag{4.30}$$

To date, there is an increasing number of two-equation eddy viscosity models. Yet, a limited number of models is sufficient to exemplify and compare nearly all existing two-equation models, at least on a theoretical level. Amongst others, Patel et al. [108] Sarkar and So [247], Wilcox [248] and Bredberg [246] have written in-depth analyses on this. Underlying work, by contrast, merely sketches the two-equation turbulence models in broad outlines.

The standard k-ε model of Launder and Spalding [249] is the most widely used and validated turbulence model. Yet, this is no surprise. The model performs particularly well in confined flows where the Reynolds shear stresses are most important; and this includes a wide range of flows with (industrial) engineering applications [190]. After all, the constant C_μ, which relates the kinematic eddy viscosity directly to $k^2.\varepsilon^{-1}$ in Eq. (4.29), and the model constants in the transport equations for k and ε rely on experiments with air and water for (similar) fundamental turbulent shear flows, i.e. channel and flat plate flow [250]. However, its poor performance for more complex flows, such as (1) some unconfined flows, (2) flows with large extra strains (e.g. swirling flows), (3) rotating flows, (4) flows driven by anisotropy of normal Reynolds stresses and (5) low-Reynolds number flows [190], made researchers come up with modifications. Especially the RNG k-ε model developed by Yakhot and Orszag [251] has attracted interest. These last researchers applied a mathematical technique called renormalization group (RNG) to derive their own k-ε model variant. This RNG procedure systematically filters

out small scales of motion from the governing equations by expressing their effects in terms of larger scale motions and a modified viscosity. As a result, the RNG k-ε includes the following refinements. The constant of the production term in the RNG model ε-equation now contains a strain-dependent correction term which makes the RNG k-ε model fit for flows that experience large rates of deformation [190]. Secondly, the scale elimination procedure in the RNG theory brings about a differential equation for turbulent viscosity. This modified definition allows to include low-Reynolds number effects which are pervasive in indoor airflow applications. Yet, effective use of this feature necessitates an appropriate treatment of the near-wall region [201]. Furthermore, the RNG theory provides an analytical formula for turbulent Prandtl numbers, while the standard k-ε model deploys user-specified constant values. For that matter, all but one of the remaining model constants rely on the RNG procedure, instead of on experimental data. Another improved k-ε model variant is the realizable model of Shih et al. [252]. It differs from the standard version in the determination of C_μ which relates the kinematic eddy viscosity directly to $k^2.\varepsilon^{-1}$ in Eq. (4.29) and in the transport equation for the dissipation rate ε. First, making C_μ a function of the mean flow (mean deformation) and the turbulence (k, ε) guarantees the 'realizability': the model satisfies particular mathematical constraints on the Reynolds stresses, consistent with the physics of turbulent flows (i.e. positivity of normal stresses and Schwarz inequality for shear stresses, see Fluent [201]). Secondly, the new model equation for dissipation rate ε, which now lacks the Reynolds stresses [250], deals with the so-called plane jet-round jet anomaly of the k-ε model: the standard k-ε model predicts the spreading rate of a planar jet reasonably well, but overestimates the one of a round jet. All in all, the realizable k-ε model, just like the RNG k-ε model, better predicts flows with strong streamline curvature, vortices and rotation [201]. Yet, the above k-ε models are not apt for wall-bounded flows because they were originally developed for flow in regions somewhat far from walls. One remedy is the use of semi-empirical, logarithmic wall functions which bridge the viscosity-affected region between the wall and the fully-turbulent region. However, this wall function approach fails when low-Reynolds number effects dominate the flow domain and high three-dimensionality occurs, as is usually the case with airflows inside buildings [104-109]. A better way is to apply the two-layer approach. In this case, the k-ε model resolves the turbulent core region of the flow and a low-Reynolds number model like the one-equation Wolfstein model [253] takes care of the viscosity-affected region. This last low-Reynolds number model solves one transport equation for turbulence, i.e. for the turbulent kinetic energy k, while it determines the turbulence length scale using an algebraic expression which includes a wall distance-based turbulent Reynolds number. Damping of the turbulent viscosity then accounts for the influence of the wall on turbulence.

The second important group of two-equation eddy viscosity models relies on the k-ω model, first conceived by Kolmogorov [254], later extended (for low-Reynolds number effects, compressibility and shear flow spreading [201]) and popularized by Wilcox [242]. In these models, the eddy viscosity is simply equal to $k.\omega^{-1}$ (Eq. (4.30)). Yet, authors like Zhai et al. [195] report that only few applied the k-ω model for indoor airflow applications. As a matter of fact, the k-ω model,

unlike the k-ε model, performs particularly well close to walls, but is sensitive to the free stream values of ω [61, 255, 256]. In response, researchers like Menter [257] suggested blending the robust and accurate formulation of the k-ω model in the near-wall region with the free stream independence of the k-ε model in the far field. This results in a so-called Shear Stress Transport (SST) k-ω model. Practically speaking, its blending function equals one in the near-wall region, so that the standard k-ω model runs, and zero away from the surface, which activates the k-ε model (which is actually converted into a k-ω formulation). Thereby, the SST k-ω model usually performs better than the standard version [61, 201].

Usability of linear eddy viscosity models

Obviously, theoretical considerations like the ones above are not enough to judge the applicability of turbulence models to – in this case – various indoor airflow applications. By contrast, simulation studies give a more decisive answer. One early but concerted research effort is the IEA Annex 20 project [194]. This international joint venture of (now) illustrious researchers like Qingyan Chen, Alfred Moser and Peter Nielsen aimed at, among other things, a thorough evaluation of the performance of complex and simplified airflow models in predicting indoor airflow patterns. Some of the participants (e.g. Chen [258], Tjelflaat [259]) tried out a turbulence model other than the standard k-ε model and noticed a profound influence of their choice on the isothermal airflow pattern. Yet, only follow-up studies, performed by themselves, their assistants or other researchers, sketched a more general picture. Not only more turbulence models were tested, but also various convection regimes were passed in review. Recently, Zhai et al. [195] started reviewing the latest developments of the major turbulence models and their application in indoor airflow modelling. These authors especially looked for applications with validation data and/or comparison of several turbulence models. Unfortunately, they failed to derive sound guidelines on which turbulence model to use when. After all, factors beyond the turbulence models themselves (e.g. numerical method, judging criteria, user skills) often obscured the results. The description of most works is not detailed enough to pinpoint the causes of the differing results. Therefore, Zhai et al. tried to descry the most popular turbulence models in indoor airflow modelling. They revealed that especially the RNG k-ε model of Yakhot and Orszag [251], the SST k-ω model of Menter [257] and the v^2f-model of Durbin [244] conciliate solution accuracy with computing time. In a follow-up study, Zhang et al. [197] tried out these popular models in a series of benchmark experiments, of which each one corresponded to a certain convection regime (natural, forced, mixed and strong natural). As expected, their results confirmed the observations of Zhai et al. In terms of solution accuracy, the RNG k-ε model of Yakhot and Orszag [251] and the SST k-ω model of Menter [257] came close to the v^2-f model of Davidson et al. [260] and the RSM model of Gibson and Launder [261]. However, the RNG k-ε model of Yakhot and Orszag and the SST k-ω model of Menter required two to five times less computation time. Obviously, repeating the literature review of Zhai et al. [195] is of little use. Yet, rearranging the discussed (and the few new) applications according to the

convection regime might better tie in with the work of Zhang et al. [197]. Table 4.1 lists some of the works which tested turbulence models for either a natural convection, mixed or forced convection regime. Hereby, the overview indicates which turbulence models the cited authors have tested, which turbulence model(s) they preferred and the quantity(ies) of interest. It clearly highlights that the reviewed works chose for natural convection the variants of the k-ε model, i.e. the RNG k-ε model (2-eq. RNG k-ε) and the realizable k-ε model (2-eq. rk-ε), instead of the standard version (2-eq. sk-ε). In case of mixed and forced convection, the RNG k-ε model is again on top. In other words, taking the cited works (which usually rely only on point variables) for granted, the RNG k-ε model is always a cut above. This ties in with the conclusions of Chen and Zhai [262] and Zhai et al. [195]. Note that also the SST k-ω seems promising, but more test cases are necessary.

Table 4.1: Recent applications of RANS turbulence models in indoor airflow modelling

	Reference	Preferred	Other	Interest
Natural convection	Chen and Xu [263]	sk-ε	own 0-eq.	Airflow
	Sharif and Liu [264]	sk-ω	LRN k-ε	Airflow
	Walsh and Leong [265]	sk-ε	RNG k-ε, RSM	Heat transfer
	Yang [266]	sk-ε/ RNG k-ε		Airflow rate
	Van Maele and Merci [250]	rk-ε	sk-ε	Airflow
	Craven and Settles [267]	RNG k-ε		Airflow
Forced convection	Voigt [268]	sk-ε/ LRN k-ε	sk-ω, SST k-ω	Airflow
	Rouaud and Havet [269]	RNG k-ε	sk-ε, RSM	Airflow
	Posner et al. [270]	laminar/ RNG k-ε	sk-ε,	Airflow
	Susin [271]	k-ω	sk-ε, RNG k-ε	Airflow
	Cao et al. [272]	SST k-ω		Airflow
Mixed convection	Chen [196]	RNG k-ε	sk-ε, LRN sk-ε, 2-layer k-ε, 2-scale k-ε,	Airflow
	Chen [273]	RSM	sk-ε	Airflow/ heat transfer
	Loomans [274]	RNG k-ε/ LRN sk-ε	sk-ε	Airflow/ heat transfer
	Costa [275]	LRN k-ε [276]	8 LRN k-ε	Airflow/ heat transfer
	Yuan et al. [277, 278]	RNG k-ε		Airflow

Mixed convection	Gebremedhin and Wu [255]	RNG k-ε	sk-ε, LRN sk-ε, sk-ω, RSM	Airflow/ heat transfer
	Sekhar and Willem [279]	RNG k-ε		Air quality
	Nahor et al. [280]	sk-ε		Airflow/ heat transfer/ mass transfer
	Zhang et al. [281]	RNG k-ε		Airflow
	Zhang and Chen [282]	sk-ε		Airflow/ Air quality
	Stamou and Katsiris [256]	SST k-ω	laminar, sk-ε, RNG k-ε	Airflow
	Kuznik et al. [283]	sk-ω	rk-ε, RNG k-ε, SST k-ω	Airflow
	Rohdin and Moshfegh [284, 285]	RNG k-ε	sk-ε, rk-ε	Airflow

4.2.3 Diffuser modelling

Annex 20: a major step forward

The airflow inside and near an air supply diffuser is often complex because of e.g. perforated plates, dampers and guide rails inside the diffuser. Calculating the flow inside such a diffuser and in the ventilated room necessitates a large number of grid points and, thus, significant computational resources [286, 287]. In response, numerous researchers (have) put a lot of effort in deriving to what extent the diffuser description can be simplified. All models rely on the strong upstream influence in the first part of the flow. Again IEA Annex 20 [194] contributed strongly to the diffuser model development. In the decades to follow, researchers kept on working on the diffuser type then used. Logically, this literature review explains the diffuser models by taking the Annex 20 diffuser as an example. Yet, the study also briefly discusses similar works on other diffuser types.

The HESCO nozzle diffuser used in Annex 20 consists of 84 round nozzles that are arranged in four identical rows in an area of 0.71m x 0.17m. The flow direction of each nozzle is adjusted with an angle of 40° upwards (Figure 4.3). Such a complicated diffuser proves particularly difficult to model (Figure 4.4). The velocity in the nozzles is quite high (3.68m.s^{-1}), but decreases rapidly due to intensive mixing of the small jets. At 0.10m away from the diffuser, the maximum velocity only comes to approximately 1.5m.s^{-1} (Figure 4.4(a)). Then, the combined jet impinges upon the ceiling where a pressure increase counterbalances the upward momentum force of the jet. From this stagnation zone, the jet spreads below the ceiling to all directions; also to the upper left corner where a recirculating zone comes into being (Figure 4.4 (b)).

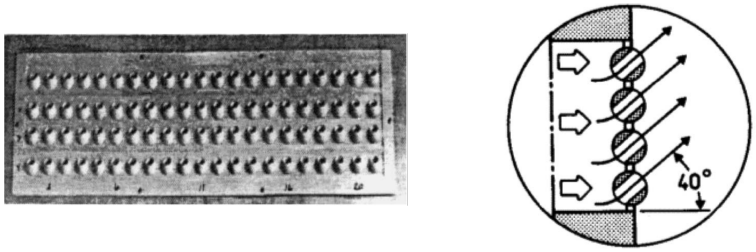

(a) (b)

Figure 4.3: (a) Picture and (b) section of the HESCO nozzle diffuser [288]

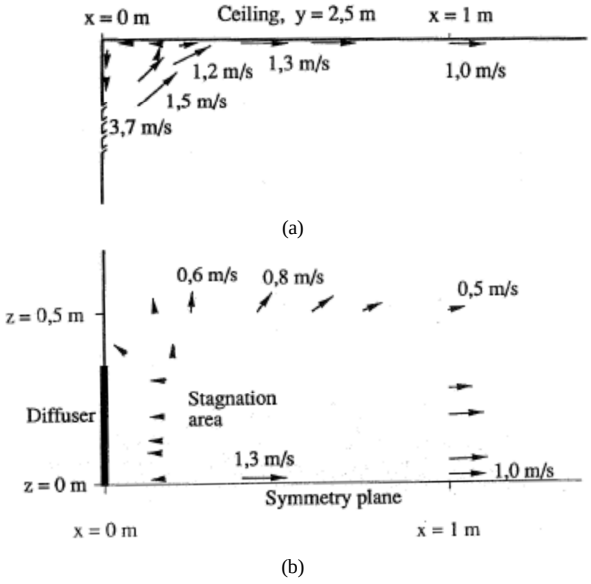

Figure 4.4: The observed flow field near the diffuser, (a) at the symmetry plane and (b) just below the ceiling. (b) only shows half of the symmetrical room [288]

Simplified geometrical model

The simplified geometrical model (SGM) approximates the openings to simplified alternatives with a reduced area – mostly the effective area, i.e. the net area utilized by the air stream in passing through the diffuser outflow. Usually single values apply to the respective parameters (like velocity, temperature, concentration and turbulence intensity) defined at this supply opening. The air supply velocity is calculated from the mass flow rate and the effective area (which is hard to determine as it depends on, among other things, the airflow rate [286, 289]). The other parameter values rely on measured data or are arbitrarily chosen. In the IEA Annex 20 project, Heikkinen [288] first represented the HESCO nozzle diffuser as

a single rectangular opening, located in the centre of the diffuser, with approximately the same effective flow area, aspect ratio and velocity direction as the real diffuser (Figure 4.5(a)). He found that this model could qualitatively recreate the airflow pattern under isothermal conditions. However, because of the limited spreading of the jet, the predicted velocity level outside the centre plane was higher than the measured one. For that same reason, Ewert et al. [290] found unacceptably high turbulent kinetic energies in the occupied zone. In response, Heikkinen increased the aspect ratio, but now the mixing in the core region and the jet penetration were overestimated even more because the jet was thick at its start. Also this model could not capture the loss in momentum due to underpressure in the area between the nozzles. Therefore, the above authors suspected that both models comprising only one diffuser plane would unlikely yield satisfactory results for other diffuser types. However, Heikkinen commented on this: 'the different codes used in Annex 20 influenced the results and the grid resolution was insufficient in the jet region, which without doubt limited the reliability of the CFD results.' Within the same international project, Chen and Moser [291] transformed the proposal of Heikkinen into 12 or 84 rectangular slots, having the same total effective area as that of the 84 round nozzles (Figure 4.5(b)-(c)). These models scored better, but the predicted velocity profiles still did not satisfactorily match the experimental data. Moreover, for non-isothermal flows, both the simplified geometrical models of Heikkinen and Chen and Moser showed poor performance: the computed air temperature was about 1°C lower than the measured value. Again, a limited grid resolution, especially near walls, limited the authority of their studies. Later Emvin and Davidson [292] extended the work on Annex 20: they concluded that the SGM would give a long penetration length in case of diffusers with small diffuser areas. Similarly, Nielsen [293] suggested using the simplified geometrical model for the special situation where the supply area is large compared with the other dimensions – as adopted by some of the authors to come.

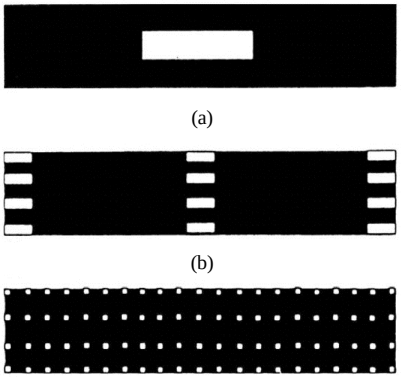

Figure 4.5: Simplified geometrical model of the HESCO nozzle diffuser with (a) the same effective area, (b) 12 slots and (c) 84 slots [291]

Djunaedy and Cheong [294] applied five models based on the SGM approach for describing a square four-way diffuser. They varied the following parameters: the area and the shape of the different diffuser planes and the magnitude and the direction of the air supply velocity assigned to each plane. They found a viable diffuser model for the case at hand, but, unfortunately, they did not extend their study to non-isothermal conditions. Also Zhao et al. [295] tested, alongside a wall-mounted displacement diffuser and a grille, an alternative SGM of a similar square ceiling diffuser, in this case for non-isothermal conditions, and observed an overall good agreement with experimental data. Modelling a slightly different cone ceiling diffuser, Sun and Smith [296] also found a satisfying agreement. Finally, Zhang et al. [297] developed a methodology to determine the boundary conditions for displacement ventilation systems in particular – resulting in basically a SGM. Given the mass conservation principle, a random mathematical function determined whether a CFD cell of the diffuser was open. Subsequently, the discharge air velocity was determined assuming the flow was uniform on the diffuser surfaces. Even for non-isothermal conditions, Zhang et al. found a good agreement with experimental data. Summing up, the SGM, adopted as a set of diffuser planes designed for a specific diffuser type, can provide a good estimate.

Momentum model

The momentum model (MM) represents the diffuser by an opening with the same gross area (Figure 4.6). However, the mass flow corresponds to the real value while the momentum force F relies on the effective velocity u_{eff} and the effective flow area A_{eff} (Eq. (4.31). This implies that the mass flow and the momentum force rely on a different velocity. Thus, to get the correct mass and momentum flows, decoupling the mass and momentum boundary conditions would be necessary. Usually uniform parameter values (velocity, temperature, concentration, turbulence intensity) apply to the MM (as with the SGM).

$$F = \rho \cdot u_{eff}^2 \cdot A_{eff} \quad where \; u_{eff} = \frac{\dot{m}}{\rho \cdot A_{eff}} \tag{4.31}$$

Chen and Moser [291] as well as Heikkinen [288] found that the MM better approximated the HESCO nozzle than the SGM. However, the initial jet mixing and the maximum jet velocities were overestimated. Heikkinen believed that increasing the number of grid points near the diffuser would improve the prediction. After all, numerical diffusion played an important role in the early jet development. Therefore, Luo and Roux [298] and Luo et al. [299] extended the above studies: using a more advanced RNG k-ε turbulence model and local mesh refinement near the diffuser, the MM yielded better agreement with the isothermal experimental data of Ewert et al. [290] and Heikkinen [300]. Only the jet velocity at the lower part of the opposite wall was underestimated. However, the incorrect prediction of the 3-D development of the jet by the isotropic turbulence model could explain the last-mentioned failing. Moreover, because the jet momentum is mainly contained in the jet centre plane, which is the main driving force of the

isothermal indoor air motion, the above authors believed that this underestimation would not greatly affect the global flow pattern inside the room. These same authors also evaluated the impact of the turbulence intensity (10%, 15% and 20%) and found only a limited influence. This is actually in line with earlier studies on other diffuser types (e.g. Awbi [301], Joubert et al. [302]) and, thus, partly justifies the often arbitrary choice of the turbulence parameters, also in case of other diffuser models.

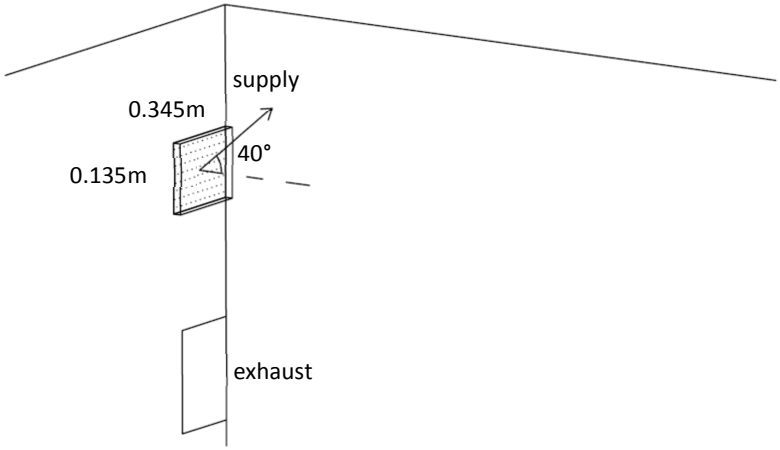

Figure 4.6: Momentum model of the HESCO nozzle diffuser

Chen et al. [303] and Jiang et al. [304] also successfully applied the MM to simulate complex diffusers for both mixing and displacement ventilation – indicating its suitability for a range of diffuser types. Especially for displacement diffusers, Yuan et al. [277] found a very good model performance. Meanwhile, Koskela [305] extended the application of the MM to a cylindrical nozzle duct. He based his MM – consisting of additional local momentum sources – on the assumption that not the jet velocities, but the induction of secondary air – creating a pressure gradient – is the main driving force. This model correctly recreated the flow pattern for four different convection regimes. Unfortunately, the absolute simulated velocities exceeded the measurement data, because in reality unsteady asymmetrical thermal plumes occurred, which probably reduced the maximum velocities. According to Koskela, performing unsteady simulations would remedy this shortcoming. Building on previous work and looking for a general method, Srebric and Chen [306] applied the promising MM to eight diffuser types. They concluded that this method is preferably used – because of its simplicity, except for diffusers with a complex jet development such as a nozzle diffuser, a slot and a valve diffuser.

Box model

The box model (BM), first shown in Nielsen [182], represents the diffuser boundary conditions on an imaginary box surface – ignoring the flow field inside the box (Figure 4.7). Originally, the box surface opposite to the diffuser uses the profiles of the velocity, the temperature, the concentration and the turbulence quantities. On the other surfaces a free boundary with zero gradients for flow parameters is specified. As a benefit, the BM makes no use of the hardly determinable effective area. However, because of e.g. the jet confinement, the self-preserving jet profiles cannot be used in general, necessitating labour-intensive measurements. In addition, the box size is a new important parameter. As explained by Nielsen [307], if the diffuser discharges multiple jets, such as the nozzle diffuser, the front surface of the box should be in the region where the diffuser jets have merged, i.e. a fully-developed jet. At the same time, the box has to be sufficiently small to avoid the impact of indoor air circulation and thermal plumes on the jet. Meanwhile, the height of the box should have a certain size compared with the thickness of the wall jet. Heikkinen [288] observed an underestimation of the velocity decay by the BM of the HESCO, possibly due to an erroneous estimation of the velocity direction. Nielsen [293, 308] however, who used a more detailed velocity description at the box surface, found a better predicted velocity decay for both a 2-D and a 3-D version of the BM. Also the measured and calculated velocities in the room agreed well. Unfortunately, the increase of the jet width barely reached the measured ratio, possibly due to the use of a linear eddy viscosity turbulence model, which prohibits the asymmetrical jet development.

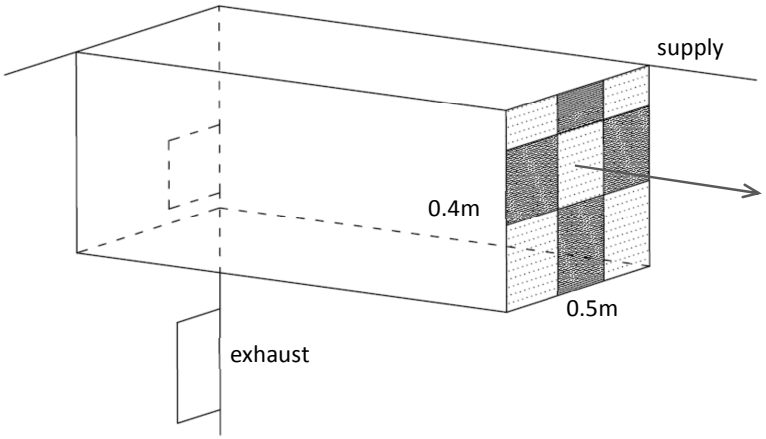

Figure 4.7: Box model of the HESCO nozzle diffuser

Huo et al. [309] extended the concept of using jet formula in the BM by developing the so-called jet main region specification method. They suggested for both the determination of the box size and the specification of the boundary conditions to use analytical jet formula – including jet profiles, decay and trajectory. Simulations of a ceiling-mounted linear and square diffuser showed promising – at least qualitative – results, even for non-isothermal conditions. However, the use of analytical formula limits the application of the jet main region specification method to a small set of simple cases. For example, as suggested by Srebric [199], the jet formula cannot model jets with multiple attachments and partially attached jets. For that reason, last-mentioned author extended the application of the original BM, defined by measured data, to several diffuser types. She proposed to use only the BM when the MM cannot capture the important flow characteristics. For diffusers like a nozzle diffuser, a slot and a valve diffuser, she defined a method of test to obtain BM diffuser data for CFD modelling. First of all, she found that the obtained distribution of air temperature and tracer gas concentration in a room were insensitive to the profiles of the temperature and contaminant concentration distribution at the box surface. And Joubert et al. [302] already casted doubt on the necessity of detailed profiles of turbulence parameters. Therefore, only the velocity profile – possibly obtained under isothermal conditions – needs to be specified while the other parameters can be set as uniform. In this case these quantities should be measured in advance or the heat and the species balances should be calculated at the box boundaries. In addition to this simplification, she suggested using smoke visualization to estimate the box size. A more practical way suggested by Grimitlyn and Pozin [310], however, is to define the box surface at a location where the buoyancy force is negligible compared with the momentum force; which is defined by the local Richardson number.

Prescribed velocity model

Gosman et al. [311] developed the prescribed velocity model (PVM) which needed fewer measured data. This model gives the boundary conditions at a simple opening analogous to the SGM while at some critical locations on a plane in front of the diffuser data are defined to correct the predicted values around the diffuser. Also the PVM uses equations from jet theory or measured data. The considerations for size and location of the plane in front of the diffuser are similar to the BM. In particular for the velocity, Nielsen [312] proposed to define the correction values by two components in two perpendicular planes. Skovgaard and Nielsen [286] and Svidt [313] found that this PVM of the HESCO diffuser gave a better correlation between the simulated and measured velocity components in comparison with the SGM. Also the thickness of the wall jet was close to the measured value. Heikkinen [288] even found a reasonably good prediction of the isothermal flow with only an x-specification of the velocities.

Fontaine et al. [314] quantitatively compared the performance of the PVM with the one of the SGM for a ceiling-mounted circular induction diffuser, commonly used in the service sector and industry. They varied primarily the model complexity – e.g. the number of critical data and of velocity components – as part of their sensitivity analysis. They found that the PVM performed significantly better. However, their study has a limited generality. For, the studied isothermal setup does not occur frequently in practice. Einberg et al. [315] applied a combination of the MM and a modified version of the PVM in validating a manufacturer diffuser model. In the diffuser, a low-velocity perforated cylindrical part was placed on top of a multi-cone diffuser. For the non-isothermal setup at hand, simulating the low-velocity part with the MM while specifying the cone diffuser with the PVM resulted in a good performance, at least far away from the industrial diffuser.

4.2.4 Conclusions: advisable simulation approaches

The above literature reviews explained the obstacles to set up a proper grid, to adequately model turbulence and to imitate the airflow due to an air supply diffuser and, more importantly, they distilled advisable simulation approaches to get round these difficulties.

With regard to the grid, in particular the grid distribution and the resolution are stumbling blocks. The solution is problem-dependent, so putting forward a proper distribution/resolution in advance is out of the question. Because of this, CFD users usually rearrange/refine(coarsen) the grid multiple times to investigate the impact of the grid a posteriori in an ad hoc manner. However, they should better perform a systematic convergence study. Actually many researchers support the use of generalized RE to estimate the discretisation error, in despite of the many shortcomings. For example, generalized RE requires multiple solutions and, thus, necessitates large computational resources. Or the applicability and reliability of generalized RE are strikingly sensitive to the problem set – like any error estimation technique: it works well for smooth, linear problems with simple physics and geometries, but possibly goes wrong when things get complex. In response, researchers have come up with a multitude of safety factors, but the various viewpoints have not converged yet. In other words, the current methodology falls short of providing strict procedures to determine the uncertainty due to discretisation. However, that does not make a convergence study less necessary.

As for turbulence modelling, researchers have developed models which are able to cope with different indoor airflow features. Unfortunately, no single turbulence model can handle all flows, at least not in an economic way. Therefore, the selection of a turbulence model is always a compromise. Yet, for general indoor airflow studies, the linear RNG k-ε model usually provides reasonably accurate results at an acceptable computing effort. However, in the near future, promising nonlinear eddy viscosity models like the v^2f-model will probably gain ascendancy over the linear turbulence models thanks to the increasing computing power [195, 262].

Finally, numerous researchers have come up with several seemingly new diffuser modelling methods. However, all can be brought down to four fundamental approaches, which were already addressed during the Annex 20 project in the early 1990s. These approaches can be divided into two groups. The SGM and the MM, part of the first group, impose the initial jet momentum directly at the air supply opening. The BM and the PVM are part of the momentum modelling in front of the air supply. Here, the momentum at some distance downstream of the diffuser acts as a boundary condition for the air supply diffuser. Every model necessitates a distinct set of input variables (Table 4.2). The reason for these multiple (adapted) models lies in the fact that no method is clearly superior. For example, a custom-made version of the SGM, which is usually far off from reality, may perform strikingly well. Or a BM based on just jet profiles is only advantageous for simple cases. Nevertheless, Srebric [199] narrowed the possibilities. From the group which models at the air supply diffuser plane, she withdrew the MM while the BM seemed the most promising model of the second group. Moreover, she tested these chosen models to simulate eight different types. After all, each type may produce significantly different flow structures. In the end, Srebric came to the following reasonable conclusion: use the MM as much as possible; only for diffusers with complex mixing such as nozzle, slot and valve diffusers, the BM is better. What's more, the BM proves particularly helpful in case of complex ductworks and multi-direction diffusers: having to measure the velocity distribution can bring to light the effects of particularities like a curved duct, a flow straightener…

Table 4.2: Input variables of the diffuser models

Diffuser model	Input variables
SGM	$\dot{m}$, A_{eff}, direction, shape, T_{sup}, turbulence parameters, concentration
MM	$\dot{m}$, A_{eff}, gross area, direction, shape, T_{sup}, turbulence parameters, concentration
BM	$\dot{m}$, jet formula or measured velocities, shape, T_{sup} or measured T_{box}, turbulence parameters, concentration
PVM	$\dot{m}$, A_{eff}, direction, shape, T_{sup}, jet formula or measured velocities, turbulence parameters, concentration

4.3 Sensitivity of the predicted convective heat transfer to the CFD simulation approach

4.3.1 Simulation experiment setup

To investigate the impact of some of the aforementioned simulation approaches on the predicted convective heat transfer, this study starts from the well-set Annex 20 case [194]. This well-known case is chosen because of the excellent original data available (e.g. measured velocity profiles near the complex diffuser which are necessary for some diffuser models) and the many follow-up studies. What's more, it is particularly challenging to model the complex HESCO nozzle diffuser – which would also be the case with commonly used diffuser types like valve and slot diffusers [199]. The Annex 20 3-D test room, basically made out of wooden sheets wrapped up with 0.10m thick insulation, has internal dimensions of 4.20m x 3.60m x 2.50m – as shown in Figure 4.8. On the front wall, the aforementioned HESCO nozzle diffuser (0.71m wide and 0.17m high) is mounted 0.20m below the ceiling, symmetrically placed between the side walls. On the same wall, an outlet (0.30m wide and 0.20m high) is located 1.70m above the floor. The window on the opposite wall, part of the original setup, is no longer included, simply to reduce the complexity, which speeds up this inter-model comparison.

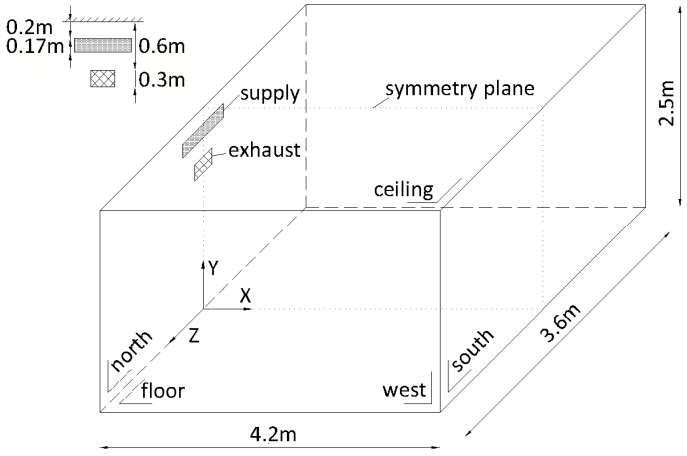

Figure 4.8: Configuration of the modified Annex 20 test room

Moreover, this study intends to check upon the simulation approaches for more than one convection regime. To this end, the air supply velocity, the air supply temperature and/or the enclosure surface temperature should be altered. As literature only reports detailed data on the case with $n=3h^{-1}$ and $T_{sup}=15°C$ (i.e. case Annex 20 E.2), changing the enclosure temperature is the best choice. Like in the original case, all surroundings – except for the now omitted warm window – are at 21°C, which brings about a mixed convection cooling regime. To define two other parameter values, this study makes use of the ratio of the modified Richardson numbers Ri' (°C.h^{-2}) of the respective cases (Eq. (4.32)). Putting these Richardson numbers against each other enables to judge the cases – or better, the convection regimes – in a strictly relative manner (Table 4.3). For example, the utmost case 3 with a Richardson number equal to one hundredth of the original, knows only a negligible natural convection part compared with the original case. Because of this, the considered regimes range from mixed to forced convection, which assumedly corresponds to night cooling applications in buildings. By the way, scaling up the enclosure temperature would prohibit the use of the momentum modelling in front of the diffuser. A higher enclosure temperature would mean a higher buoyancy force. And the plane at which the flow characteristics are to be defined, would shift towards the diffuser, for which no experimental data are available.

$$Ri' = \frac{T_{w,avg} - T_{sup}}{n^2} \tag{4.32}$$

Table 4.3: Boundary conditions defining the convection regimes

Case	Convection regime	n (h^{-1})	T_{sup} (°C)	$T_{w,avg}$ (°C)	$Ri'_x.Ri'^{-1}_1$ (-)
1 (original)	Mixed	3.00	15.00	21.00	1.00
2	Primarily forced	3.00	15.00	15.60	0.10
3	Forced	3.00	15.00	15.06	0.01

Checking out several parameter combinations for these three convection regimes quickly imposes too high computational demands. Therefore, this study not only limits the number of parameter possibilities, but also varies only one parameter at a time (i.e. one-at-a-time method). Remind that this simple sensitivity analysis method passes over high-order effects, which are usually not insignificant. For example, in a grid refinement study, the turbulence modelling influences considerably the grid convergence properties. Anyhow, the reference case relies on an intermediate grid resolution, models turbulence with the aid of RNG k-ε model and represents the HESCO nozzle diffuser by the SGM (Figure 4.9). Starting from this, the study evaluates in turn the impact of changing the setting of one of the parameters (i.e. grid, turbulence modelling and diffuser modelling). Details on these parameter settings are part of the next paragraph, which presents an overall picture of the adopted simulation approach.

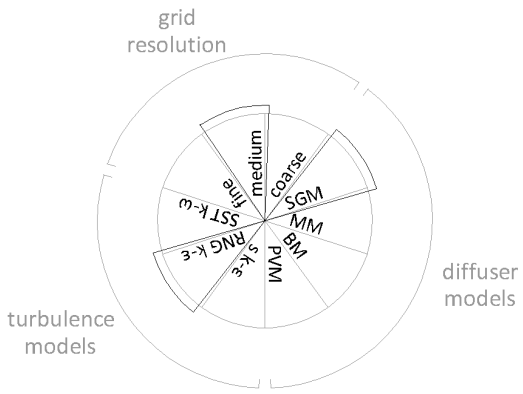

Figure 4.9: Parameter combinations

4.3.2 Simulation approach

Numerical method

Information on CFD-related studies preferably starts with stating which numerical method is used. Underlying study uses the commercial CFD package Fluent 6.3 [201], which relies on the finite volume discretisation process. To linearize the discretised (nonlinear and coupled) equations and to solve the resultant linear equation system, this study uses the included segregated pressure-based solver. In this numerical method, the pressure field comes from a pressure correction equation which is obtained by manipulating the continuity and momentum equations. This way, at each iteration the velocity field corrected by the pressure not only satisfies the momentum equations but also continuity. In this study, the PISO algorithm takes care of this pressure-velocity coupling. Meanwhile, to control the change of variables during the iterative process, Fluent suggests default under-relaxation factors. However, for the cases at hand, in particular the mixed convection regime, these defaults need to be reduced [201].

The simulation model comes in 3-D. This way, the solver can take into account the inherent three-dimensionality of the airflow. Yet, to limit the number of grid cells, a symmetry condition applies to the transversal section: here, the gradients of flow parameters in the normal direction of the surfaces equal zero. After all, the flow asymmetry in the Annex 20 E.2 case shown by, amongst others, Fossdal [316] and Luo et al. [299] is of little account in this inter-model comparison. The grid merely consists of rectangular parallelepipeds, i.e. a special type of hexahedra. Due to this, the lines connecting the midpoints of neighbouring cells are ideally parallel to the respective normal vectors of the cell surfaces, thus, also at walls. Near these wall boundaries, the grid resolution obviously gets high – just like near the air supply and the exhaust. It is created in such a way that the y^+ and Re_y conditions for resolving the boundary layer are met (deduced by trial and error), in all meshes. To test the impact of the grid and possibly to apply generalized RE,

underlying study defines multiple grids. Three grids are systematically coarsened twice, each resulting in a fine, medium and coarse variant (Figure 4.9). A constant non-integer refinement ratio of 1.5 is adopted, in line with the recommendations of Ferziger and Perić [200], Stern et al. [204] and Roache [220]. This results in three triplets, named after their finest resolution variant: 144x81x63, 162x99x72 and 171x99x72. Note that these triplets differ from each other not only in grid resolution, but also in grid distribution. By way of example, Figure 4.10 shows the grid (at the symmetry plane, the floor and the north wall) of the medium variant of triplet 171x99x72. Meanwhile, just because of the finite (volume) representation of the flow equations, the solver needs to replace the variable values at the cell surfaces with values at the cell centres, i.e. the grid points, with the aid of discretisation schemes. The second-order central difference scheme is used for the diffusion terms and the second-order upwind scheme for the convection terms. For that matter, higher-order discretisation schemes for convection, which are usually more difficult to converge, do not necessarily improve the prediction [317]. For the Annex 20 E.2 case, Luo and Roux even found using the higher-order QUICK scheme a great degradation of the results [298]. Further, to interpolate the pressure values at the faces, the PRESTO! scheme comes in. Brief background information on these schemes is in the manual of Fluent [201].

Similarly, the transient terms in the transport equations necessitate temporal discretisation. After all, this study relies solely on time-dependent simulations, even though steady-state boundary conditions prevail. However, the associated time step size is not a part of aforementioned sensitivity study. Some of the grids with a large time step size do not converge (fast enough). Therefore, the sensitivity study defines for all simulations one relatively small time step size, i.e. 0.1s. Random qualitative checks with grids which do converge, show only inappreciable differences with regard to the predicted convective heat fluxes. Meanwhile, all simulations use a second-order implicit time discretisation scheme.

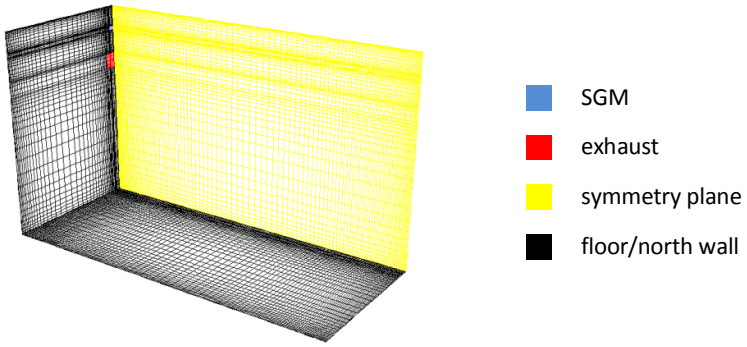

Figure 4.10: Grid of the medium variant of triplet 171x99x72

Turbulence modelling

The second parameter of this sensitivity study is the turbulence model (Figure 4.9). The standard k-ε model of Launder and Spalding [241], the most widely used and validated turbulence model, is part of the parametric set; if only to provide a point of comparison. Next to this, this study includes two more accurate models: the versatile RNG k-ε model of Yakhot and Orszag and the promising SST k-ω model of Menter [257]. All three models are available in the used CFD package, i.e. Fluent. Yet, the two k-ε models require a further specification: that is, the near-wall modelling approach. Recalling that wall functions mess up the convective heat transfer prediction, this study uses the two-layer approach. In this case, the specified HRN k-ε takes care of the turbulent core region of the flow while the one-equation model of Wolfstein [253] resolves the viscosity-affected region.

Boundary conditions: air supply diffuser

The diffuser modelling method makes up the final parameter of this sensitivity study (Figure 4.9). Note that the quantities and calculations discussed in this section mostly apply to the actual configuration while the simulations take only half of the room and, thus, half of the diffuser (model) into account. Only one – not necessarily the optimal – version of each diffuser model is tested, in spite of the plentiful variations. That much is true for the SGM. For example, Heikkinen [288] first represented the HESCO nozzle diffuser as a single rectangular opening with the same effective flow area ($0.00855m^2 \approx 0.045m \times 0.189m$) and aspect ratio (±1/4) as the real diffuser but quickly came up with alternatives. One of them had greater dimensions ($0.062m \times 0.180m = 0.011m^2$) which gave approximately the same maximum velocity at the opening as in the nozzles, that is $3.68m.s^{-1}$, while an increased aspect ratio (±1/3) improved the prediction of the (isothermal) flow field. Yet, underlying study adopts the original approach. Otherwise, the SGM delivers a too high cooling power. Further, the flow is directed upwards at an angle of 40°. Its turbulence intensity assumedly equals 10% [286]. Finally, the air supply temperature is set equal to 15°C. In Fluent, all these properties define the so-called 'velocity inlet boundary condition' – a default type which applies to incompressible flows [201].

The MM represents the diffuser as an opening with the same gross area. However, the momentum flux relies on the actual mass flow rate and the effective flow area. Therefore, this method would necessitate a separate description of the boundary conditions for the continuity and momentum equations, a feature which a commercial CFD package like Fluent does not support. Fortunately, there is a workaround [298]: specifying the total mass flow rate at the air supply opening and adding a momentum source to a volume adjacent to the opening (Figure 4.6). This opening, defined as a 'velocity inlet boundary condition', measures 0.135m by 0.69m and is located 2.13m above the floor, consistent with Heikkinen's suggestion [288]. It supplies at an angle of 40° air at 15°C, at a reduced velocity so that the ventilative cooling rate matches reality. The turbulence intensity is again 10%. The momentum source is defined by some momentum force and a volume. The momentum force is equal to the difference between the effective momentum

and the momentum originating from the simplified opening (see Eq. (4.31)). More specifically, the velocity at the exit of the nozzle opening ($3.68 m.s^{-1}$) and the effective flow area ($0.00855 m^2$) determine the effective momentum and the momentum coming from the simplified opening relies on the area of this opening ($0.135m \times 0.69m = 0.93m^2$) and the velocity derived from the airflow rate ($0.315 m^3.s^{-1} / 0.93 m^2 = 0.34 m.s^{-1}$). The momentum force of the added source is equal to 0.13N. As for the source volume, Luo and Roux [298] determined an optimum dimension for this particular case. They recommended that the dimension of the source cell in the streamwise direction should be between 0.014m and 0.018m. Underlying study picks 0.015m by which the source volume is equal to $0.135m \times 0.69m \times 0.015m = 0.0014 m^3$. As a result, the momentum source defined in Fluent becomes $0.13N / 0.0014 m^3 = 93 N.m^{-3}$ (x-momentum = $71 N.m^{-3}$, y-momentum = $59 N.m^{-3}$, z-momentum = $0 N.m^{-3}$).

The BM is established differently. The procedure starts with defining the box size. Just like Heikkinen [288], Ewert et al. [290] and Srebric [199], this study relies a box of 1.0m x 1.0m x 0.4m (Figure 4.7). Each side surface of the box is defined as a 'symmetry plane'. This means that all the diffuser information is centred on the front surface. What's more, only the velocity profile needs to be specified while the other parameters can be set as uniform [199]. This detailed velocity distribution is really necessary: the x-velocities measured by Heikkinen [300] at x=1.0m under isothermal conditions show that the jet has a strong 3-D feature (Figure 4.11). Coincidentally, aforementioned data should suffice to define the velocity distribution at the front box surface [199, 318]. After all, Figure 4.4(b) indicates that the velocity at x=1.0m is primarily oriented along the x-direction, which permits the use of the x-velocity magnitude. Secondly, the front box surface is assumed to be in the region where the jets have merged and the impact of indoor air and buoyancy forces is still negligible, allowing the use of isothermal data. Following Srebric and Chen [318], underlying study subdivides the front surfaces into 3x3 patches. Each patch gets a normal averaged velocity based on Heikkinen's data. Further, the turbulence intensity equals 10%. The temperature at the box front is derived from the mass/heat balance at the box boundaries (Eq. (4.33)) [318]. As shown in Figure 4.12, $\dot{m}_{sup}$, $\dot{m}_{box}$ and $\Delta\dot{m}$ stand for the mass flow rate through the air supply, the front surface of the box respectively the remaining box boundaries. T_{sup} and T_{exh} correspond to the temperature at the air supply and the exhaust.

$$T_{box} = \frac{\left(\dot{m}_{\text{sup}} \cdot T_{\text{sup}} + \Delta\dot{m} \cdot T_{exh}\right)}{\dot{m}_{box}} \tag{4.33}$$

All the terms on the right-hand side are known prior to the simulations, except for the average exhaust temperature. To determine this last-mentioned quantity, underlying study relies on a theoretical heat balance of the test configuration (Eq. (4.34)). This equation starts from the idea that the exhaust temperature equals the indoor air temperature (ideal mixing). Furthermore, it makes use of the convection coefficients of NBN 62-002 [136]. Obviously, this rough estimate determines to a large extent the practicability of the BM. Ideally, each iteration the simulator

calculates the energy balance for the box volume. Unfortunately, this requires large computational resources. Yet, some test simulations which set this T_{exh} in Eq. (4.33) equal to the temperature obtained at the virtual box boundaries in simulations with the SGM, revealed no significant difference.

$$T_{exh} = \frac{\left[c_{a,\mathrm{sup}} \cdot \dot{m}_{\mathrm{sup}} \cdot T_{\mathrm{sup}} + \sum \left(h_{c,i} \cdot A_i \cdot T_{w,i} \right) \right]}{c_{a,\mathrm{sup}} \cdot \dot{m}_{\mathrm{sup}} + \sum \left(h_{c,i} \cdot A_i \right)} \tag{4.34}$$

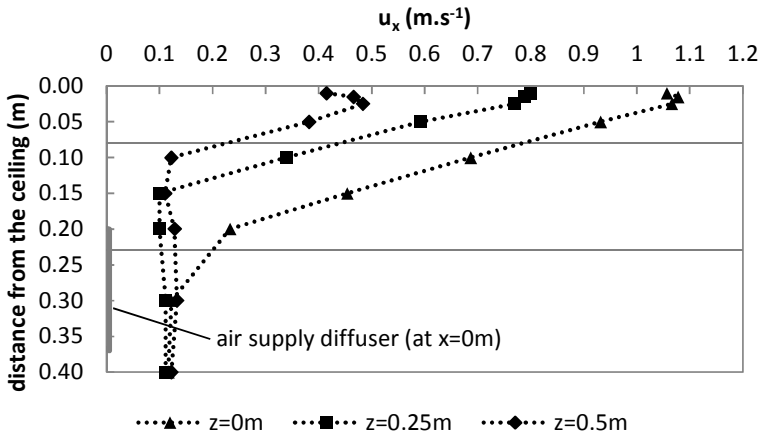

Figure 4.11: Measured velocity magnitude in x-direction at x=1.0m [300]

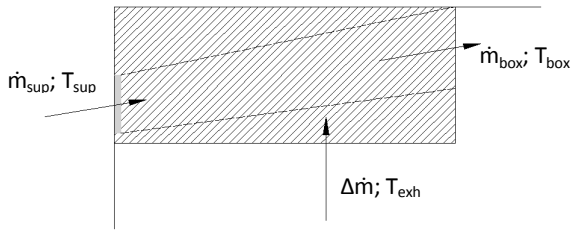

Figure 4.12: Sketch of the theoretical mass/heat balance at the box boundaries

Finally, the PVM is a hybrid of aforementioned approaches and, thus, needs little explanation. A simple 'velocity inlet opening' similar to the SGM brings in the correct ventilative cooling rate while the x-direction velocities measured by Heikkinen [300] are defined in a plane 1m away from the diffuser (see BM).

Boundary conditions: exhaust

A 'pressure outlet boundary condition' represents the exhaust. At the opening the gauge pressure is set as zero using the Dirichlet condition. This type of boundary condition specifies the values a solution needs to take on the boundary of the domain. Luo and Roux [298] also tested the Neumann condition, which specifies the values that the derivative of a solution is to take on the boundary. They found no difference between the predictions. Yet, Fluent [201] recommends the Dirichlet condition as it offers better stability and convergence. In case of backflow, the air supply temperature of the exhaust equals the value obtained with Eq. (4.34) while the turbulence intensity is assumed to be 1% [298].

Boundary conditions: surface boundary

The wall boundary conditions bound fluid and solid regions. For viscous flows, Fluent specifies by default the no-slip boundary condition. Meanwhile, this study imposes a fixed wall surface temperature, in accordance with Table 4.3.

Material properties

A final step in setting up the model is defining the physical properties of the air. In this case, these properties include: viscosity, heat capacity, thermal conductivity and density. All are assumed to be temperature-dependent, but not necessarily in a similar fashion. This study considers viscosity, heat capacity and thermal conductivity just as piecewise-linear functions of temperature. On the other hand, things get more complicated when considering the air density. As previously mentioned, indoor air behaves like an incompressible fluid. This implies that the pressure variations are so small that the density remains unaffected. However, the temperature (and concentration) variations do affect the density. Therefore, the conservation equations still need to take a variable density into account. To this end, CFD provides two approaches: the Boussinesq approximation and the incompressible ideal gas model. The first one is very popular because of its robustness. This method treats density as a constant in all equations but one: only the buoyancy term in the momentum equation includes a linear relation between temperature and density. However, this Boussinesq approximation is only valid for cases with (undefined) small temperature differences. Therefore, the second approach gets preference. The incompressible ideal gas model includes the influence of temperature (and concentration) variations on the density in all conservation equations while neglecting the effect of pressure variations. As shown by Eq. (4.35), the density relates the universal gas constant R, the molecular weight of the gas M and the temperature T only to the operating pressure p_{op} and not to the local relative pressure field. This operating pressure p_{op} is equal to the atmospheric pressure (101325Pa).

$$\rho = \frac{M \cdot p_{op}}{R \cdot T} \tag{4.35}$$

4.3.3 Results

Grid convergence study

Every solid CFD study starts with assessing the influence of the computational grid on the prediction(s) [191]. Because of the large computational expense it is difficult to obtain a grid independent solution. Instead, CFD users should trace the grid convergence. This implies that the solution asymptotically approaches the exact solution to the governing equations. A sufficiently fine grid then means that further refinement only results in a marginal improvement of the solution. Unfortunately, many CFD users take this (too) literally. They just compare the results on two to three randomly chosen grids, hoping for the best. However, there is a growing body of opinion that CFD users should at least try a more systematic grid convergence assessment like generalized RE [228, 229]. The resulting estimates of the discretisation error and of the exact solution are particularly useful in validation exercises (e.g. code validation) and comparative studies (on e.g. turbulence modelling, diffuser modelling). That is why underlying preparatory grid convergence study initially applies generalized RE. It actually explores – as previously mentioned – nine grids, making up three triplets, for a single convection regime, i.e. mixed convection (Table 4.3).

Obviously, generalized RE requires a check on the applicability conditions beforehand. As explained in section 4.2.1, the solutions should be first and foremost in the asymptotic range. This implies that Eq. (4.14) holds. Yet, in practice, some relative differences are tolerable. This study postulates a maximum arbitrarily chosen difference of 10%. Another, more stringent condition is that the solutions should be monotonically convergent. Such solution behaviour generally corresponds to a ratio of solution changes between zero and one. Table 4.4 displays these two assessment criteria for point variables as well as (derived) integral quantities obtained from the three triplets. The reminder at the bottom retakes the classification of the solution behaviour as in Figure 4.1 and clarifies when the solutions are close to the asymptotic range. First, the deviant solution behaviour of triplet 162x99x72 strikes the eye. Almost every mentioned quantity displays divergent behaviour, which prohibits generalized RE. Without doubt, this originates more likely from a poor grid distribution than from insufficient grid resolution. The grid density near the air supply is significantly lower in case of triplet 162x99x72, which causes problems in particular for the coarse grid(s). By contrast, triplets 144x81x63 and 171x99x72 – of which the grid distributions are more alike – exhibit more promising results. The ratio of solution changes of almost all local air temperatures are between zero and one while most integral quantities show either oscillatory or monotonic convergence. Moreover, the relative difference Δ_r is usually (much) lower than 10% and, thus, most (monotonically convergent) solutions are close to the asymptotic range. However, attaining monotonic convergence for local velocities proves to be hard. Considerable velocity fluctuations hinder from applying generalized RE. After all, the outcomes mentioned here (and the ones to come) are not based on averages over time, but rely on instantaneous readings because of the unstable behaviour

and the laborious convergence of the simulations on low-density grids. Applying higher grid resolutions was unfortunately impossible at the time. Nevertheless, grid convergence not only depends on the grid resolution but also on the grid distribution and the selected quantity – as previously mentioned.

Table 4.4: Ratio of solution changes R and difference from the asymptotic range Δ_r

	144x81x63		162x99x72		171x99x72	
	R	Δ_r	R	Δ_r	R	Δ_r
T_a@1.4;1.0;0	0.2	**0%**	-0.8	n/a	1.0	**0%**
T_a@1.4;1.0;1.0	0.3	**0%**	-1.2	n/a	0.2	**0%**
T_a@1.4;2.0;0	0.4	**0%**	-1.6	n/a	0.8	**0%**
T_a@1.4;2.0;1.0	0.0	n/a	6.6	n/a	-5.5	n/a
T_a@3.0;1.0;0	0.2	**0%**	-2.0	n/a	0.2	**0%**
T_a@3.0;1.0;1.0	0.3	**0%**	-1.8	n/a	-0.4	n/a
T_a@3.0;2.0;0	0.5	**1%**	-0.8	n/a	0.7	**0%**
T_a@3.0;2.0;1.0	0.1	**0%**	6.8	n/a	0.3	**0%**
u@1.4;1.0;0	1.4	n/a	4.4	n/a	1.2	n/a
u@1.4;1.0;1.0	15.1	n/a	65.4	n/a	10.4	n/a
u@1.4;2.0;0	1.7	n/a	3.3	n/a	0.1	**2%**
u@1.4;2.0;1.0	2.1	n/a	0.5	26%	-135.3	n/a
u@3.0;1.0;0	-1.0	n/a	-2.7	n/a	4.9	n/a
u@3.0;1.0;1.0	-1.4	n/a	-5.6	n/a	-2.7	n/a
u@3.0;2.0;0	0.1	**3%**	2.5	n/a	3.8	n/a
u@3.0;2.0;1.0	-1.4	n/a	-5.6	n/a	-2.7	n/a
$T_{a,avg}$	0.2	**0%**	-1.7	n/a	-0.1	n/a
$(T_{exh}-T_{sup}).(T_w-T_{sup})^{-1}$	0.4	**1%**	-1.5	n/a	-0.2	n/a
$Q_{conv,ceiling}$	-0.7	n/a	3.9	n/a	5.3	n/a
$Q_{conv,floor}$	2.0	n/a	0.6	**7%**	0.4	**7%**
$Q_{conv,north}$	0.1	**0%**	-6.7	n/a	-1.3	n/a
$Q_{conv,south}$	0.5	11%	1.2	n/a	0.7	**6%**
$Q_{conv,west}$	-0.7	n/a	-0.1	n/a	-0.1	n/a

Ratio of solution changes	Interval	Behaviour	Fill
$R=\frac{(f_2-f_1)}{(f_3-f_2)}$	$0 < R < 1$	monotonic convergence	
	$\lvert R\rvert > 1$	divergence	
	$R < 0$	oscillatory behaviour	

Asymptotic range when	Marking
$\Delta_r < 0.10$ in $\varepsilon_{D,1} = (1 \pm \Delta_r) \cdot \frac{\varepsilon_{D,2}}{r^p}$ (see Eq. (4.14))	**bold**

The above analysis indicates the feasibility of the three triplets to provide an error band and an exact value estimate with the aid of generalized RE. Yet, it does not show how the solutions on the nine grids actually relate to each other. To explore this, the two graphs part of Figure 4.13 depict, by way of example, boxplots (min, 25%, median, 75%, max) of the air temperature along two verticals predicted by the nine grids. Also the results of the medium grid of triplet 171x99x72 and where possible the corresponding error bands defined by the GCI and the exact value estimates are included. Further, the right-hand side of each graph sketches the grid distribution of aforementioned grid and the position of the air supply (SGM) and the exhaust. First of all, the relatively small spread is conspicuous. The $25^{th}/75^{th}$ percentile deviates from the median by at most 0.1°C. At the same time, the minimum outlier stands out. Furthermore, many air temperatures in the symmetry plane enable to apply generalized RE, whereas along vertical x=3.0m;z=1.0m the applicability conditions hold merely on five grid lines. Actually, the grid expands pretty fast in the z-wise direction, resulting in a too coarse grid near vertical x=3.0m;z=1.0m. This indicates that the promising grid convergence for local air temperatures as observed in Table 4.4 is not necessarily persistent. As a consequence, integral quantities assumedly have the best chance of exhibiting grid convergence. Finally, the estimated exact temperatures are usually higher than the ones predicted by the respective grids.

Figure 4.14 examines the matter further by setting the predicted temperature and velocity at x=3.0m;y=1.0m;z=1.0m and the convective heat flux at the south wall against the total number of points of the respective nine grids. The predictions are grouped according to the grid triplet while the colouring indicates the solution behaviour and the line thickness the difference from the asymptotic range, as in Table 4.4 (further note the resemblance with Figure 4.1). At the same time, a boxplot (min, 25%, median, 75%, max) on every right border briefly expresses the spread and the skew of the data and helps to identify the outliers. Finally, every graph includes on the right-hand side, when possible (i.e. triplet close to the asymptotic range and monotonically convergent), the estimated exact value (based on Eq. (4.10)) and the error band defined by the GCI (based on Eq. (4.11) and Eq. (4.15)) on the medium grid of triplet 171x99x72. A look at the boxplots reveals that the spread of the velocity predictions exceeds the others by far, in two ways. On the one hand, most of the predicted velocities deviate more from the median in relative terms. On the other, the minimum/maximum velocities are not so far off from the $25^{th}/75^{th}$ percentile. Again, the use of instantaneous readings is probably involved. What's more, triplet 144x81x63 mostly causes the outliers. Especially its coarse grid solution differs from the others, whereas the fine grid solutions are more alike (except for the ones of u@3.0;1.0;1.0). This means that the grid distribution becomes more important when the grid resolution diminishes. Yet, if generalized RE is possible, the mentioned finer grid solutions can still deviate strongly from the estimated exact value. For example, the convective heat flux prediction on the medium grid of triplet 171x99x72 exhibits a considerable GCI. Unfortunately, this is the maximum feasible grid resolution for the sensitivity analysis to come. Moreover, as this grid does not enable to apply generalized RE for all quantities of interest, the following refrains from stating the error bands.

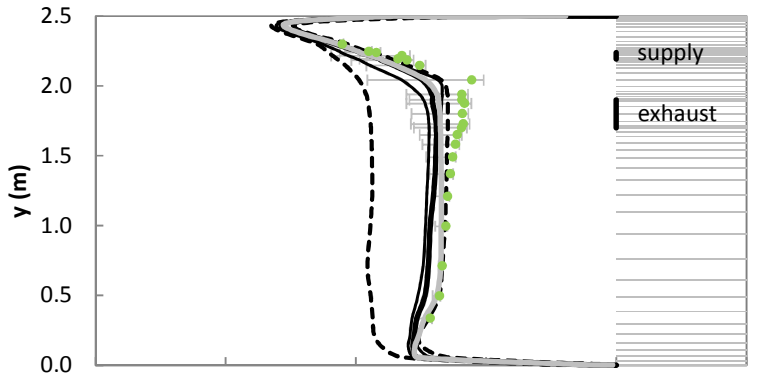

(a)

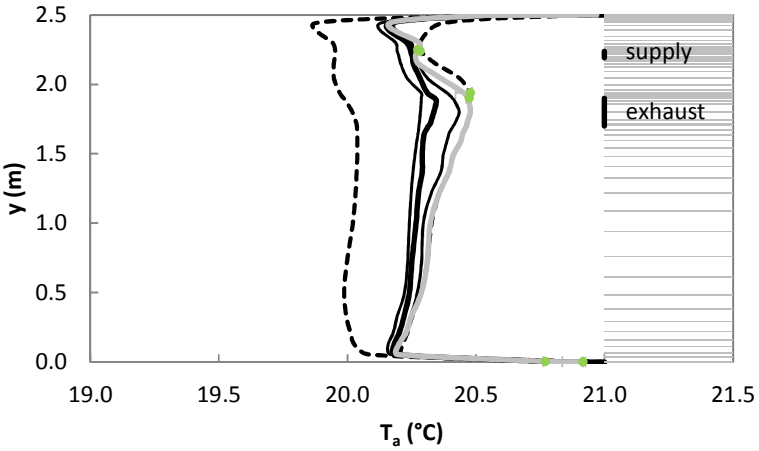

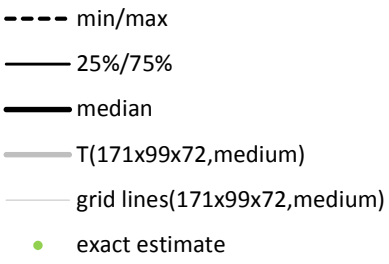

(b)

Figure 4.13: Air temperature along (a) x=3.0m;z=0m and (b) x=3.0m;z=1.0m based on nine grids

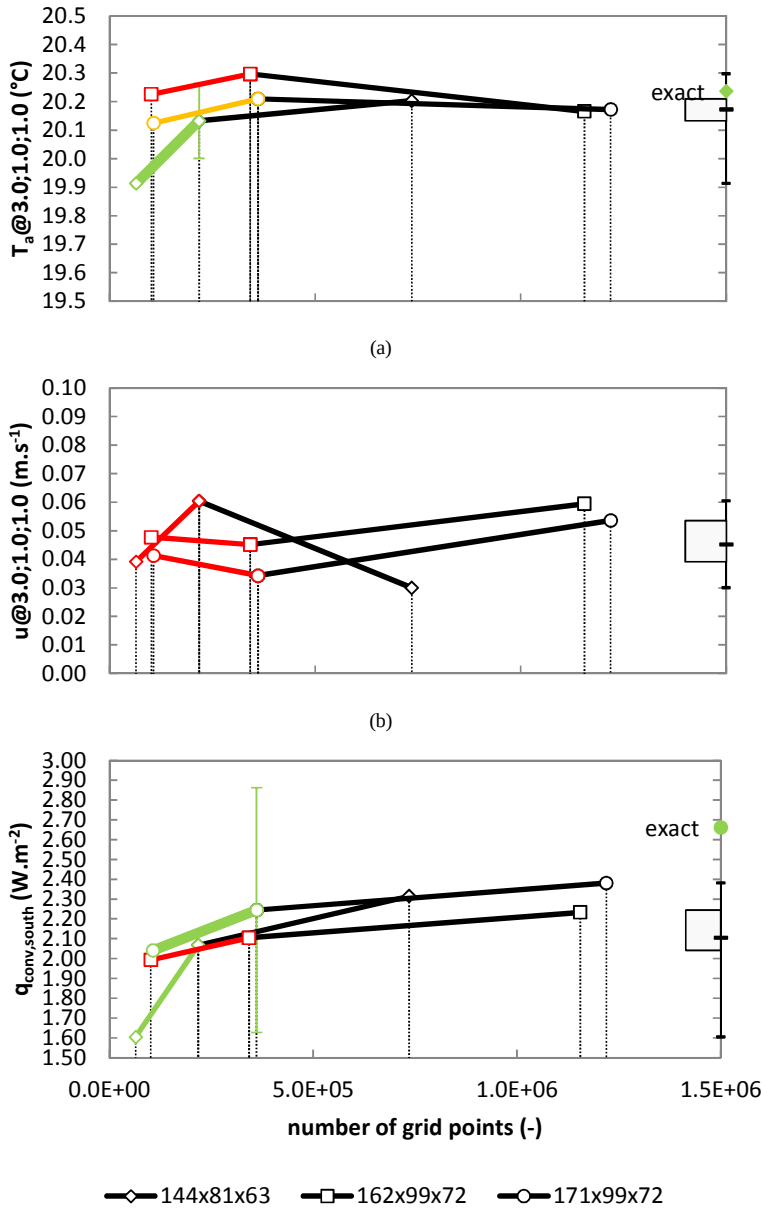

Figure 4.14: (a) Air temperature at x=3.0m;y=1.0m;z=1.0m, (b) velocity at x=3.0m;y=1.0m;z=1.0m and (c) convective heat flux at the south wall for nine different grids (the colours indicate the solution behaviour as in Table 4.4)

Sensitivity analysis

The centrepieces of this section are Figure 4.15 and Figure 4.16. Both assess the sensitivity of the convective heat flow predictions to the simulation approach for the three studied convection regimes. However, each figure takes a slightly different approach. On the one hand, Figure 4.15 highlights the importance of the studied simulation categories, i.e. grid (grid), turbulence modelling (turb) and diffuser modelling (diff). To this end, the graphs only comprise the results of the reference case (i.e. medium grid of 171x99x72, RNG k-ε model and SGM) and the minimum/maximum predictions. Figure 4.16, on the other hand, shows full details on all mentioned simulation choices. The left y-axis depicts the total figures (dashed line bars) while the right y-axis holds the internal distribution (full line bars). The marking on the right of each column represents the relation to the reference case. For that matter, the convective heat flow at the ceiling excludes the heat transfer at the (virtual) box surface (Figure 4.7), to enable a consistent comparison of the diffuser models. Yet, the convective heat flow at the ceiling would be at least 1.5 times as large when the whole of the ceiling was taken into account. To help explain the tendencies in aforementioned graphs, Figure 4.17 shows for all studied convection regimes how the simulation choices influence the air temperature and the velocity magnitude along vertical x=3.0m;z=0. Also Figure 4.18 improves understanding, this time by plotting the predicted velocity decay of the jet along horizontal y=2.45m;z=0. Further, Figure 4.19 and Figure 4.20 display the temperature respectively velocity magnitude contours for convection regime $Ri'_x.Ri'^{-1}_1=1.00$. In short, the profiles in Figure 4.17 and Figure 4.18 assess the influence of the simulation approach quantitatively while the contour plots in Figure 4.19 and Figure 4.20 provide a qualitative yet richer inspection.

At first, Figure 4.15 gives the impression that, irrespective of the convection regimes, the convective heat flow distribution shows the following order: Q_{conv} at the ceiling at the top, followed by the convective heat flows at the south wall, the west wall and the floor and finally the one at the northerly wall. However, closer inspection reveals various sensitivities. First, the solution intervals of the convective heat flows at the ceiling and at the west wall clearly increase as the ratio $Ri'_x.Ri'^{-1}_1$ approaches 1.00. As a matter of fact, the increasing buoyancy deflects the jet from the ceiling, by which the jet actually spreads more. So, both turbulence modelling and diffuser modelling (the grid is not considered here) become more important as the mechanism of fluid flow tends towards mixed convection (see min/max). Next to this, the convective heat flow predictions at the ceiling and at the south wall exhibit the largest solution intervals. The diffuser modelling approach actually influences the predictions more than the grid and the – even less important – turbulence modelling approach do. So, it is not surprising that the convective heat flow at a surface along/on which the jet flows/impinges, is particularly sensitive to the simulation approach. Logically, the north wall which is directed away from the jet, experiences the least impact. Further, the reference case, with the SGM, usually predicts the lowest convective heat flow of the diffuser modelling approaches, except at the ceiling.

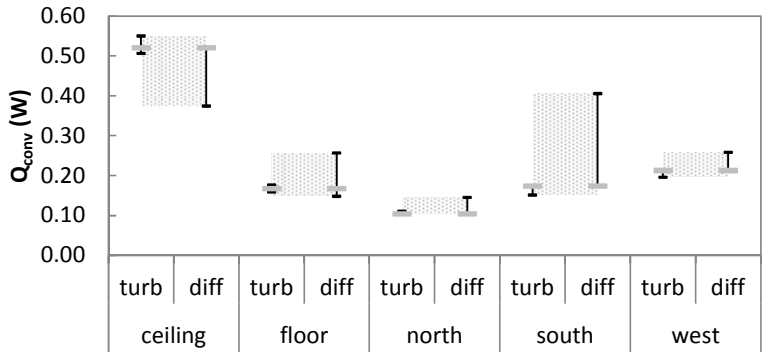

(a)

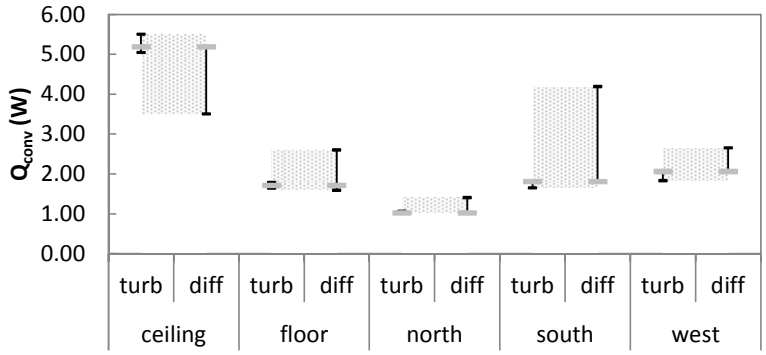

(b)

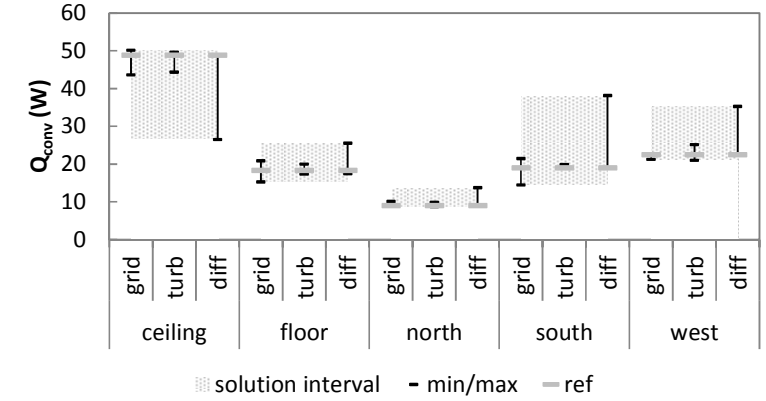

(c)

Figure 4.15: Sensitivity of the convective heat flow to the respective studied simulation approach categories for (a) $\underline{Ri'_x.Ri'^{-1}_l=0.01}$, (b) $\underline{Ri'_x.Ri'^{-1}_l=0.10}$ and (c) $\underline{Ri'_x.Ri'^{-1}_l=1.00}$

Figure 4.16 indicates that these last findings actually hold true for all simulation cases which comprise the SGM. Another grid or a different turbulence model actually matters little. The SGM introduces a small air jet, which impinges upon the ceiling with a still high velocity magnitude (Figure 4.19, Figure 4.20). The subsistent high mixing leads to a rapid velocity decay, in all three convection regimes (Figure 4.18). However, the small jet, assisted by the Coanda effect, spreads along the ceiling in the x- and the z-direction and reaches the south wall for then to deflect to the floor and the west wall (Figure 4.19, Figure 4.20). The PVM, on the other hand, unexpectedly leads to a similar total convective heat flow. Even more striking is the reduced convective heat flow at the ceiling (Figure 4.16). After all, the increased velocity level (Figure 4.17, Figure 4.18, Figure 4.20) indicates otherwise. However, the path lines of virtual particles released from the air supply (not shown here) reveal that, next to increasing the velocity magnitude, the x-specification of the velocities in a plane 1m away from the diffuser also redirects the jet. Because of this, the jet impinges to a larger extent upon the south wall (higher Q_{conv} at the south wall), yet it leaves some part of the air near the ceiling undisturbed (lower Q_{conv} at the ceiling). The cases which exhibit the most deviant behaviour are the ones with the MM and the BM. The convective heat flow at the ceiling is far less, the distribution of the convective heat flows depends strongly on the convection regime and the total convective heat flow is always a cut above the results of other diffuser models. And this while both the MM and the BM generally outperform (that is to say, in terms of accuracy) the previous two diffuser models. The BM actually best approximates the HESCO nozzle diffuser – were it not that the upfront estimate of the air supply temperature might result in the wrong cooling power (see section 4.3.2). Therefore, the cases with the MM and the BM merit particular attention. The MM introduces, in comparison with the SGM, a thicker jet (in y- and z-direction) with a lower momentum. This leads to less mixing in the stagnation zone and, thus, a smaller velocity decay (Figure 4.17, Figure 4.18). Yet, the strong directionality of the jet limits the convective heat flow at the ceiling (cf the PVM). Over and above this, the increasing buoyancy results in a larger spread in the y- (and the z-)direction (Figure 4.17). The fractions of the convective heat flow at the ceiling and the one at the south wall then decrease in favour of the ones at the other surfaces (Figure 4.16). As a matter of fact, in spite of the increasing buoyancy, the relative increase of the total convective heat flow (in comparison with the reference case) remains unchanged at 109%. Similar causes explain the comparable results obtained with the BM. However, this diffuser model magnifies the tendencies: an even lower convective heat flow at the ceiling, a larger sensitivity of the distribution to the convection regime and a constant relative increase of the total convective heat flow of 120% instead of 109%.

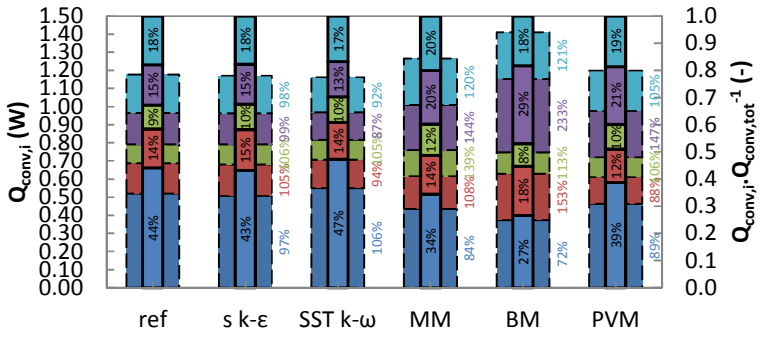

(a)

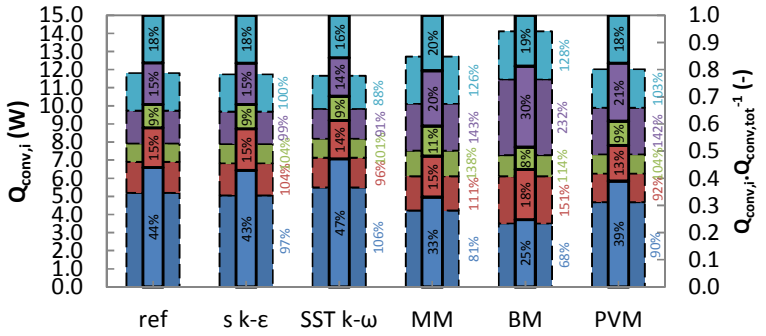

(b)

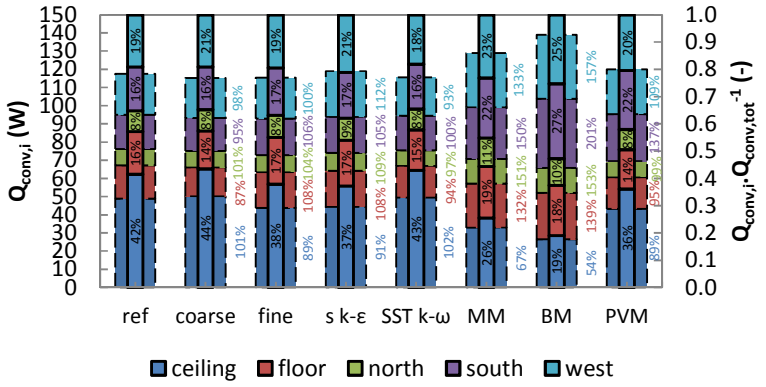

(c)

Figure 4.16: Sensitivity of the convective heat flow to the respective simulation choices for (a) $\underline{Ri'_x.Ri'^{-1}_1=0.01}$, (b) $\underline{Ri'_x.Ri'^{-1}_1=0.10}$ and (c) $\underline{Ri'_x.Ri'^{-1}_1=1.00}$ (black percentages apply to $Q_{conv,i}.Q_{conv,tot}^{-1}$; coloured percentages indicate how the $Q_{conv,i}$ of the respective cases relate to the ones of the reference case)

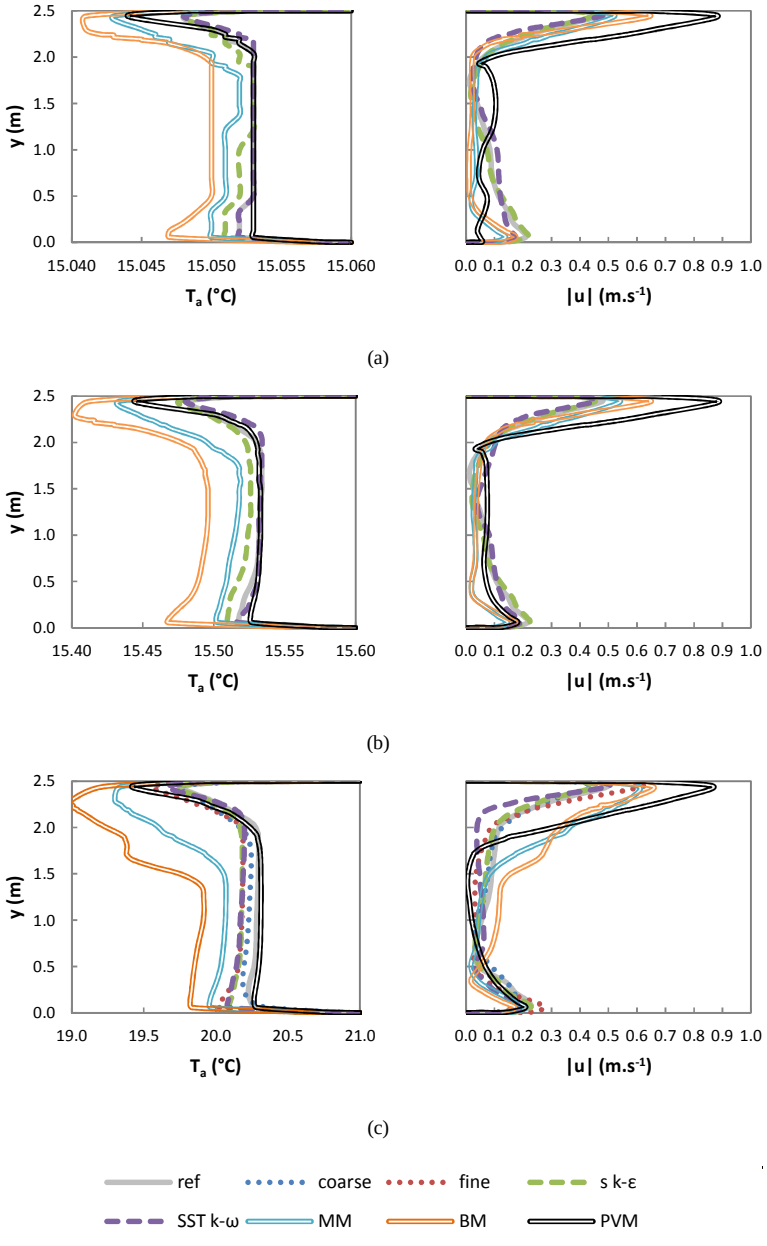

Figure 4.17: Air temperature and velocity magnitude at x=3.0m;z=0 for (a) $\underline{Ri'_x.Ri'^{-1}_1}$=0.01, (b) $\underline{Ri'_x.Ri'^{-1}_1}$=0.10 and (c) $\underline{Ri'_x.Ri'^{-1}_1}$=1.00

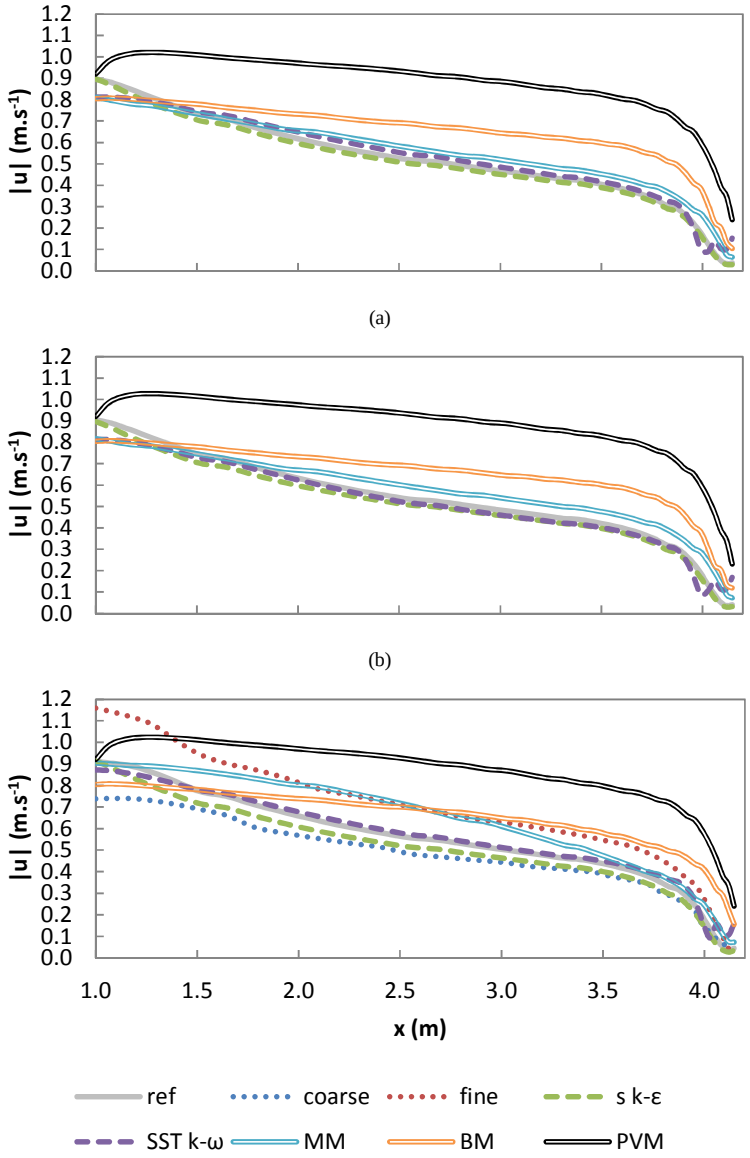

Figure 4.18: Velocity decay at y=2.45m;z=0
for (a) $\underline{Ri'_x.Ri'^{-1}_1=0.01}$, (b) $\underline{Ri'_x.Ri'^{-1}_1=0.10}$ and (c) $\underline{Ri'_x.Ri'^{-1}_1=1.00}$

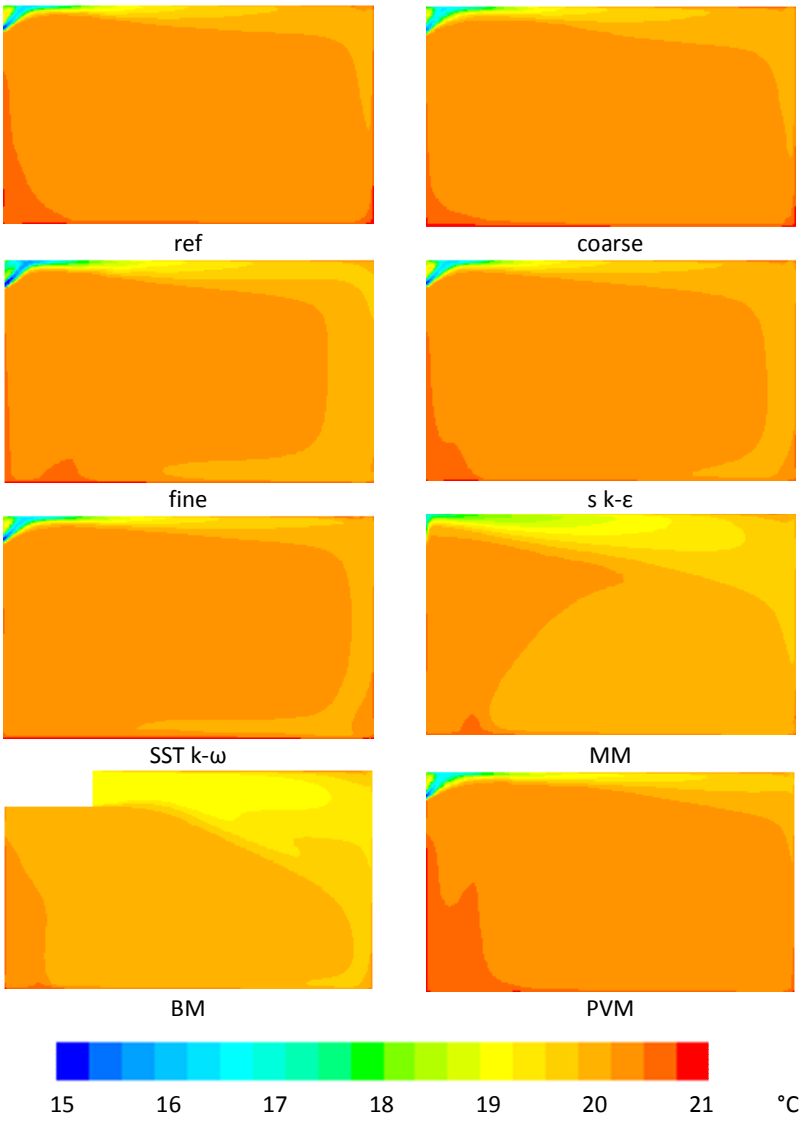

Figure 4.19: Temperature contours at the symmetry plane for $Ri'_x.Ri'^{-1}_1=1.00$

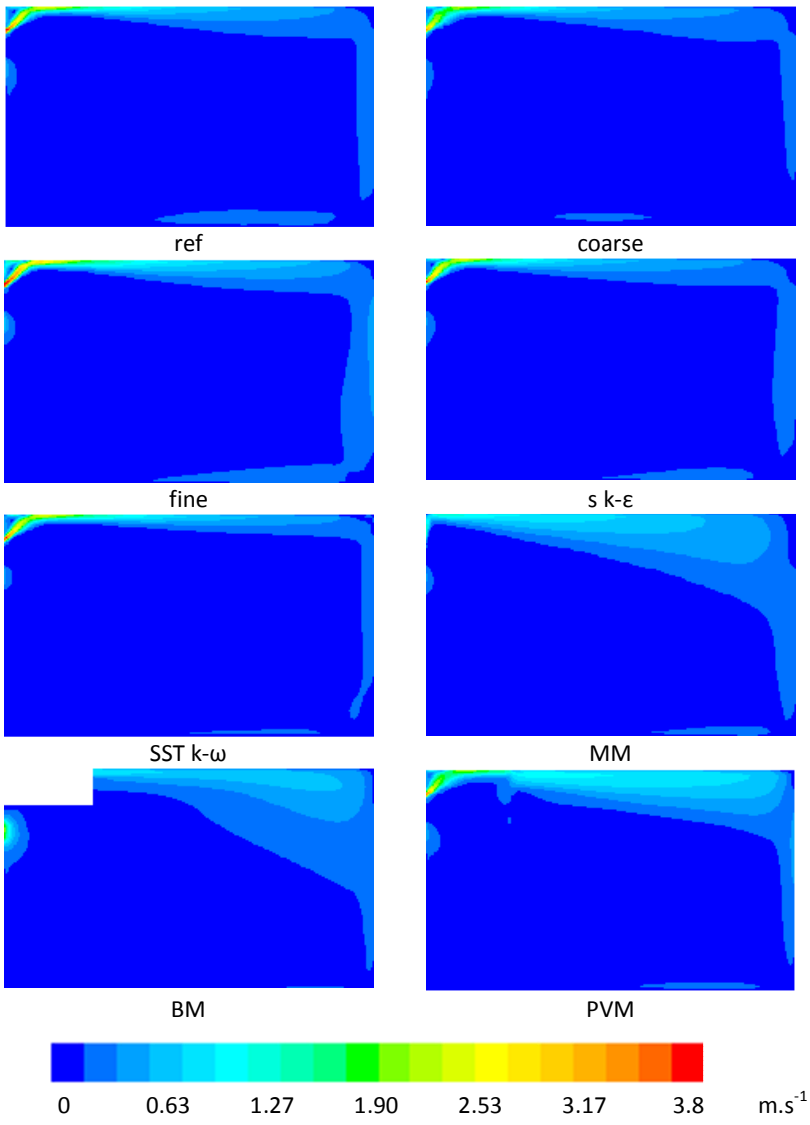

Figure 4.20: Velocity magnitude contours at the symmetry plane for $Ri'_x.Ri'^{-1}_1=1.00$

4.3.4 Conclusions: establishing a proper simulation approach is difficult but important

The above grid convergence study showed that uncertainty estimation based on generalized RE is anything but easy. First fulfilling the applicability conditions is difficult. As a matter of fact, the convergence properties depend on more than just the grid resolution. For example, a proper grid layout helps to economize on the grid resolution and consequently multiplies the chances of success. Or derived integral quantities are less sensitive to an inadequate local grid distribution and, thus, usually exhibit sooner the desired asymptotic solution behaviour. And well, if some quantities fulfil the requirements, the resulting uncertainty estimates are fairly large. So, it is not surprising that many authors rely rather on a qualitative evaluation of the results on two or three randomly chosen grids.

Yet, the subsequent sensitivity analysis revealed that the grid is not necessarily the greatest concern. In this study, the diffuser modelling approach influences the predictions considerably more than the grid or the turbulence modelling approach do. And this holds true as long as the jet dominates the indoor airflow pattern (i.e. roughly from forced to mixed convection). What's more, the two assumedly most accurate diffuser models, i.e. the MM and the BM, are particularly sensitive to the increasing buoyancy. That is to say, the relative increase of the total convective heat flow remains unchanged, but the distribution of the convective heat flows changes substantially. All things considered, CFD users have to consciously weigh up the simulation options for the case at hand, including the ones which take considerable effort to implement (like the BM). Now, taking the outcomes of the literature review and of the sensitivity analysis for granted, the simulation study on how the design of a generic landscape office affects the convective heat flux during night cooling can start. This study is described in the next chapter.

5

Global surrogate-based optimization of room/system design

This chapter deals with the extensive simulation study on a generic night cooled landscape office. The goals are to provide more insight into how the room/system design of a landscape office affects the convective heat transfer during night cooling and to find optimal design solutions. To this end, the author deploys surrogate modelling to drive an optimization procedure. The first section introduces the concept of this surrogate-based optimization and explains why it is so useful for this study. Next, the chapter discloses the experimental design. This includes a description of the simulation experiment setup, an overview of how the geometry/grid generator, the CFD solver and the surrogate modelling software all fit together and details on both the CFD simulation approach and the surrogate modelling. The chapter concludes with an in-depth discussion of the simulation results. This chapter was submitted in adapted form to the Building and Environment Journal [319].

5.1 Engineering via surrogate modelling

Experienced CFD users can accurately extract the convective heat flux from CFD simulations indeed. Yet the large computational demands of CFD remain a major stumbling block. As a consequence, even though conflating BES with CFD is technically possible (e.g. [102, 320, 321]), it is a dead letter in rapid building design. Without doubt, researchers and software developers work hard on ways out. However, they will probably not succeed overnight. In the meantime, deploying CFD to investigate the convective heat flux in specific case problems

can provide new insights and might inspire other studies. Yet, still it is necessary to limit the number of simulations. After all, already a limited number of variables makes the parameter space of a design problem grow rampant (i.e. the so-called curse of dimensionality). One popular way is to apply approximation methods to produce a model which to some extent comes close to the (unknown) reference model. In particular the so-called data-driven approximation methods are prevalent: they disregard the dynamics of the deterministic simulation model (or better, simulator) and focus on the input-output relationship. The drawback is that they lack traceability. Data-driven modelling is also often referred to as black-box modelling, response surface modelling, metamodelling, behavioural modelling or surrogate modelling and can be subdivided into forward and inverse surrogate modelling. Classic forward surrogate modelling approximates the response of the simulator to a set of design parameters while inverse surrogate modelling starts from the target performance and tries to find the corresponding input values. Another distinction of surrogate modelling relies on whether the surrogate model itself is the goal (global) or it is used to drive an optimization (local). Obviously, also intermediate forms, taking the best of global and local modelling, exist. One such popular example is global surrogate-based optimization (SBO). This procedure iteratively scans the complete design space for new data points which provide the greatest information gain. This way, it enhances concurrently the global accuracy of the surrogate model (exploration) and the accuracy near optima (exploitation); through fewer simulations. Yet, the goal of global SBO remains optimization; the surrogate model is merely a bonus. Readers looking for more details on surrogate modelling are referred to the reference works of Keane and Nair [322], Forrester et al. [323] and Gorissen [324].

The workflow of surrogate modelling is, according to Meckesheimer [325], always pretty much the same: (1) model formulation (requires defining design objectives, and identifying input and output parameters), (2) design selection (requires choosing the type of experimental design), (3) metamodel fitting (requires specifying the type and functional form of the surrogate model), (4) assessment of the surrogate model (requires specifying the performance criteria as well as choosing an appropriate validation strategy), (5) gaining insight from the surrogate model (merely to understand the behaviour of the reference model or to redefine the region of interest) and (6) using the surrogate model to explore trade-offs, to optimize the design… However, interpretation of each step varies from case to case. The seemingly interminable number of interdependent possibilities, having all their merits and demerits, even challenges experts in the field; let alone laymen like engineers. Last-mentioned group of people merely want a globally/locally accurate surrogate model as fast as possible, with minimal overhead [326]. Guidance on selecting and setting up such techniques or perhaps even a ready-made computer program is no luxury for them. One such convenient computer tool connecting the two worlds is the Matlab surrogate modelling (SUMO) toolbox [327]. Basically, this toolbox drives a simulator to produce a surrogate model within the accuracy and time constraints set by the user. It incorporates for each step of the surrogate modelling process numerous plugins (microkernel design), which are all easily configurable through a central XML file.

Of course, it allows to add, remove or replace these components. Further, the SUMO toolbox provides extensive logging and profiling capabilities, which helps to track the modelling process and to understand the modelling decisions. At the latest, a graphical user interface tool enables to visually explore the model, assess its quality and export it for use in other software. Successful applications of the SUMO toolbox are plentiful: e.g. aerodynamic modelling [328], automotive data modelling [329], blood flow data modelling [330], optimization of microwave filters and identification of electrical properties of textile antennas [331].

Underlying study is just another such application, now in building engineering. It intends to find with the aid of a global SBO procedure how the room/system design of a generic landscape office influences the convective heat flux during night cooling and which design solutions are most profitable. After all, night cooling is frequently applied in landscape offices, because they are unoccupied at night and require a limited additional investment costs [56]. To this end, a fully-automated framework of data sampling (SUMO), geometry and grid generation (Gambit [201]), CFD solving (Fluent [201]) and surrogate modelling (SUMO) generates several surrogate models. These surrogate models indicate how the convective heat flux in the night cooled landscape office relates to several room/system design parameters, which are subdivided into ventilation concept, thermal mass distribution, geometry and driving force for convective heat transfer. Strictly speaking, these surrogate models merely guide the data sampling towards the global optimum. Yet, they can also provide additional rough-hewn insights into the global behaviour. Where necessary, the analysis relies on airflow parameters to explain the observed tendencies. Next to this, these surrogate models can help to improve BES modelling in two ways. They indicate profitable design solutions for which new convection correlations can be derived (possibly with the aid of CFD-based surrogate modelling). Or derived more globally accurate surrogate models can be coupled with BES.

5.2 Experimental design

5.2.1 Simulation experiment setup

Annex 20 2-D case as a starting point

Landscape offices usually have a large longitudinal section compared with the crosscut. This often brings along the use of line-shaped diffusers and band windows. All in all, this leads, roughly speaking, to 2-D airflow patterns, influenced by 3-D eddies. Meanwhile, 3-D simulations render underlying study computationally infeasible. So, it is not a bad choice to limit the problem to a 2-D case. As a matter of fact, this study starts from the well-elaborated 2-D Annex 20 case [194].

This simple case dates back to the scale model experiments of Schwenke [332] in the mid-seventies of the previous century, but not until the early nineties it found acceptance as a valuable benchmark. Since then, numerous researchers have made use of it. References [268, 271, 273, 333, 334] are merely a smattering of examples found on www.cfd-benchmarks.com [335]. Figure 5.1 depicts this Annex 20 2-D setup (note that Schwenke used dimensionless variables to describe the case). Basically, it concerns a rather long (L_r/H_r=3.0) and wide (W_r/H_r=1.0 or 4.7) ventilated room having on either side a wall-to-wall opening. The air supply on the left side is merely a rather high channel (h_{sup}/H_r=0.056), which obviously differs from practical diffusers. However, this simple description leads to a fully-developed flow between two walls, which in simulations does not necessitate an approximating diffuser model (cf chapter 4) and still relaxes the number of grid points near the opening [336]. Meanwhile, the height of the exhaust opening h_{exh} is to the height of the room H_r as sixteen is to one. The air supply conditions for the velocity are given by Eq. (5.1). Further, Eq. (5.2) and Eq. (5.3) give the air supply conditions for the turbulent kinetic energy k and the dissipation rate ε, which correspond to a turbulence intensity I of 4%.

$$\mathrm{Re} = \frac{h_{sup} \cdot u_{sup}}{\nu} = 5000 \tag{5.1}$$

$$k = \frac{3}{2} \cdot \left(u_{sup} \cdot I\right)^2 \tag{5.2}$$

$$\varepsilon = 0.09^{3/4} \cdot \frac{k^{3/2}}{l} \quad where \quad l = \frac{h_{sup}}{10} \tag{5.3}$$

The case with all enclosure surfaces at 20°C ties in with the so-called Annex 20 2-D1 case: isothermal flow at a Reynolds number of 5000 in a room with H_r=3.0m (air change rate n equal to $10.2h^{-1}$). Here, the obvious benchmark focus is the velocity (at the midplane, i.e. where edge effects assumedly are of little account, $x=H_r$, $x=2H_r$, $y=0.5h_{sup}$, $y=H_r-0.5h_{sup}$). On the other hand, the reference case with a constant heat flux added along the floor – which is raised in succeeding experiments – represents the Annex 20 2-D2 case: representative of summer cooling at a range of Richardson numbers and a Reynolds number equal to 5000 in a room with H_r=3.0m (air change rate n equal to $10.2h^{-1}$). Critical factor in this experimental campaign is the impact of the Richardson number (Eq. (5.4)) on the jet penetration. Now the streamlines at the midplane act as a reference. Also underlying study relies on these data to validate the CFD simulation approach.

$$Ri = \frac{\beta \cdot g \cdot h_{sup} \cdot \left(T_w - T_{sup}\right)}{u_{sup}^2} \tag{5.4}$$

(a)

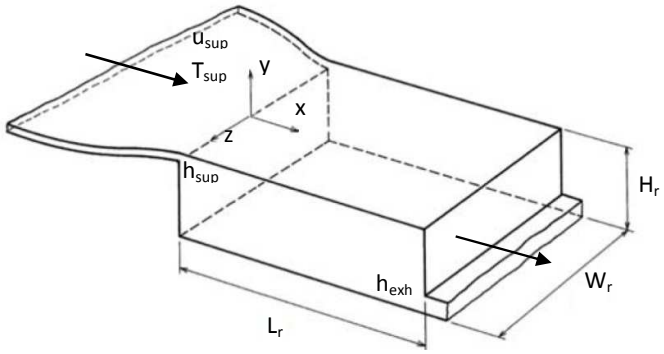

(b)

Figure 5.1: (a) Picture and (b) blueprint of Annex 20 2-D experiment setup [335]

Parameterization

This simple reference case enables a straightforward parameterization for the global SBO study. Table 5.1 states all considered design parameters with their respective categories/continuous interval. As previously mentioned, this study identifies among the design parameters four subsets: ventilation concept, location of isothermal plane, geometry and driving force for convective heat transfer.

Table 5.1 Overview of parameters for global SBO

Parameter	Type	Min	Max
-	Ventilation concept	Single sided/cross/under floor	
-	Location isothermal plane	Floor/ceiling	
L_r (m)	Geometry	4.5	9.0
H_{sup} (m)		0+BL	2.6-BL (4.0)
H_{exh} (m)		0+BL	2.6-BL
$h_{sup/exh}$ (m)		0.1	0.5
α (°)		60	120
(T_w-T_{sup}) (°C)	Driving force	1	10
n (h^{-1})		1.5	10

Where BL = boundary layer

The first subset, i.e. ventilation concept, which apparently matches its single input parameter, makes a clear-cut distinction: cross, single sided or under floor ventilation (Figure 5.2). Another such subset concurring with a single variable, is the location of the isothermal plane. Here, the choice between floor and ceiling means that the surface in question is at a higher temperature than the supplied air while the remaining surfaces behave adiabatically (Figure 5.3). As a matter of fact, starting from steady-state boundary conditions, the one warm surface represents a thermally heavy finishing while the adiabatic surfaces correspond to light structures. Further, the subset geometry comprises the length of the room L_r, the distance of the air supply to the zero point (0,0) H_{sup}, the distance of the exhaust opening to the zero point (0,0) H_{exh}, the height of the air supply/exhaust $h_{sup/exh}$ and the inclination angle of the air supply α (Figure 5.3). Now, continuous numerical intervals apply, in contrast with the previous two categorical variables (i.e. without numerical meaning) (Table 5.1). Note that, for programming simplicity, the bounds of H_{sup} and H_{exh} are corrected for the boundary layer thickness BL. For that same reason, H_{sup} is limited to 4.0m in case of under floor ventilation. Also mark in Figure 5.3 that underlying study constantly makes use of a quite long exhaust channel, simply to incorporate the possible recirculation flow. Otherwise, the CFD solver often stalls [268]. The last subset, i.e. driving force for convective heat transfer takes into account the relative magnitudes of the forced convection component, defined by the air change rate n, and of its natural convection equivalent, represented by the temperature difference between the one warm surface and the supplied air (T_w-T_{sup}). The air supply temperature T_{sup} equals 15°C in every simulation. The continuous intervals of these last two (quantitative) input variables determine many different convection regimes: these regimes range from predominantly forced convection over mixed convection to predominantly natural convection (Richardson numbers between 0.01 and 1770). Note that stating the type of the variables is not trivial as it indicates whether or not the variable involved can be part of the surrogate modelling process. In this study, the ventilation concept and the thermal mass distribution are categorical subsets and cannot be part of a surrogate model. Therefore, this study defines three (cf ventilation concept) times two (cf thermal mass distribution) base cases and lets SUMO built for each one of them a surrogate model which incorporates the subsets geometry and driving force for convective heat transfer. The acronyms denoting the different base cases, consist of the designation of the ventilation concept (cross, single sided, under floor) and the name of the surface which is at a higher temperature (floor, ceiling), separated by a hyphen.

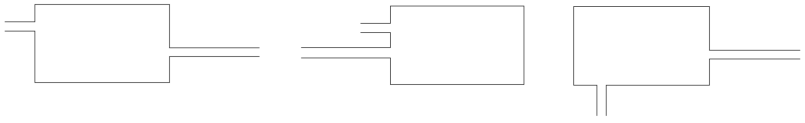

(a) (b) (c)

Figure 5.2: Ventilation concepts: (a) cross, (b) single sided and (c) under floor

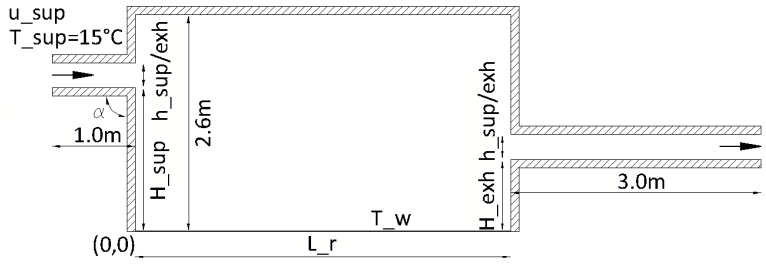

Figure 5.3: Schematic simulation experiment setup

Mind that many design parameters and boundary conditions are still left unvestigated. Without doubt, window specifications, conditions in adjacent rooms, (thermal) properties of the surroundings, temperature gradients in the walls, furniture… will influence the airflow. However, the approach used in this study is new and there is only a limited simulation time available. Therefore, this pilot study focusses only on primary design parameters/boundary conditions.

5.2.2 GAMBIT + FLUENT + SUMO = surrogate model

The SUMO toolbox itself is a set of Matlab [337] scripts which by default controls the whole process and takes care of the data sampling and the surrogate modelling. So, to code the interplay with the simulator(s), SUMO users logically end up with Matlab. Yet, this does not cause any problem. On the contrary, the complete and up-to-date documentation is particularly helpful at the beginning of the coding and in case of problems the large user community can help out. In particular for this study, setting up a Matlab function to read in, manipulate and evaluate the journal files typically used to control Gambit and Fluent, is relatively straightforward. All in all, this enables a fully-automated repeating workflow of sampling (SUMO), geometry and grid generation (Gambit), CFD solving (Fluent) and surrogate modelling (SUMO).

Figure 5.4 shows this sequence in more detail. In general, the workflow starts with SUMO sampling input parameter values. Then, the custom-made Matlab function receives these new specifications and calculates derived quantities. For example, having the length of the room, the height of the air supply and the air change rate, the Matlab function determines the corresponding air supply turbulence properties. Subsequently, the Matlab function reads in a generic Gambit journal file, fills in the geometrical parameters and evaluates the script. Gambit is launched, the grid built and, before closing, exported to a Fluent compatible mesh file. Once the Matlab function has registered this mesh file, it reads in the generic Fluent journal file 'steady/isothermal', fills in the parameters involving the subset driving force for convective heat transfer and evaluates the script: a first Fluent simulation takes off. The moment that the Matlab function registers the corresponding saved Fluent file, it reads in a second generic Fluent journal file, i.e. 'steady/non-isothermal', fills in the necessary quantities and evaluates it. A first so-

called steady/non-isothermal Fluent case is launched. At the end of this simulation, the Matlab function performs a double check. First, it verifies whether the number of iterations performed during the so-called loop A exceeds 6000. In the second place, the Matlab function checks, again by means of a generic journal file, whether or not the heat flux imbalance is smaller than the heat flux at the one warm surface. If not, the Matlab function extracts, with another journal file, the simulated temperature at the exhaust and implements it into a new 'steady/non-isothermal' Fluent simulation. On the other hand, once one of aforementioned conditions is fulfilled, the Matlab function moves to loop B. Now, the workflow continues with unsteady RANS simulations (controlled in a similar fashion). To advance to loop C, again one of two conditions needs to be fulfilled. Either the number of time steps in loop B exceeds 6000 or the heat flux imbalance equals at the most 10% of the convective heat flux at the one warm surface. Loop C introduces solution adaptive grid refinement, which efficiently reduces the numerical error in the solution, with minimal numerical cost. At this stage, severe convergence criteria hold. If the convective heat flux at the warm surface is higher than $0.1 W.m^{-2}$, the heat flux imbalance needs to be smaller than $0.05 W.m^{-2}$ and 1% of the surface heat flux. Otherwise, the heat flux imbalance can go up to 10% of the surface heat flux. Only then, the final Fluent simulation, now without further grid adaptation, starts. The time-averaged convective heat flux at the one warm surface obtained from this last simulation is then used by SUMO to update the surrogate model. When some simulation time is left and the sample budget is not used up, the sequence starts over again. For that matter, to speed up the simulations, the Matlab function enables parallel processing for all Fluent simulations except the first one. The first time Fluent reads in the grid, a single process is necessary. Otherwise, the partitioning of the grid for parallel processing goes wrong.

At first sight, the sequence of different Fluent simulations looks rather laborious. However, experience indicates that this procedure reaches much faster a converged solution. The preliminary steady-state simulations provide a reasonable estimate of the airflow. Meanwhile, loop B corrects for unsteadiness before the grid adaptive simulations of loop C come in. Moreover, adjusting the backflow temperature is no luxury. After all, a badly chosen backflow temperature often slows down the convergence rate or leads even to a wrong solution. Furthermore, in this study, only the heat imbalance acts as a convergence criterion. As a matter of fact, monitoring residuals and target quantities leaves considerable room for interpretation while getting to a small heat imbalance proves to be a more severe target (see section 4.2.1).

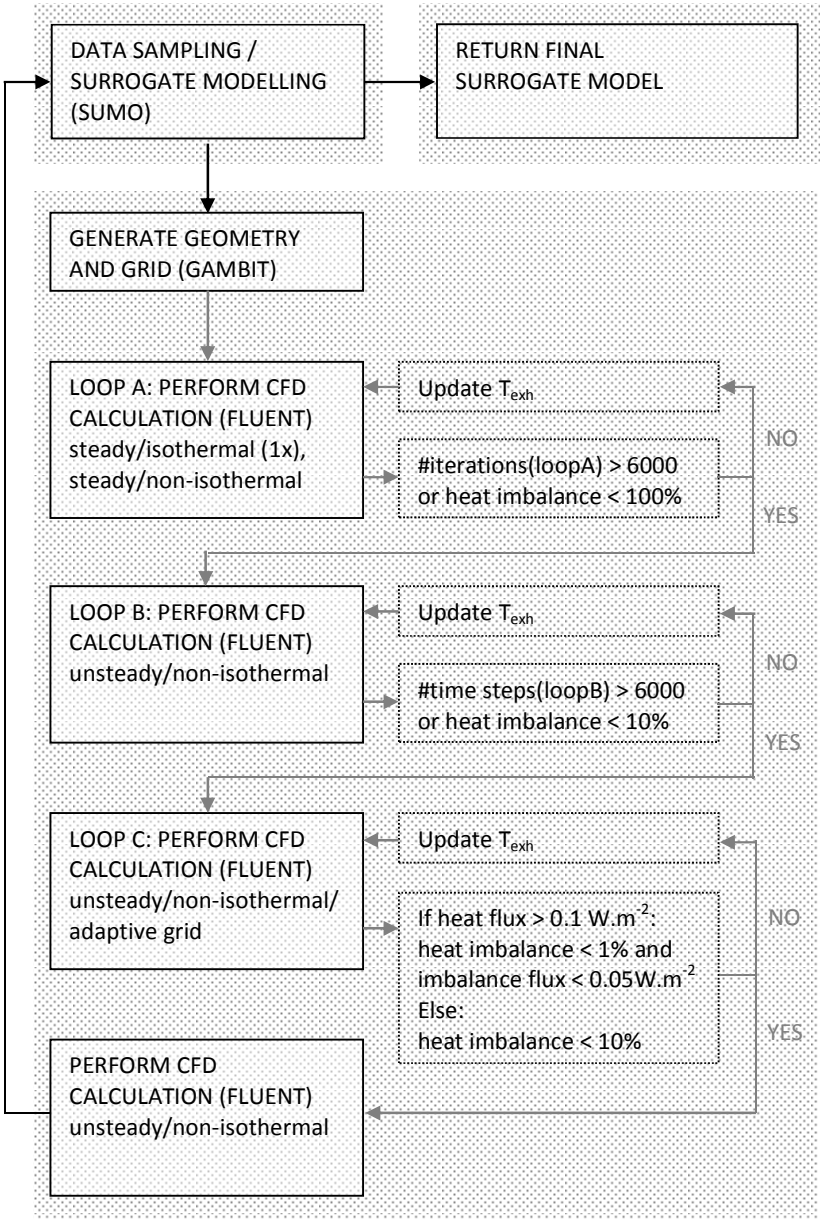

Figure 5.4: Flow chart of Gambit, Fluent and SUMO

5.2.3 CFD simulation approach

Geometry/grid generation

Feeding the geometry into Gambit is a straightforward procedure. Drawing up a proper grid, however, usually involves a great deal of trial and error (see chapter 4). A way to sidestep this handicap in a fully-automated process is solution adaptive grid refinement. As a matter of fact, Figure 5.4 already sketched the principle. First, a sequence of CFD simulations on a generic grid provides an estimate of the airflow. Then, the CFD software refines the grid on the fly, which, in the end, leads to an optimal grid distribution. Incidentally, this grid adaptation procedure also saves on computational resources (e.g. [338, 339]). However, there are some pitfalls to avoid [201]. For example, the base grid must be fine enough to adequately capture the major flow features (cf loop A and loop B in Figure 5.4). Or grid adaptation must only start when the prior CFD solution has reached a sufficient convergence level (except when convergence stalls prematurely; cf convergence criteria loop B in Figure 5.4). Also the selection of the refinement variable(s) determines the success of grid adaptation. Finally, refining some regions of the solution domain too much is no-go: the subsequent large gradients in cell volume reduce without doubt the solution accuracy.

This study puts three distinct parameterized Gambit journal files forward. These tie in with the investigated ventilation concepts (cross, single sided, under floor). Once read into Gambit, each one of them brings forth the case-specific geometry and the corresponding generic grid. To homogenize the resulting grids, this study opts for a clear zoning (Figure 5.5(a)). Otherwise, the few size functions sometimes mess up the grid. First, size functions start from the points connecting the air supply/exhaust with the room, indicated with ‘size function (vertex source)’. This way, the grid resolution increases near these openings. Obviously, this implies the use of an unstructured or pave mesh; which is preferably limited in space. Therefore, this study restricts the use of an unstructured mesh with quadrilateral elements to the immediate proximity of the air supply/exhaust (indicated with ‘quad/pave’). However, these zones are sufficiently wide so that the enclosed pave mesh fits the adjoining structured or map meshes. For that matter, the inner zone comprises a structured grid made out of square elements (indicated with ‘quad/map (square)’. The remaining zones include rectangular elements (indicated with ‘quad/map’). On the one hand, this last-mentioned mesh type allows size functions in the air supply/exhaust to continue the x-wise expansion of the cells (y-wise in the air supply in case of under floor ventilation). On the other, the height of the cells in the middle zones can gradually diminish towards the surface boundaries. Here, a dense boundary layer mesh is present, simply to fulfil the near-wall modelling conditions (y^+<4-5 and Re_y<200) [201].

Fluent allows to refine (or coarsen) the grid based on either geometrical or numerical solution data. This study goes for the second option to tune the grid with the simulated airflow at hand. It makes use of a gradient adaptation function. This approach assumes that maximum discretisation errors occur in high-gradient regions, which, as a result, need refinement. To this end, Fluent provides three

possibilities. However, for the cases at hand, only the so-called curvature function does a good job. This approach bases the error indicator on the Laplacian of the selected solution variable. In other words, it relies on the rate at which the gradient of the solution changes, which proves especially helpful for smooth solutions. For that matter, this Laplacian needs to be normalized. After all, re-adjusting the coarsen and refine thresholds during an automatic dynamic adaptation process would be a hopeless task. Further, neighbouring cells are not allowed to differ by more than one level of refinement, simply to avoid excessive cell volume variations, while the minimum cell volume is bounded. The solution variable used for all this is the turbulent kinetic energy. Out of four tested variables (temperature, pressure, velocity and turbulent kinetic energy), it showed the best validation results. It refines in particular the jet and near-wall regions (Figure 5.5(c)).

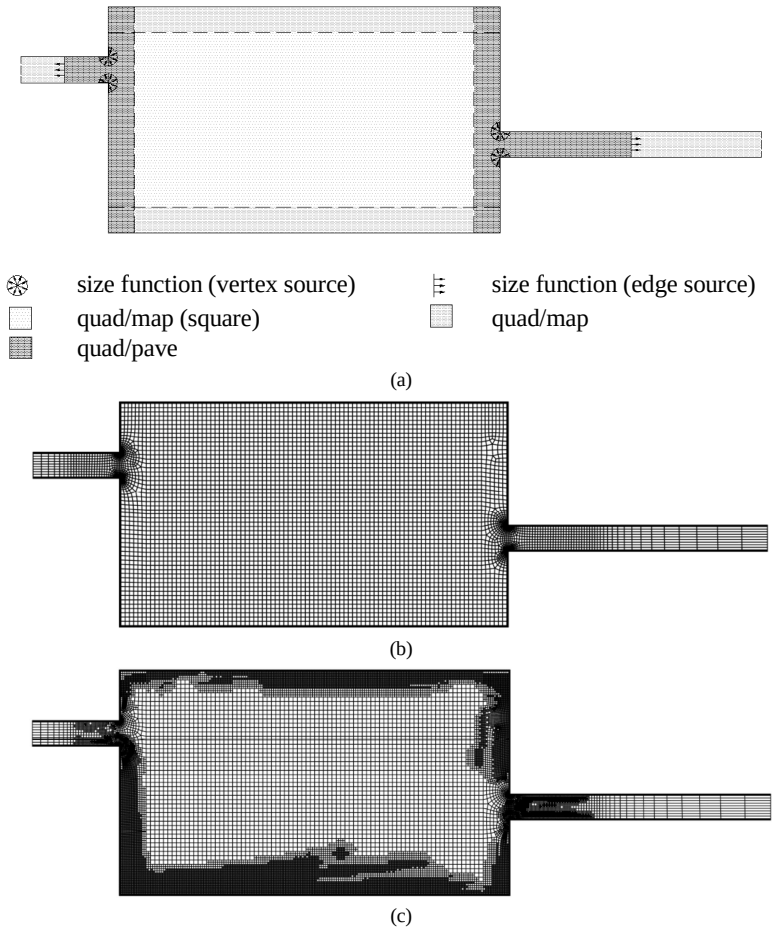

Figure 5.5: (a) Scheme of grid, (b) base version and (c) some adapted grid

CFD solver settings

This study applies virtually the same settings as the base case of chapter 4. For that reason, this paragraph only sketches out the main points. First, the pressure-based solver again takes care of the linearization and the solution of the discretised equations. The PISO algorithm is once more responsible for the pressure-velocity coupling. Also the same reduced under-relaxation factors control the change of variables throughout the iterations. Meanwhile, the second-order upwind scheme guarantees the interpolation of the convection terms; the PRESTO! scheme the interpolation of pressure. Similarly, a time discretisation scheme is necessary. After all, this study relies on time-dependent simulations. A first-order implicit time discretisation with a time step of 60s was used. Test simulations with other time step sizes (like 10s, 30s and 120s) revealed no appreciable effect.

Further, to model turbulence, this study reuses the RNG k-ε model. This model performs best, in terms of accuracy, computing efficiency and robustness, over a wide range of convection regimes (see chapter 4). This versatility is no luxury for underlying study: the driving forces for convective heat transfer come in a wide variety. Meanwhile, the simulations obviously need to resolve the near-wall region. Otherwise, the prediction of the convective heat transfer goes wrong (see chapter 1). In case of the used high-Reynolds number model, the two-layer approach urges itself. The RNG k-ε model then takes care of the fully-turbulent region while the one-equation model of Wolfstein [253] resolves the viscosity-affected near-wall region.

The boundary conditions depend for the most part on the parameter values set by the SUMO toolbox (Table 5.1). The air supply boundary conditions rely largely on the length of the room L_r, the height of the air supply $h_{sup/exh}$ and the air change rate n. The air supply velocity u_{sup} actually comes from Eq. (5.5) which comprises all aforementioned parameters. The corresponding turbulence intensity I relies on Eq. (5.6) which is an empirical correlation for fully-developed pipe flows, found in the Fluent manual [201]. Mind you, the used Reynolds number definition resembles the one used in Annex 20 (Eq. (5.1)). Likewise, the turbulent kinetic energy k comes down to Eq. (5.2) and the definition of the turbulent dissipation rate ε to Eq. (5.3), as suggested by Fluent. Meanwhile, the air supply temperature T_{sup} equals 15°C in all simulations. For that matter, uniform values of the (derived) quantities apply to the 'velocity inlet boundary condition', located at one end of the air supply duct. By this, a fully-developed flow occurs at the other end of the air supply duct (making an approximating diffuser model unnecessary).

$$u_{sup} = \frac{n \cdot \left(L_r \cdot 2.6m \cdot 1.0m\right)}{3600 \cdot \left(h_{sup/\,exh} \cdot 1.0m\right)} \tag{5.5}$$

$$I = 0.16 \cdot \mathrm{Re}^{-1/8} \tag{5.6}$$

A ‘pressure outlet boundary condition’ represents the exhaust. The gauge pressure at the opening is set as zero using the Dirichlet condition. In case of backflow, the air supply temperature of the exhaust equals the updated mass-averaged temperature near this opening (Figure 5.4) while the turbulence intensity is assumed to be equal to the one of the air supply. Furthermore, all surfaces but one (floor or ceiling) behave adiabatically. This one isothermal surface gets its temperature directly from the SUMO toolbox. As the boundary conditions remain constant during each simulation, the walls have no mass.

Further, the physical properties of the air need to be defined. As was the case with the sensitivity analysis in chapter 4, the viscosity, heat capacity and thermal conductivity are piece-wise functions of temperature. As for the variable air density, the incompressible ideal gas model comes in.

Finally, radiation is not included in the simulations. For, the calculation of longwave radiation takes a lot of time in Fluent and it is believed that during night cooling radiative heat transfer is of less importance than convective heat transfer. Yet, if radiation were taken into account, the temperature of the walls other than the isothermal plane would be higher and, thus, greater buoyancy forces would work against the jet flow.

5.2.4 SUMO settings

Data collection strategy

Building a surrogate model implies first and foremost populating a dataset. The selection of these specific sets of parameter values traditionally relies on design of experiments (DOE). Originally, this umbrella term, introduced in 1935 by Fisher [340], covered techniques which aim at getting as much information as possible from a limited one-shot set of physical experiments. The first DOE techniques (e.g. central composite design, Box-Behnken design) put most sample points at the extremes of the parameter space. This way, they lead to a reliable trend extraction in spite of the randomness in the physical experiments. Readers interested in more details on such DOE techniques are referred to Eriksson et al. [341]. On the other hand, the rise of computer-based experimentation made researchers develop new DOE techniques. After all, randomness is no longer an issue – that is to say, in case of deterministic simulation models. As a consequence, these DOE techniques can sample in the interior of the parameter space (e.g. orthogonal array sampling, Latin hypercube sampling). Advantageously, this space-filling feature helps to minimize the bias error, i.e. the difference between the functional form of the true response trend and the one of the predicted trend. For more info on designing computer experiments, the reference book of Fang et al. [342] and the review paper of Kleijnen et al. [343] prove particularly useful. Now, there is a growing body of opinion that sequential design, also known as adaptive sampling, is a better way: the multiple new adaptive sampling methods cannot be denied (e.g. [343-346]). Adaptive sampling addresses the main shortcoming of DOE: that is, the up-front number of sample points and their distribution over the parameter space are not necessarily appropriate. In adaptive sampling, the (repeating) sequence of (1)

generating a (multiple) candidate sample point(s), based on an intermediate surrogate model, (2) performing a simulation(s), (3) generating/updating the model as best one can (i.e. an internal loop) until some target is reached, basically samples only (more) points where needed and, thus, prevents the expensive cost of oversampling. However, not all adaptive sampling strategies are equally suited. For example, for global SBO (used in this study), it is crucial that the strategy strikes the correct balance between exploration (i.e. enhancing the general accuracy of the surrogate model) and exploitation (i.e. enhancing the accuracy of the surrogate model in the region of the (intermediate) optimum).

One such popular strategy is the expected improvement algorithm, which underlying study also uses. Kuschner [347] already came up with this concept in 1964, but not until the late 1990s the computer science community picked it up. In particular the efficient global optimization algorithm of Jones et al. [348, 349] popularized it. The expected improvement algorithm escapes the local minima and usually converges asymptotically to the global optimum (i.e. the absolute minimum); and, thus, reconciles exploration and exploitation. Another advantage is that the maximum value of expected improvement helps users to track the progress of the optimization. In addition to this, the expected improvement algorithm needs no user-defined problem-specific parameter(s) (that is, it is non-parametric) [350]. To introduce expected improvement, underlying study relies on a graphical illustration. Figure 5.6 shows how an intermediate surrogate model, based on ten sample points, approximates an arbitrary one-variable reference model, which is actually unknown. For that matter, the function value at any point x is treated as the realization of a normally distributed variable Y(x), with mean $\hat{y}=f(x)$ and variance $\hat{s}^2=\sigma^2(x)$ (i.e. a Gaussian process). Close to the sample points, the prediction is accurate. However, the surrogate model completely misses the ball in the data-sparse region on the right-hand side of the plot (i.e. where coincidentally the global optimum lies). The probability density function (PDF) (cf φ in Eq. (5.7)) at e.g. x=2.4 indicates a large uncertainty in the function value. What's more, the tail of the PDF extends below the line $y=f_{min}$, which means that the function value can improve on the current best simulated function value f_{min}. The corresponding shaded area under the PDF matches the cumulative distribution $P(Y(x)\leq f_{min})$ (cf Φ in Eq. (5.8)), or better, the probability of improvement PoI(x).

$$P\left(a \leq Y(x) \leq b\right) = \int_a^b Y(x) \cdot dy = \varphi\left(\frac{f_{\min} - \hat{y}}{\hat{s}}\right) \tag{5.7}$$

$$PoI(x) = P\left(Y(x) \leq f_{\min}\right) = \int_{-\infty}^{f_{\min}} Y(x) \cdot dy = \Phi\left(\frac{f_{\min} - \hat{y}}{\hat{s}}\right) \tag{5.8}$$

Probability of improvement may then already indicate the possibility of a better minimum, it does not quantify how large the improvement will be. By contrast, the first moment of the shaded area, better known as expected improvement, does! For continuous functions, expected improvement E[I(x)] equals every possible improvement at x, i.e. I(x), multiplied by the associated likelihood (Eq. (5.9)). For

that matter, the equivalent closed form notation (Eq. (5.10)) helps to better understand the functioning of this expected improvement algorithm. The first term on the right-hand side represents the difference between the current simulated minimum f_{min} and the predicted value $\hat{y}$ times the probability that Y(x) is smaller than f_{min}. The second term stands for the standard deviation of Y(x) multiplied by the probability that Y(x) equals f_{min}. As a consequence, the expected improvement is large where Y(x) is likely smaller than f_{min} and/or where there is a high uncertainty in the prediction value itself. On the other hand, at sample points, the prediction variance $\hat{s}^2$ equals zero and, thus, the expected improvement is nil. Readers wanting to see the progress of an expected improvement-based optimization of a one-variable test function, should check out Forrester et al. [350].

$$E[I(x)] = \int_{-\infty}^{f_{min}} I \cdot Y(x) \cdot dy \quad where \quad I = \max[f_{min} - Y(x), 0] \tag{5.9}$$

$$E[I(x)] = \begin{cases} (f_{min} - \hat{y}) \cdot \Phi\left(\frac{f_{min} - \hat{y}}{\hat{s}}\right) + \hat{s} \cdot \varphi\left(\frac{f_{min} - \hat{y}}{\hat{s}}\right) & if \quad \hat{s}^2 > 0 \\ 0 & if \quad \hat{s}^2 = 0 \end{cases} \tag{5.10}$$

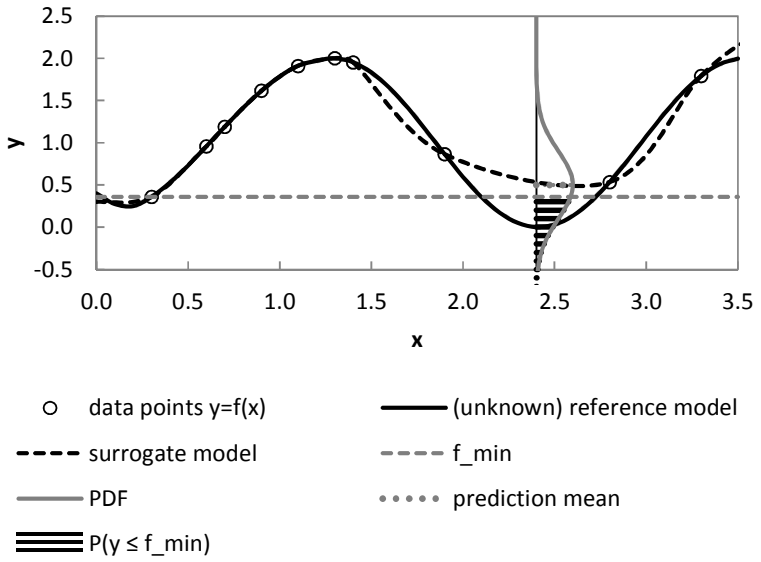

Figure 5.6: Graphical illustration of expected improvement

The optimization procedure normally includes all parameters from the start. However, the CFD simulations in this study are so expensive that it is better to increase sequentially the number of parameters. This leaves the opportunity to check on the intermediate optimization results and associated surrogate models. For that matter, this explains the presence of collinear points in the plots to come. The sampling actually starts from a Latin hypercube design which includes only two parameters, i.e. the distance of the air supply to the zero point H_{sup} and the distance of the exhaust opening to the zero point H_{exh}. From there on, adaptive sampling comes in, initially superadding two more parameters, the air change rate n and the temperature difference between the one warm surface and the supplied air (T_w-T_{sup}). Later on, the remaining parameters, i.e. the height of the air supply/exhaust $h_{sup/exh}$, the inclination angle of the air supply α and the length of the room L_r are also part of the parameter space. To determine the next sample point in this iterative process, the competitive dividing rectangles (DIRECT) algorithm of Jones et al. [351] optimizes the expected improvement algorithm. When the DIRECT algorithm fails to find a unique sample, the optimization of the fall back criterion starts. The model then looks for the parameter combination that has the largest prediction variance.

Modelling strategy

Once the data collection strategy is fixed, it is necessary to choose how to build a surrogate model from the scattered data. Generally, interpolation surrogate models approximate best deterministic computer experiments. Such a model is usually a linear combination of polynomial terms, which model the trend over the parameter space, and special 'basis function' terms, which 'pull' the surrogate model through the observed data [349]. In particular the form of the basis function, which quantifies the correlation of (nearby) points, determines the usability of the corresponding interpolation technique. In particular kriging [352] stands out, because its basis function includes tuneable parameters. This statistical feature of the basis function not only allows to compute an interpolator (or 'predictor'), but it also enables to estimate the potential error in the predictor. Precisely this bonus is necessary to apply the expected improvement algorithm. Therefore, this study deploys ordinary kriging – called kriging in the remainder.

Basically, kriging tries to construct, from n sample points $\mathbf{x}_i$ (where $\mathbf{x}_i$ is a d-dimensional vector $\mathbf{x}_i=(\mathbf{x}_{i1}\ \mathbf{x}_{i2}\ \ldots\ \mathbf{x}_{id})'$) and the n corresponding function values $y_i=y(\mathbf{x}_i)$, a surrogate model with minimal prediction variance. Yet, there is more to kriging than meets the eye. Kriging assumes that the function being studied is a realization of a Gaussian stochastic process $Y(\mathbf{x}_i)=\mu+Z(\mathbf{x}_i)$. The constant mean μ (i.e. a constant polynomial) replaces the regression terms while the zero-mean, stationary, Gaussian stochastic process $Z(\mathbf{x}_i)$, with variance σ^2 and parametric correlation function Eq. (5.11), corresponds to the basis function terms.

$$Corr\left[Y(\mathbf{x}_i), Y(\mathbf{x}_j)\right] = \exp\left(-\sum_{\ell=1}^{d} \theta_\ell \cdot \left| x_{i\ell} - x_{j\ell} \right|^{p_\ell} \right) \tag{5.11}$$

This correlation function implies that the random variables $Y(\mathbf{x}_i)$ and $Y(\mathbf{x}_j)$ – and, thus, the function values $y(\mathbf{x}_i)$ and $y(\mathbf{x}_j)$ – correlate better when their sample points $\mathbf{x}_i$ and $\mathbf{x}_j$ are closer, i.e. their Euclidean distance in the ℓ^{th} input dimension of the sample points $\mathbf{x}_i$ and $\mathbf{x}_j$ is smaller. The first (tuneable) correlation parameter in Eq. (5.11), i.e. θ_ℓ ($\geq$0), indicates the importance of input dimension ℓ: the higher θ_ℓ is, the faster the correlation decreases with distance. The other one, i.e. p_ℓ, determines the smoothness of the function in the ℓ^{th} input dimension. For example, p_ℓ=1 yields the exponential correlation function; p_ℓ=2 gives the so-called Gaussian correlation function. Underlying study sets p_ℓ equal to two. As a consequence, the behaviour of the function only depends on the parameters μ, σ^2 and $\boldsymbol{\theta}_\ell$, of which the (estimated) values should maximize the probability (i.e. the likelihood) of the sampled data. Whilst deriving the predictor value for an additional point $\mathbf{x}^*$ – which is either an old point or a new one, the aim is obviously once again maximizing the – now 'augmented' – likelihood. The derivation of this kriging predictor is out of scope. Instead, this work restricts itself to stating the standard formula, i.e. the best linear unbiased predictor (BLUP) (Eq. (5.12)):

$$y(\mathbf{x}^*) = \mu + \mathbf{r}^T\mathbf{R}^{-1}(\mathbf{y} - \mathbf{1}\mu) \tag{5.12}$$

where $\mathbf{r}=\{\mathrm{Corr}[Y(\mathbf{x}^*),Y(\mathbf{x}_1)] \ldots \mathrm{Corr}[Y(\mathbf{x}^*),Y(\mathbf{x}_n)]\}^T$ is the vector of correlations between $\mathbf{x}^*$ and the n sample points, $\mathbf{R}$ is the n x n correlation matrix whose $(i,j)^{th}$ entry is given by Eq. (5.11) and $\mathbf{1}$ denotes the n-dimensional vector with ones. Now, the generalized least squares (GLS) determines the constant process mean μ and the process variance σ^2 while the sequential quadratic programming (SQP) algorithm determines $\boldsymbol{\theta}_\ell$ so that the probability of the sampled data is at his maximum. For that matter, the predictor is more reliable when the 'augmented' likelihood drops off dramatically as one moves away from the optimal value of $y(\mathbf{x}^*)$. Note that this closely relates to the mean squared error of the predictor (or better, prediction variance), i.e. $\sigma^2(\mathbf{x}^*)$ (Eq. (5.13)). This last-mentioned formula has the intuitive property that at any sampled point, it equals zero.

$$\sigma^2(\mathbf{x}^*) = \sigma^2\left(1 - \mathbf{r}^T\mathbf{R}^{-1}\mathbf{r} + \frac{\left(1 - \mathbf{r}^T\mathbf{R}^{-1}\mathbf{r}\right)^2}{\mathbf{1}^T\mathbf{R}^{-1}\mathbf{1}}\right) \tag{5.13}$$

5.3 Results

5.3.1 Validation by means of the Annex 20 2-D2 case

To guarantee the reliability of the simulation results, validating the simulation model(s) is essential. However, there's no data for the case(s) at hand. Fortunately, the previously described Annex 20 2-D2 case for which experimental data are available [332], can take over this validation role. The larger room height and a constant heat flux at the floor instead of a fixed temperature actually do not pose any problem. This Annex 20 2-D2 case was meant to be a benchmark for mixed convection flows. Raising the constant heat flux added along the floor in succeeding experiments enabled to determine at which Richardson number the cool jet deflects from the ceiling. The smoke visualisations of Schwenke [332] indicated that the jet immediately fell down when Ri exceeded 0.02. An intermediate status lacked. The subsequent simulation studies by e.g. Chen [353], Lemaire [354], Said [355] and Vogl [356] also predicted a sudden turning punt indeed, yet at higher Richardson numbers, ranging from 0.12 to 0.20 [194]. Most likely, this discrepancy resulted from the use of rough grids, inapt wall functions and simple turbulence models. However, these options were the best they could get.

Underlying validation study obviously adopts the CFD simulation approach described in section 5.2.3. However, one thing is still missing: that is, the grid resolution. After all, determining the grid resolution in advance is impossible. Hence, this study starts from the work of Voigt [268]. He punctually tried three grid resolutions on the isothermal Annex 20 2-D1 case and suggested using the intermediate resolution having an overall grid density of 682cells.m^{-2}. However, this limited grid resolution is not enough for the non-isothermal Annex 20 2-D2 case: the simulations have difficulty converging. Therefore, this validation study directly switches over to the fine grid resolution of Voigt, i.e. 2730cells.m^{-2} (equal to the fourfold of the intermediate grid density).

Now, plotting contours or path lines of the succeeding simulations would enable to determine whether the jet also deflects at a Richardson number around 0.02. However, a more concise way is to trace the distance from the zero point in the x-direction at which the x-wall shear stress at the ceiling becomes negative, x_{re} (i.e. the point of deflection). Figure 5.7 depicts this criterion x_{re} as a function of the Richardson number Ri for the simulations performed in this validation study. The graph also gives the measured point of deflection by Schwenke and, for comparison's sake, the ones obtained from simulations by the aforementioned researchers. Clearly, the adopted simulation approach in conjunction with a grid density of 2730cells.m^{-2} approximates the measured deflection point better than the reported works do. For that matter, quadrupling this grid resolution again changes nothing. In other words, the suggested CFD approach and grid density are apt for the validation case. The author of this study assumes this is also the case for other cases.

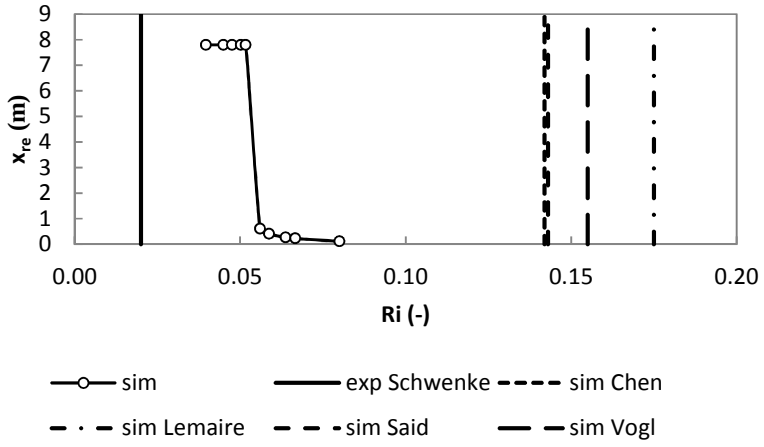

Figure 5.7: Location of the deflection point as a function of the Richardson number

5.3.2 Pareto optimality

Above all, this study looks for optimal solutions. In particular the design of fan-assisted night cooling is faced with the trade-off between the convective heat flux by night and the nocturnal air change rate. A higher air change rate results in a higher convective heat flow indeed, yet it implies a higher energy use of the fans. So, it is interesting to assess the accompanying Pareto optimality. Figure 5.8 depicts for the six combinations of ventilation concept and thermal mass distribution the convective heat flux-air change rate Pareto fronts. Each Pareto front is based on one of the six surrogate models and indicates the maximum attainable convective heat fluxes for the full range of n and (T_w-T_{sup})=10°C for each base case. The error bars are derived from the prediction variance and indicate the 95% confidence intervals (large confidence in the predicted optima). Note that in this and the analysis to come the room length L_r is fixed at 4.5m. For, at larger room lengths the surrogate models exhibit a too large prediction variance to draw conclusions. First, the graph confirms that in general the convective heat flux increases with increasing air change rate. In addition, four out of six cases exhibit roughly a bi-linear relationship. What's more, this bi-linear relation depends on the thermal mass distribution: the slope is higher at low air change rates in cases with thermal mass at the floor while cases with a warm ceiling exhibit a higher slope at high air change rates. Outsiders are 'under floor-floor', which shows a peak convective heat flux at an air change rate lower than the maximum, and 'single sided-ceiling', which displays a flat course. What's more important, the cases with thermal mass at the floor clearly outperform the ones with a warm ceiling. They produce convective heat fluxes which are two to eighteen times as high. Among these cases with thermal mass at the floor, cross ventilation results in the highest convective heat flux. Among the others, single sided ventilation seems superior.

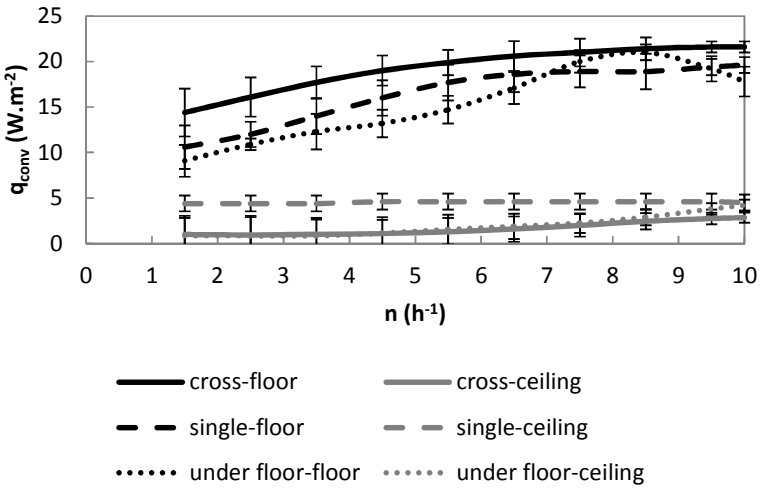

Figure 5.8: Convective heat flux-air change rate Pareto front

The explanation of aforementioned tendencies goes as follows. Increasing the air change rate lowers the indoor air temperature and augments the indoor air velocity and, thus, leads to an increase of the convective heat flux. What's more, it also changes the ratio of buoyancy to inertia forces. In general, the cool jet falls down because of gravity – which explains why the cases with thermal mass at the floor result in the highest convective heat fluxes. However, an increasing air change rate leads to a higher momentum and, thus, a deeper jet penetration. This implies that at some point, the jet no longer just impacts upon the floor but also stirs the air near the ceiling. This causes the aforementioned bi-linear relationship in most cases. The deviant behaviour of 'under floor-floor' is because at air change rates higher than 8.5h^{-1} the jet momentum is so high that the supplied cool air no longer spreads over the whole of the warm floor (Figure 5.9). The nearly constant and high convective heat flux in case of 'single sided-ceiling' is due to the global SBO itself. The expected improvement algorithm guided the optimization procedure towards cases with a high temperature difference, a high air change rate, a small air supply/exhaust height and the exhaust on top of the air supply near the ceiling. In this case, the exhaust removes the air near the warm ceiling while most of the indoor air approximates the air supply temperature. So it is no wonder that the air jet does not fall to the ground but turns upwards and impinges upon the ceiling (Figure 5.10). However, at lower air change rates, there are too few sample points to correct this peak convective heat flux predicted by the surrogate model. The overall best performance of the cross ventilation concept in case thermal mass is at the floor is because it usually does not lead to short circuits between the air supply and the exhaust (as with single sided ventilation) and does not necessarily direct the jet away from the warm floor (as with under floor ventilation).

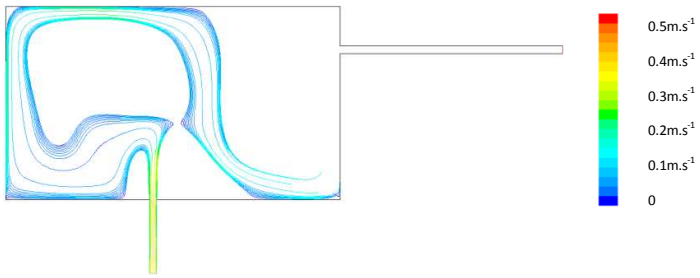

Figure 5.9: Streamlines (coloured by velocity magnitude) of case 'under floor-floor', L_r=4.5m, H_{sup}=1.93m, H_{exh}=1.97m, $h_{sup/exh}$=0.10m, n=10h^{-1}, (T_w-T_{sup})=10°C

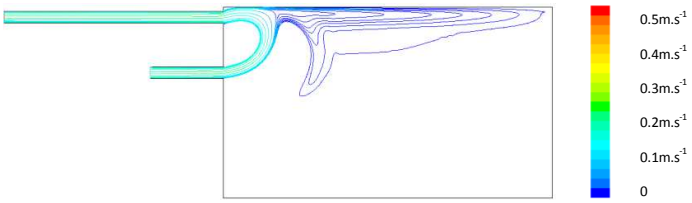

Figure 5.10: Streamlines (coloured by velocity magnitude) of case 'single sided-ceiling', L_r=4.5m, H_{sup}=1.63m, H_{exh}=2.38m, $h_{sup/exh}$=0.15m, n=8.74h^{-1}, (T_w-T_{sup})=10°C

5.3.3 Sensitivity

The above analysis already revealed that the thermal mass distribution more than the ventilation concept determines the maximum attainable convective heat flux. However, it did not pinpoint the sensitivity to the geometrical parameters, including the distance of the air supply to the zero point H_{sup}, the distance of the exhaust to the zero point H_{exh}, the air supply/exhaust height $h_{sup/exh}$ and the inclination angle of the air supply α. Therefore, Figure 5.11 depicts for the respective base cases the minimum and maximum convective heat flux, with L_r=4.5m, (T_w-T_{sup})=10°C and n=10h^{-1}. Also the results of frequently used geometries are part of the graph. The geometrical parameter values determining these reference cases are H_{sup}=2.4m (cross)/0.5m (single sided)/1.0m (under floor), H_{exh}=2.4m, $h_{sup/exh}$=0.1m and α=90°. The error bars of the minimum and maximum convective heat fluxes are again derived from the prediction variance and indicate the 95% confidence intervals. First of all, this graph also shows the large differences due to the thermal mass distribution: the convective heat fluxes in cases with a thermally massive floor are usually much higher than the ones in cases with a warm ceiling. What's more, the base cases with thermal mass at the floor are, relatively speaking, less sensitive to the geometry. Among these cases, cross ventilation is the most robust ventilation concept, which is actually also the case when thermal mass is at the ceiling. Single sided ventilation, on the other hand, is particularly sensitive to the geometry. Finally, it seems that the frequently used geometries lead especially to low convective heat fluxes in case of a warm ceiling.

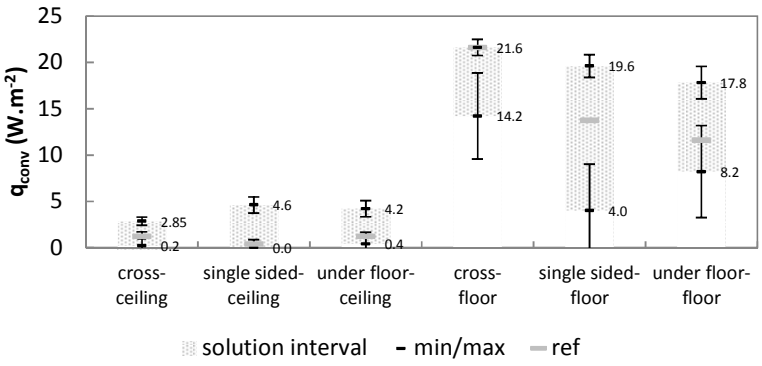

Figure 5.11: Sensitivity of the convective heat flux to the geometry (with L_r=4.5m, (T_w-T_{sup})=10°C and n=10h^{-1})

The reason why the cases with thermal mass at the floor are less sensitive to the geometry is the same as why they determine more than the ventilation concept the maximum attainable convective heat flux: the cool jet generally falls down because of gravity – as previously mentioned. Why cross ventilation is quite robust and single sided ventilation not is because there's little chance that cross ventilation leads to short circuits between the air supply and the exhaust.

5.3.4 Overall relationships

Research setup

The above Pareto analysis indicated the best performance of the respective ventilation concepts/thermal mass distributions. The subsequent sensitivity analysis further illustrated in which cases the room/system design matters. However, neither of the two analyses pinpointed which values of the quantitative parameters, part of the subsets geometry and driving force, led to the extremes. Also the overall relationships between the convective heat flux and these quantitative parameters remained unexplored – should the surrogate models allow to deduce this. Therefore, this section provides a detailed view of the surrogate models of the base cases with thermal mass at the ceiling respectively at the floor. The predicted convective heat flux as well as the associated prediction variance is part of the analysis. This way, it is easy to check whether the observed tendencies truly hold. However, now the author applies a fair confidence interval for the derived uncertainty, that is 68% instead of 95%. After all, the number of sample points used in the respective optimization procedures, ranging from 81 to 148, is insufficient to provide a globally accurate seven-dimensional model. The centrepieces of this analysis are contour plots (Figure 5.12-Figure 5.23) which show for the six base cases how the convective heat flux/prediction variance relates to the distance of the air supply to the zero point H_{sup} (x-axis of each contour plot) and the distance of the exhaust to the zero point H_{exh} (y-axis of each contour plot).

Each individual contour plot corresponds to one combination of fixed values of the remaining five quantitative parameters, i.e. the length of the room L_r, the height of the air supply/exhaust $h_{sup/exh}$, the inclination angle of the air supply α, the temperature difference between the one warm surface and the supplied air (T_w-T_{sup}) and the air change rate n (i.e. a slice). The two x-axes of the graph itself include discrete values of $h_{sup/exh}$ and α while in the y-direction the two axes apply to (T_w-T_{sup}) and n. L_r always equals 4.5m. The black dots in the contour plots are projections of sample points. Their dimension indicates their distance to the slice. Sample points of which at least one of the parameter values deviates by more than 40% of the total parameter interval from the corresponding parameter value of the slice, are left out. Finally, note that the surrogate models rely on the negative of the convective heat flux. This is because the expected improvement algorithm directs the solution procedure towards the global minimum. At the back of this section, Figure 5.24 enlarges the typical contour plots of the respective bases cases (for $h_{sup/exh}$=0.1m, α=90°, (T_w-T_{sup})=10°C, n=10h^{-1}).

Thermal mass at the ceiling

Figure 5.12 and Figure 5.13 depict the contour plots of the convective heat flux respectively prediction variance of case 'cross-ceiling'. The slices with a large temperature difference, a high air change rate and a small air supply/exhaust height contain the globally optimal convective heat flux. They indicate that in particular locating the air supply near the warm ceiling pays off. The position of the exhaust seems less stringent. The preferred inclination angle of the air supply, on the other hand, remains unclear, because of the large prediction variance. This lack of accuracy actually applies to most of the slices and, thus, prohibits further investigation of the general relationships. Anyhow, why the global optimum occurs at aforementioned parameter combination is logical. The high temperature difference between the ceiling and the supplied air and the high air change rate introduce a high cooling energy while the small air supply near the warm ceiling forces up the convective heat transfer (this reasoning actually returns several times in the description to come).

Figure 5.14 and Figure 5.15 reveal for case 'single sided-ceiling' that again the combination of a large temperature difference, a high air change rate and a small air supply at the top leads to peak convective heat fluxes. However, in this instance the position of the exhaust does matter. Locating the exhaust on top of the air supply near the ceiling is particularly beneficial. However, also putting the exhaust as far away as possible from this air supply (i.e. at the bottom) results in a considerable convective heat flux. However, for this last-mentioned configuration, the relation between the convective heat flux and the air supply/exhaust height is predicted incorrectly. Normally the absolute convective heat flux increases with a decreasing air supply/exhaust height. By contrast, the surrogate model predicts otherwise for this last configuration, probably because of the lack of data points in this region (in spite of a small prediction variance). Further, the impact of the inclination angle of the air supply once again cannot be discerned: the prediction variance is limited indeed, yet this is also because of the limited number of sample

points for angles other than 90°. Similar general appreciations apply to the other convection regimes with a smaller temperature difference and/or a lower air change rate. However, the difference in impact between the geometrical parameters is less marked. Why the configuration with the exhaust on top of the air supply near the ceiling can produce particularly high convective heat fluxes, was already explained in the previous section 5.3.2: the jet simply turns towards the ceiling. The second good configuration, i.e. air supply at the top and exhaust near the floor, always leads to a short circuit of the supplied air between the air supply and the exhaust indeed. Yet the jet stirs the air near the ceiling and it induces a fair heat/momentum transfer to the indoor air as it streams to the exhaust at the bottom.

Figure 5.16 and Figure 5.17 show the results of case 'under floor-ceiling'. Again the combination of a high temperature difference, a high air change rate and a small air supply/exhaust leads to the overall highest convective heat fluxes. However, not the position of the air supply but the one of the exhaust now gets priority. Putting the exhaust at the top leads to the optimal convective heat flux. Yet, these contour plots with the optimal convective heat flux also reveal a second good exhaust position, that is, near the floor. However, as the air supply/exhaust height increases, this second optimum disappears. Also the absolute value of the former optimum diminishes with increasing $h_{sup/exh}$. Further, the limited number of sample points prevents from assessing the impact of the inclination angle of the air supply. The contour plots of the other convection regimes (with a smaller temperature difference and/or a lower air change rate) do not indicate a different behaviour, should they be sufficiently accurate (the ones of the smallest temperature difference are not). So, putting the exhaust near the ceiling and minimizing the air supply height is generally the best choice. As a matter of fact, in this case the exhaust at the top removes the usually warm air near the ceiling and, thus, prohibits air stratification (remember 'single sided-ceiling'). In addition, limiting the air supply height leads to a higher jet momentum by which the jet better stirs the air near the ceiling. Note that in such cases, the exhaust may also be located at the bottom: the chances of turning the strong jet directly towards the exhaust at the bottom are small.

Thermal mass at the floor

Figure 5.18 and Figure 5.19 display the contour plots of the convective heat flux respectively the prediction variance of case 'cross-floor'. The optimal convective heat flux is where the temperature difference between the warm floor and the supplied air and the air change rate reach their maximum. The air supply/exhaust height, on the other hand, seems to be of little importance while the impact of the inclination angle is uncertain. In this instance, the air supply is best at the ceiling, the exhaust can be anywhere. For that matter, this optimum resembles the one of 'cross-ceiling'. However, the corresponding contour plots of convection regimes with a smaller temperature difference indicate that the convective heat flux diminishes as the exhaust approaches the top. Conversely, the remaining contour plots do not enable to discern differences because of the air supply/exhaust configuration. A reasoning somewhat similar to the one of 'cross-ceiling' explains

the observed optimum. First, the large temperature difference between the floor and the supplied air and the high air change rate result in a high cooling energy. Secondly, in such mixed convection regime, the cold air supplied at the top accelerates due to gravity and finally spreads over the whole of the floor. That is also why the air supply/exhaust height matters little. Having in addition the exhaust near the bottom prohibits the development of a retarding recirculation flow on the right-hand side of the room.

Figure 5.20 and Figure 5.21 reveal that the convective heat flux plots of 'single sided-floor' bear resemblance to those of its counterpart 'single sided-ceiling'. Multiple optima occur at a high temperature difference, a high air change rate and a small air supply/exhaust height. However, the optima are less distinct. Putting the exhaust on top of the air supply or locating the air supply in the upper region of the side wall and the exhaust at the bottom yield both a considerable profit. The impact of the inclination angle of the air supply cannot be deduced, again because of the limited number of sample points. The remaining contour plots show pretty much the same. The ones with $(T_w-T_{sup})=1°C$, however, are not accurate enough to discern notable differences. The above tendencies resemble the ones of case 'single sided-ceiling', so the explanations must run in parallel. Now, the air jet always falls to the ground, even in case the exhaust is on top of the air supply near the ceiling. So, to profit from the gravitational acceleration, it is best to put the air supply at the top. The position of the exhaust simply determines whether short circuits occur. Putting it on top of the air supply or as far away near the bottom increases the chances of success. For that matter, note the resemblance of this base case to the setup with a thermally massive floor in the PASLINK test cell discussed in chapter 3. Unfortunately, a cross-comparison is impossible because of the surrogate model exhibits a too large prediction variance in the regions of interest.

The final two graphs, i.e. Figure 5.22 and Figure 5.23, show the results of 'under floor-floor'. Obviously the optimal convective heat fluxes occur when the temperature difference between the floor and the supplied air and the air change rate are maximal and the air supply/exhaust height minimal. In this case, putting the exhaust at the top only slightly enhances the convective heat flux. The air supply position and its inclination angle are also of little account (now the prediction variance for angles other than 90° is reasonably small). What's more, as the buoyancy force becomes more important, the configuration (including $h_{sup/exh}$, α, H_{sup} and H_{exh}) becomes even less influential. These findings contrast to a large extent with 'under floor-ceiling' for which in particular $h_{sup/exh}$ and H_{exh} are important. However, in case of 'under floor-floor', the room is heated from below by which the cold jet falls sooner to the ground. In all cases, the jet spreads over the whole of the floor.

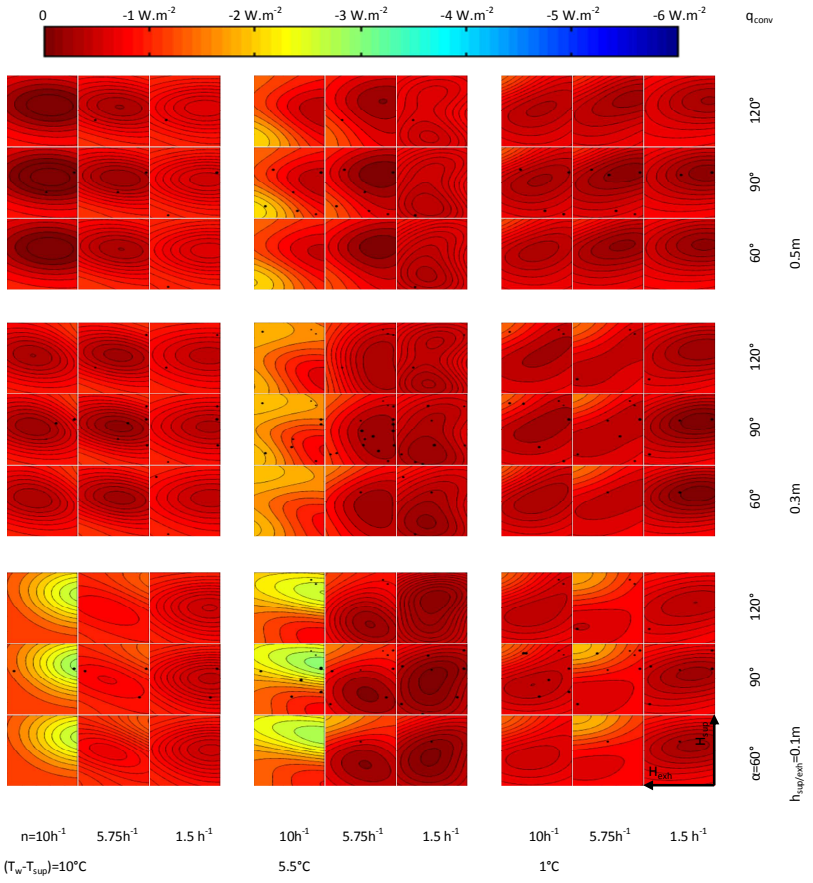

Figure 5.12: Contour plots of the convective heat flux of case 'cross-ceiling' (for L_r=4.5m, based on 88 samples)

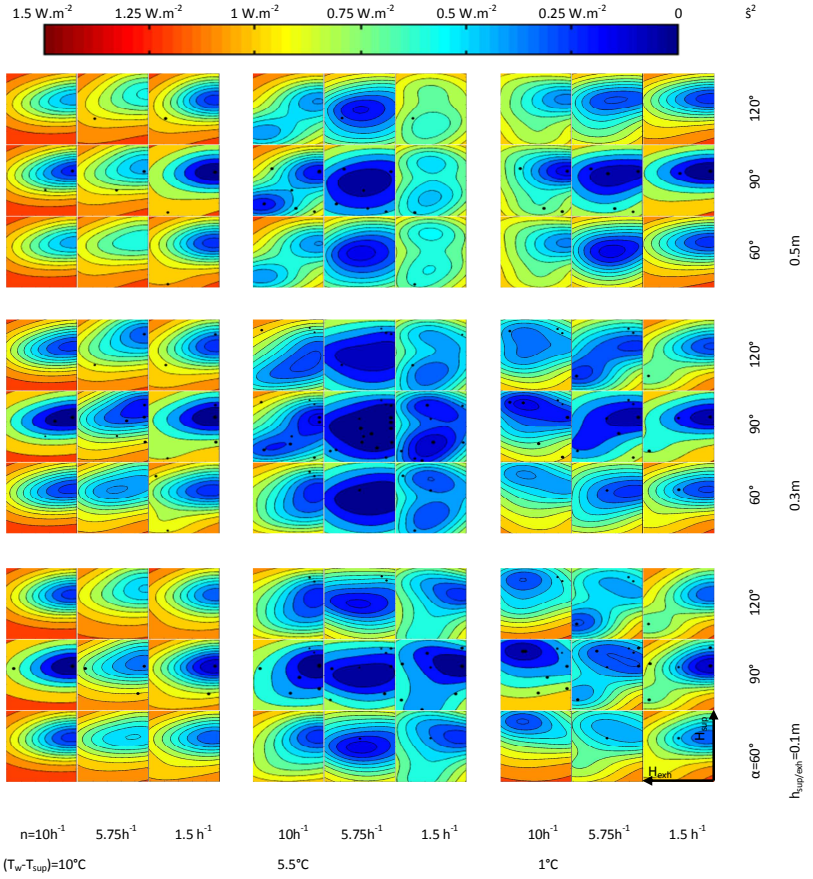

Figure 5.13: Contour plots of the prediction variance in the convective heat flux of case 'cross-ceiling' (for L_r=4.5m, based on 88 samples)

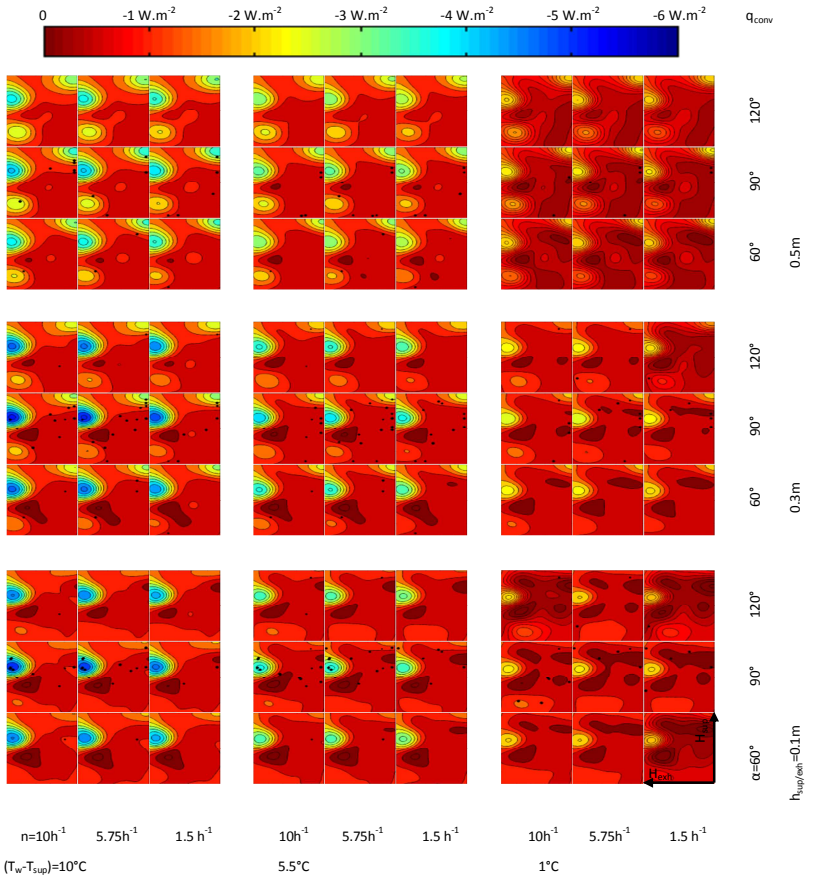

Figure 5.14: Contour plots of the convective heat flux of case 'single sided-ceiling' (for L_r=4.5m, based on 81 samples)

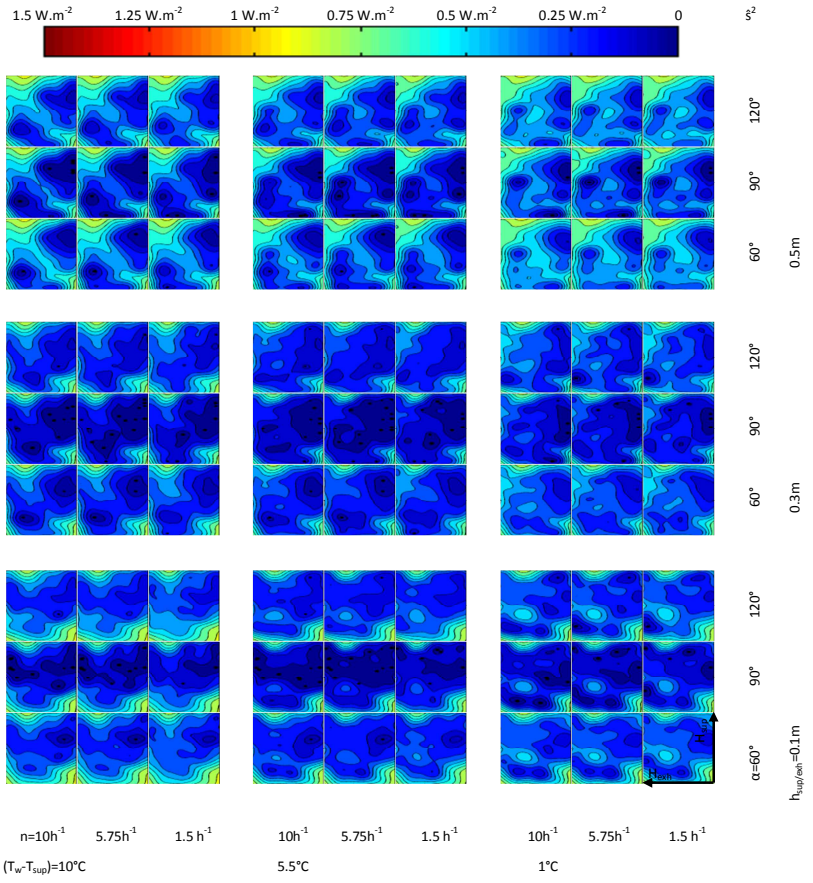

Figure 5.15: Contour plots of the prediction variance in the convective heat flux of case 'single sided-ceiling' (for L_r=4.5m, based on 81 samples)

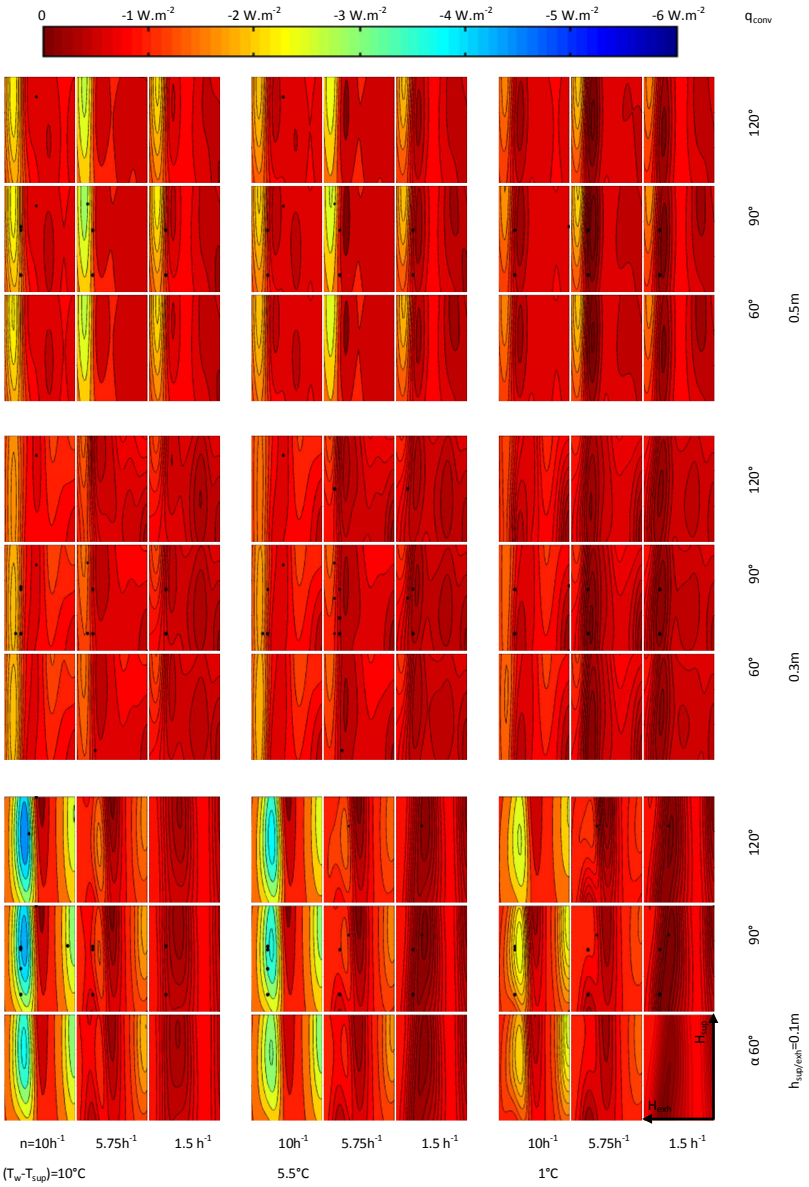

Figure 5.16: Contour plots of the convective heat flux of case 'under floor-ceiling' (for L_r=4.5m, based on 101 samples)

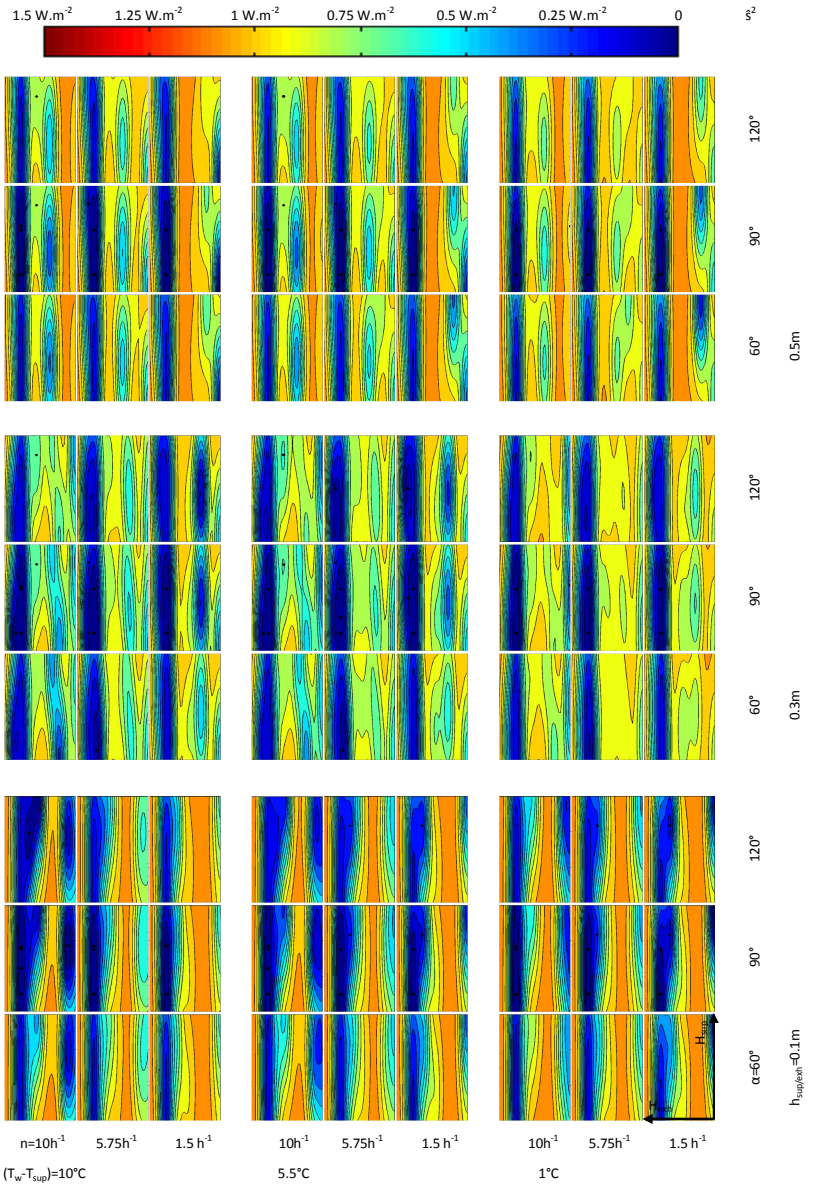

Figure 5.17: Contour plots of the prediction variance in the convective heat flux of case 'under floor-ceiling' (for L_r=4.5m, based on 101 samples)

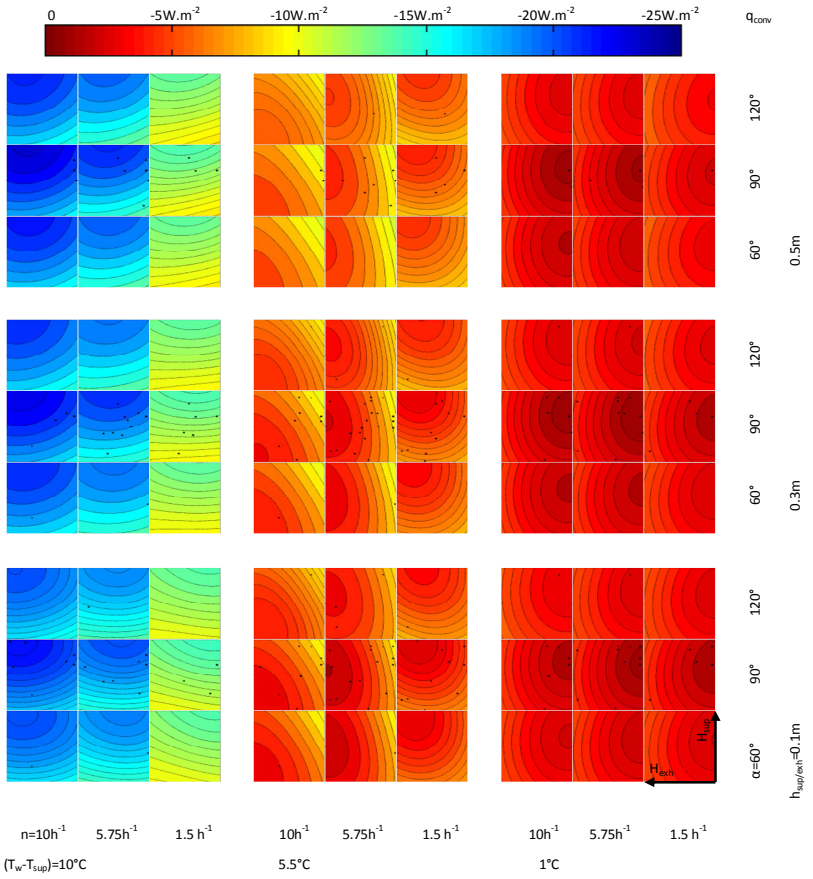

Figure 5.18: Contour plots of the convective heat flux of case 'cross-floor' (for L_r=4.5m, based on 103 samples)

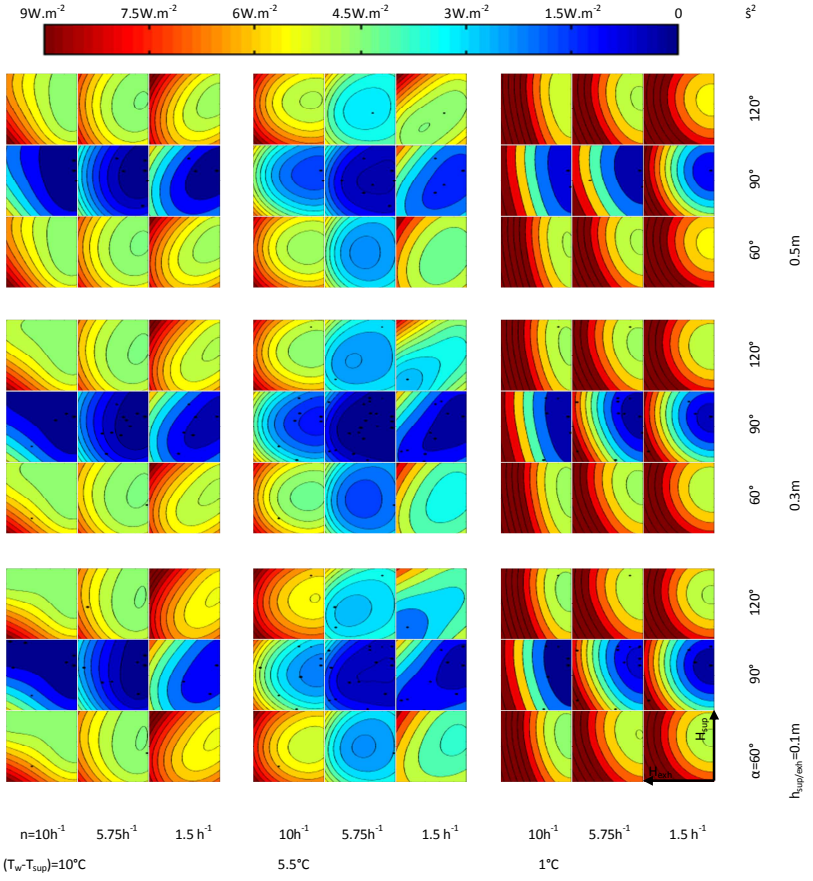

Figure 5.19: Contour plots of the prediction variance in the convective heat flux of case 'cross-floor' (for L_r=4.5m, based on 103 samples)

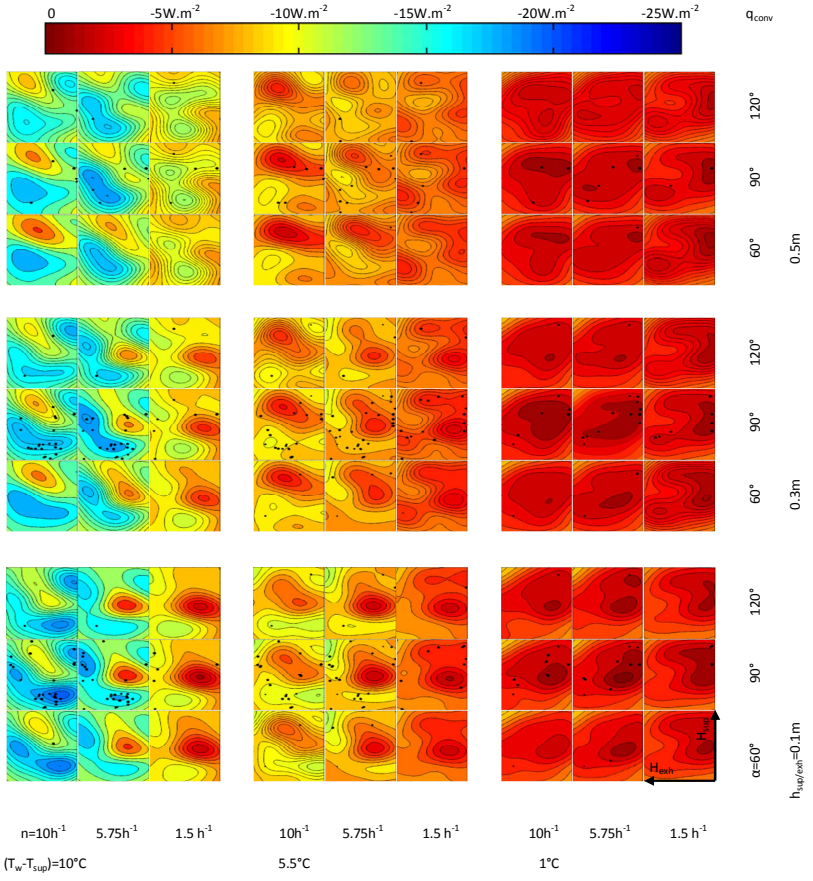

Figure 5.20: Contour plots of the convective heat flux of case 'single sided-floor' (for L_r=4.5m, based on 148 samples)

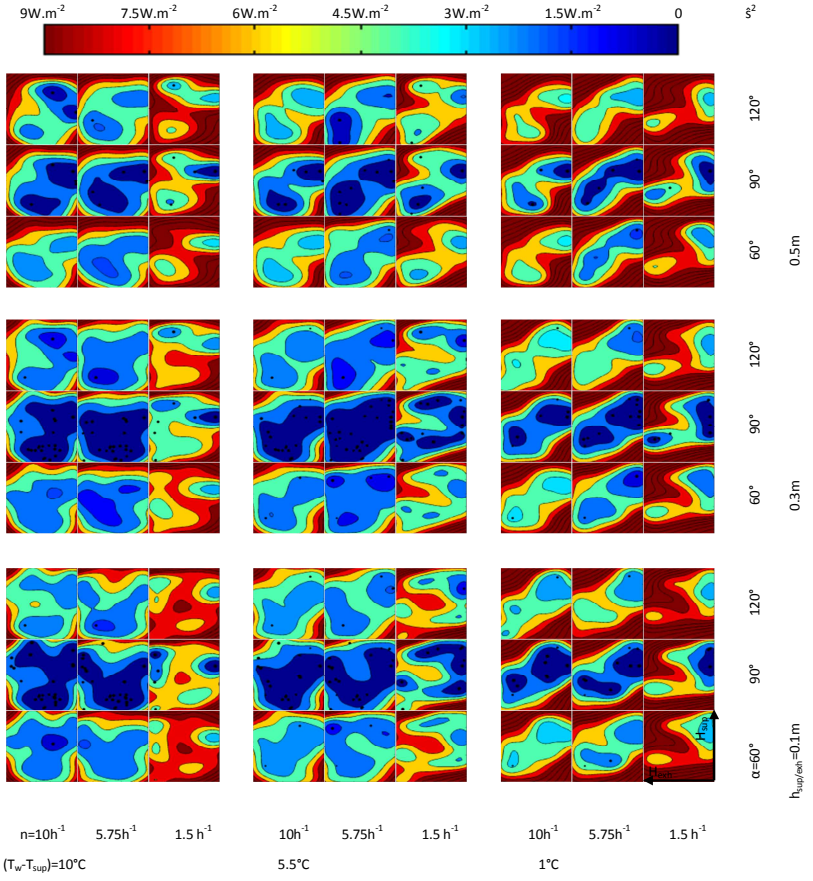

Figure 5.21: Contour plots of the prediction variance in the convective heat flux of case 'single sided-floor' (for L_r=4.5m, based on 148 samples)

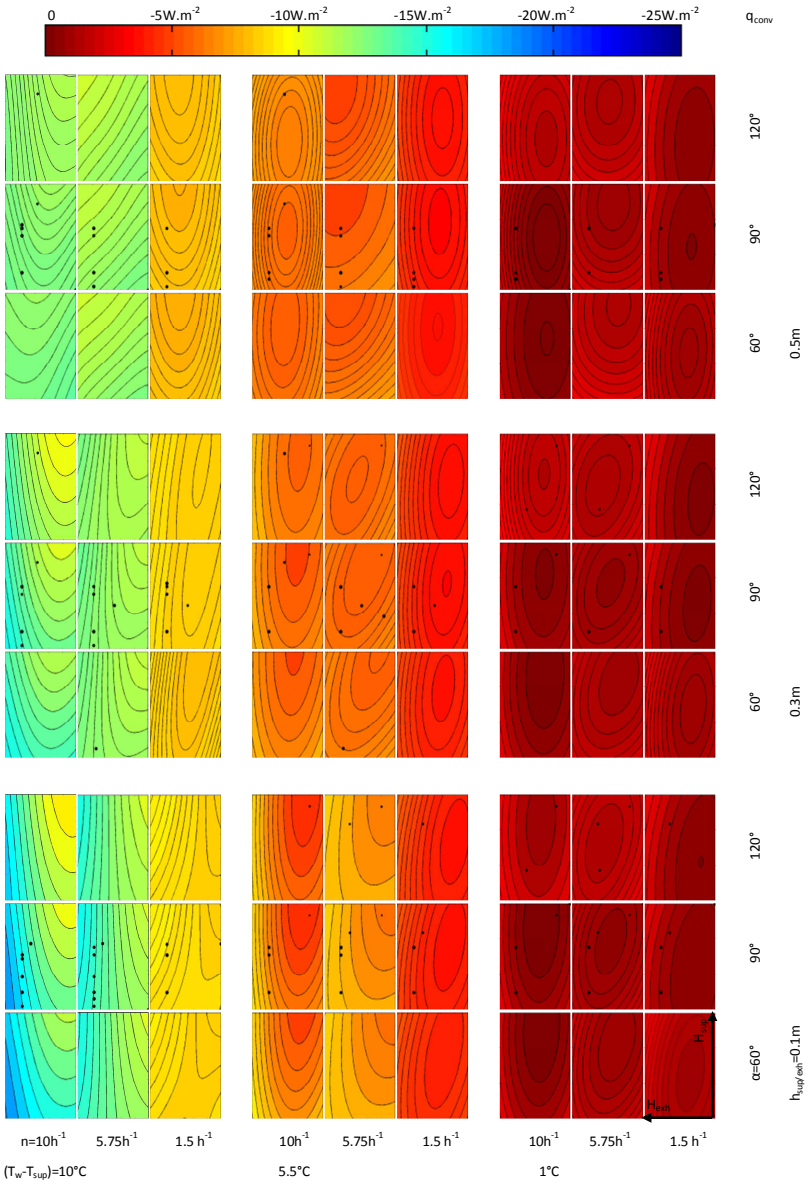

Figure 5.22: Contour plots of the convective heat flux of case 'under floor-floor' (for L_r=4.5m, based on 100 samples)

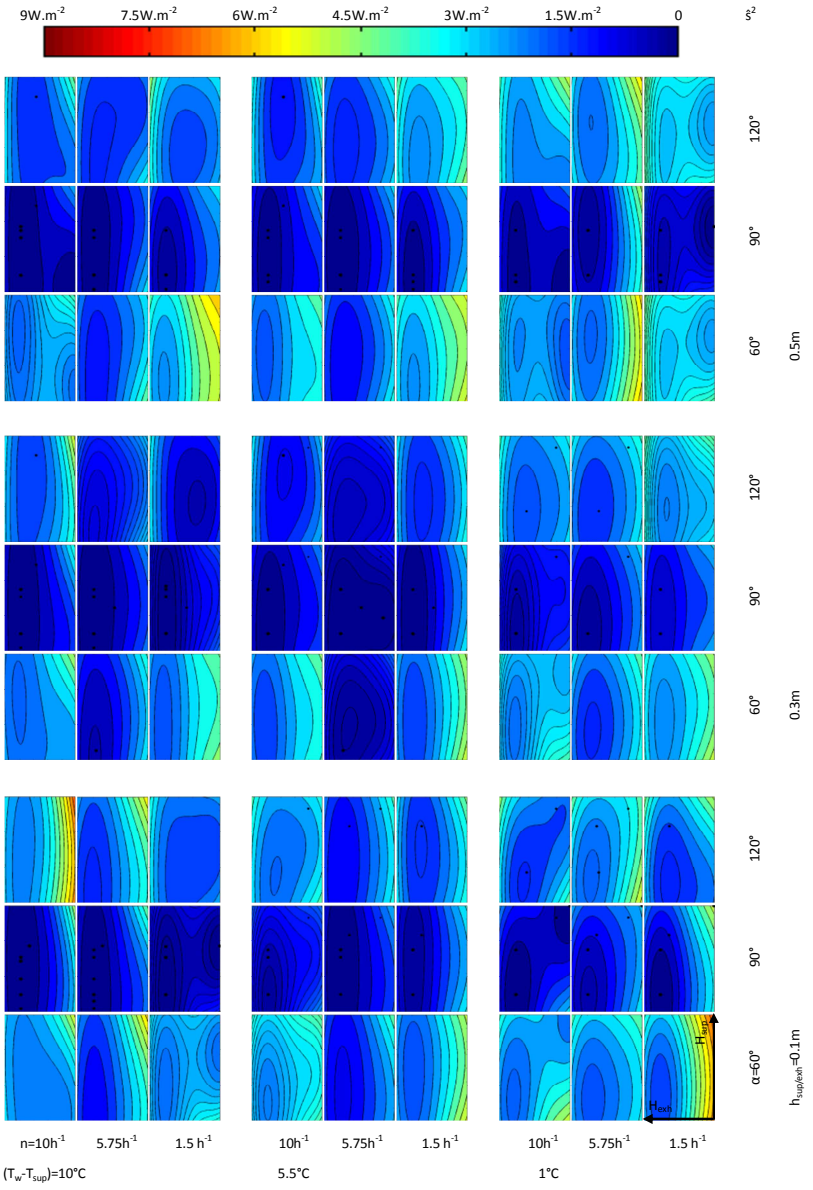

Figure 5.23: Contour plots of the prediction variance in the convective heat flux of case 'under floor-floor' (for L_r=4.5m, based on 100 samples)

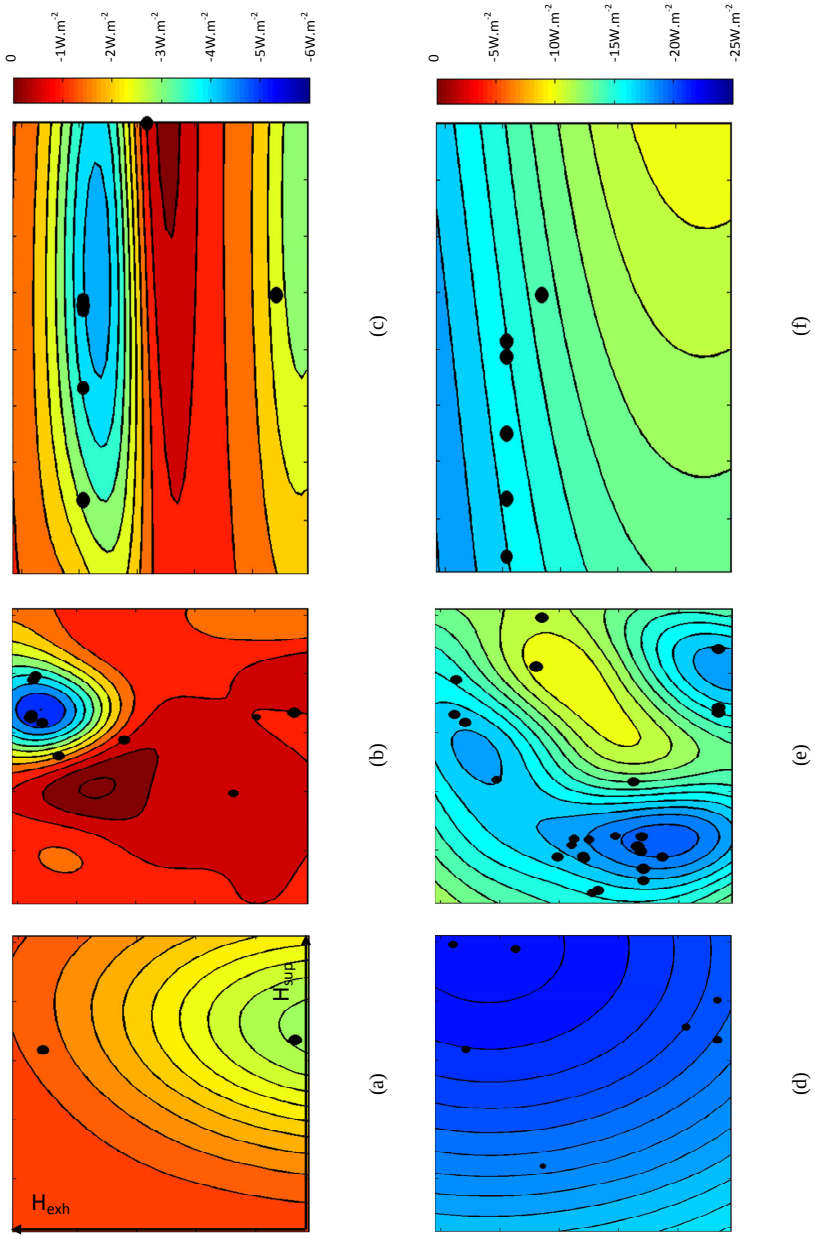

Figure 5.24: Typical contour plots of the convective heat flux of case (a) 'cross-ceiling', (b) 'single sided-ceiling', (c) 'under floor-ceiling', (d) 'cross-floor', (e) 'single sided-floor' and (f) 'under floor-floor' (for L_r=4.5m, α=90°, $h_{sup/exh}$=0.1m, (T_w-T_{sup})=10°C, n=10h^{-1})

5.4 Conclusions: optimizing the room/system design makes a difference

This work partly answered how to engineer best a night cooled landscape office and provides rough-hewn insights into the relation between the convective heat flux and the room/system design. To this end, it did not walk the beaten tracks. It deployed a fully-automated configuration of data sampling, geometry/grid generation, CFD solving and surrogate modelling to determine optimal sets of room/system design parameters. The initiating Pareto analysis revealed that increasing the air change rate augments the convective heat flux indeed. Yet, the degree of change depends on the thermal mass distribution. For example, in case of thermal mass at the ceiling, considerable air change rates are necessary to lead to an appreciable effect. What's more, in particular the thermal mass distribution determines the maximum attainable convective heat flux. Cases with thermal mass at the floor produce convective heat fluxes which are two to eighteen times as high as the ones in case of thermal mass at the ceiling. Furthermore, these well-performing cases with thermal mass at the floor are, relatively speaking, less sensitive to the geometry. And among these cases, the performance of cross ventilation surpasses the ones of both single sided ventilation and under floor ventilation. Among the cases with a thermally massive ceiling, on the other hand, single sided ventilation seems superior. However, while cross ventilation is generally a robust ventilation concept, single sided ventilation is particularly sensitive to the geometry.

The subsequent analysis of the surrogate models indicated that in general it is not a bad choice to put the air supply at the top. Either the jet stirs the air near the thermally massive ceiling or it profits from the acceleration due to gravity as it falls to the thermally massive floor. Yet, this point is much more stringent in case of a thermally massive ceiling. That is also why it is particularly important to limit the air supply height in case of a thermally massive ceiling: this increases the jet momentum. The exhaust position, on the other hand, is of little importance in case of cross ventilation. However, single sided ventilation is particularly sensitive to it: the exhaust must be located on top of the air supply or as far away as possible at the bottom to avoid short circuits between the air supply and the exhaust. Finally, under floor ventilation generally benefits from an exhaust near the ceiling. Only in case of a thermally massive ceiling, it is also necessary to limit the air supply height.

However, this does not mean that everything has been sorted out. First of all, the CFD simulations did not include radiation and, thus, most likely the inertia forces were overestimated. So e.g. the jet of an under floor ventilation system would not reach the ceiling for a given Richardson number. Further, the limited accuracy of the surrogate models hindered a complete comparison of the investigated design parameters. For example, in many cases the prediction variance was too large to assess the impact of the inclination angle of the air supply. Next to it, this pilot study left many design parameters uninvestigated. If e.g. furniture were included, there would probably be a smaller difference in convective heat flux

between the two thermal mass distributions. And finally, the findings cannot just be extrapolated to the regimes by day. During the day the predominantly natural convection heat transfer at the ceiling is usually larger than the one at the floor, certainly in case of high internal heat loads. So it could be perfectly possible that in general a case with thermal mass at the ceiling performs better than one with a thermally massive floor.

Nevertheless, these CFD-based surrogate models and surrogate modelling in conjunction with CFD in general can make a valuable contribution to the advancement of BES modelling. Either future studies can derive new convection correlations for the indicated profitable design solutions. Or a perhaps better approach is to derive more globally accurate surrogate models which can be coupled with BES. To this end, the global SBO procedure used in this study can be continued or can be used for other typical cases. Or future studies can rely on co-kriging to come more rapidly to usable surrogate models. This co-kriging strategy implies that many low-resolution simulations and a few high-res simulations are combined.

6

Conclusions and perspectives

6.1 Conclusions

Night cooling, especially in offices, attracts growing interest. For, it can improve the summer comfort and can lower the cooling need. However, the extent to which building designers succeed in finding an optimal night cooling design depends strongly on the simulation tool they use. Today, stand-alone BES programs are quite popular, but the way they model the convective heat transfer raises questions. They model this complex heat transfer by a CHTC which usually relies on case-specific experimental data. Therefore, this thesis evaluated whether this modelling approach suffices to accurately predict the night cooling performance and further investigated the impact of the room/system design on the convective heat transfer during night cooling.

The work began with a literature review which highlighted the limitations of using convection correlations in BES. First of all, the review revealed that the methodology used to derive the convection correlations narrows the limits of application. Secondly and more importantly, the literature review indicated that the correlations merely apply to specific cases. As a matter of fact, the researchers involved successively filled the major gaps: they developed correlations for distinct cases which had not been studied yet. A pragmatic approach to use convection correlations in BES nonetheless – as already suggested by a number of people, is to categorize all situations into a discrete number of regimes for which specific correlations apply. The subsequent BES-based sensitivity analysis in this thesis confirmed that such an approach is no luxury. It demonstrated that the choice of

the convection correlations can be of the same importance as the choice of design parameters.

The above approach, however, does not enable to investigate the influence of a parameter (value) other than the ones considered in the experimental setup on which the convection correlations rely. The experimental study in the PASLINK cell nicely substantiated this. These experiments revealed that especially in case of heterogeneously distributed mass the air supply/exhaust configuration has a profound influence on the convective heat transfer and that convection correlations should not be used when the setup and the convection regime differ a lot from those of the corresponding experiments. So, it is necessary to further investigate in detail how room/system design parameters affect the convective heat transfer. To this end, researchers can perform more experiments. However, experiments alone are perhaps not sufficient to study many parameters which apply to a wide range – even though they will always be needful. Fortunately, CFD can be a valuable supplement to experiments as it provides much faster, more complete results, at a reduced financial cost; on condition that CFD users make sure that the simulation tool can accurately represent reality and know how to address the inherent error sources.

Setting up CFD simulations properly is not an easy task. The IEA Annex 20 project already indicated that the largest contributor to numerical solution error is the one caused by an inadequate grid resolution and identified as key modelling error sources turbulence modelling and the description of the air supply opening(s). The literature review in underlying thesis revealed that many researchers support the use of generalized Richardson extrapolation to estimate the error due to the grid, in spite of the many shortcomings. However, the various viewpoints on which safety factor to use have not converged yet. As for turbulence, researchers have developed models which are able to cope with different indoor airflow features, but no single turbulence model can handle all flows, at least not in an economic way. Nevertheless, many CFD users put forward the linear RNG k-ε model because it would provide reasonably accurate results at an acceptable computing effort. Furthermore, to avoid the costly direct simulation of air supply diffusers, researchers have come up with a range of models. However, all can be brought down to four fundamental approaches, of which only two are truly promising. The momentum model should be used as much as possible. Only for diffusers with complex mixing such as nozzle, slot and valve diffusers, the box model would perform better. And especially this diffuser modelling deserves the attention of CFD users. The CFD-based sensitivity analysis, part of underlying thesis, revealed that the diffuser modelling approach influences the predictions considerably more than the grid and the turbulence modelling approach do. And this holds true as long as the jet dominates the indoor airflow pattern (i.e. roughly from forced to mixed convection).

Having discussed the materials of a good CFD simulation, the thesis eventually described the extensive simulation study on how the room/system design of a landscape office affects the convective heat transfer during night cooling. The surrogate models obtained indicated that the thermal mass distribution rather than the ventilation concept determines the maximum attainable convective heat flux.

Cases with thermal mass at the floor usually result in a significantly higher convective heat flux. Next to it, this study revealed that cross ventilation is the overall best performing and most robust ventilation concept if the thermal mass is located at the floor. For cases with a thermally massive ceiling however, single sided ventilation leads to the highest convective heat flux; on condition that the geometry of the room does not result in a short circuit between the air supply and the exhaust. As a matter of fact, in case of single sided ventilation the exhaust is generally best located on top of the air supply or as far away as possible at the bottom. The air supply should be at the top, and this also holds for cross ventilation. Under floor ventilation usually benefits from an exhaust near the ceiling and in case of a thermally massive ceiling from a limited air supply height. However, this does not mean everything has been sorted out. The limited global accuracy of the surrogate models hindered a complete comparison. Next to it, this study left many design parameters uninvestigated and, finally, the findings cannot just be extrapolated to the regimes by day.

6.2 Perspectives

In particular with the global surrogate-based optimization study, this work contributes to the advancement of BES modelling. On the one hand, the derived CFD-based surrogate models can help to refine existing correlations or develop new ones. As a matter of fact, these surrogate models not only highlight the optimal design solutions, they also roughly demonstrate the importance of the room/system design parameters. On the other hand, a perhaps more profitable application is to couple such surrogate models with BES. To this end, the surrogate models derived in this study can be refined by continuing the global SBO procedure. This will lead to globally more accurate surrogate models. Also new surrogate models can be derived for different sets of room/system design parameters (e.g. inclusion of a heat source, several diffuser types), perhaps with the aid of more complex CFD simulation models (e.g. 3-D, with longwave radiation modelling). In this case, the framework developed in this work can be deployed. Or these future studies can rely on co-kriging to come more rapidly to usable surrogate models.

Publications

Journal publications as first author

K. Goethals, A. Janssens, Quasi-steady-state bepalingsmethode: opengaande ramen in kantoren en scholen, TVVL-magazine, 40 (2) (2010) 40-45.

K. Goethals, H. Breesch, A. Janssens, Sensitivity analysis of predicted night cooling performance to internal convective heat transfer modeling, Energy and Buildings, 43 (9) (2011) 2429-2441.

K. Goethals, M. Delghust, G. Flamant, M. De Paepe, A. Janssens, Experimental investigation of the impact of room/system design on mixed convection heat transfer, Accepted for publication in Energy and Buildings.

K. Goethals, I. Couckuyt, T. Dhaene, A. Janssens, Sensitivity of night cooling performance to room/system design: surrogate models based on CFD, Submitted to Building and Environment.

Publications in proceedings of conferences as first author

K. Goethals, A. Janssens, Sensitivity analysis of thermal performance to convective heat transfer at internal building surfaces, in: Building Physics Symposium in honour of Prof. H. Hens, Leuven, 2008, pp. 147-150.

K. Goethals, A. Janssens, Sensitivity analysis of thermal predictions to the modelling of direct solar radiation entering a zone, in: Roomvent 2009: 11th international conference on air distribution in rooms, Busan, 2009, pp. 1179-1186.

K. Goethals, A. Janssens, Sensitivity analysis of predicted convective heat transfer at internal building surfaces to diffuser modelling in CFD, in: Building Simulation 2009: 11th international IBPSA conference and exhibition, Glasgow, 2009, pp. 450-457.

K. Goethals, A. Janssens, Turbulent mixed convection cooling in an enclosure with different inlet and outlet configurations, in: CLIMA 2010: 10th REHVA world congress, Antalya, 2010.

K. Goethals, A. Janssens, Quasi-steady-state calculation method of temporary increased ventilation during daytime, in: 1st Central European symposium on buildings physics, Cracow, 2010, pp. 477-484.

K. Goethals, A. Janssens, Quasi-steady-state maandgemiddelde bepalingsmethode van de impact van opengaande ramen in kantoor- en schoolgebouwen, in: Verslagen van IBPSA-NVL event, Eindhoven, 2010.

K. Goethals, A. Janssens, Mixed convection cooling in an enclosure with different inlet and outlet configurations, in: Buildair 2010: 5th international symposium on building and ductwork airtightness, Copenhagen/Lyngby, 2010.

K. Goethals, A. Janssens, Evaluation of the applicability of the overheating indicator for offices and schools, in: NSB 2010: 9th Nordic symposium on building physics, Tampere, 2011, pp. 1185-1192.

K. Goethals, A. Janssens, Experimental analysis of the impact of room/system design on night ventilation performance, in: Roomvent 2011: 12th international conference on air distribution in rooms, Trondheim, 2011.

K. Goethals, M. Delghust, G. Flamant, M. De Paepe, A. Janssens, Experimental investigation of the impact of room/system design on night cooling performance, in: 5th international building physics conference, Accepted, Kyoto, 2012.

K. Goethals, I. Couckuyt, A. Janssens, T. Dhaene, Sensitivity of night cooling performance to room/system design: surrogate models based on CFD, in: 5th international building physics conference, Accepted, Kyoto, 2012.

Publications in proceedings of conferences as co-author

J. Laverge, K. Goethals, A. Janssens, *Convective heat transfer coefficients in mechanical ventilation: a sensitivity analysis*, in: Roomvent 2009: 11th international conference on air distribution in rooms, Busan, 2009, pp. 313-318.

H. Breesch, K. Goethals, A. Janssens, *Development of a quasi-steady-state assessment method of night cooling*, in: NSB 2011: 9th Nordic symposium on building physics, Tampere, 2011, pp. 1177-1184.

References

[1] Contribution of working groups I, II and III to the fourth assessment report of the intergovernmental panel on climate change, IPCC, Geneva, 2007.
[2] International Energy Agency, World energy outlook 2008, Paris, 2008.
[3] United Nations, Kyoto protocol to the United Nations framework convention on climate change, Kyoto, 1998, pp. 20.
[4] European Commission, The EU climate and energy package.
[5] Directorate-General for Energy and Transport, European energy and transport trends to 2030 - Update 2007, in, Office for Official Publications of the European Communities, 2007, pp. 156.
[6] Department of Trade and Industry, Energy consumption in the United Kingdom, London, 2001, pp. 46.
[7] Japan Air Conditioning and Refrigeration News, Japan Refrigeration and Air Conditioning Industry Association, Estimates of world demand for air conditioners, Tokyo, 2005.
[8] R. Thomas, Environmental design: an introduction for architects and engineers, Spon Press, 1996, pp. 240.
[9] P. Waide, J. Adnot, Energy efficiency and certification of central air conditioners, Armines, 2003, pp. 91.
[10] M. Santamouris, Passive cooling of buildings, Advances of solar energy, (2005) 57.
[11] M. Christenson, H. Manz, D. Gyalistras, Climate warming impact on degree-days and building energy demand in Switzerland, Energy Conversion and Management, 47 (6) (2006) 671-686.

[12] D.H. Rosenthal, H.K. Gruenspecht, E.A. Moran, Effects of global warming on energy use for space heating and cooling in the United States, The Energy Journal, 16 (2) (1995) 77-96.
[13] D.B. Belzer, M.J. Scott, R.D. Sands, Climate change impacts on US commercial building energy consumption: an analysis using sample survey data, Energy Sources, 18 (1996) 117-140.
[14] S. Pretlove, T. Oreszczyn, Climate change: impact on the environmental design of buildings, Building Services Engineering Research and Technology, 19 (1) (1998) 58-61.
[15] C. Cartalis, A. Synodinou, M. Proedrou, A. Tsangrassoulis, M. Santamouris, Modifications in energy demand in urban areas as a result of climate changes: an assessment for the southeast Mediterranean region, Energy Conversion and Management, 42 (14) (2001) 1647-1656.
[16] T. Frank, Climate change impacts on building heating and cooling energy demand in Switzerland, Energy and Buildings, 37 (11) (2005) 1175-1185.
[17] Cooling our communities: a guidebook on tree planting and light-coloured surfacing, in: H. Akbari, S. Davis, S. Dorsano, J. Huang, S. Winnett (Eds.), Lawrence Berkeley National Laboratory, Berkeley, 1992, pp. 217.
[18] M. Kolokotroni, I. Giannitsaris, R. Watkins, The effect of the London urban heat island on building summer cooling demand and night ventilation strategies, Solar Energy, 80 (4) (2006) 383-392.
[19] M. Santamouris, Natural ventilation in urban areas, AIVC Ventilation information paper, (2004) 10.
[20] M.A. Humphreys, Field studies of thermal comfort compared and applied, Building Services Engineering Research and Technology, 44 (1976) 5-27.
[21] J.L. Stoops, The physical environment and occupant thermal perceptions in office buildings - an evaluation of sampled data from five European countries, Chalmers University of Technology, 2001.
[22] E. Shove, Comfort, cleanliness and convenience, Berg, Oxford, 2003.
[23] C.J. Andrews, Anticipating air conditioning's impact on the world's electricity producers, The Energy Journal, 10 (3) (1989) 107-120.
[24] C.J. Schweiger, A new absorption chiller to establish combined cold, ASHRAE Transactions, 102 (1) (1996) 10.
[25] J. Hernandez-Santoyo, A. Sanchez-Cifuentes, Trigeneration: an alternative for energy savings, Applied Energy, 76 (1-3) (2003) 219-227.
[26] M. Santamouris, D. Assimakopoulos, Passive cooling of buildings, James and James Science Publishers, London, 1996.
[27] M.D. Ruud, J.W. Mitchel, S.A. Klein, Use of building thermal mass to offset cooling loads, ASHRAE Transactions, 96 (2) (1990) 10.
[28] F. Allard, E. Dascalaki, K. Limam, M. Santamouris, Natural ventilation studies within the EC PASCOOL Joule II project, Air Infiltration Review, 17 (4) (1996) 1-4.
[29] P. Blondeau, M. Sperandio, F. Allard, Night ventilation for building cooling in summer, Solar Energy, 61 (5) (1997) 327-335.
[30] M. Zimmermann, J. Andersson, Annex 28: Low energy cooling - Case study buildings, 1998.

[31] R.Z. Høseggen, Dynamic use of the building structure - Energy performance and thermal environment, Norwegian University of Science and Technology, 2007.
[32] M. Kolokotroni, A. Aronis, Cooling-energy reduction in air-conditioned offices by using night ventilation, Applied Energy, 63 (4) (1999) 241-253.
[33] E. Shaviv, A. Yezioro, I.G. Capeluto, Thermal mass and night ventilation as passive cooling design strategy, Renewable Energy, 24 (3-4) (2001) 445-452.
[34] B. Givoni, Passive low energy cooling of buildings, Van Nostrand Reinhold, New York, 1994.
[35] C.A. Balaras, The role of thermal mass on the cooling load of buildings. An overview of computational methods, Energy and Buildings, 24 (1) (1996) 1-10.
[36] B. Givoni, Effectiveness of mass and night ventilation in lowering the indoor daytime temperatures. Part I: 1993 experimental periods, Energy and Buildings, 28 (1) (1998) 25-32.
[37] H. Breesch, Natural night ventilation in office buildings - Performance evaluation based on simulation uncertainty and sensitivity analysis, Ghent University, 2006.
[38] J. Laverge, K. Goethals, A. Janssens, Convective heat transfer coefficients in mechanical ventilation: a sensitivity analysis, in: Roomvent 2009: 11th international conference on air distribution in rooms, Busan, 2009, pp. 313-318.
[39] S. Szokolay, Passive and low energy design for thermal and visual comfort - Passive and low energy ecotechniques, in: International PLEA conference, Mexico City, 1984, pp. 8.
[40] J. Pfafferott, S. Herkel, M. Jaschke, Design of passive cooling by night ventilation: evaluation of a parametric model and building simulation with measurements, Energy and Buildings, 35 (11) (2003) 1129-1143.
[41] J. Van der Maas, F. Flourentzou, Passive cooling by night ventilation, in: European conference on energy performance and indoor climate in buildings, Lyon, 1994.
[42] S. Goulart, Thermal inertia and natural ventilation - Optimisation of thermal storage as a cooling technique for residential building in Southern Brazil, Architectural Association School of Architecture, 2004.
[43] C. Diaz, Climate-responsive design for non-domestic buildings in warm climates - Optimisation of thermal mass for indoor cooling, Architectural Association School of Architecture, 1994.
[44] E. Maldonado, S. Yannas, H. Goncalves, Studies of the thermal performance of buildings in summer in southern Europe, International Journal of Sustainable Energy, 19 (1) (1997) 161-178.
[45] V. Soebarto, A new approach to passive design for residential buildings in a tropical climate, in: International PLEA conference, Brisbane, 1999.
[46] S. Szokolay, Dilemmas of warm-humid climate house design: heavy versus lightweight and cooling effect of air movement, in: International PLEA conference, Cambridge, 2000.
[47] J. Axley, S. Emmerich, A method to assess the suitability of a climate for natural ventilation of commercial buildings, in: Indoor Air, Monterey, 2002.

[48] N. Artmann, H. Manz, P. Heiselberg, Climatic potential for passive cooling of buildings by night-time ventilation in Europe, Applied Energy, 84 (2) (2007) 187-201.
[49] S. Roaf, P. Haves, J. Orr, Climate change and passive cooling in Europe, in: International PLEA conference, Lisbon, 1998, pp. 4.
[50] U. Eicker, M. Huber, P. Seeberger, C. Vorschulze, Limits and potentials of office building climatisation with ambient air, Energy and Buildings, 38 (6) (2006) 574-581.
[51] A. Loudon, Summertime temperatures in buildings, Building Research Establishment, Watford, 1968.
[52] J. Balcomb, R. Jones, Workbook for workshop on advanced passive solar design, Balcomb Solar Associates, Bled, 1988.
[53] H. Asan, Investigation of wall's optimum insulation position from maximum time lag and minimum decrement factor point of view, Energy and Buildings, 32 (2) (2000) 197-203.
[54] E. Kossecka, J. Kosny, Influence of insulation configuration on heating and cooling loads in a continuously used building, Energy and Buildings, 34 (4) (2002) 321-331.
[55] J. Balcomb, Heat storage and distribution inside passive solar buildings, Los Alamos National Laboratory, Los Alamos, 1983.
[56] M. Kolokotroni, Annex 28: low energy cooling - Night ventilation in commercial buildings, 1995.
[57] C.A. Balaras, Heat attenuation, in: M. Santamouris, D. Assimakopoulos (Eds.) Passive cooling in buildings, James and James, London, 1996, pp. 35.
[58] B. Givoni, Performance and applicability of passive and low-energy cooling systems, Energy and Buildings, 17 (3) (1991) 177-199.
[59] V. Gerosa, M. Santamouris, A. Tsangrasoulis, G. Guarracino, Experimental evaluation of night ventilation phenomena, Energy and Buildings, 29 (2) (1999) 141-154.
[60] CIBSE guide A: environmental design, The Chartered Institution of Building Services Engineers, London, 2006.
[61] J. Franke, A. Hellsten, H. Schlünzen, B. Carissimo, COST - Best practice guideline for the CFD simulation of flows in the urban environment, University of Hamburg, Hamburg, 2007.
[62] T. Cebecci, P. Bradshaw, Physical and computational aspects of convective heat transfer, First ed., Springer-Verlag, New York, 1984.
[63] H. Schlichting, K. Gersten, Boundary layer theory, Eight ed., Springer-Verlag, Berlin, 2000.
[64] J. Hensen, Application of modelling and simulation to HVAC systems, in: 30th international conference MOSIS, Technical University of Ostrava, Krnov, 1996, pp. 1-6.
[65] J.A. Clarke, Energy simulation in building design, Second ed., Butterworth-Heinemann, Oxford, 2001.
[66] L.G. Spielvogel, Comparisons of energy analysis computer programs, Building Services Engineering Research and Technology, 2 (1) (1981).

[67] R.D. Busch, Methods of energy analysis, in: B.D. Hunn (Ed.) Fundamentals of building energy dynamics, MIT Press, Cambridge, 1996, pp. 448.
[68] J.L.M. Hensen, N. Nakahara, Energy and building performance simulation: current state and future issues - Preface, Energy and Buildings, 33 (4) (2001) VII-IX.
[69] J.W. Hand, The ESP-r cookbook, Energy Systems Research Unit, Glasgow, 2008.
[70] University of Illinois, Lawrence Berkeley National Laboratory, EnergyPlus, in, 2009.
[71] S. Citherlet, J. Hand, Assessing energy, lighting, room acoustics, occupant comfort and environmental impacts performance of building with a single simulation program, Building and Environment, 37 (8-9) (2002) 845-856.
[72] D. Bourgeois, C. Reinhart, I. Macdonald, Adding advanced behavioural models in whole building energy simulation: a study on the total energy impact of manual and automated lighting control, Energy and Buildings, 38 (7) (2006) 814-823.
[73] P. Steskens, Modelling of the hygrothermal interactions in between the indoor environment and the building envelope, Technical University of Denmark, 2009.
[74] M. Steeman, Hygrothermal modelling for building energy simulation applications, Ghent University, 2010.
[75] The Royal Institute of Technology, BRIS, Stockholm, 1963.
[76] General American Transportation Corporation, Computer program for analysis of energy utilization in postal facilities: user's manual, Niles, 1967.
[77] D.G. Stephenson, G.P. Mitalas, Cooling load calculations by thermal response factor, ASHRAE Transactions, 73 (1) (1967) 8.
[78] R.a.A.-C.E. American Society of Heating, Inc., ASHRAE Handbook - Fundamentals, 2009.
[79] T. Kusuda, NBSLD: the computer program for heating and cooling loads in buildings, in: NBS Building Science, National Bureau of Standards, Washington, 1976.
[80] D.J. McLean, The simulation of solar energy systems, University of Strathclyde, 1982.
[81] D. Tang, Modelling of heating and air conditioning systems, University of Strathclyde, 1985.
[82] T.W. Maver, J.A. Clarke, Major extensions to the ESP system, in: Science and Engineering Research Council (Ed.), Glasgow, 1984.
[83] G.N. Walton, Thermal analysis research program reference manual, in: US Department of Energy (Ed.), Washington D.C., 1983.
[84] Physibel, Capsol: multizone transient heat transfer, Maldegem, 2002.
[85] Solar Energy Laboratory, TRNSYS 16.01 - A transient system simulation program, Madison, 2006.
[86] National Institute of Standards and Technology, CONTAM - Multizone modeling software, Gaithersburg.
[87] Lawrence Berkeley National Laboratory, COMIS, Berkeley, 1988.

[88] F. Haghighat, A.C. Megri, A comprehensive validation of two airflow models - COMIS and CONTAM, International Journal of Indoor Air Quality and Climate, 6 (4) (1996) 278-288.
[89] R. Upham, A validation study of the airflow and contaminant migration computer model CONTAM as applied to tall buildings, Pennsylvania State University, Pennsylvania, 1997.
[90] S. Emmerich, Validation of multizone IAQ modelling of residential-scale buildings: a review, ASHRAE Transactions, 107 (2) (2001) 618-625.
[91] L.Z. Wang, Q.Y. Chen, Evaluation of some assumptions used in multizone airflow network models, Building and Environment, 43 (10) (2008) 1671-1677.
[92] Solar Energy Laboratory, TRNSYS 17.01 - A transient system simulation program, Madison, 2011.
[93] H. Bouia, Modélisation simplifiée d'écoulements de convection mixte internes: application aux échanges thermo-aérauliques dans les locaux, Université de Poitiers, 1993.
[94] E. Wurtz, J. Nataf, F.C. Winkelmann, Two and three-dimensional natural and mixed convection simulation using modular zonal models in buildings, International Journal of Heat and Mass Transfer, 42 (1999) 923-940.
[95] C. Inard, Contribution à l'étude due couplage thermique entre un émetteur de chauffage et un local. Etudes expérimentales en chambres climatiques, National Institute of Applied Sciences, 1988.
[96] C. Inard, H. Bouia, P. Dalicieux, Prediction of air temperature distribution in buildings with a zonal model, Energy and Buildings, 24 (2) (1996) 125-132.
[97] M. Musy, Automatic generation of zonal models to perform airflow and thermal simulation in buildings, University of La Rochelle, 1999.
[98] F.T.M. Nieuwstadt, J.G.M. Eggels, R.J.A. Janssen, M.B.J.M. Pourquie, Direct and large-eddy simulations of turbulence in fluids, Future Generation Computer Systems, 10 (2-3) (1994) 185-205.
[99] F. Off, A. Moser, P. Suter, Transient numerical modelling of heat transfer by radiation and convection in an atrium with thermal inertia, in: Roomvent 1996: 5th international conference on air distribution in rooms, Yokohama, 1996, pp. 6.
[100] L. Mora, J. Gadgil, E. Wurtz, Comparing zonal and CFD model predictions of isothermal indoor airflows to experimental data, International Journal of Indoor Environment and Health, 13 (2) (2003) 77-85.
[101] C.O.R. Negrao, Conflation of computational fluid dynamics and building thermal simulation, University of Strathclyde, 1995.
[102] I. Beausoleil-Morrison, The adaptive coupling of heat and air flow modelling within dynamic whole-building simulation, University of Strathclyde, 2000.
[103] A. Novoselac, Combined airflow and energy simulation program for building mechanical system design, Pennsylvania State University, 2005.
[104] J. Niu, J. van der Kooi, Grid optimization of k-ε turbulence model simulation of natural convection in rooms, in: Roomvent 1992: 3rd international conference on air distribution in rooms, Aalborg, 1992, pp. 17.
[105] H.B. Awbi, Calculation of convective heat transfer coefficients of room surfaces for natural convection, Energy and Buildings, 28 (2) (1998) 219-227.

[106] G.P. Hammond, Profile analysis of heat/mass transfer across the plane wall jet, in: 7th international heat transfer conference, Munich, 1982, pp. 349-355.
[107] C.K.G. Lam, K. Bremhorst, A modified form of the k-ε model for predicting wall turbulence, Journal of Fluids Engineering-Transactions of the ASME, 103 (3) (1981).
[108] V.C. Patel, W. Rodi, G. Scheuerer, Turbulence models for near-wall and low Reynolds-number flows - A review, AIAA Journal, 23 (9) (1985) 1308-1319.
[109] H.C. Chen, V.C. Patel, Near-wall turbulence models for complex flows including separation, AIAA Journal, 26 (6) (1988) 641-648.
[110] K. Goethals, H. Breesch, A. Janssens, Sensitivity analysis of predicted night cooling performance to internal convective heat transfer modelling, Energy and Buildings, 43 (9) (2011) 2429-2441.
[111] ASHRAE, ASHRAE Handbook - Fundamentals, 2009.
[112] NBN, NBN EN ISO 13791: thermal performance of buildings - Internal temperatures in summer of a room without mechanical cooling - General criteria and calculation procedures, in, Brussels, 2008.
[113] J.A. Clarke, Internal convective heat transfer coefficients: a sensitivity study, University of Strathclyde, Glasgow, 1991.
[114] A.J.N. Khalifa, Natural convective heat transfer coefficient - a review II. Surfaces in two- and three-dimensional enclosures, Energy Conversion and Management, 42 (4) (2001) 505-517.
[115] K.J. Lomas, C. Martin, H. Eppel, M. Watson, D. Bloomfield, Empirical validation of thermal building simulation programs using test room data - Volume 1: final report, International Energy Agency, 1994.
[116] S.R. Delaforce, E.R. Hitchin, D.M.T. Watson, Convective heat transfer at internal surfaces, Building and Environment, 28 (2) (1993) 211-220.
[117] K.J. Lomas, The UK applicability study: an evaluation of thermal simulation programs for passive solar house design, Building and Environment, 31 (3) (1996) 197-206.
[118] G. Clark, Passive cooling systems, in: J. Cook (Ed.) Passive cooling, MIT Press, Cambridge, 1989, pp. 92.
[119] N. Artmann, H. Manz, P. Heiselberg, Parameter study on performance of building cooling by night-time ventilation, Renewable Energy, 33 (12) (2008) 2589-2598.
[120] F. Alamdari, G.P. Hammond, Improved data correlations for buoyancy-driven convection in rooms, Building Services Energy Research and Technology, 4 (3) (1983) 106-112.
[121] S.W. Churchill, R. Usagi, General expression for correlation of rates of transfer and other phenomena, AIChE Journal, 18 (6) (1972) 1121-&.
[122] P. Arnold, G.P. Hammond, A. Irving, C. Martin, The influence of sun patches on buoyancy-driven air movement and heat transfer within a passive solar test cell, Proceedings of ASME heat transfer division, 361 (1) (1998) 47-57.
[123] A.J.N. Khalifa, R.H. Marshall, Validation of heat transfer coefficients on interior buildings surfaces using a real-sized indoor test cell, International Journal of Heat and Mass Transfer, 33 (10) (1990) 2219-2236.

[124] H.B. Awbi, A. Hatton, Natural convection from heated room surfaces, Energy and Buildings, 30 (3) (1999) 233-244.
[125] A.J.N. Khalifa, Heat transfer processes in buildings, University of Wales College, 1989.
[126] J.D. Spitler, C.O. Pedersen, D.E. Fisher, Interior convective heat transfer in buildings with large ventilative flow rates, ASHRAE Transactions, 97 (1991) 505-515.
[127] J.D. Spitler, C.O. Pedersen, D.E. Fisher, P.F. Menne, J. Cantillo, An experimental facility for investigation of interior convective heat transfer, ASHRAE Transactions, 97 (1991) 497-504.
[128] D.E. Fisher, An experimental investigation of mixed convection heat transfer in a rectangular enclosure, University of Illinois, 1995.
[129] H.B. Awbi, A. Hatton, Mixed convection from heated room surfaces, Energy and Buildings, 32 (2) (2000) 153-166.
[130] L. Neiswanger, G.A. Johnson, V.P. Carey, An experimental study of high Rayleigh number mixed convection in a rectangular enclosure with restricted inlet and outlet openings, Journal of Heat Transfer-Transactions of the ASME, 109 (2) (1987) 446-453.
[131] D.E. Fisher, C.O. Pederson, Convective heat transfer in building energy and thermal load calculations, ASHRAE Transactions, 103 (2) (1997) 137-148.
[132] H. Breesch, A. Janssens, Performance evaluation of passive cooling in office buildings based on uncertainty and sensitivity analysis, Solar Energy, 84 (8) (2010) 1453-1467.
[133] J.E. Seem, Modeling of heat transfer in buildings, University of Wisconsin-Madison, 1987.
[134] X.Q. Li, Y. Chen, J.D. Spitler, D. Fisher, Applicability of calculation methods for conduction transfer function of building constructions, International Journal of Thermal Sciences, 48 (7) (2009) 1441-1451.
[135] R.D. Taylor, C.O. Pedersen, D.E. Fisher, R.J. Liesen, L.K. Lawrie, Impact of simultaneous simulation of building and mechanical systems in heat balance based energy analysis programs, in: 3rd international conference on system simulation in buildings, Liege, 1990.
[136] NBN, NBN B 62-002: calculation of thermal transmittance coefficients of walls and buildings, Brussels, 2008.
[137] BBRI, Insulation, ventilation and heating in newly built dwellings: results of a survey, Brussels, 1999.
[138] A. Litvak, M. Kilberger, K. Guillot, Field measurement results of the air tightness of 64 French dwellings, in: Roomvent 2000: 7th international conference on air distribution in rooms, Reading, 2000, pp. 1093-1098.
[139] A. Litvak, M. Kilberger, K. Guillot, D. Boze, Air tightness of French dwellings: results from field measurement studies, in: 21th AIVC conference, AIVC, The Hague, 2000.
[140] A. Martin, J. Fletcher, Night cooling strategies, in: Final report 11621/4, BSRIA, Berkshire, 1996.
[141] ISSO, Research report 32: assumptions for thermal simulations, Rotterdam, 1994.

[142] K. Goethals, J. Laverge, A. Janssens, Sensitivity analysis of thermal predictions to the modelling of direct solar radiation entering a zone, in: K.W. Kim, B.W. Olesen (Eds.) Roomvent 2009: 11th international conference on air distribution in rooms, Busan, 2009.
[143] P. Wilkins, M. Hosni, Heat gain from office equipment, ASHRAE Journal, 42 (6) (2000) 33-43.
[144] K. van der Linden, A.C. Boerstra, A.K. Raue, S.R. Kurvers, Thermal indoor climate building performance characterized by human comfort response, Energy and Buildings, 34 (7) (2002) 737-744.
[145] A.C. van der Linden, A.C. Boerstra, A.K. Raue, S.R. Kurvers, R.J. de Dear, Adaptive temperature limits: a new guideline in The Netherlands: a new approach for the assessment of building performance with respect to thermal indoor climate, Energy and Buildings, 38 (1) (2006) 8-17.
[146] K. Goethals, M. Delghust, G. Flamant, M. De Paepe, A. Janssens, Experimental investigation of the impact of room/system design on mixed convection heat transfer, Accepted for publication in Energy and Buildings.
[147] L. Peeters, I. Beausoleil-Morrison, A. Novoselac, Internal convective heat transfer modeling: critical review and discussion of experimentally derived correlations, Energy and Buildings, 43 (9) (2011) 2227-2239.
[148] N. Artmann, R.L. Jensen, H. Manz, P. Heiselberg, Experimental investigation of heat transfer during night-time ventilation, Energy and Buildings, (2010) 366-374.
[149] P. Wouters, L. Vandaele, P. Voit, N. Fisch, The use of outdoor test cells for thermal and solar building research within the PASSYS project, Building and Environment, 28 (2) (1993) 107-113.
[150] L. Vandaele, P. Wouters, The PASSYS Services, Summary report of the PASSYS Project, BBRI, Brussels, 1994.
[151] E. Maldonado, Upgrading PASSYS test cells with a pseudo-adiabatic shell (construction manual), University of Porto, Porto, 1995.
[152] E. Hahne, R. Pfluger, Improvements on PASSYS test cells, Solar Energy, 58 (4-6) (1996) 239-246.
[153] Trox UK Ltd., http://www.troxuk.co.uk/uk/products/air_diffusers/air_grilles/at/index.html, 2011.
[154] DIN, DIN 4715: raumkühlflächen - Leistungsmessung bei freier Strömung Prüfregeln, Berlin, 1993.
[155] D. Zukowska, A. Melikov, Thermal plume above a simulated sitting person with different complexity of body geometry, in: Roomvent 2007: 10th international conference on air distribution in rooms, FINVAC, Helsinki, 2007, pp. 191-198.
[156] W.K.P. van Loon, H.M.H. Bastings, E.J. Moors, Calibration of soil heat flux sensors, Agricultural and Forest Meteorology, 92 (1) (1998) 1-8.
[157] NBN, NBN EN ISO 6946: building components and building elements - Thermal resistance and thermal transmittance - Calculation method, Brussels, 2009.
[158] R. Siegel, J. Howell, Thermal radiation heat transfer, Fourth ed., Taylor & Francis, New York, 2002.

[159] A. Zukauskas, J. Ziugdza, Heat transfer of a cylinder in crossflow, Hemisphere Publishing, New York, 1985.
[160] V.T. Morgan, The overall convective heat transfer from smooth circular cylinders, Advances of heat transfer, 11 (1975) 1999-1264.
[161] A.B. Wang, Z. Travnicek, On the linear heat transfer correlation of a heated circular cylinder in laminar crossflow using a new representative temperature concept, International Journal of Heat and Mass Transfer, 44 (2001) 4635-4647.
[162] G.K. Sharma, S.P. Sukhatme, Combined free and forced convection heat transfer from a heated tube to a transverse air stream, Journal of Heat Transfer-Transactions of the ASME, 91 (1969) 457-459.
[163] V.T. Morgan, The overall convective heat transfer from smooth circular cylinders, Advances in Heat Transfer, 11 (1975) 199-264.
[164] A.P. Hatton, D.D. James, H.W. Swire, Combined forced and natural convection with low-speed air flow over horizontal cylinders, Journal of Fluid Mechanics, 42 (1970) 17-31.
[165] th-industrie, http://th-industrie.com, 2010.
[166] ASHRAE, ANSI/ASHRAE standard 70-2006: method of testing for rating the performance of air outlets and inlets, Atlanta, 2006.
[167] S.H. Patankar, Numerical heat transfer and fluid flow, First ed., Hemisphere Publishing Corporation, Washington, New York, London, 1980.
[168] Physibel, VOLTRA: 3D transient heat transfer, Maldegem.
[169] D. Shepard, A two-dimensional interpolation function for irregularly-spaced data, in: 23rd national conference ACM, ACM, New York, 1968, pp. 517-524.
[170] K.J. Lomas, H. Eppel, Sensitivity analysis techniques for building thermal simulation programs, Energy and Buildings, 19 (1) (1992) 21-44.
[171] N. Bowler, Y.Q. Huang, Model-based characterization of homogeneous metal plates by four-point alternating current potential drop measurements, IEEE Transactions on Magnetics, 41 (6) (2005) 2102-2110.
[172] CEN, EN 13163: thermal insulation products for buildings - Factory made products of expanded polystyrene (EPS) - Specification, Brussels, 2008.
[173] BS, BS EN 315: plywood - Tolerances and dimensions, 2000.
[174] ISO, ISO/FDIS 10456: Building materials and products - Hygrothermal properties - Tabulated design values and procedures for determining declared and design thermal values, Geneva, 2007.
[175] I. Macdonald, Quantifying the effects of uncertainty in building simulation, University of Strathclyde, 2002.
[176] BS, BS EN 1602: thermal insulating products for building applications - Determination of the apparent density, 1997.
[177] A. Willockx, Using the inverse heat conduction problem and thermography for the determination of local heat transfer coefficients and fin effectiveness for longitudinal fins, Ghent University, 2009.
[178] N. Artmann, Cooling of the building structure by night-time ventilation, Aalborg University, 2010.
[179] M. Steeman, M. Van Belleghem, M. De Paepe, A. Janssens, Experimental validation and sensitivity analysis of a coupled BES-HAM model, Building and Environment, 45 (10) (2010) 2202-2217.

[180] A. Saltelli, K. Chan, E.M. Scott, Sensitivity analysis, John Wiley & Sons Ltd., Chichester, 2000.
[181] J. Sacks, W.J. Welch, T.J. Mitchell, H.P. Wynn, Design and analysis of computer experiments, Statistical Science, 4 (4) (1989) 409-435.
[182] P.V. Nielsen, Flow in air conditioned rooms, Technical University of Denmark, 1974.
[183] G.C. da Graca, Q. Chen, L.R. Glicksman, L.K. Norford, Simulation of wind-driven ventilative cooling systems for an apartment building in Beijing and Shanghai, Energy and Buildings, 34 (1) (2002) 1-11.
[184] T. Catalina, J. Virgone, F. Kuznik, Evaluation of thermal comfort using combined CFD and experimentation study in a test room equipped with a cooling ceiling, Building and Environment, 44 (8) (2009) 1740-1750.
[185] G.H. Yeoh, R.K.K. Yuen, S.C.P. Cheung, W.K. Kwok, On modelling combustion, radiation and soot processes in compartment fires, Building and Environment, 38 (6) (2003) 771-785.
[186] H.J. Steeman, Modelling local hygrothermal interaction between airflow and porous materials for building applications, Ghent University, 2009.
[187] H.J. Steeman, M. Van Belleghem, A. Janssens, M. De Paepe, Coupled simulation of heat and moisture transport in air and porous materials for the assessment of moisture related damage, Building and Environment, 44 (10) (2009) 2176-2184.
[188] A.M. Malkawi, G. Augenbroe, Advanced building simulation, Taylor & Francis, New York, 2003.
[189] Z.Q. Zhai, Application of computational fluid dynamics in building design: aspects and trends, Indoor and Built Environment, 15 (4) (2006) 305-313.
[190] H.K. Versteeg, W. Malalasekera, An introduction to computational fluid dynamics: the finite volume method, Second ed., Pearson Education Limited, Essex, 2007.
[191] D.N. Sorensen, P.V. Nielsen, Quality control of computational fluid dynamics in indoor environments, Indoor Air, 13 (1) (2003) 2-17.
[192] W.L. Oberkampf, F.G. Blottner, Issues in computational fluid dynamics: code verification and validation, Sandia National Laboratories, Albuquerque, 1997.
[193] M. Casey, T. Wintergerste, Quality and trust in industrial CFD: best practice guidelines, in: T.A.C. European Research Community On Flow (Ed.), 2000.
[194] A.D. Lemaire, Annex 20 - Air flow patterns within buildings. Room air and contaminant flow - Evaluation of computational methods, TNO Building and Construction, Delft, 1993.
[195] Z.Q. Zhai, Z. Zhang, W. Zhang, Q. Chen, Evaluation of various turbulence models in predicting airflow and turbulence in enclosed environments by CFD - Part 1: summary of prevalent turbulence models, HVAC&R Research, 13 (6) (2007) 853-870.
[196] Q. Chen, Comparison of difference k-ε models for indoor air flow computations, Numerical Heat Transfer Part B: Fundamentals, 28 (3) (1995) 353-369.

[197] Z. Zhang, Z.Q. Zhai, W. Zhang, Q.Y. Chen, Evaluation of various turbulence models in predicting airflow and turbulence in enclosed environments by CFD - Part 2: comparison with experimental data from literature, HVAC&R Research, 13 (6) (2007) 871-886.
[198] Q. Chen, J. Srebric, A procedure for verification, validation and reporting of indoor environment CFD analyses, HVAC&R Research, 8 (2) (2002) 201-216.
[199] J. Srebric, Simplified methodology for indoor environment design, Massachusetts Institute of Technology, 2000.
[200] J.H. Ferziger, M. Perić, Computational methods for fluid dynamics, Third ed., Springer Verlag, Berlin, Heidelberg, New York, 2002.
[201] Fluent Inc., Fluent 6.3.26, Lebanon, 2006.
[202] C.J. Roy, F.G. Blottner, Methodology for turbulence model validation: application to hypersonic flows, Journal of Spacecraft and Rockets, 40 (3) (2003) 313-325.
[203] C.J. Roy, C.C. Nelson, T.M. Smith, C.C. Ober, Verification of Euler/Navier-Stokes codes using the method of manufactured solutions, International Journal for Numerical Methods in Fluids, 44 (6) (2004) 599-620.
[204] F. Stern, R.V. Wilson, H.W. Coleman, E.G. Paterson, Comprehensive approach to verification and validation of CFD simulations - Part 1: methodology and procedures, Journal of Fluids Engineering-Transactions of the ASME, 123 (4) (2001) 793-802.
[205] J.H. Ferziger, M. Perić, Further discussion of numerical errors in CFD, International Journal for Numerical Methods in Fluids, 23 (1996) 1263-1274.
[206] J.W. Slater, NPARC Alliance CFD verification and validation website, 2008.
[207] W.L. Oberkampf, T.G. Trucano, C. Hirsch, Verification, validation and predictive capability in computational engineering and physics, Sandia National Laboratories, Albuquerque, 2003.
[208] F. Menter, B. Hemstrom, M. Henrikkson, R. Karlsson, A. Latrobe, A. Martin, P. Muhlbauer, M. Scheuerer, B. Smith, T. Takacs, S. Willemsen, CFD best practice guidelines for CFD code validation for reactor-safety applications, Report EVOL-ECORA-D01, 2002.
[209] C.E. Fothergill, P.T. Roberts, A.R. Packwood, Flow and dispersion around storage tanks. A comparison between numerical and wind tunnel simulations, Wind and Structures, 5 (2-4) (2002) 89-100.
[210] J. Faragher, Probabilistic methods for the quantification of uncertainty and error in computational fluid dynamics simulations, DSTO Platforms Sciences Laboratory, Victoria, 2004.
[211] C. Hirsch, V. Bouffioux, F. Wilquem, CFD simulation of the impact of new buildings on wind comfort in an urban area, in: G. Augusti, C. Borri, C. Sacré (Eds.) Impact of wind and storm on city life and built environment, Nantes, 2002, pp. 164-171.
[212] A. Scaperdas, S. Gilham, Thematic area 4: best practice advice for civil construction and HVAC, The QNET-CFD Network Newsletter, 2 (4) (2004) 28-33.

[213] J.G. Bartzis, D. Vlachogiannis, A. Sfetsos, Thematic area 5: best practice advice for environmental flows, The QNET-CFD Network Newsletter, 2 (4) (2004) 34-39.
[214] G. Schroeder, K.H. Schlünzen, F. Schimmel, Use of (weighted) essentially non-oscillating advection schemes in a mesoscale model, Quarterly Journal of the Royal Meteorological Society, 132 (2006) 1509-1526.
[215] C.J. Roy, Review of code and solution verification procedures for computational simulation, Journal of Computational Physics, 205 (1) (2005) 131-156.
[216] C.J. Freitas, The issue of numerical uncertainty, in: 2nd international conference on CFD in the minerals and process industries, Melbourne, 1999, pp. 29-34.
[217] T.J. Barth, M.G. Larson, A posteriori error estimation for higher order godunov finite volume methods on unstructured meshes, in: R. Herbin, D. Kroner (Eds.) Finite volumes for complex applications III, Hermes Science Publishing Ltd, London, 2002.
[218] L.F. Richardson, The approximate arithmetical solution by finite differences of physical problems involving differential equations with an application to the stresses in a masonry dam, Transactions of the Royal Society of London, 210 (1910) 307-357.
[219] L.F. Richardson, The deferred approach to the limit, Transactions of the Royal Society of London, 226 (1927) 229-361.
[220] P.J. Roache, Verification and validation in computational science and engineering, Hermosa, Socorro, 1998.
[221] H.W. Coleman, F. Stern, A. Di Mascio, E. Campana, The problem with oscillatory behavior in grid convergence studies, Journal of Fluids Engineering-Transactions of the ASME, 123 (2) (2001) 438-439.
[222] I. Celik, O. Karatekin, Numerical experiments on application of Richardson extrapolation with nonuniform grids, Journal of Fluids Engineering-Transactions of the ASME, 119 (3) (1997) 584-590.
[223] W.L. Oberkampf, T.G. Trucano, Validation methodology in computational fluid dynamics, Sandia National Laboratories, Denver, 2000.
[224] W.L. Oberkampf, T.G. Trucano, Verification and validation in computational fluid dynamics, Progress in Aerospace Sciences, 38 (3) (2002) 209-272.
[225] I. Babuska, H.S. Oh, Pollution problem of the p-version and h-p-versions of the finite-element method, Communications in Applied Numerical Methods, 3 (6) (1987) 553-561.
[226] J.T. Oden, Y.S. Feng, S. Prudhomme, Local and pollution error estimation for Stokesian flows, International Journal for Numerical Methods in Fluids, 27 (1998) 33-39.
[227] W.L. Oberkampf, T.G. Trucano, Verification and validation benchmarks, Sandia National Laboratories, Albuquerque, 2007.
[228] I. Celik, G. U., P. Roache, C.J. Freitas, H. Coleman, P.E. Raad, Procedure for estimation and reporting of uncertainty due to discretization in CFD applications, Journal of Fluids Engineering-Transactions of the ASME, (2008).

[229] P.J. Roache, Perspective: a method for uniform reporting of grid refinement studies, Journal of Fluids Engineering-Transactions of the ASME, 116 (3) (1994) 405-413.
[230] R.W. Johnson, E.D. Hughes, Quantification of uncertainty in computational fluid dynamics, in: ASME/JSME fluids engineering and laser anemometry conference, Hilton Head, 1995.
[231] T. Xing, F. Stern, Factors of safety for Richardson extrapolation, University of Iowa, Iowa City, 2009.
[232] l. Eça, M. Hoekstra, A verification exercise for two 2-D steady incompressible turbulent flows, in: P. Neittaanmäki, T. Rossi, K. Majava, O. Pironneau (Eds.) European congress on computational methods in applied sciences and engineering, University of Jyväskylä, Jyväskylä, 2004.
[233] P.J. Roache, Criticisms of the "correction factor" verification method, Journal of Fluids Engineering-Transactions of the ASME, 125 (4) (2003).
[234] R. Wilson, S. Jun, F. Stern, Discussion: criticisms of the "Correction factor" verification method 1, Journal of Fluids Engineering-Transactions of the ASME, 126 (4) (2004).
[235] R. Wilson, F. Stern, Verification and validation for RANS simulation of a naval surface combatant, in: Aerospace Sciences Meeting, Reno, 2002.
[236] R.W. Logan, C.K. Nitta, Comparing ten methods for solution verification and linking to model validation, Journal of Aerospace Computing, Information and Communication, 3 (2006) 354-373.
[237] O. Reynolds, On the dynamical theory of incompressible viscous fluids and the determination of the criterion (reprinted from papers on mechanical and physical subjects, Vol. 2, 535-577, 1901), Proceedings of the Royal Society of London Series A: Mathematical and Physical Sciences, 451 (1941) (1895) 5-47.
[238] J. Boussinesq, Théorie de l' écoulement tourbillant, Mémoires présentés par divers savants à l'Académie des Sciences, 23 (1897) 46-50.
[239] L. Prandtl, Bericht über Untersuchungen zur ausgebildeten Turbulenz, Zeitschrift für Angewandte Mathematik und Mechanik, 5 (1925) 136-139.
[240] P. Spalart, S. Allmaras, A one-equation turbulence model for aerodynamic flows, AIAA, 1992.
[241] B.E. Launder, D.B. Spalding, The numerical computation of turbulent flows, Computer Methods in Applied Mechanics and Engineering, 3 (2) (1974).
[242] D.C. Wilcox, Reassessment of the scale-determining equation for advanced turbulence models, AIAA Journal, 26 (11) (1988) 1299-1310.
[243] B. Merci, E. Dick, J. Vierendeels, D. Roekaerts, T.W.J. Peeters, Application of a new cubic turbulence model to piloted and bluff-body diffusion flames, Combustion and Flame, 126 (1-2) (2001) 1533-1556.
[244] P.A. Durbin, Separated flow computations with the k-ε-υ2 model, AIAA Journal, 33 (4) (1995) 659-664.
[245] B.E. Launder, G.J. Reece, W. Rodi, Progress in development of a Reynolds-stress turbulence closure, Journal of Fluid Mechanics, 68 (15) (1975) 537-566.
[246] J. Bredberg, On two-equation eddy-viscosity models, Chalmers University of Technology, Göteborg, 2001.

[247] A. Sarkar, R.M.C. So, A critical evaluation of near-wall two-equation models against direct numerical simulation data, International Journal of Heat and Fluid Flow, 18 (2) (1997) 197-208.
[248] D.C. Wilcox, Turbulence modeling for CFD, Third ed., DCW Industries, La Cañada, 2006.
[249] B.E. Launder, D.B. Spalding, Lectures in mathematical models of turbulence, Academic Press, London, 1972.
[250] K. Van Maele, B. Merci, Application of two buoyancy-modified k-ε turbulence models to different types of buoyant plumes, Fire Safety Journal, 41 (2) (2006) 122-138.
[251] V. Yakhot, S.A. Orszag, Renormalization group analysis of turbulence. I. Basic theory, Journal of Scientific Computing, 1 (1) (1986).
[252] T.-H. Shih, W.W. Liou, A. Shabbir, Y. Zhigang, Z. Jiang, A new k-ε eddy viscosity model for high Reynolds number turbulent flows, Computers & Fluids, 24 (3) (1995).
[253] M. Wolfstein, The velocity and temperature distribution of one-dimensional flow with turbulence augmentation and pressure gradient, International Journal of Heat and Mass Transfer, 12 (1969) 301-318.
[254] A.N. Kolmogorov, Equations of turbulent motion of an incompressible fluid, Izv Akad Nauk SSR Ser Phys, 6 (1/2) (1942) 56.
[255] K.G. Gebremedhin, B. Wu, Characterization of flow field in a ventilated space and simulation of heat exchange between cows and their environment, Journal of Thermal Biology, 28 (4) (2003) 301-319.
[256] A. Stamou, I. Katsiris, Verification of a CFD model for indoor airflow and heat transfer, Building and Environment, 41 (9) (2006) 1171-1181.
[257] F.R. Menter, Two-equation eddy-viscosity turbulence models for engineering applications, AIAA Journal, 32 (8) (1994) 1598-1605.
[258] G.Y. Chen, Simulation of test case B (forced convection, isothermal) - IEA Annex 20, Research item 1.21, ETH, Zurich, 1990.
[259] P.O. Tjelflaat, F. Frydenlund, Simulation of test case B (forced convection, isothermal) - IEA Annex 20, Research item 1.19, SINTEF, Trondheim, 1990.
[260] L. Davidson, P.V. Nielsen, Sveningsson, Modification of the υ²f-model for computing the flow in a 3D wall jet, Turbulence Heat and Mass Transfer, 4 (2003) 577-584.
[261] M.M. Gibson, B.E. Launder, Ground effects on pressure fluctuations in the atmospheric boundary layer, Journal of Fluid Mechanics, 86 (1978) 491-511.
[262] G.Y. Chen, Z. Zhai, The use of CFD tools for indoor environmental design, in: A. Malkawi, G. Augenbroe (Eds.) Advanced Building Simulation, Spon Press, New York, 2004, pp. 119-140.
[263] G.Y. Chen, W.R. Xu, A zero-equation turbulence model for indoor airflow simulation, Energy and Buildings, 28 (2) (1998) 137-144.
[264] M.A.R. Sharif, W. Liu, Numerical study of turbulent natural convection in a side-heated square cavity at various angles of inclination, Numerical Heat Transfer Part A: Applications, 43 (7) (2003) 693-716.

[265] P.C. Walsh, W.H. Leong, Effectiveness of several turbulence models in natural convection, International Journal of Numerical Methods for Heat & Fluid Flow, 14 (5-6) (2004) 633-648.
[266] T. Yang, CFD and field testing of a naturally ventilated full-scale building, University of Nottingham, 2004.
[267] B.A. Craven, G.S. Settles, A computational and experimental investigation of the human thermal plume, Journal of Fluids Engineering-Transactions of the ASME, 128 (6) (2006) 1251-1258.
[268] L.K. Voigt, Comparison of turbulence models for numerical calculation of air flow in an Annex 20 room, Technical University of Denmark, Lyngby, 2000.
[269] O. Rouaud, M. Havet, Computation of the airflow in a pilot scale clean room using k-ε turbulence models, International Journal of Refrigeration-Revue Internationale Du Froid, 25 (3) (2002) 351-361.
[270] J.D. Posner, C.R. Buchanan, D. Dunn-Rankin, Measurement and prediction of indoor air flow in a model room, Energy and Buildings, 35 (5) (2003) 515-526.
[271] R.M. Susin, G.A. Lindner, V.C. Mariani, K.C. Mendonca, Evaluating the influence of the width of inlet slot on the prediction of indoor airflow: comparison with experimental data, Building and Environment, 44 (5) (2009) 971-986.
[272] G. Cao, M. Ruponen, R. Paavilainen, J. Kurnitski, Modelling and simulation of the near-wall velocity of a turbulent ceiling attached plane jet after its impingement with the corner, Building and Environment, 46 (2) (2011) 489-500.
[273] Q. Chen, Prediction of room air motion by Reynolds-stress models, Building and Environment, 31 (3) (1996) 233-244.
[274] M.G.L.C. Loomans, The measurement and simulation of indoor airflow, Eindhoven University of Technology, 1998.
[275] J.J. Costa, L.A. Oliveira, D. Blay, Test of several versions for the k-ε type turbulence modelling of internal mixed convection flows, International Journal of Heat and Mass Transfer, 42 (23) (1999) 4391-4409.
[276] Y. Nagano, M. Hishida, Improved form of the k-ε model for wall turbulent shear flows, Journal of Fluids Engineering-Transactions of the ASME, 109 (2) (1987) 156-160.
[277] X. Yuan, Q. Chen, L. Glicksman, Y. Hu, X. Yang, Measurements and computations of room air flow with displacement ventilation, ASHRAE Transactions, 105 (1) (1999) 340-352.
[278] X. Yuan, Q. Chen, L. Glicksman, Models for prediction of temperature difference and ventilation effectiveness with displacement ventilation, ASHRAE Transactions, 105 (1) (1999) 353-367.
[279] S.C. Sekhar, H.C. Willem, Impact of airflow profile on indoor air quality - a tropical study, Building and Environment, 39 (3) (2004) 255-266.
[280] H.B. Nahor, M.L. Hoang, P. Verboven, M. Baelmans, B.M. Nicolai, CFD model of the airflow, heat and mass transfer in cool stores, International Journal of Refrigeration-Revue Internationale Du Froid, 28 (3) (2005) 368-380.
[281] L. Zhang, T.T. Chow, Q. Wang, K.F. Fong, L.S. Chan, Validation of CFD model for research into displacement ventilation, Architectural Science Review, 48 (4) (2005) 305-316.

[282] Z. Zhang, Q. Chen, Experimental measurements and numerical simulations of particle transport and distribution in ventilated rooms, Atmospheric Environment, 40 (18) (2006) 3396-3408.
[283] F. Kuznik, G. Rusaouën, J. Brau, Experimental and numerical study of a full scale ventilated enclosure: comparison of four two equations closure turbulence models, Building and Environment, 42 (3) (2007) 1043-1053.
[284] P. Rohdin, B. Moshfegh, Numerical modelling of industrial indoor environments: a comparison between different turbulence models and supply systems supported by field measurements, Building and Environment, 46 (11) (2011) 2365-2374.
[285] P. Rohdin, B. Moshfegh, Numerical predictions of indoor climate in large industrial premises. A comparison between different k-ε models supported by field measurements, Building and Environment, 42 (11) (2007) 3872-3882.
[286] M. Skovgaard, P.V. Nielsen, Modelling complex geometries in CFD - applied to air ventilated rooms, in: 12th AIVC conference, Ottawa, 1991, pp. 183-200.
[287] M. Cehlin, B. Moshfegh, Numerical modeling of a complex diffuser in a room with displacement ventilation, Building and Environment, 45 (10) (2010) 2240-2252.
[288] J. Heikkinen, Modelling of supply air terminal for room airflow simulation, in: 12th AIVC conference, Ottawa, 1991, pp. 24-27.
[289] R.L. Jensen, D. Holm, P.V. Nielsen, Detailed measurement on a HESCO diffuser, in: Roomvent 2007: 10th international conference on air distribution in rooms, FINVAC, Helsinki, 2007.
[290] M. Ewert, U. Renz, N. Vogl, M. Zeller, Definition of the flow parameters at the room inlet devices - Measurements and calculations, in: 12th AIVC conference, Ottawa, 1991, pp. 231-237.
[291] Q. Chen, A. Moser, Simulation of a multiple nozzle diffuser, in: Ottawa, 12th AIVC conference, 1991, pp. 1-14.
[292] P. Emvin, L. Davidson, A numerical comparison of three inlet approximations of the diffuser in case E1 Annex 20, in: Roomvent 1996: 5th international conference on air distribution in rooms, Yokohama, 1996, pp. 219-226.
[293] P.V. Nielsen, Description of supply openings in numerical models for room air distribution, ASHRAE Transactions, 98 (1992) 963-971.
[294] E. Djunaedy, K.W.D. Cheong, Development of a simplified technique of modelling four-way ceiling air supply diffuser, Building and Environment, 37 (4) (2002) 393-403.
[295] B. Zhao, X.T. Li, Q.S. Yan, A simplified system for indoor airflow simulation, Building and Environment, 38 (4) (2003) 543-552.
[296] Y. Sun, T.F. Smith, Air flow characteristics of a room with square cone diffusers, Building and Environment, 40 (5) (2005) 589-600.
[297] T. Zhang, K. Lee, Q. Chen, A simplified approach to describe complex diffusers in displacement ventilation for CFD simulations, Indoor Air, 19 (3) (2009) 255-267.

[298] S. Luo, B. Roux, Modeling of the HESCO nozzle diffuser used in IEA Annex-20 experiment test room, Building and Environment, 39 (4) (2004) 367-384.
[299] S. Luo, J. Heikkinen, B. Roux, Simulation of air flow in the IEA Annex 20 test room - Validation of a simplified model for the nozzle diffuser in isothermal test cases, Building and Environment, 39 (12) (2004) 1403-1415.
[300] J. Heikkinen, Measurement of test case B2, B3, E2 and E3 (isothermal and summer cooling cases). Research item No. 1.16F and 1.17SF, Technical Research Centre of Finland, Espoo, 1991.
[301] H.B. Awbi, Application of computational fluid dynamics in room ventilation, Building and Environment, 24 (1) (1989) 73-84.
[302] P. Joubert, A. Sandu, C. Beghein, F. Allard, Numerical study of the influence of inlet boundary conditions on the air movement in a ventilated room, in: Roomvent 1996: 5th international conference on air distribution in rooms, Yokohama, 1996, pp. 235-242.
[303] Q. Chen, P. Suter, A. Moser, A database for assessing indoor airflow, air quality and draught risk, ASHRAE Transactions, 97 (2) (1991) 150-163.
[304] Z. Jiang, Q. Chen, A. Moser, Comparison of displacement and mixing diffusers, Indoor Air, 2 (3) (1992) 168-179.
[305] H. Koskela, Momentum source model for CFD-simulation of nozzle duct air diffuser, Energy and Buildings, 36 (10) (2004) 1011-1020.
[306] J. Srebric, Q.Y. Chen, Simplified numerical models for complex air supply diffusers, HVAC&R Research, 8 (3) (2002) 277-294.
[307] P.V. Nielsen, Models for the prediction of room air distribution, in: 12th AIVC conference, 1991, pp. 55-71.
[308] P.V. Nielsen, The box method - a practical procedure for introduction of an air supply device in CFD calculation, Aalborg University, Aalborg, 1997.
[309] Y. Huo, F. Haghighat, S. Zhang, C.Y. Shaw, A systematic approach to describe the air terminal device CFD simulation for room air distribution analysis, Building and Environment, 35 (6) (2000) 563-576.
[310] M.I. Grimitlyn, G.M. Pozin, Fundamentals of optimizing air distribution in ventilated spaces, ASHRAE Transactions, 99 (1) (1993) 1128-1138.
[311] A.D. Gosman, P.V. Nielsen, A. Restivo, J.H. Whitelaw, The flow properties of rooms with small ventilation openings, Journal of Fluids Engineering-Transactions of the ASME, 102 (3) (1980) 316-323.
[312] P.V. Nielsen, Representation of boundary conditions at supply openings (IEA Annex 20), Aalborg University, Aalborg, 1989.
[313] K. Svidt, Investigation of inlet boundary conditions for numerical prediction of air flow in livestock buildings, in: Roomvent 1994: 4th international conference on air distribution in rooms, Krakow, 1994.
[314] J.R. Fontaine, F. Biolley, R. Rapp, J.C. Sérieys, J.C. Cunin, Analysis of a 3-dimensional ventilation flow - Experimental validation on a water scale-model of numerical simulations, Numerical Heat Transfer Part A: Applications, 26 (4) (1994) 431-451.

[315] G. Einberg, K. Hagstrom, P. Mustakallio, H. Koskela, S. Holmberg, CFD modelling of an industrial air diffuser - Predicting velocity and temperature in the near zone, Building and Environment, 40 (5) (2005) 601-615.
[316] S. Fossdal, Measurement of test case E - Mixed convection, summer cooling, in: IEA Annex 20, 1990.
[317] J. Srebric, Q. Chen, Simplified diffuser boundary conditions for numerical room airflow models - Final report for ASHRAE RP-1009, Massachusetts Institute of Technology, Cambridge, 2000.
[318] J. Srebric, Q. Chen, A method of test to obtain diffuser data for CFD modelling of room airflow (RP-1009), ASHRAE Transactions, 107 (2) (2001) 108-116.
[319] K. Goethals, I. Couckuyt, T. Dhaene, A. Janssens, Sensitivity of night cooling performance to room/system design: surrogate models based on CFD, submitted to Building and Environment, (2012).
[320] E. Djunaedy, External coupling between building energy simulation and computational fluid dynamics, Eindhoven University of Technology, 2005.
[321] M. Mirsadeghi, Co-simulation of building energy simulation and computational fluid dynamics for whole-building heat, air and moisture engineering, Eindhoven University of Technology, 2010.
[322] A. Keane, P. Nair, Computational approaches for aerospace design: the pursuit of excellence, John Wiley & Sons Ltd., Chichester, 2005.
[323] A. Forrester, A. Sobester, A. Keane, Engineering design via surrogate modelling: a practical guide, John Wiley & Sons Ltd., Chichester, 2008.
[324] D. Gorissen, Grid-enabled adaptive surrogate modelling for computer aided engineering, Ghent University/University of Antwerp, 2010.
[325] M. Meckesheimer, A framework for metamodel-based design: subsystem metamodel assessment and implementation issues, Pennsylvania State University, 2001.
[326] D. Gorissen, T. Dhaene, F. De Truck, Evolutionary model type selection for global surrogate modelling, Journal of Machine Learning Research, 10 (2009) 2039-2078.
[327] D. Gorissen, I. Couckuyt, P. Demeester, T. Dhaene, K. Crombecq, A surrogate modeling and adaptive sampling toolbox for computer based design, Journal of Machine Learning Research, 11 (2010) 2051-2055.
[328] D. Gorissen, K. Crombecq, I. Couckuyt, T. Dhaene, Automatic approximation of expensive functions with active learning, in: Foundations of computational intelligence volume 1: learning and approximation, Springer Verlag, 2009, pp. 35-62.
[329] D. Gorissen, I. Couckuyt, E. Laermans, T. Dhaene, Multiobjective global surrogate modeling, dealing with the 5-percent problem, Engineering with Computers, 26 (1) (2010) 81-98.
[330] J. Degroote, I. Couckuyt, J. Vierendeels, P. Segers, T. Dhaene, Inverse modelling of an aneurysm's stiffness using surrogate-based optimization of a three-dimensional fluid-structure interaction simulation, in: ECCOMAS thematic conference: CFD and optimization, ECCOMAS, Antalya, 2011.

[331] I. Couckuyt, F. Declercq, T. Dhaene, H. Rogier, Surrogate-based infill optimization applied to electromagnetic problems, Advances in design optimization of microwave/RF circuits and systems (special issue), 20 (2010) 492.
[332] H. Schwenke, Über das Verhalten ebener horizontaler Zuluftstrahlen im begrenzten Raum, Luft- und Kältetechnik, (1975).
[333] P.V. Nielsen, The selection of turbulence models for prediction of room airflow, ASHRAE Transactions, 104 (1) (1998) 1119-1127.
[334] D.N. Sorensen, C.J. Weschler, Modeling-gas phase reactions in indoor environments using computational fluid dynamics, Atmospheric Environment, 36 (1) (2002) 9-18.
[335] P.V. Nielsen, CFD-benchmarks.com, Aalborg.
[336] P.V. Nielsen, Specification of a two-dimensional test case, Aalborg University, Aalborg, 1990.
[337] MathWorks, Matlab, Natick, 2011.
[338] T.J. Baker, Mesh adaptation strategies for problems in fluid dynamics, Finite Elements in Analysis and Design, 25 (3-4) (1997) 243-273.
[339] D.S. McRae, r-Refinement grid adaptation algorithms and issues, Computer Methods in Applied Mechanics and Engineering, 189 (4) (2000) 1161-1182.
[340] R.A. Fisher, The design of experiments, Olyver and Boyd, Edinburgh, 1935.
[341] L. Eriksson, E. Johansson, N. Kettaneh-Wold, C. Wikström, S. Wold, Design of experiments: principles and applications, MKS Umetrics AB, 2008.
[342] K. Fang, R. Li, A. Sudjianto, Design and modeling for computer experiments, Chapman & Hall/CRC, London, 2006.
[343] J.P.C. Kleijnen, S.M. Sanchez, T.W. Lucas, T.M. Cioppa, A user's guide to the brave new world of designing simulation experiments, Informs Journal on Computing, 17 (3) (2005) 263-289.
[344] N.V. Queipo, R.T. Haftka, W. Shyy, T. Goel, R. Vaidyanathan, P.K. Tucker, Surrogate-based analysis and optimization, Progress in Aerospace Sciences, 41 (1) (2005) 1-28.
[345] V.C.P. Chen, K.L. Tsui, R.R. Barton, M. Meckesheimer, A review on design, modeling and applications of computer experiments, IIEE Transactions, 38 (4) (2006) 273-291.
[346] G.G. Wang, S. Shan, Review of metamodeling techniques in support of engineering design optimization, Journal of Mechanical Design, 129 (4) (2007) 370-380.
[347] H.J. Kuschner, A new method of locating the maximum point of an arbitrary multipeak curve in the presence of noise, Journal of Basic Engineering, 86 (1964) 97-106.
[348] D. Jones, M. Scholau, W.J. Welch, Efficient global optimization of expensive black-box functions, Journal of Global Optimization, 13 (4) (1998) 455-492.
[349] D.R. Jones, A taxonomy of global optimization methods based on response surfaces, Journal of Global Optimization, 21 (4) (2001) 345-383.
[350] A. Forrester, D. Jones, Global optimization of deceptive functions with sparse sampling, in: 12th AIAA/ISSMO multidisciplinary analysis and optimization conference, Victoria, 2008.

[351] D.R. Jones, C.D. Perttunen, B.E. Stuckman, Lipschitzian optimization without the Lipschitz constant, Journal of Optimization Theory and Applications, 79 (1) (1993) 157-181.
[352] D.G. Krige, A statistical approach to some basic mine valuation problems on the Witwatersand, Journal of the Chemical, Metallurgical and Mining Engineering Society of South Africa, 52 (6) (1951) 119-139.
[353] Q. Chen, Simulation of simple test cases, Swiss Federal Institute of Technology Zurich, Zurich, 1991.
[354] A.D. Lemaire, Simulation of simple test cases 2D-1, 2D-2, TNO Building and Construction, Delft, 1991.
[355] M.N. Said, Simulation of a two-dimensional benchmark test case, Institute for Research in Construction, Ottawa, 1991.
[356] N. Vogl, U. Renz, Simulation of simple test cases, Lehrstuhl für Wärmeübertragung und Klimatechnik, Aachen, 1991.